Scientific
Research
Publishing

Journal of
Modern Physics

9 772153 119007   04

https://www.scirp.org/journal/jmp

Table of Contents

Volume 12   Number 4   March 2021

Journal of Modern Physics (JMP)
Journal Information

SUBSCRIPTIONS

SERVICES

Advertisements

Advertisement Sales Department, E-mail: service@scirp.org

Reprints (minimum quantity 100 copies)

Reprints Co-ordinator, Scientific Research Publishing, Inc., USA.

E-mail: sub@scirp.org

COPYRIGHT

PRODUCTION INFORMATION

Experimental Validation and Application of a Phased Array Ultrasonic Testing Model on Sound Field Optimization

Xiangyu Lei[1*], Håkan Wirdelius[1], Anders Rosell[2]

[1]Department of Industrial and Materials Science, Chalmers University of Technology, Gothenburg, Sweden
[2]GKN Aerospace Sweden AB, Flygmotorvägen 1, Trollhättan, Sweden
Email: *xlei@chalmers.se

Abstract

In safety dominant industries, nondestructive evaluation (NDE) is crucial in quality assurance and assessment. Phased array ultrasonic testing (PAUT) as one of the NDE methods is more promising compared with conventional ultrasonic testing (UT) method in terms of inspection speed and flexibility. To incorporate PAUT, the techniques should be qualified, which traditionally is performed by extensive physical experiments. However, with the development of numerical models simulating UT method, it is expected to complement or partly replace the experiments with the intention to reduce costs and operational uncertainties. The models should be validated to ensure its consistency to reality. This validation work can be done by comparing the model with other validated models or corresponding experiments. The purpose of current work focuses on the experimental validation of a numerical model, simSUNDT, developed by the Chalmers University of Technology. Validation is conducted by comparing different data presentations (A-, B- and C-scan) from experimental and simulated results with some well-defined artificial defects. Satisfactory correlations can be observed from the comparisons. After the validation, sound field optimization work aiming at retrieving maximized echo amplitude on a certain defect can be started using the model. This also reveals the flexibility of parametric studies using simulation models.

Keywords

Experiments, Simulation, Validation, Sound Field Optimization

1. Introduction

In safety prioritized industries such as aerospace industry, newly adopted and

advanced technologies of Additive Manufacturing (AM) enable innovative designs of complex-shaped components and have the potential to broaden the manufacturing possibilities. Since the safety aspect is crucial and must not be compromised, these new manufacturing approaches demand even higher accuracy and reliability in quality assessments. Nondestructive evaluation (NDE) is used to ensure the quality and integrity of the manufactured components and among others, conventional ultrasonic testing (UT) has been widely used in industries [1]. Within this area, the phased array ultrasonic testing (PAUT) technique has many possible advantages over conventional single-element UT methods in terms of operational flexibility and increased inspection speed [2]. However, the complexity and flexibility of PAUT raise the need of understanding the technique in qualification and evaluation procedures. There is also a need of adjustment for AM-specific defect characteristics and geometrical constraints of specific parts.

The traditional approach to qualification work is associated with extensive and expensive physical experiments. However, with the development of mathematical modelling of NDE methods in the last decades, the experimental work can be supported or partly replaced by the model-based data, provided that the model itself has been validated [3]. The validation of the mathematical model can be done by comparing it with other already validated models, but it should ultimately be compared with physical experiments in all perspectives to ensure its accuracy. Some works had been devoted to experimental validation of a simulation model in terms of PAUT, see for example [4] and [5].

The phased array (PA) probe model implemented in a UT simulation software, simSUNDT, developed by the Chalmers University of Technology, had been validated to some extent in terms of maximum echo amplitude towards well-defined artificial defects, *i.e.* side-drilled holes (SDHs) [6]. In the current paper, the model is to be further validated by comparing the data presentations (A-, B- and C-scan). These are retrieved from both experiments and corresponding simulations, which address some well-defined artificial defects in noise-free test specimens. Satisfactory correlations can be observed from the comparisons and the model can be concluded as an alternative to the corresponding experiments. The generated sound fields towards a certain type of defect, *i.e.* surface breaking crack, are optimized with the help of this validated model as an applied practice. The optimization in this work aims at retrieving a maximized echo amplitude by adjusting the combination of probe angle and focusing distance, which is easy and essential to change in the phased array configuration. The possibility and procedure of using the simulation model in sound field optimization work is hereby investigated.

2. simSUNDT Software

The simSUNDT software, developed at Chalmers University of Technology, composes of a Windows-based processor for simulation definition and result

analysis. A mathematical kernel, UTDefect, which conducts the actual mathematical modelling [7] [8] [9] [10], has been validated by comparing with previous done and in literature available experiments [7] [8] [9] [11]. The 3D elastodynamic wave equation that defines the wave propagation in a homogeneous half space is solved by using vector wave functions [10]. The modelled geometry can be described as a plate bounded by the scanning surface, on which rectangular mesh is used to define the scanning sequence. Scattering by defects is solved using analytical or semi-analytical methods.

The simSUNDT can simulate the entire NDE inspection. In order to accomplish this, calibration option with reference reflector is available. These reflectors include side-drilled hole (SDH) [12] and flat-bottom hole (FBH), which is represented by a cylindrical cavity and an open circular crack, respectively.

The volumetric and crack-like defects are available types of defect to be simulated. The volumetric ones include a spherical/spheroid cavity (pore), a spherical inclusion (isotropic material differing from the surrounding material, *i.e.* slag) and a cylindrical cavity (SDH). Crack-like ones include rectangular/circular crack (lack of fusion) and strip-like crack (fatigue crack). Tilting planar back surface could also be modelled for the strip-like crack, but it is otherwise assumed parallel to the scanning surface. The surface-breaking strip-like crack and rectangular crack close to the back surface can be used to model the corresponding defects in the test piece.

The conventional contact probe is represented as the boundary conditions representing a plane wave in the far-field at a certain angle. Different traction conditions represent different probe types under the effective area and are assumed to be zero elsewhere. This enables the possibilities of simulating any types of the probe available on the market, by specifying related parameters such as wave types, crystal size and shape, angles, frequency ranges, contact conditions, etc. In addition, it is also possible to suppress the mode-converted wave component in the simulation to eventually facilitate the analysis of the received signal. By modelling the receiver, a reciprocity argument [13] is applied. The arrangement of the probe can be chosen among pulse-echo, separate with fixed transmitter and tandem configuration (TOFD).

Above principles are the same for the PA probe model, *i.e.* the individual element is represented by the corresponding boundary conditions. The individual boundary conditions are translated into the main coordinate system and a PA wave front with certain nominal angle is formulated by constructive phase interference.

3. Experiments

3.1. Experimental Instruments and Test Specimens

The data acquisition hardware TOPAZ64 is a portable 64-channel PAUT device. It is connected to a computer with data communication through Gigabyte Ethernet cable. Operations are monitored on software UltraVision, which pro-

vides real-time data presentation and visualization. The linear PA probe connected to TOPAZ64 is labelled as LM-5MHz, which contains 64 elements that generate longitudinal waves. As indicated by its nomination, the nominal center frequency is 5 MHz and bandwidth (−6 dB) is 74%. Table 1 lists some key specifications of this probe. In addition, two plastic wedges with and without angle labelled as LM-55SW and LM-0LW, respectively, are incorporated in all experiments to protect the probe surface and to facilitate fixation of the probe on the mechanized gantry system. This gantry system is motor-controlled in horizontal (x-y) plane while the vertical position (z-axis) is manually adjusted at this moment. The bottom end of the z-axis has a spring load fork that can clamp the wedge with probe. The motors are embedded with encoders so that the horizontal position of the probe can be obtained and read by UltraVision to present position-related visualizations.

There are two stainless-steel test specimens with different artificial defects (SDH and surface breaking crack) included in this work, see Figure 1. The first specimen (#1) has 6 SDHs (2 mm in diameter) at depth from 10 mm to 60 mm with increment of 10 mm. The second one (#2) has 5 vertical surface breaking cracks (tilt angle of 0-degree) with height of 0.5 mm, 2 mm, 5 mm, 10 mm and 15 mm. Table 2 summarizes the overall dimension and acoustic properties of

Table 1. Specification of the linear PA probe used in the experiment.

Specification	Value
Total elements	64
Total length (mm)	38.3
Elevation (mm)	10
Pitch (mm)	0.6
Kerf	0.1
Center frequency (MHz)	5
Relative bandwidth (%)	74
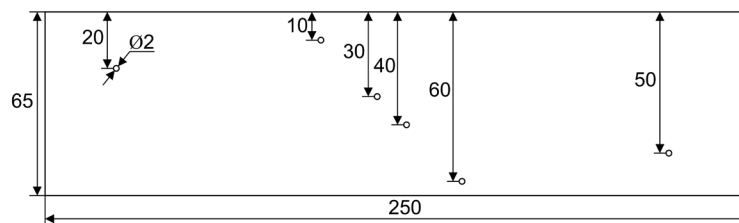
(a) Test specimen #1 with SDHs at different depth
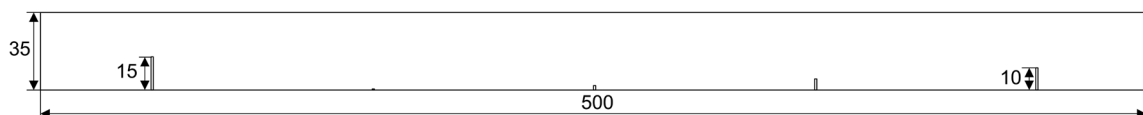
(b) Test specimen #2 with cracks, height from left to right is 15 mm, 0.5 mm (too small to be seen in the figure), 2 mm, 5 mm, 10 mm

Figure 1. Sketch profiles of the test specimens.

Table 2. Dimensions and acoustic properties of specimens.

No.	Length (mm)	Height (mm)	Width (mm)	L-wave speed (m/s)	T-wave speed (m/s)
#1	250	65	39	5640	3110
#2	500	35	50	5573	3150

these specimens and all these defects span through the entire width of each specimen.

3.2. Experimental Configurations

The validations presented in the current work aim at comparing different data presentations (A-scan from the maximum echo amplitude, B- and C-scans) between physical experiments and corresponding simulations. Data acquisition is performed in pulse-echo mode and the probe inspects a test specimen with one-line scan on the specimen surface to obtain the signals from all involved defects at once.

On the first test specimen (#1), only the SDH at 50 mm depth is studied under four inspection cases, *i.e.* (a) non-angled sound beam without focusing effect; (b) non-angled sound beam with focusing at 50 mm depth; (c) 45-degree angled sound beam without focusing effect and (d) 45-degree angled sound beam with focusing at 50 mm depth. The direct echo from the SDH is stored as received signal.

On the second test specimen (#2), all cracks except the largest one (height of 15 mm) are studied under two general inspection cases, *i.e.* (a) 45-degree angled sound beam without focusing effect and (b) 45-degree angled sound beam with focusing at 35 mm depth. The surface breaking cracks are positioned so that the openings are on the bottom surface and corner echoes are the received signals.

Within all these inspection cases, only the central 16 elements are activated in non-focusing cases to prevent ghost images, whereas all 64 elements are activated to generate proper focusing effect.

4. Simulation Configuration

To compare with experimental data presentations, the corresponding one-line scan simulations must cover a certain scan interval. This is to ensure that the maximum echo amplitude from the defect of interest can be retrieved to be presented in A-scan, and that sufficient amount of scan positions can be covered to visualize the defect in B-scan and echo dynamic curve in C-scan. Furthermore, the sampling time steps of A-scan signals should be small enough to ensure the accuracy of detailed comparisons. Under above reasons, all simulations for validation purpose are conducted in large scan and time intervals with scan increment of 0.1 mm and time step of 0.005 μs. These simulation parameters were determined in such a way that the resulted data presentations have a decent resolution to be compared with experiments. Parameters related to the PA probe

are set in accordance with the physical probe as in Table 1.

As expected, the simulation time is positively correlated with the amount of scan and time positions, as well as the complexity of studied defect and inspection scenario. The simulation times of cracks with height of 5 mm and 10 mm involving focusing effect were observed to be extensively long using above mentioned simulation configurations. To avoid this, only certain scan and time intervals where the maximum echo amplitudes are expected were simulated for these two cracks with focusing effect, while still keeping the scan increment of 0.1 mm and time step of 0.005 μs unchanged. For this reason, the B-scan comparisons are neglected for these two cases due to insufficient scan positions.

5. Probe Skew Angle Sensitivity

For the physical experiments, there could be some practical uncertainties in the system affecting the results, one example is the probe skew angle. In order to explore if the minor variation of the probe skew angle can influence the received data, some parametric studies were performed with a set of probe skew angles, ranging from −5˚ to 5˚ with an increment of 0.5˚. The simulations were performed towards the SDH at 50 mm depth in test specimen #1 under the inspection case of 45-degree angled beam with 50 mm focus depth, just as the case (d) on test specimen #1 in the experimental configurations. These simulated results are compared with available experimental data.

6. Optimization of Received Signal

It is noted that the optimization of the received signal is equivalent to the sound field in this pulse-echo situation. With the help of this simulation model and its flexibility of parametric studies, the generated sound field from a PA probe is explored to be optimized in order to receive a maximized echo amplitude towards a crack, which has a specific character, *i.e.* size and tilt angle. The considered decision variables to this optimization problem are the probe (beam) angle and focus distance in this work.

The optimization algorithm considered in this work is heuristic Nelder-Mead based Simplex method [14] [15] that solves non-linear single-objective optimization problems. This method compares the objective values at each chosen simplex vertex and moves the next simplex vertex accordingly based on the result evaluations using different operation strategies, *i.e.* reflection, expansion, contraction and shrink.

The optimization procedure using Simplex algorithm is conducted using software modeFrontier (2020R1), in which the decision variables to an optimization problem are explored. Simulation outputs from simSUNDT can be imported into modeFrontier to help with optimization evolution according to the chosen algorithm.

As mentioned earlier, the simulation towards a large crack where the focusing effect is involved takes extensive simulation time. It is therefore inefficient and

unfeasible to conduct the actual optimization work based on the simulation configuration (large scan interval, small scan increment, nominal probe bandwidth of 74%, etc.) described in simulation configuration for validation purpose. Based on previous simulation experiences, the simulation time depends positively on the number of involved wave frequencies. Therefore, variations of probe bandwidth are investigated in Table 3 in terms of simulation time and the influence on interested simulation output, *i.e.* the maximum echo amplitude. The simulated defect is a surface breaking crack (opening at bottom surface) with 10 mm height and 0-degree tilt angle, corresponds to the 10 mm height crack in test specimen #2. Simulation scenario is 45-degree probe angle and 49.49 mm focus distance (corresponds to 35 mm focus depth). The scan interval is chosen so that within which the maximum echo amplitude is expected to appear. Scan positions are uniformly distributed inside this interval.

The maximum echo amplitude of 76.8 dB in investigation No.1 obtained with nominal probe bandwidth of 74% is taken as a standard value to upcoming variants (No.2 and 3). Investigation No.2 where bandwidth changes to only 0.02% gives its maximum echo amplitude of 76.9 dB, which differs only 0.1% from the standard value but reduces the simulation time significantly up to 91% if keeping all other parameters unchanged. Moreover, monochromatic frequency spectrum (bandwidth of 0%, only a center frequency content) simulated in investigation No.3 reduces almost 99% of standard simulation time, but the maximum echo amplitude of interest changed 8% to the standard value. These three investigated cases show that the second simulation scheme (bandwidth of 0.02%) could be considered reasonable and should be used in the later optimizations.

7. Results and Discussion

7.1. Validity of Simulation Model

The model is validated in this work by comparing experiments and simulations in terms of data presentations (A-, B- and C-scans), see Figures 2-10, where all signals are normalized to their corresponding maximum values for easy comparison purposes. All simulated results are presented in black colour and experimental ones are in red colour. In A-scans, the experimental peaks (red dotted lines) are shifted in time so that they coincide with simulated peaks (black solid lines) for comparison purpose. The amount of shifted time could be correlated to e.g. experimental condition and setup, etc. In B-scans, the simulated and experimental results are ordered to the left and right, respectively. In C-scans, the

Table 3. Optimization condition investigations.

No.	BW. (%)	Scan pos.	Time pos.	Max. amp. (dB)	Time (h)
1	74	35	14,448	76.8	64
2	0.02	35	14,448	76.9	6
3	0	35	-	83	0.13
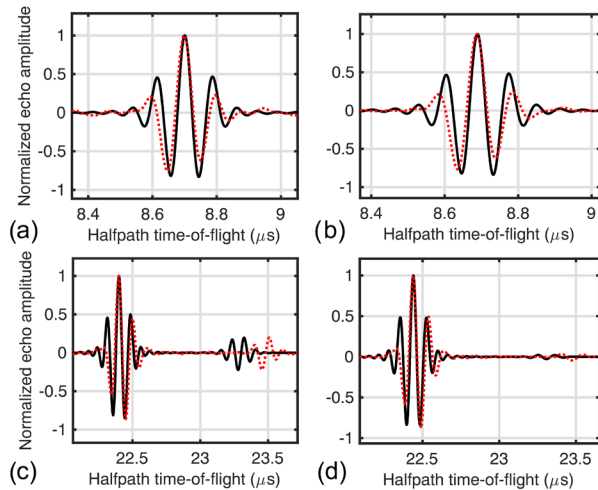
Figure 2. A-scan comparisons between simulations (black solid lines) and experiments (red dotted lines) on SDH at 50 mm depth in test specimen #1 under case: (a) non-angled beam without focusing effect, (b) non-angled beam with 50 mm focus depth, (c) 45-degree angled beam without focusing effect and (d) 45-degree angled beam with 50 mm focus depth.
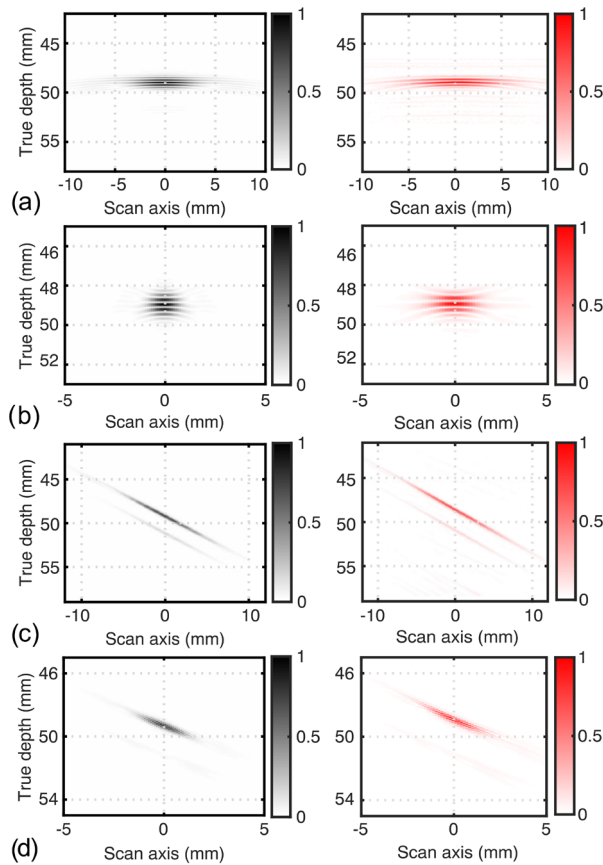
Figure 3. B-scan comparisons between simulations (grey scaled to the left) and experiments (red scaled to the right) on SDH at 50 mm depth in test specimen #1 under case: (a) non-angled beam without focusing effect, (b) non-angled beam with 50 mm focus depth, (c) 45-degree angled beam without focusing effect and (d) 45-degree angled beam with 50 mm focus depth.
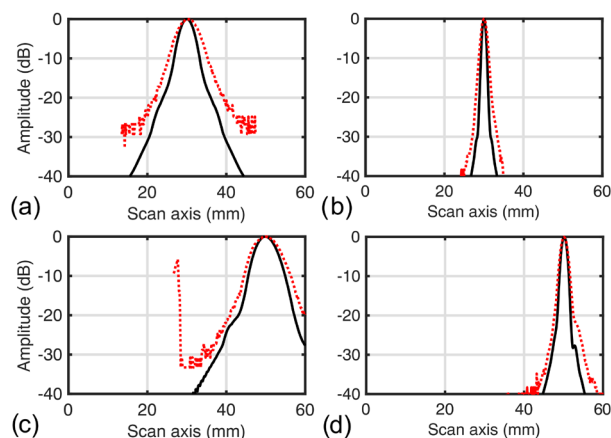
Figure 4. C-scan (echo dynamic curve) comparisons between simulations (black solid lines) and experiments (red dotted lines) on SDH at 50 mm depth in test specimen #1 under case: (a) non-angled beam without focusing effect, (b) non-angled beam with 50 mm focus depth, (c) 45-degree angled beam without focusing effect and (d) 45-degree angled beam with 50 mm focus depth.

peaks (respective amplitude of 0 dB corresponds to the scan position where the maximum echo amplitude is detected) are also shifted to facilitate the comparisons.

Comparisons for the SDH at 50 mm depth in test specimen #1 are shown in **Figures 2-4**. The experimental A-scans are shifted by (a) 0.01 µs, (b) −0.001 µs, (c) 0.29 µs and (d) 0.2 µs. Good correlations can be seen in all A- and C-scan comparisons. In one of the A-scans, case (c), a second somewhat weaker pulse can be observed. This is identified as a satellite pulse correlated to the surface wave traveling round the SDH. The mismatch of this weaker wave between simulation and experiment could then be explained by inaccuracy of actual SDH diameter in the test specimen. This weaker pulse in case (d) diminishes since the wave energy is focused and mostly reflected. B-scans show indifferentiable shapes except for the second case, which could be caused by a variation in contact-condition affected beam divergence, but the overall comparisons show good consistency. The echo dynamic curves above −10 dB correlate well.

Comparisons for the four surface breaking cracks (height of 0.5 mm, 2 mm, 5 mm and 10 mm) in test specimen #2 without focusing effect are shown in **Figures 5-7**. The experimental A-scans are shifted by (a) 0.06 µs, (b) 0.04 µs, (c) 0.01 µs and (d) 0.05 µs. The wave form of the smallest crack (height 0.5 mm) does not correlate as good as others and the reason might be that the smallest crack stands more for a volumetric defect than a crack, which was actually modelled and simulated. All B-scans show indifferentiable shapes.

Comparisons for the four surface breaking cracks (height of 0.5 mm, 2 mm, 5 mm and 10 mm) in test specimen #2 with 35 mm focus depth are shown in **Figures 8-10**. The experimental A-scans are shifted by (a) −0.27 µs, (b) −0.27 µs, (c) −0.14 µs and (d) −0.12 µs. As mentioned in simulation configuration that only a certain scan and time interval where the corresponding maximum echo amplitude is expected was simulated for cracks with height of 5 mm and 10 mm, their

Figure 5. A-scan comparisons between simulations (black solid lines) and experiments (red dotted lines) on different surface breaking cracks in test specimen #2 without focusing effect, crack height: (a) 0.5 mm, (b) 2 mm, (c) 5 mm, (d) 10 mm.
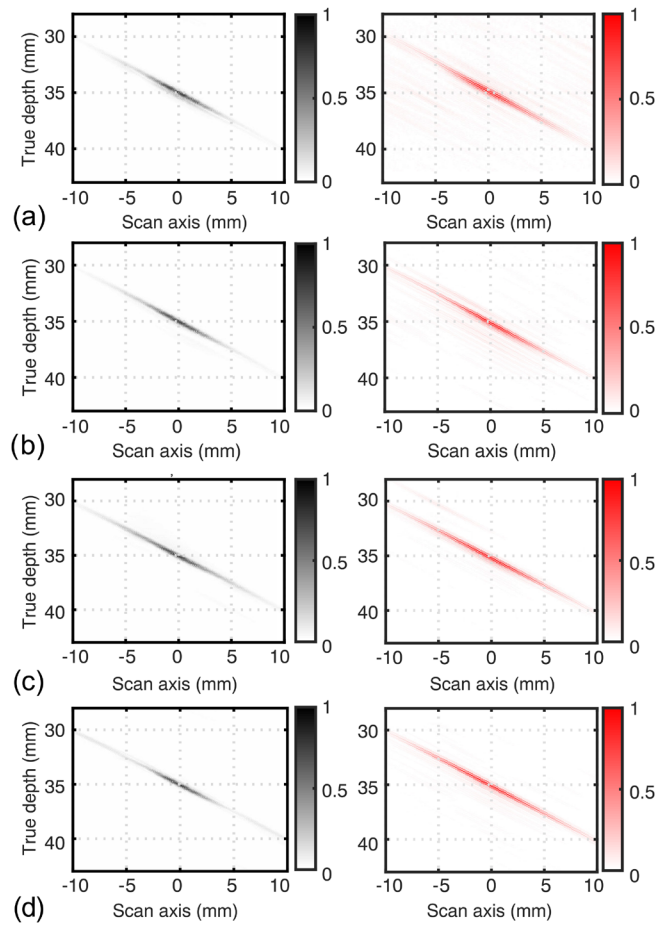
Figure 6. B-scan comparisons between simulations (grey scaled to the left) and experiments (red scaled to the right) on different surface breaking cracks in test specimen #2 without focusing effect, crack height: (a) 0.5 mm, (b) 2 mm, (c) 5 mm, (d) 10 mm.
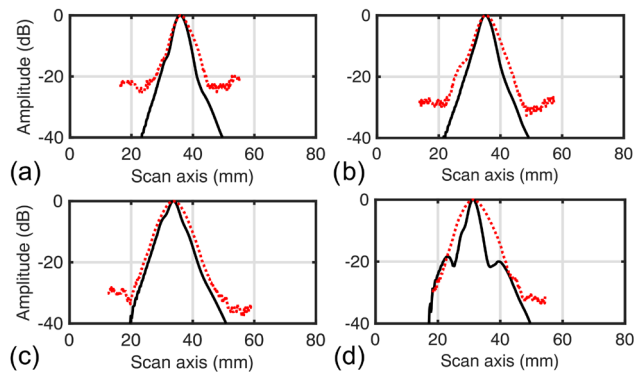
Figure 7. C-scan (echo dynamic curve) comparisons between simulations (black solid lines) and experiments (red dotted lines) on different surface breaking cracks in test specimen #2 without focusing effect, crack height: (a) 0.5 mm, (b) 2 mm, (c) 5 mm, (d) 10 mm.
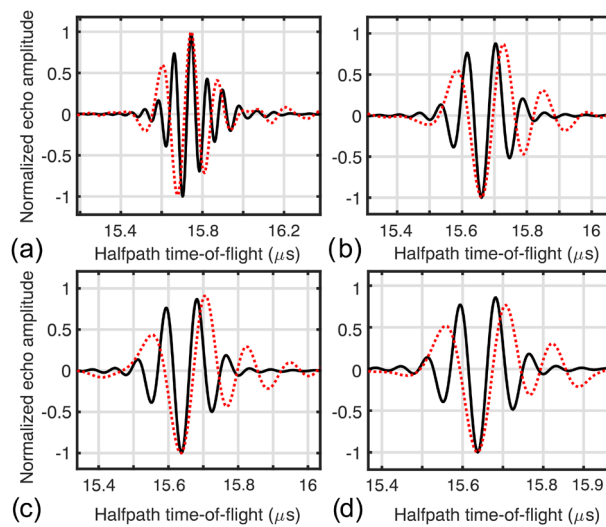
Figure 8. A-scan comparisons between simulations (black solid lines) and experiments (red dotted lines) on different surface breaking cracks in test specimen #2 with 35 mm focus depth, crack height: (a) 0.5 mm, (b) 2 mm, (c) 5 mm, (d) 10 mm
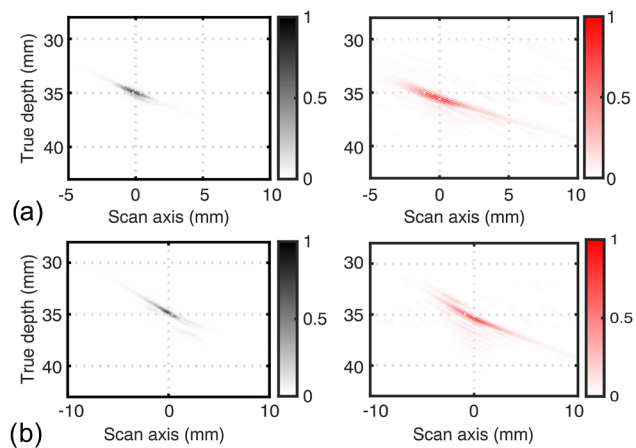
Figure 9. B-scan comparisons between simulations (grey scaled to the left) and experiments (red scaled to the right) on different surface breaking cracks in test specimen #2 with 35 mm focus depth, crack height: (a) 0.5 mm, (b) 2 mm, (c) 5 mm, (d) 10 mm.
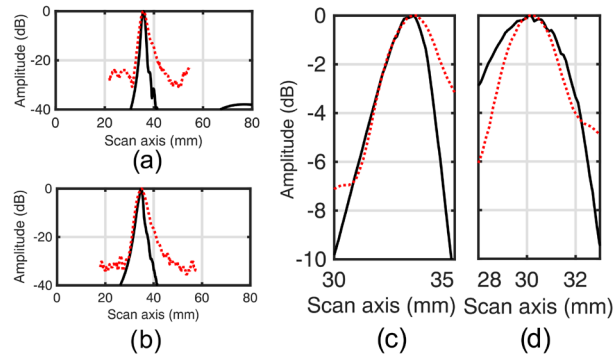
Figure 10. C-scan (echo dynamic curve) comparisons between simulations (black solid lines) and experiments (red dotted lines) on different surface breaking cracks in test specimen #2 with 35 mm focus depth, crack height: (a) 0.5 mm, (b) 2 mm, (c) 5 mm, (d) 10 mm.

B-scans are incomplete and incomparable to experiments and are thus neglected in **Figure 9**. This also influences their C-scans in **Figure 10** that only a small scan interval is comparable to experiments. It is noticed in **Figure 9** that the B-scans at depth around 35 mm are identical while the experimental shapes have bottom part (tail) that simulations do not. These tails could be caused by beam divergence variations and possible further residual corner echos in experiments since the sound beam is focused at the backwall of the test specimen.

7.2. Probe Skew Angle Sensitivity

With the help of the model flexibility, a set of simulations were conducted with only the probe skew angle being varied from −5° to 5° with an increment of 0.5°. This results in 21 simulations under the case of 45-degree angled beam with focus depth at 50 mm towards an SDH at 50 mm depth in test specimen #1. By comparing all these simulated A-scans with experiments, where the nominal physical probe skew angle is 0-degree, it is observed in **Figure 11** that a simulated probe skew angle of ±3.5 gives better A-scan waveform correlation to the experiment, even if the waveform shape does not differ that much.

Figure 12 presents the maximum echo amplitudes for each simulated received signal under these probe skew angles. The values are normalized with the maximum echo amplitude obtained at probe skew angle of 0-degree. It can be noticed that the normalized amplitude level is symmetric along 0-degree skew angle, which indicates that the waveforms in A-scans are the same for the symmetric probe skew angles.

7.3. Sound Field Optimization

As mentioned in the optimization process that a bandwidth of 0.02% instead of the nominal 74% is used in the simulations for optimization work, which generates sufficiently accurate maximum echo amplitude while less time-consuming. An initialized sound field optimization work is conducted towards a surface breaking crack, which has a height of 10 mm and tilt angle of 0-degree that
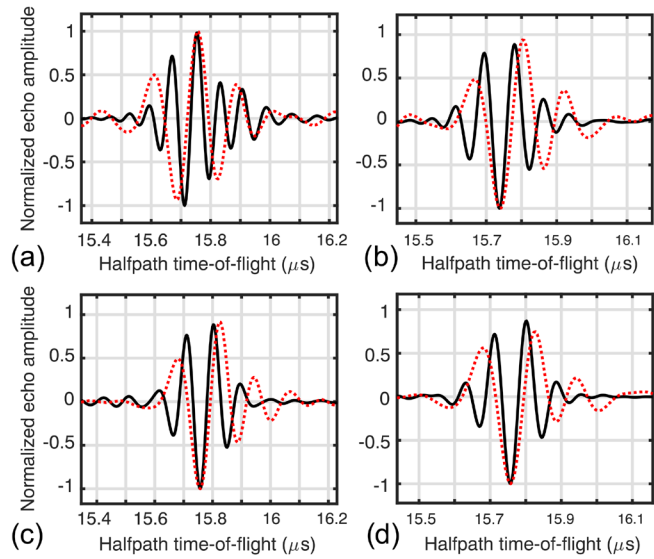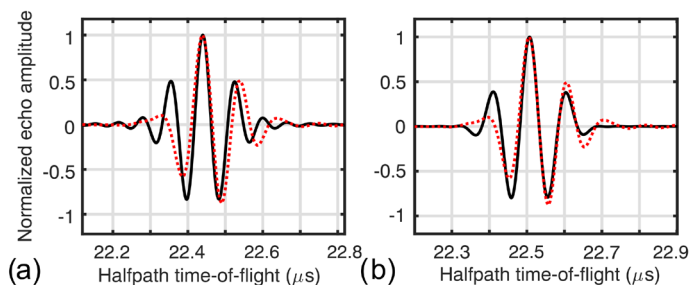
Figure 11. A-scan comparisons between simulations (black solid lines) and experiments (red dotted lines) on SDH at 50 mm depth in test specimen #1 under the case of 45-degree angled beam with 50 mm focus depth, simulated probe skew angle of 0-degree in (a) and ±3.5-degree in (b).
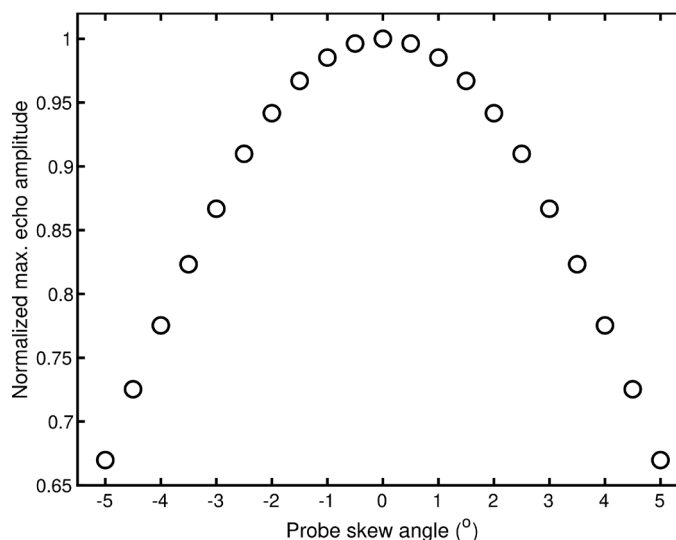
Figure 12. Maximum echo amplitude (normalized at 0-degree probe skew angle, expressed in percentage) for each simulated probe skew angle under the inspection of SDH at 50 mm depth in test specimen #1 in the case of 45-degree angled beam with 50 mm focus depth.

corresponds to the 10 mm height crack on test specimen #2. The crack opening is on the bottom surface of the test specimen, so the received signal (maximum echo amplitude) is the corner echo from the crack. The decision variables are the probe (beam) angle and focusing distance. **Figure 13** shows the iteration processes of the optimization for this crack. It can be seen that after around 20 iterations, a maximized (optimal) echo amplitude of around 80.2 dB can be found under an optimal combination of 48-degree probe angle and 45.2 mm focusing distance (corresponds to a focusing depth of 30.2 mm at this angle), *i.e.* the optimal solution. Comparing with the second case in **Table 3**, where the same crack is simulated but with an original combination of 45-degree probe angle and 49.49 mm focusing distance, it is obvious that the received maximum echo amplitude is larger using the optimal solution, *i.e.* 80.2 dB > 76.9 dB.

Noticing the third investigation case in **Table 3** where the unique monochromatic frequency spectrum is simulated, the accuracy of obtained maximum echo
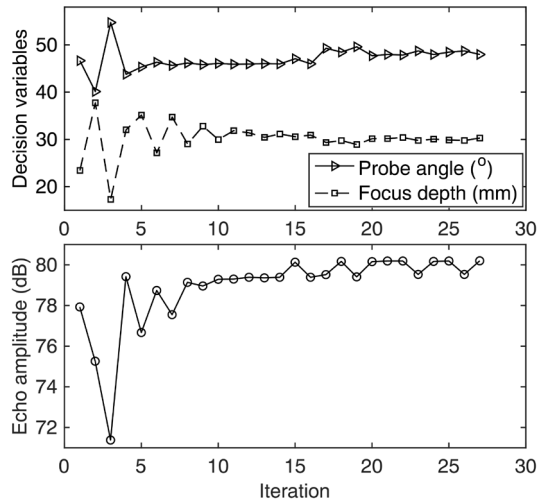
Figure 13. Optimization iterations of decision variables (probe angle and focus depth) to maximize the echo amplitude towards a surface breaking crack with height of 10 mm and tilt angle of 0-degree, simulation bandwidth is 0.02%.
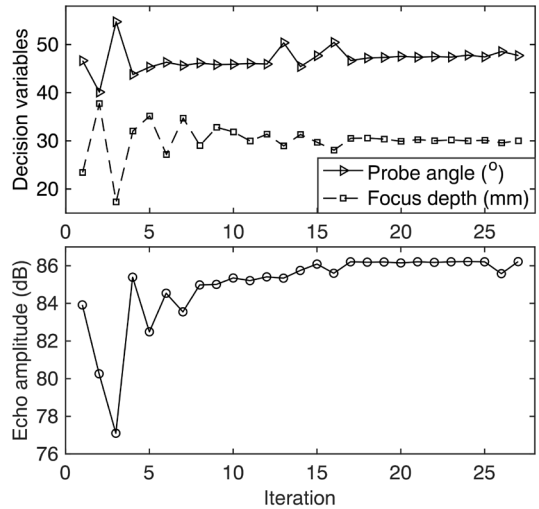
Figure 14. Optimization iterations of decision variables (probe angle and focus depth) to maximize the echo amplitude towards a surface breaking crack with height of 10 mm and tilt angle of 0-degree, simulation frequency is monochromatic (bandwidth is 0%).

amplitude cannot be guaranteed, but the simulation time is reduced significantly. Thus, an optimization trial is performed using this monochromatic frequency configuration towards the same defect, *i.e.* surface breaking crack with 10 mm height and 0-degree tilt angle. The optimization iterations can be seen in **Figure 14** and the optimal combination of decision variables is found to be 48-degree probe angle and 45 mm focusing distance (corresponds to a focusing depth of 30 mm at this angle), which gives the maximized echo amplitude of 86.2 dB. Comparing this optimal solution to the previous one using 0.02% bandwidth, it is found that the optimal combinations of the probe angle and focusing distance are almost the same whereas the maximized echo amplitudes differ. Note that it is the combination of decision variables that matters to the optimization prob-

lem, therefore, it is reasonable to believe that a monochromatic frequency configuration can be used in the further similar optimization processes.

The increase in received signal amplitude from the surface breaking crack with 10 mm height and 0-degree tilt angle by using optimal parameter set is visible in Table 4. The optimal solution using nominal 74% bandwidth are compared with the original one (*i.e.* nominal bandwidth of 74% and the parameter combination of 45-degree beam angle with 35 mm focus depth). A 4.1 dB increased amplitude than original is observed. Besides, the experimental echo amplitude comparison using the original combination and the optimal one is also presented in Table 4 to verify that the optimal solution ensures an improvement of the received echo amplitude. Note that these amplitude results in the table are normalized by the one using the original combination, *i.e.* 76.8 dB with bandwidth of 74%.

After the above observations, Figure 15 presents an optimization case towards a surface breaking crack with height of 10 mm and tilt angle of 5-degree using monochromatic frequency configuration. After around 20 iterations, the optimal combination (optimal solution) of probe angle of 56-degree and focusing distance of 46.3 mm (corresponds to a focusing depth of 26 mm at this angle) is

Table 4. Normalized comparisons of received signal amplitude using original and optimal combinations of decision variables and with different simulated bandwidth, normalization reference is 76.8 dB.

	Simulated amplitude delta (dB)	Experimental amplitude delta (dB)
Original (BW74%)	0	0
Optimal (BW74%)	+4.1	+1.4
Optimal (BW0.02%)	+3.4	-
Optimal (BW0%)	+9.4	-
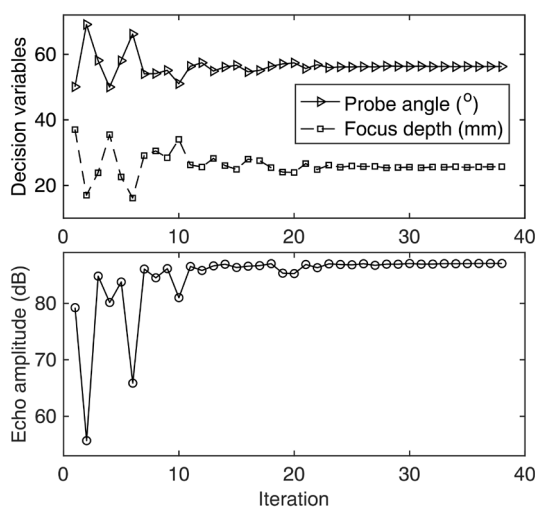
Figure 15. Optimization iterations of decision variables (probe angle and focus depth) to maximize the echo amplitude towards a surface breaking crack with height of 10 mm and tilt angle of 5-degree, simulation frequency is monochromatic (bandwidth is 0%).

found, which gives the maximized echo amplitude of 87.1 dB. This optimal solution is also verified afterwards by using 0.02% bandwidth, which gives the maximized echo amplitude of 81.4 dB under probe angle of 56-degree and focusing distance of 46.9 mm.

8. Conclusions

Numerical models in UT have many potential benefits to be a complement of physical experimental work and to the understanding of the techniques. To ensure the validity of these models, validation is essential, either by comparison to other validated models or to corresponding experimental scenarios. In the current work, the PA probe model included in the UT simulation software simSUNDT is further validated experimentally in terms of data presentation comparisons, *i.e.* A-, B- and C-scans. These data presentations under different inspection scenarios show satisfactory correlations to corresponding experiments in general, and confirm the validity of the simulation model.

After the model is validated, it is further used in exploring the optimized sound field generated by a PA probe. The sound field optimization aims at retrieving the maximized echo amplitude as a function of the defect characteristics (size and tilt angle) by adjusting a combination of decision variables, *i.e.* probe angle and focusing distance, of PA probe. A surface breaking crack with certain height and tilt angle is considered as the targeted defect. It is observed before the optimization work that, instead of using the nominal probe parameter (*i.e.* bandwidth), a change of this parameter not only maintains the echo amplitude level, but also significantly reduces the simulation time. Thus, this is used as an approach in the optimization process. It is then found by comparing this optimization result with the one obtained using monochromatic frequency configuration that, the latter configuration ends up with the same optimal combination of decision variables as the first one, even if the obtained maximized echo amplitudes differ. In other words, the monochromatic configuration can reduce the simulation time significantly while still results in a set of reasonable optimal decision variables. A brief experimental verification of the optimal solution is presented accordingly and the improvement of sound field, *i.e.* the received signal amplitude in current situation, using the optimal solution is clearly observed. Thus, this optimization scheme can be used in optimization work with other defect characteristics.

Acknowledgements

Conflicts of Interest

The authors declare no conflicts of interest regarding the publication of this paper.

References

[1] Hagemaier, D. (1974) *SAE Transactions*, **83**, 2767-2796. https://doi.org/10.4271/740811

[2] Drinkwater, B.W. and Wilcox, P.D. (2006) *NDT & E International*, **39**, 525-541. https://doi.org/10.1016/j.ndteint.2006.03.006

[3] Holmer, G., Daniels, W. and Zettervall, T. (2017) Evaluation of the Simulation Software CIVA for Qualification Purpose. https://www.stralsakerhetsmyndigheten.se/publikationer/rapporter/sakerhet-vid-karnkraftverken/2017/201729

[4] Lopez, A.B., Santos, J., Sousa, J.P., Santos, T.G. and Quintino, L. (2019) *Journal of Nondestructive Evaluation*, **38**, 1-11. https://doi.org/10.1007/s10921-019-0600-y

[5] Chatillon, S., Robert, S., Calmon, P., Daniel, G., Cartier, F., *et al.* (2015) *AIP Conference Proceedings*, **1650**, 1847-1855. https://doi.org/10.1063/1.4914810

[6] Lei, X., Wirdelius, H. and Rosell, A. (2020) *Ultrasonics*, **108**, Article ID: 106217. https://doi.org/10.1016/j.ultras.2020.106217

[7] Jansson, P.A. (2000) *AIP Conference Proceedings*, **509**, 57-64. https://doi.org/10.1063/1.1306034

[8] Boström, A. and Eriksson, A.S. (1993) *Proceedings of the Royal Society of London. Series A*: *Mathematical and Physical Sciences*, **443**, 183-201. https://doi.org/10.1098/rspa.1993.0139

[9] Bövik, P. and Boström, A. (1997) *The Journal of the Acoustical Society of America*, **102**, 2723-2733. https://doi.org/10.1121/1.420326

[10] Boström, A. and Wirdelius, H. (1995) *The Journal of the Acoustical Society of America*, **97**, 2836-2848. https://doi.org/10.1121/1.411850

[11] Wirdelius, H. (2007) Experimental validation of the UTDefect simulation software. *Proceedings of* 6*th International Conference on NDE in Relation to Structural Integrity for Nuclear and Pressurized Components*, Budapest, 8-10 October 2007.

[12] Boström, A. and Bövik, P. (2003) *International Journal of Solids and Structures*, **40**, 3493-3505. https://doi.org/10.1016/S0020-7683(03)00150-1

[13] Auld, B.A. (1979) *Wave Motion*, **1**, 3-10. https://doi.org/10.1016/0165-2125(79)90020-9

[14] Grešovnik, I. (2007) Simplex Algorithms for Nonlinear Constraint Optimization Problems.

[15] Poles, S. (2003) The Simplex Method.

Rabi Oscillations, Entanglement and Teleportation in the Anti-Jaynes-Cummings Model

Christopher Mayero*, Joseph Akeyo Omolo, Onyango Stephen Okeyo

Department of Physics and Materials Science, Maseno University, Maseno, Kenya
Email: *cmayero@yahoo.com

Abstract

This paper provides a scheme for generating maximally entangled qubit states in the anti-Jaynes-Cummings interaction mechanism, so called entangled anti-polariton qubit states. We demonstrate that in an initial vacuum-field, Rabi oscillations in a cavity mode in the anti-Jaynes-Cummings interaction process, occur in the reverse sense relative to the Jaynes-Cummings interaction process and that time evolution of entanglement in the anti-Jaynes-Cummings interaction process takes the same form as in the Jaynes-Cummings interaction process. With the generated anti-polariton qubit state as one of the initial qubits, we present quantum teleportation of an atomic quantum state by applying entanglement swapping protocol achieving an impressive maximal teleportation fidelity $F_\rho = 1$.

Keywords

Jaynes-Cummings, Anti-Jaynes-Cummings, Rabi Oscillations, Entanglement, Entanglement Swapping, Teleportation, Maximal Teleportation Fidelity

1. Introduction

The basic model of quantized light-matter interaction describing a two-level atom coupled to a single mode of quantized electromagnetic radiation is the quantum Rabi model (QRM) [1] [2] [3] [4] [5] initially introduced by Rabi, Isidor Isaac [6] [7] to discuss the phenomenon of nuclear magnetic resonance in a semi-classical way. The Jaynes-Cummings (JC) Hamiltonian [3] [4] [5] [8] and the anti-Jaynes-Cummings (AJC) Hamiltonian [3] [4] [5] are both generated from the QRM.

Exact analytical solutions of the eigenvalue equation for the QRM have been

determined in [1] [2] [9] [10]. However, a major challenge in the QRM that remained an outstanding problem over the years is that while the JC component has a conserved excitation number operator and is invariant under the corresponding $U(1)$ symmetry operation, a conserved excitation number and corresponding $U(1)$ symmetry operators for AJC component had never been determined. Recently, it has been shown that the operator ordering principle distinguishes the JC and AJC Hamiltonians [3] [4] [5] as normal and anti-normal order components of the QRM. In this approach the JC interaction represents the coupling of a two-level atom to the rotating positive frequency component of the field mode while the AJC interaction represents the coupling of the two-level atom to the anti-rotating (anti-clockwise or counter-rotating [2] [3] [4] [5] [8] [11]) negative frequency component of the field mode, because the electromagnetic field mode is composed of positive and negative frequency components [12]. The long-standing challenge of determining a conserved excitation number and corresponding $U(1)$ symmetry operators for the AJC component was finally solved in [3]. The discovery and proof of a conserved excitation number operator of the AJC Hamiltonian [3] now means that dynamics generated by the AJC Hamiltonian is exactly solvable, as demonstrated in the polariton and anti-polariton qubit (photospin qubit) models in [4] [5].

Noting that fundamental features namely: collapses and revivals in the atomic inversion [13], generation of Schrödinger cat states of the quantized field [14] [15], transfer of atomic coherence to the quantized field [16], vacuum-field Rabi oscillations in a cavity [17] and many more have been extensively studied in the JC model in both theory and experiment in quantum optics, we now focus attention on the AJC model which has not received much attention over the years due to the erroneously assumed lack of a conserved excitation number operator.

We observe that the failure of the JC interaction component to account for some experimental features characterised by blue-sideband transitions has driven various workers to apply numerical methods to probe the full QRM into the ultrastrong coupling (USC) and deep strong coupling (DSC) regimes [18] [19] [20] [21] [22] to *indirectly* monitor the dynamical effects of the AJC interaction component. However, even such advanced approaches do not give explicitly the dynamical features generated solely by the AJC interaction. Fortunately, the reformulation developed in [3] [4] [5], drastically simplifies exact solutions of the AJC model, which we shall here apply.

In this paper, we are interested in analysis of quantum state configuration of the qubit states in the AJC model, entanglement of qubits in the AJC model and the application of the entangled qubit state vectors in teleportation of an entangled atomic quantum state.

The content of this paper is therefore summarized as follows. Section 2 presents an overview of the theoretical model. In Section 3, Rabi oscillations in the AJC model are studied. In Section 4, entanglement of AJC qubit state vectors is analysed. In Section 5, teleportation as an application of entanglement is pre-

sented. AJC state engineering and experimental implementation is briefly discussed in Section 6 and finally Section 7 presents the conclusion.

2. The Model

The quantum Rabi model of a quantized electromagnetic field mode interacting with a two-level atom is generated by the Hamiltonian [3]

$$\hat{H}_R = \frac{1}{2}\hbar\omega\left(\hat{a}^\dagger\hat{a} + \hat{a}\hat{a}^\dagger\right) + \hbar\omega_0\hat{s}_z + \hbar\lambda\left(\hat{a} + \hat{a}^\dagger\right)\left(\hat{s}_+ + \hat{s}_-\right) \tag{1}$$

noting that the free field mode Hamiltonian is expressed in normal and anti-normal order form $\frac{1}{2}\hbar\omega\left(\hat{a}^\dagger\hat{a} + \hat{a}\hat{a}^\dagger\right)$. Here, $\omega, \hat{a}, \hat{a}^\dagger$ are quantized field mode angular frequency, annihilation and creation operators, while $\omega_0, \hat{s}_z, \hat{s}_+, \hat{s}_-$ are atomic state transition angular frequency and operators. The Rabi Hamiltonian in Equation (1) is expressed in a symmetrized two-component form [3] [4] [5]

$$\hat{H}_R = \frac{1}{2}\left(\hat{H} + \hat{\bar{H}}\right) \tag{2}$$

where $\hat{H}$ is the standard JC Hamiltonian interpreted as a polariton qubit Hamiltonian expressed in the form [3]

$$\hat{H} = \hbar\omega\hat{N} + 2\hbar\lambda\hat{A} - \frac{1}{2}\hbar\omega; \quad \hat{N} = \hat{a}^\dagger\hat{a} + \hat{s}_+\hat{s}_-$$

$$\hat{A} = \alpha\hat{s}_z + \hat{a}\hat{s}_+ + \hat{a}^\dagger\hat{s}_-; \quad \alpha = \frac{\omega_0 - \omega}{2\lambda} \tag{3}$$

while $\hat{\bar{H}}$ is the AJC Hamiltonian interpreted as an anti-polariton qubit Hamiltonian in the form [3]

$$\hat{\bar{H}} = \hbar\omega\hat{\bar{N}} + 2\hbar\lambda\hat{\bar{A}} - \frac{1}{2}\hbar\omega; \quad \hat{\bar{N}} = \hat{a}\hat{a}^\dagger + \hat{s}_-\hat{s}_+$$

$$\hat{\bar{A}} = \bar{\alpha}\hat{s}_z + \hat{a}\hat{s}_- + \hat{a}^\dagger\hat{s}_+; \quad \bar{\alpha} = \frac{\omega_0 + \omega}{2\lambda}. \tag{4}$$

In Equations (3) and (4), $\hat{N}, \hat{\bar{N}}$ and $\hat{A}, \hat{\bar{A}}$ are the respective polariton and anti-polariton qubit conserved excitation numbers and state transition operators.

Following the physical property established in [5], that for the field mode in an initial vacuum state only an atom in an initial excited state $|e\rangle$ entering the cavity couples to the rotating positive frequency field component in the JC interaction mechanism, while only an atom in an initial ground state $|g\rangle$ entering the cavity couples to the anti-rotating negative frequency field component in an AJC interaction mechanism, we generally take the atom to be in an initial excited state $|e\rangle$ in the JC model and in an initial ground state $|g\rangle$ in the AJC model.

Considering the AJC dynamics, applying the state transition operator $\hat{\bar{A}}$ from Equation (4) to the initial atom-field *n*-photon ground state vector $|g, n\rangle$, the basic qubit state vectors $|\psi_{gn}\rangle$ and $|\bar{\phi}_{gn}\rangle$ are determined in the form ($n = 0, 1, 2, \cdots$) [5]

$$\left|\psi_{gn}\right\rangle = \left|g,n\right\rangle; \quad \left|\overline{\phi}_{gn}\right\rangle = -\overline{c}_{gn}\left|g,n\right\rangle + \overline{s}_{gn}\left|e,n+1\right\rangle \tag{5}$$

with dimensionless interaction parameters $\overline{c}_{gn}$, $\overline{s}_{gn}$ and Rabi frequency $\overline{R}_{gn}$ defined as

$$\overline{c}_{gn} = \frac{\overline{\delta}}{2\overline{R}_{gn}}; \quad \overline{s}_{gn} = \frac{2\lambda\sqrt{n+1}}{\overline{R}_{gn}}; \quad \overline{R}_{gn} = 2\lambda\overline{A}_{gn}$$

$$\overline{A}_{gn} = \sqrt{(n+1) + \frac{\overline{\delta}^2}{16\lambda^2}}; \quad \overline{\delta} = \omega_0 + \omega \tag{6}$$

where we have introduced sum frequency $\overline{\delta} = \omega_0 + \omega$ to redefine $\overline{\alpha}$ in Equation (4).

The qubit state vectors in Equation (5) satisfy the qubit state transition algebraic operations

$$\hat{\overline{A}}\left|\psi_{gn}\right\rangle = \overline{A}_{gn}\left|\overline{\phi}_{gn}\right\rangle; \quad \hat{\overline{A}}\left|\overline{\phi}_{gn}\right\rangle = \overline{A}_{gn}\left|\psi_{gn}\right\rangle \tag{7}$$

In the AJC qubit subspace spanned by normalized but non-orthogonal basic qubit state vectors $\left|\psi_{gn}\right\rangle$, $\left|\overline{\phi}_{gn}\right\rangle$ the basic qubit state transition operator $\hat{\overline{\varepsilon}}_g$ and identity operator $\hat{\overline{I}}_g$ are introduced according to the definitions [5]

$$\hat{\overline{\varepsilon}}_g = \frac{\hat{\overline{A}}}{\overline{A}_{gn}}; \quad \hat{\overline{I}}_g = \frac{\hat{\overline{A}}^2}{\overline{A}_{gn}^2} \quad \Rightarrow \quad \hat{\overline{I}}_g = \hat{\overline{\varepsilon}}_g^2 \tag{8}$$

which on substituting into Equation (7) generates the basic qubit state transition algebraic operations

$$\hat{\overline{\varepsilon}}_g\left|\psi_{gn}\right\rangle = \left|\overline{\phi}_{gn}\right\rangle; \quad \hat{\overline{\varepsilon}}_g\left|\overline{\phi}_{gn}\right\rangle = \left|\psi_{gn}\right\rangle$$

$$\hat{\overline{I}}_g\left|\psi_{gn}\right\rangle = \left|\psi_{gn}\right\rangle; \quad \hat{\overline{I}}_g\left|\overline{\phi}_{gn}\right\rangle = \left|\overline{\phi}_{gn}\right\rangle \tag{9}$$

The algebraic properties $\hat{\overline{\varepsilon}}_g^{2k} = \hat{\overline{I}}_g$ and $\hat{\overline{\varepsilon}}_g^{2k+1} = \hat{\overline{\varepsilon}}_g$ easily gives the final property [5]

$$e^{-i\theta\hat{\overline{\varepsilon}}_g} = \cos(\theta)\hat{\overline{I}}_g - i\sin(\theta)\hat{\overline{\varepsilon}}_g \tag{10}$$

which is useful in evaluating time-evolution operators.

The AJC qubit Hamiltonian defined within the qubit subspace spanned by the basic qubit state vectors $\left|\psi_{gn}\right\rangle$, $\left|\overline{\phi}_{gn}\right\rangle$ is then expressed in terms of the basic qubit states transition operators $\hat{\overline{\varepsilon}}_g$, $\hat{\overline{I}}_g$ in the form [5]

$$\hat{\overline{H}}_g = \hbar\omega\left(n + \frac{3}{2}\right)\hat{\overline{I}}_g + \hbar\overline{R}_{gn}\hat{\overline{\varepsilon}}_g. \tag{11}$$

We use this form of the AJC Hamiltonian to determine the general time-evolving state vector describing Rabi oscillations in the AJC dynamics in Section 3 below.

3. Rabi Oscillations

The general dynamics generated by the AJC Hamiltonian in Equation (11) is described by a time evolving AJC qubit state vector $\left|\overline{\Psi}_{gn}(t)\right\rangle$ obtained from the time-dependent Schrödinger equation in the form [5]

$$\left|\overline{\Psi}_{gn}(t)\right\rangle = \hat{\overline{U}}_g(t)\left|\psi_{gn}\right\rangle; \quad \hat{\overline{U}}_g(t) = e^{-\frac{i}{\hbar}\hat{\overline{H}}_g t} \tag{12}$$

where $\hat{\overline{U}}_g(t)$ is the time evolution operator. Substituting $\hat{\overline{H}}_g$ from Equation (11) into Equation (12) and applying appropriate algebraic properties [5], we use the relation in Equation (10) to express the time evolution operator in its final form

$$\hat{\overline{U}}_g(t) = e^{-i\omega t\left(n+\frac{3}{2}\right)}\left\{\cos\left(\overline{R}_{gn}t\right)\hat{\overline{I}}_g - i\sin\left(\overline{R}_{gn}t\right)\hat{\overline{\varepsilon}}_g\right\} \tag{13}$$

which we substitute into equation Equation (12) and use the qubit state transition operations in Equation (9) to obtain the time-evolving AJC qubit state vector in the form

$$\left|\overline{\Psi}_{gn}(t)\right\rangle = e^{-i\omega t\left(n+\frac{3}{2}\right)}\left\{\cos\left(\overline{R}_{gn}t\right)\left|\psi_{gn}\right\rangle - i\sin\left(\overline{R}_{gn}t\right)\left|\overline{\phi}_{gn}\right\rangle\right\} \tag{14}$$

This time evolving state vector describes Rabi oscillations between the basic qubit states $\left|\psi_{gn}\right\rangle$ and $\left|\overline{\phi}_{gn}\right\rangle$ at Rabi frequency $\overline{R}_{gn}$.

In order to determine the length of the Bloch vector associated with the state vector in Equation (14), we introduce the density operator

$$\hat{\overline{\rho}}_{gn}(t) = \left|\overline{\Psi}_{gn}(t)\right\rangle\left\langle\overline{\Psi}_{gn}(t)\right| \tag{15a}$$

which we expand to obtain

$$\begin{aligned}\hat{\overline{\rho}}_{gn}(t) = \cos^2\left(\overline{R}_{gn}t\right)\left|\psi_{gn}\right\rangle\left\langle\psi_{gn}\right| + \frac{i}{2}\sin\left(2\overline{R}_{gn}t\right)\left|\psi_{gn}\right\rangle\left\langle\overline{\phi}_{gn}\right| \\ - \frac{i}{2}\sin\left(2\overline{R}_{gn}t\right)\left|\overline{\phi}_{gn}\right\rangle\left\langle\psi_{gn}\right| + \sin^2\left(\overline{R}_{gn}t\right)\left|\overline{\phi}\right\rangle\left\langle\overline{\phi}\right|.\end{aligned} \tag{15b}$$

Defining the coefficients of the projectors in Equation (15b) as

$$\overline{\rho}_{gn}^{11}(t) = \cos^2\left(\overline{R}_{gn}t\right); \quad \overline{\rho}_{gn}^{12}(t) = \frac{i}{2}\sin\left(2\overline{R}_{gn}t\right)$$
$$\overline{\rho}_{gn}^{21}(t) = -\frac{i}{2}\sin\left(2\overline{R}_{gn}t\right); \quad \overline{\rho}_{gn}^{22}(t) = \sin^2\left(\overline{R}_{gn}t\right) \tag{15c}$$

and interpreting the coefficients in Equation (15c) as elements of a 2×2 density matrix $\overline{\rho}_{gn}(t)$, which we express in terms of standard Pauli operator matrices I, σ_x, σ_y and σ_z as

$$\overline{\rho}_{gn}(t) = \begin{pmatrix}\overline{\rho}_{gn}^{11}(t) & \overline{\rho}_{gn}^{12}(t) \\ \overline{\rho}_{gn}^{21}(t) & \overline{\rho}_{gn}^{22}(t)\end{pmatrix} = \frac{1}{2}\left(I + \vec{\overline{\rho}}_{gn}(t)\cdot\vec{\sigma}\right) \tag{15d}$$

where $\vec{\sigma} = (\sigma_x, \sigma_y, \sigma_z)$ is the Pauli matrix vector and we have introduced the time-evolving Bloch vector $\vec{\overline{\rho}}_{gn}(t)$ obtained in the form

$$\vec{\overline{\rho}}_{gn}(t) = \left(\overline{\rho}_{gn}^x(t), \overline{\rho}_{gn}^y(t), \overline{\rho}_{gn}^z(t)\right) \tag{15e}$$

with components defined as

$$\begin{aligned}\overline{\rho}_{gn}^x(t) &= \overline{\rho}_{gn}^{12}(t) + \overline{\rho}_{gn}^{21}(t) = 0 \\ \overline{\rho}_{gn}^y(t) &= i\left(\overline{\rho}_{gn}^{12}(t) - \overline{\rho}_{gn}^{21}(t)\right) = -\sin\left(2\overline{R}_{gn}t\right) \\ \overline{\rho}_{gn}^z(t) &= \overline{\rho}_{gn}^{11}(t) - \overline{\rho}_{gn}^{22}(t) = \cos\left(2\overline{R}_{gn}t\right)\end{aligned} \tag{15f}$$

The Bloch vector in Equation (15e) takes the explicit form

$$\vec{\bar{\rho}}_{gn}(t) = \left(0, -\sin\left(2\bar{R}_{gn}t\right), \cos\left(2\bar{R}_{gn}t\right)\right) \tag{15g}$$

which has unit length obtained easily as

$$\left|\vec{\bar{\rho}}_{gn}(t)\right| = 1 \tag{15h}$$

The property that the Bloch vector $\vec{\bar{\rho}}_{gn}(t)$ is of unit length (the Bloch sphere has unit radius), clearly shows that the general time evolving state vector $\left|\bar{\Psi}_{gn}(t)\right\rangle$ in Equation (14) is a pure state.

We now proceed to demonstrate the time evolution of the Bloch vector $\vec{\bar{\rho}}_{gn}(t)$ which in effect describes the geometric configuration of states. We have adopted class 4 Bloch-sphere entanglement of a quantum rank-2 bipartite state [23] [24] to bring a clear visualization of this interaction. In this respect, we consider the specific example (which also applies to the general *n*-photon case) of an atom initially in ground state $\left|g\right\rangle$ entering a cavity with the field mode starting off in an initial vacuum state $\left|0\right\rangle$, such that the initial atom-field state is $\left|g,0\right\rangle$. It is important to note that in the AJC interaction process the initial atom-field ground state $\left|g,0\right\rangle$ is an absolute ground state with both atom and field mode in the ground state $\left|g\right\rangle$, $\left|0\right\rangle$, in contrast to the commonly applied initial atom-field ground state $\left|e,0\right\rangle$ in the JC model where only the field mode $\left|0\right\rangle$ is in the ground state and the atom in the excited state $\left|e\right\rangle$.

In the specific example starting with an atom in the ground state $\left|g\right\rangle$ and the field mode in the vacuum state $\left|0\right\rangle$ the basic qubit state vectors $\left|\psi_{g0}\right\rangle$ and $\left|\bar{\phi}_{g0}\right\rangle$, together with the corresponding entanglement parameters, are obtained by setting $n = 0$ in Equations (5) and (6) in the form

$$\left|\psi_{g0}\right\rangle = \left|g,0\right\rangle; \quad \left|\bar{\phi}_{g0}\right\rangle = -\bar{c}_{g0}\left|g,0\right\rangle + \bar{s}_{g0}\left|e,1\right\rangle;$$

$$\bar{c}_{g0} = \frac{\bar{\delta}}{2\bar{R}_{g0}}; \quad \bar{s}_{g0} = \frac{2\lambda}{\bar{R}_{g0}}; \quad \bar{R}_{g0} = \frac{1}{2}\sqrt{16\lambda^2 + \bar{\delta}^2} \tag{16}$$

$$\left|g,0\right\rangle = \left|g\right\rangle \otimes \left|0\right\rangle; \quad \left|e,1\right\rangle = \left|e\right\rangle \otimes \left|1\right\rangle$$

The corresponding Hamiltonian in Equation (11) becomes ($n = 0$)

$$\hat{\bar{H}}_g = \frac{3}{2}\hbar\omega\hat{\bar{I}}_g + \hbar\bar{R}_{g0}\hat{\bar{\varepsilon}}_g \tag{17}$$

The time-evolving state vector in Equation (14) takes the form ($n = 0$)

$$\left|\bar{\Psi}_{g0}(t)\right\rangle = e^{-i\frac{3}{2}\omega t}\left\{\cos\left(\bar{R}_{g0}t\right)\left|\psi_{g0}\right\rangle - i\sin\left(\bar{R}_{g0}t\right)\left|\bar{\phi}_{g0}\right\rangle\right\} \tag{18}$$

which describes Rabi oscillations at frequency $\bar{R}_{g0}$ between the initial separable qubit state vector $\left|\psi_{g0}\right\rangle$ and the entangled qubit state vector $\left|\bar{\phi}_{g0}\right\rangle$.

The Rabi oscillation process is best described by the corresponding Bloch vector which follows from Equation (15g) in the form ($n = 0$)

$$\vec{\bar{\rho}}_{g0}(t) = \left(0, -\sin\left(2\bar{R}_{g0}t\right), \cos\left(2\bar{R}_{g0}t\right)\right) \tag{19}$$

The time evolution of this Bloch vector reveals that the Rabi oscillations be-

tween the basic qubit state vectors $\left|\psi_{g0}\right\rangle$, $\left|\bar{\phi}_{g0}\right\rangle$ describe circles on which the states are distributed on the Bloch sphere as we demonstrate in **Figure 1**.

In **Figure 1** we have plotted the AJC Rabi oscillation process with respective Rabi frequencies $\bar{R}_{g0}$ determined according to Equation (16) for various values of sum frequency $\bar{\delta} = \omega_0 + \omega$. We have provided a comparison with plots of the corresponding JC process in **Figure 2**.

To facilitate the desired comparison of the AJC Rabi oscillation process with the standard JC Rabi oscillation process plotted in **Figure 2**, we substitute the redefinition $\bar{\delta} = \omega_0 + \omega = \delta + 2\omega$ to express the Rabi frequency $\bar{R}_{g0}$ in Equation (16) in the form

$$\bar{R}_{g0} = \frac{1}{2}\sqrt{16\lambda^2 + (\delta + 2\omega)^2}. \tag{20}$$

In the present work, we have chosen the field mode frequency $\omega = 2\lambda$ ($\lambda = 0.5\omega$) such that for both AJC and JC processes we vary only the detuning frequency $\delta = \omega_0 - \omega$. The resonance case $\delta = 0$ in the JC interaction now means $\bar{\delta} = 2\omega = 4\lambda$ in the AJC interaction.

For various values of $\delta = \lambda, 3\lambda, 0$, we use the general time evolving state vector in Equation (18), with $\bar{R}_{g0}$ as defined in Equation (20) to determine the coupled qubit state vectors $\left|\psi_{g0}\right\rangle$, $\left|\bar{\phi}_{g0}\right\rangle$ in Equation (16) by setting $\bar{R}_{g0}t = \frac{\pi}{2}$, describing half cycle of Rabi oscillation as presented below. In each case we have an accumulated global phase factor which does not affect measurement results [25] [26] [27], but we have maintained them here in Equations (21a)-(21c) to explain the continuous time evolution over one cycle.

$$\delta = \lambda; \bar{\delta} = 5\lambda : \left|g,0\right\rangle \rightarrow e^{-i\pi\frac{79}{82}}\left\{-\frac{5}{\sqrt{41}}\left|g,0\right\rangle + \frac{4}{\sqrt{41}}\left|e,1\right\rangle\right\} \rightarrow e^{-i\pi\frac{79}{41}}\left|g,0\right\rangle \tag{21a}$$

$$\delta = 3\lambda; \bar{\delta} = 7\lambda : \left|g,0\right\rangle \rightarrow e^{-i\pi\frac{113}{130}}\left\{-\frac{7}{\sqrt{65}}\left|g,0\right\rangle + \frac{4}{\sqrt{65}}\left|e,1\right\rangle\right\} \rightarrow e^{-i\pi\frac{113}{65}}\left|g,0\right\rangle \tag{21b}$$

$$\delta = 0; \bar{\delta} = 4\lambda : \left|g,0\right\rangle \rightarrow e^{-i\pi}\left\{-\frac{1}{\sqrt{2}}\left|g,0\right\rangle + \frac{1}{\sqrt{2}}\left|e,1\right\rangle\right\} \rightarrow e^{-i\pi2}\left|g,0\right\rangle \tag{21c}$$

The AJC Rabi oscillations for cases $\delta = \lambda, 3\lambda, 0$ are plotted as red, black and blue circles in **Figure 1**, while the corresponding plots in the JC process are provided in **Figure 2** as a comparison. Here, **Figure 1** is a Bloch sphere entanglement [23] that corresponds to a 2-dimensional subspace of $\mathbb{C}^2 \otimes \mathbb{C}^2$

$\text{Span}\left\{\left|g,0\right\rangle, -\bar{c}_{g0}\left|g,0\right\rangle + \bar{s}_{g0}\left|e,1\right\rangle\right\}$ with $\bar{c}_{g0} = \frac{\bar{\delta}}{2\bar{R}_{g0}}$ and $\bar{s}_{g0} = \frac{2\lambda}{\bar{R}_{g0}}$ while

Figure 2 is a Bloch sphere entanglement corresponding to a 2-dimensional subspace of $\mathbb{C}^2 \otimes \mathbb{C}^2$ $\text{Span}\left\{\left|e,0\right\rangle, c_{e0}\left|e,0\right\rangle + s_{e0}\left|g,1\right\rangle\right\}$ with $c_{e0} = \frac{\delta}{2R_{e0}}$ and $s_{e0} = \frac{2\lambda}{R_{e0}}$, where we recall that, in the JC interaction the initial atom-field ground state with the field mode in the vacuum state is $\left|e,0\right\rangle$.
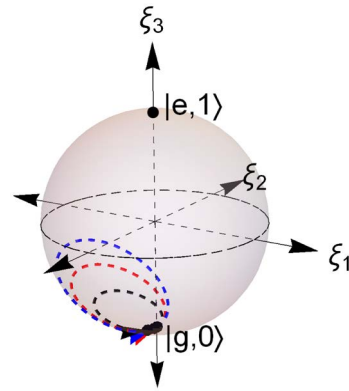
Figure 1. Rabi oscillations in AJC interaction mechanism. The Rabi oscillations for values of sum frequencies are shown by red ($\overline{\delta} = 5\lambda; \delta = \lambda$), black ($\overline{\delta} = 7\lambda; \delta = 3\lambda$) and blue ($\overline{\delta} = 4\lambda; \delta = \omega_0 - \omega = 0$).
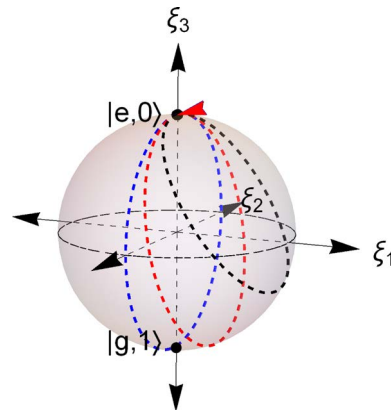
Figure 2. Rabi oscillations in JC interaction mechanism. Here, blue circle is at resonance with detuning $\delta = \omega_0 - \omega = 0$, red circle is for detuning $\delta = \lambda$ and black circle for detuning $\delta = 3\lambda$.

In **Figure 1** we observe:

1) that due to the larger sum frequency $\overline{\delta} = \delta + 2\omega$ in the AJC interaction process as compared to the detuning frequency δ in the JC interaction process, the Rabi oscillation circles in the much faster AJC process are much smaller compared to the corresponding Rabi oscillation circles in the slower JC interaction process. This effect is in agreement with the assumption usually adopted to drop the AJC interaction components in the rotating wave approximation (RWA), noting that the fast oscillating AJC process averages out over time. We have demonstrated the physical property that the size of the Rabi oscillations curves decreases with increasing Rabi oscillation frequency by plotting the AJC oscillation curves for a considerably larger Rabi frequency $\overline{R}_{g0}$ where we have set the field mode frequency $\omega = 10\lambda$ ($\lambda = 0.1\omega$) in **Figure 3**. It is clear in **Figure 3** that for this higher value of the Rabi frequency $\overline{R}_{g0}$ the Rabi oscillation curves almost converge to a point-like form;

2) that Rabi oscillations in the AJC interaction process as demonstrated in **Figure 1** occur in the left hemisphere of the Bloch sphere while in the JC interaction
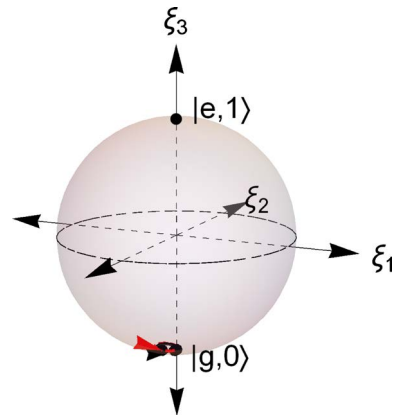
Figure 3. Rabi oscillations in AJC interaction mechanism. The Rabi oscillations for values of sum frequencies are shown by red ($\bar{\delta} = 21\lambda; \delta = \lambda$) and black ($\bar{\delta} = 23\lambda; \delta = 3\lambda$).

process the oscillations occur in the right hemisphere as demonstrated in **Figure 2**. This demonstrates an important physical property that the AJC interaction process occurs in the reverse sense relative to the JC interaction process;

3) an interesting feature that appears at resonance specified by $\delta = 0$. While in the JC model plotted in **Figure 2** the Rabi oscillation at resonance $\delta = 0$ (blue circle) lies precisely on the *yz*-plane normal to the equatorial plane, the corresponding AJC Rabi oscillation (blue circle in **Figure 1**) is at an axis away from the *yz*-plane about the south pole of the Bloch sphere. This feature is due to the fact that the frequency detuning $\bar{\delta} = 2\omega$ takes a non-zero value under resonance $\delta = 0$ such that the AJC oscillations maintain their original forms even under resonance.

We note that the qubit state transitions described by the Bloch vector in the AJC process (**Figure 1**) are blue-side band transitions characterized by the sum frequency $\bar{\delta} = \omega_0 + \omega = \delta + 2\omega$ according to the definition of the Rabi frequency $\bar{R}_{g0}$ in Equation (20).

The geometric configuration of the state space demonstrated on the Bloch-sphere in **Figure 2** determined using the approach in [5] agrees precisely with that determined using the semi-classical approach in [28] corresponding to a 2-dimensional subspace of $\mathbb{C}^2$ Span $\{|e\rangle, |g\rangle\}$. In the approach [28], at resonance where detuning $\delta = 0$ the atomic population is inverted from $|e\rangle$ to $|g\rangle$ and the Bloch-vector $\vec{r} = (\sin(\theta)\cos(\phi), \sin(\theta)\sin(\phi), \cos(\theta))$ describes a path along the *yz*-plane on the Bloch-sphere. For other values of detuning, the atom evolves from $|e\rangle$ to a linear superposition of $|e\rangle$ and $|g\rangle$ and back to $|e\rangle$ and the Bloch-vector $\vec{r}$ describes a circle about the north pole of the Bloch-sphere.

4. Entanglement Properties

In quantum information, it is of interest to measure or quantify the entanglement of states. In this paper we apply the von Neumann entropy as a measure of entanglement. The von Neumann entropy [29] [30] [31] [32] [33] of a quantum

state $\hat{\rho}$ is defined as

$$S(\hat{\rho}) = -tr(\hat{\rho} \log_d \hat{\rho}) = -\sum_i \lambda_i \log_d \lambda_i \tag{22}$$

where the logarithm is taken to base *d*, *d* being the dimension of the Hilbert space containing $\hat{\rho}$ and λ_i's are the eigenvalues of $\hat{\rho}$. It follows that $0 \le S(\hat{\rho}) \le 1$, where $S(\hat{\rho}) = 0$ if and only if $\hat{\rho}$ is a pure state.

Further, the von Neumann entropy of the reduced density matrices of a bipartite pure state $\hat{\rho}_{AB} = |\psi_{AB}\rangle\langle\psi_{AB}|$ is a good and convenient entanglement measure $E(\hat{\rho}_{AB})$. The entanglement measure defined as the entropy of either of the quantum subsystem is obtained as

$$E(\hat{\rho}_{AB}) = -tr(\hat{\rho}_A \log_2 \hat{\rho}_A) = -tr(\hat{\rho}_B \log_2 \hat{\rho}_B) \tag{23}$$

where for all states we have $0 \le E(\hat{\rho}_{AB}) \le 1$. Here the limit 0 is achieved if the pure state is a product $|\psi\rangle = |\psi_A\rangle \otimes |\psi_B\rangle$ and 1 is achieved for maximally entangled states, noting that the reduced density matrices are maximally mixed states.

In this section we analyse the entanglement properties of the qubit state vectors and the dynamical evolution of entanglement generated in the AJC interaction.

4.1. Entanglement Analysis of Basic Qubit State Vectors $|\psi_{g0}\rangle$ and $|\bar{\phi}_{g0}\rangle$

Let us start by considering the entanglement properties of the initial state $|\psi_{g0}\rangle$ which according to the definition in Equation (16) is a separable pure state. The density operator of the qubit state vector $|\psi_{g0}\rangle = |g,0\rangle$ is obtained as

$$\hat{\rho}_{g0} = |g,0\rangle\langle g,0| \tag{24a}$$

Using the definition $|g,0\rangle = |g\rangle \otimes |0\rangle$, we take the partial trace of $\hat{\rho}_{g0}$ in Equation (24a) with respect to the field mode and atom states respectively, to obtain the respective atom and field reduced density operators $\hat{\rho}_A$, $\hat{\rho}_F$ in the form (subscripts $A \equiv$ atom and $F \equiv$ field)

$$\hat{\rho}_A = tr_F(\hat{\rho}_{g0}) = |g\rangle\langle g|; \quad \hat{\rho}_F = tr_A(\hat{\rho}_{g0}) = |0\rangle\langle 0| \tag{24b}$$

which take explicit 2×2 matrix forms

$$\hat{\rho}_A = \begin{pmatrix} 0 & 0 \\ 0 & 1 \end{pmatrix}; \quad \hat{\rho}_F = \begin{pmatrix} 1 & 0 \\ 0 & 0 \end{pmatrix} \tag{24c}$$

The trace of $\hat{\rho}_A$, $\hat{\rho}_A^2$ and $\hat{\rho}_F$, $\hat{\rho}_F^2$ of the matrices in Equation (24c) are

$$tr(\hat{\rho}_A) = tr(\hat{\rho}_A^2) = 1; \quad tr(\hat{\rho}_F) = tr(\hat{\rho}_F^2) = 1 \tag{24d}$$

The unit trace determined in Equation (24d) proves that the initial qubit state vector $|\psi_{g0}\rangle = |g,0\rangle$ is a pure state.

Next, we substitute the matrix form of $\hat{\rho}_A$ and $\hat{\rho}_F$ from Equation (24c) into Equation (23) to obtain equal von Neumann entanglement entropies

$$E(\hat{\rho}_{g0}) = S(\hat{\rho}_A) = S(\hat{\rho}_F) = 0 \tag{24e}$$

which together with the property in Equation (24d) quantifies the initial qubit state vector $|\psi_{g0}\rangle = |g,0\rangle$ as a pure separable state, agreeing with the definition in Equation (16).

We proceed to determine the entanglement properties of the (transition) qubit state vector $|\bar{\phi}_{g0}\rangle$ defined in Equation (16). For parameter values $\delta = \lambda, \bar{\delta} = 5\lambda$ we ignore the phase factor in Equation (21a), to write the transition qubit state vector in the form

$$\delta = \lambda; \bar{\delta} = 5\lambda : |\bar{\phi}_{g0}\rangle = -\frac{5}{\sqrt{41}}|g,0\rangle + \frac{4}{\sqrt{41}}|e,1\rangle \tag{25a}$$

The corresponding density operator of the state in Equation (25a) is

$$\hat{\bar{\rho}}_{g0} = \frac{25}{41}|g,0\rangle\langle g,0| - \frac{20}{41}|g,0\rangle\langle e,1| - \frac{20}{41}|e,1\rangle\langle g,0| + \frac{16}{41}|e,1\rangle\langle e,1| \tag{25b}$$

which takes the explicit 4×4 matrix form

$$\hat{\bar{\rho}}_{g0} = \begin{pmatrix} 0 & 0 & 0 & 0 \\ 0 & \dfrac{16}{41} & -\dfrac{20}{41} & 0 \\ 0 & -\dfrac{20}{41} & \dfrac{25}{41} & 0 \\ 0 & 0 & 0 & 0 \end{pmatrix} \tag{25c}$$

with eigenvalues $\lambda_1 = 1$, $\lambda_2 = 0$, $\lambda_3 = 0$, $\lambda_4 = 0$. Applying Equation (22), its von Neumann entropy

$$S(\hat{\bar{\rho}}_{g0}) = 0 \tag{25d}$$

quantifying the state $|\bar{\phi}_{g0}\rangle$ in Equation (25a) as a bipartite pure state.

Taking the partial trace of $\hat{\bar{\rho}}_{g0}$ in Equation (25b) with respect to the field mode and atom states respectively, we obtain the respective atom and field reduced density operators $\hat{\bar{\rho}}_A, \hat{\bar{\rho}}_F$ together with their squares in the form

$$\hat{\bar{\rho}}_A = tr_F(\hat{\bar{\rho}}_{g0}) = \frac{25}{41}|g\rangle\langle g| + \frac{16}{41}|e\rangle\langle e|; \quad \hat{\bar{\rho}}_A^2 = \frac{625}{1681}|g\rangle\langle g| + \frac{256}{1681}|e\rangle\langle e|$$

$$\hat{\bar{\rho}}_F = tr_A(\hat{\bar{\rho}}_{g0}) = \frac{25}{41}|0\rangle\langle 0| + \frac{16}{41}|1\rangle\langle 1|; \quad \hat{\bar{\rho}}_F^2 = \frac{625}{1681}|0\rangle\langle 0| + \frac{256}{1681}|1\rangle\langle 1| \tag{25e}$$

The trace of $\hat{\bar{\rho}}_A^2$ and $\hat{\bar{\rho}}_F^2$ in Equation (25e) gives

$$tr(\hat{\bar{\rho}}_A^2) = tr(\hat{\bar{\rho}}_F^2) = \frac{881}{1681} < 1 \tag{25f}$$

demonstrating that $\hat{\bar{\rho}}_A$ and $\hat{\bar{\rho}}_F$ are mixed states, satisfying the general property $tr(\hat{\rho}_\chi^2) < 1$ for a mixed state $\hat{\rho}_\chi$.

To quantify the mixedness we determine the length of the Bloch vector along the z-axis as follows

$$r_z = tr(\hat{\bar{\rho}}_A\hat{\sigma}_z) = tr(\hat{\bar{\rho}}_F\hat{\sigma}_z) = \frac{9}{41} \tag{25g}$$

which shows that the reduced density operators $\hat{\bar{\rho}}_A, \hat{\bar{\rho}}_F$ are non-maximally mixed states.

The eigenvalues (λ_1, λ_2) of $\hat{\bar{\rho}}_A$ and $\hat{\bar{\rho}}_F$ are $\left(\dfrac{16}{41}, \dfrac{25}{41}\right)$ and $\left(\dfrac{25}{41}, \dfrac{16}{41}\right)$ respectively, which on substituting into Equation (22), gives equal von Neumann entanglement entropies

$$E\left(\hat{\bar{\rho}}_{g0}\right) = S\left(\hat{\bar{\rho}}_A\right) = S\left(\hat{\bar{\rho}}_F\right) = -\frac{16}{41}\log_2\left(\frac{16}{41}\right) - \frac{25}{41}\log_2\left(\frac{25}{41}\right) = 0.964957 \quad (25h)$$

Taking the properties in Equations (25d), (25f)-(25h) together clearly characterizes the qubit state $\left|\bar{\phi}_{g0}\right\rangle$ in Equation (25a) as an entangled bipartite pure state. However, since $S\left(\hat{\bar{\rho}}_A\right) = S\left(\hat{\bar{\rho}}_F\right) < 1$ the state is not maximally entangled. Similarly, the transition qubit state vector $\left|\bar{\phi}_{g0}\right\rangle = -\dfrac{7}{\sqrt{65}}\left|g,0\right\rangle + \dfrac{4}{\sqrt{65}}\left|e,1\right\rangle$ obtained for $\delta = 3\lambda, \bar{\delta} = 7\lambda$ in Equation (21b) is an entangled bipartite pure state, but not maximally entangled.

Finally, we consider the resonance case $\delta = 0$, characterized by $\bar{\delta} = 4\lambda$ in the AJC model. Ignoring the phase factor in Equation (21c) the transition qubit state vector $\left|\bar{\phi}_{g0}\right\rangle$ takes the form

$$\delta = 0; \bar{\delta} = 4\lambda : \left|\bar{\phi}_{g0}\right\rangle = -\frac{1}{\sqrt{2}}\left|g,0\right\rangle + \frac{1}{\sqrt{2}}\left|e,1\right\rangle \quad (26a)$$

The corresponding density operator of the state in Equation (26a) is

$$\hat{\bar{\rho}}_{g0} = \frac{1}{2}\left|g,0\right\rangle\left\langle g,0\right| - \frac{1}{2}\left|g,0\right\rangle\left\langle e,1\right| - \frac{1}{2}\left|e,1\right\rangle\left\langle g,0\right| + \frac{1}{2}\left|e,1\right\rangle\left\langle e,1\right| \quad (26b)$$

which takes the explicit 4×4 matrix form

$$\hat{\bar{\rho}}_{g0} = \begin{pmatrix} 0 & 0 & 0 & 0 \\ 0 & \dfrac{1}{2} & -\dfrac{1}{2} & 0 \\ 0 & -\dfrac{1}{2} & \dfrac{1}{2} & 0 \\ 0 & 0 & 0 & 0 \end{pmatrix} \quad (26c)$$

with eigenvalues $\lambda_1 = 1, \lambda_2 = 0, \lambda_3 = 0, \lambda_4 = 0$. Applying Equation (22) its von Neumann entropy

$$S\left(\hat{\bar{\rho}}_{g0}\right) = 0 \quad (26d)$$

quantifying the state in Equation (26a) as a bipartite pure state.

Taking the partial trace of $\hat{\bar{\rho}}_{g0}$ in Equation (26b) with respect to the field mode and atom states respectively, we obtain the respective atom and field reduced density operators $\hat{\bar{\rho}}_A, \hat{\bar{\rho}}_F$ together with their squares in the form

$$\hat{\bar{\rho}}_A = tr_F\left(\hat{\bar{\rho}}_{g0}\right) = \frac{1}{2}\left|g\right\rangle\left\langle g\right| + \frac{1}{2}\left|e\right\rangle\left\langle e\right|; \quad \hat{\bar{\rho}}_A^2 = \frac{1}{4}\left|g\right\rangle\left\langle g\right| + \frac{1}{4}\left|e\right\rangle\left\langle e\right|$$

$$\hat{\bar{\rho}}_F = tr_A\left(\hat{\bar{\rho}}_{g0}\right) = \frac{1}{2}\left|0\right\rangle\left\langle 0\right| + \frac{1}{2}\left|1\right\rangle\left\langle 1\right|; \quad \hat{\bar{\rho}}_F^2 = \frac{1}{4}\left|0\right\rangle\left\langle 0\right| + \frac{1}{4}\left|1\right\rangle\left\langle 1\right| \quad (26e)$$

The trace of $\hat{\bar{\rho}}_A^2$ and $\hat{\bar{\rho}}_F^2$ in Equation (26e) is

$$tr\left(\hat{\bar{\rho}}_A^2\right) = tr\left(\hat{\bar{\rho}}_F^2\right) = \frac{1}{2} < 1 \quad (26f)$$

which reveals that the reduced density operators $\hat{\bar{\rho}}_A, \hat{\bar{\rho}}_F$ are mixed states. To quantify the mixedness, we determine the length of the Bloch vector along the *z*-axis as follows

$$r_z = tr\left(\hat{\bar{\rho}}_A \hat{\sigma}_z\right) = tr\left(\hat{\bar{\rho}}_F \hat{\sigma}_z\right) = 0 \tag{26g}$$

showing that the reduced density operators $\hat{\bar{\rho}}_A$ and $\hat{\bar{\rho}}_F$ are maximally mixed states.

The eigenvalues (λ_1, λ_2) of $\hat{\bar{\rho}}_A$ and $\hat{\bar{\rho}}_F$ are $\left(\frac{1}{2}, \frac{1}{2}\right)$ respectively which on substituting into Equation (22), gives equal von Neumann entanglement entropies

$$E\left(\hat{\bar{\rho}}_{g0}\right) = S\left(\hat{\bar{\rho}}_A\right) = S\left(\hat{\bar{\rho}}_F\right) = -\frac{1}{2}\log_2\left(\frac{1}{2}\right) - \frac{1}{2}\log_2\left(\frac{1}{2}\right) = 1 \tag{26h}$$

The unit entropy determined in Equation (26h) together with the properties in Equations (26d)-(26g) quantifies the transition qubit state determined at resonance $\delta = 0$ in Equation (26a) (or Equation (21c)) as a maximally entangled bipartite pure state. Due to this maximal entanglement property, we shall use the resonance transition qubit state $\left|\bar{\phi}_{g0}\right\rangle$ in Equation (26a) to implement teleportation by an entanglement swapping protocol in Section 5 below.

Similar proof of entanglement of the AJC qubit states is easily achieved for all possible values of sum frequency parameter $\bar{\delta} = \omega_0 + \omega$, confirming that in the initial vacuum-field AJC interaction, reversible transitions occur only between a pure initial separable qubit state vector $\left|\psi_{g0}\right\rangle$ and a pure entangled qubit state vector $\left|\bar{\phi}_{g0}\right\rangle$. This property of Rabi oscillations between an initial separable state and an entangled transition qubit state occurs in the general AJC interaction described by the general time evolving state vector $\left|\bar{\Psi}_{gn}(t)\right\rangle$ in Equation (14).

4.2. Entanglement Evolution

Let us consider the general dynamics of AJC interaction described by the general time-evolving qubit state vector $\left|\bar{\Psi}_{gn}(t)\right\rangle$ in Equation (14). Substituting $\left|\bar{\Psi}_{gn}(t)\right\rangle$ from Equation (14) into Equation (15a) and using the definitions of $\left|\psi_{gn}\right\rangle, \left|\bar{\phi}_{gn}\right\rangle$ in Equation (5) the density operator takes the form

$$\begin{aligned}
\hat{\bar{\rho}}_{gn}(t) = &\left\{\cos^2\left(\bar{R}_{gn}t\right) + \bar{c}_{gn}^2\sin^2\left(\bar{R}_{gn}t\right)\right\}|g,n\rangle\langle g,n| \\
&+ \left\{i\bar{s}_{gn}\cos\left(\bar{R}_{gn}t\right)\sin\left(\bar{R}_{gn}t\right) - \bar{c}_{gn}\bar{s}_{gn}\sin^2\left(\bar{R}_{gn}t\right)\right\}|g,n\rangle\langle e,n+1| \\
&+ \left\{-i\bar{s}_{gn}\cos\left(\bar{R}_{gn}t\right)\sin\left(\bar{R}_{gn}t\right) - \bar{c}_{gn}\bar{s}_{gn}\sin^2\left(\bar{R}_{gn}t\right)\right\}|e,n+1\rangle\langle g,n| \\
&+ \left\{\bar{s}_{gn}^2\sin^2\left(\bar{R}_{gn}t\right)\right\}|e,n+1\rangle\langle e,n+1|
\end{aligned} \tag{27}$$

The reduced density operator of the atom is determined by tracing over the field states, thus taking the form

$$\hat{\bar{\rho}}_A(t) = P_g(t)|g\rangle\langle g| + P_e(t)|e\rangle\langle e| \tag{28}$$

after introducing the general time evolving atomic state probabilities $P_g(t)$, $P_e(t)$ obtained as

$$P_g(t) = \cos^2\left(\overline{R}_{gn}t\right) + \overline{c}_{gn}^2\sin^2\left(\overline{R}_{gn}t\right)$$
$$P_e(t) = \overline{s}_{gn}^2\sin^2\left(\overline{R}_{gn}t\right) \tag{29}$$

where the dimensionless interaction parameters $\overline{c}_{gn}$, $\overline{s}_{gn}$ are defined in Equation (6) and the Rabi frequency takes the form

$$\overline{R}_{gn} = \frac{1}{2}\sqrt{16\lambda^2(n+1)+\overline{\delta}^2} \tag{30}$$

Expressing $\hat{\overline{\rho}}_A(t)$ in Equation (28) in 2×2 matrix form

$$\hat{\overline{\rho}}_A(t) = \begin{pmatrix} P_e(t) & 0 \\ 0 & P_g(t) \end{pmatrix} \tag{31}$$

We determine the quantum system entanglement degree $E(t)$ defined in Equation (23) as

$$E(t) = -tr\left(\hat{\overline{\rho}}_A(t)\right)\log_2\left(\hat{\overline{\rho}}_A(t)\right) = -tr\left(\begin{pmatrix} P_e(t) & 0 \\ 0 & P_g(t) \end{pmatrix}\begin{pmatrix} \log_2 P_e(t) & 0 \\ 0 & \log_2 P_g(t) \end{pmatrix}\right) \tag{32}$$

which takes the final form

$$E(t) = -P_e(t)\log_2 P_e(t) - P_g(t)\log_2 P_g(t) \tag{33}$$

Using the definitions of the dimensionless parameters $\overline{c}_{gn}$, $\overline{s}_{gn}$ and the Rabi frequency $\overline{R}_{gn}$ in Equations (6), (30), we evaluate the probabilities in Equation (29) and plot the quantum system entanglement degree $E(\tau)$ in Equation (33) against scaled time $\tau = \lambda t$ for arbitrarily chosen values of sum frequency $\overline{\delta} = 2\lambda, 6\lambda, 8\lambda$ and photon number $n = 1, 2, 3, 6$ in **Figures 4-6**.

The graphs in **Figures 4-6** show the effect of photon number n and sum frequency $\overline{\delta} = \omega_0 + \omega$ on the dynamical behavior of quantum entanglement measured by the von Neumann entropy $E(\tau)$ ($\min E(\tau) = 0$; $\max E(\tau) = 1$).
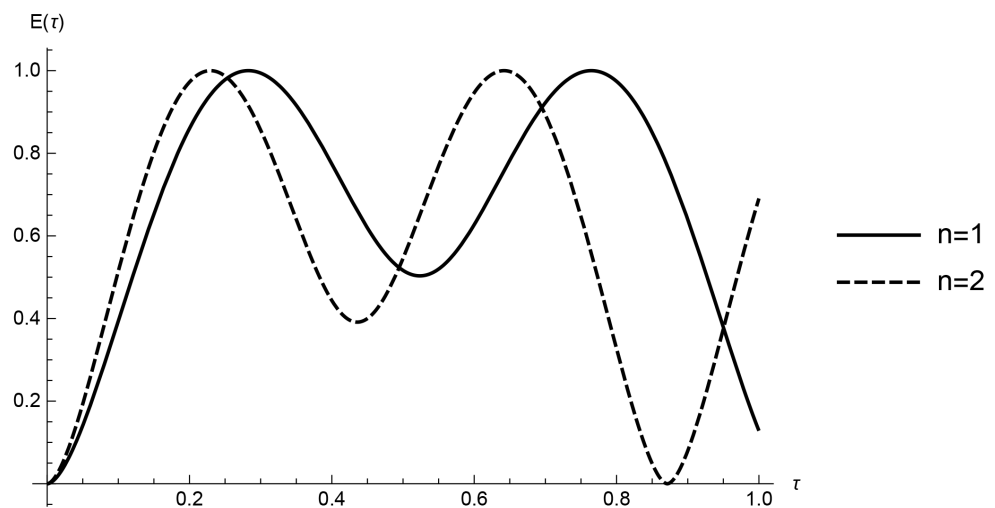
Figure 4. Degree of entanglement against scaled time for sum frequency $\overline{\delta} = 2\lambda$ when $n = 1$ and $n = 2$.
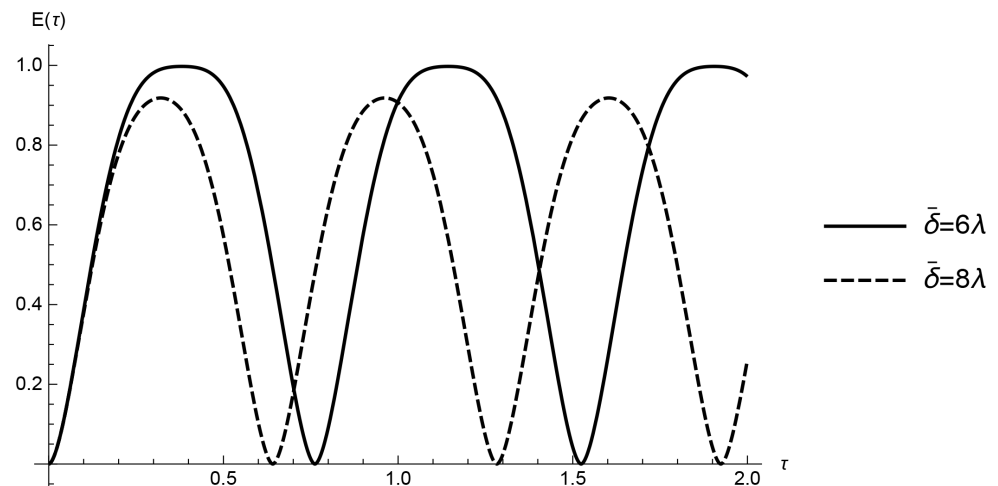
Figure 5. Degree of entanglement against scaled time for sum frequency $\bar{\delta} = 6\lambda$ and $\bar{\delta} = 8\lambda$ when $n = 1$.
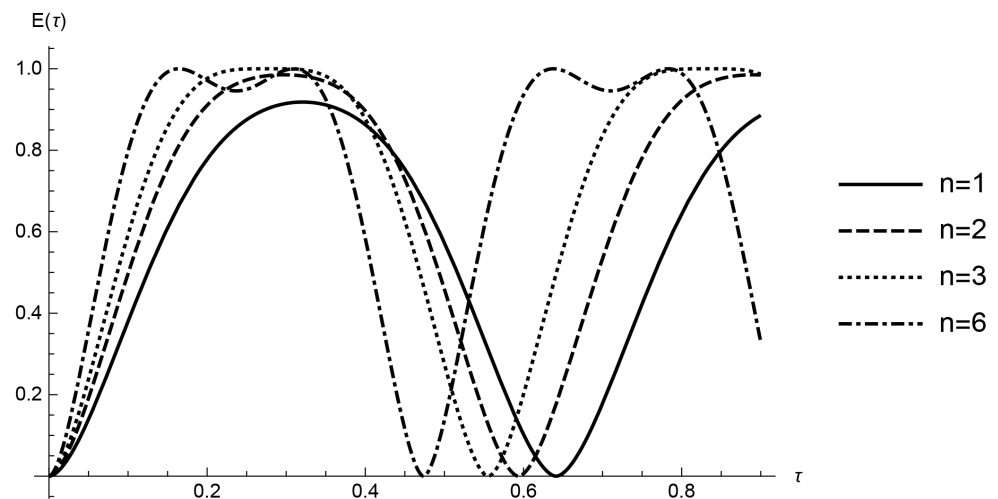
Figure 6. Degree of entanglement against scaled time for sum frequency $\bar{\delta} = 8\lambda$ when $n = 1$, $n = 2$, $n = 3$ and $n = 6$.

In the three figures, the phenomenon of entanglement sudden birth (ESB) and sudden death (ESD) is observed during the time evolution of entanglement similar to that observed in the JC model [34] [35] [36]. In ESB there is an observed creation of entanglement where the initially un-entangled qubits are entangled after a very short time interval. For fairly low values of photon numbers n and sum frequency $\bar{\delta}$ as demonstrated in **Figure 4** for $\bar{\delta} = 2\lambda$ plotted when $n = 1$, $n = 2$, the degree of entanglement rises sharply to a maximum value of unity ($E(\tau)_{\max}$) at an entangled state, stays at the maximum level for a reasonably short duration, decreases to a local minimum, then rises back to the maximum value before falling sharply to zero ($E(\tau)_{\min}$) at the separable state. The local minimum disappears for larger values of sum frequency $\bar{\delta} \geq 6\lambda$ at low photon number n and re-emerge at high photon number $n \geq 4$ (see **Figure 5** and **Figure 6**) as examples. However, in comparison to the resonance case

$\delta = 0$ in the JC model [36] we notice a long-lived entanglement at $E(\tau)_{\max} = 1$ in the cases of $\bar{\delta} = 6\lambda$ plotted when $n = 1$ in **Figure 5** and $\bar{\delta} = 8\lambda$ plotted when $n = 3$ in **Figure 6**. The process of ESB and ESD then repeats periodically, consistent with Rabi oscillations between the qubit states.

In **Figure 4** and **Figure 6** sum frequencies are kept constant at $\bar{\delta} = 2\lambda$ and $\bar{\delta} = 8\lambda$ respectively and photon number *n* is varied in each case. We clearly see that the frequency of oscillation of $E(\tau)$ increases with an increase in photon number *n*. This phenomenon in which the frequency of oscillation of $E(\tau)$ increases with an increase in photon number *n* is also observed in the JC model [35] [36].

To visualize the effect of sum frequency parameter $\bar{\delta}$ on the dynamics of $E(\tau)$, we considered values of sum frequency set at $\bar{\delta} = 6\lambda$ and $\bar{\delta} = 8\lambda$ for photon number $n = 1$ in **Figure 5**. It is clear that the frequency of oscillation of $E(\tau)$ increases with an increase in sum frequency $\bar{\delta} = \omega_0 + \omega$. In the JC model when detuning $\delta = \omega_0 - \omega$ is set at off resonance $\delta \neq 0$ results into a decrease in the frequency of oscillation of $E(\tau)$ as seen in [35] [36] [37] in comparison to the resonance case $\delta = 0$.

Finally, for $\bar{\delta} = 8\lambda$ plotted when $n = 1$ in **Figure 5** and in **Figure 6** in comparison to $\bar{\delta} = 6\lambda$ plotted when $n = 1$ in **Figure 5**, it is clear in **Figure 5** that the degree of entanglement $E(\tau)$ decreases at a high value of sum frequency a phenomenon similar to the JC model in [37]. The observed decrease in degree of entanglement is due to the property that the system loses its purity and the entropy decreases when the effect of sum frequency is considered for small number of photons *n*. This is remedied when the effect of sum frequency is considered for higher photon numbers *n* as shown in **Figure 6**.

5. Teleportation

In the present work we consider an interesting case of quantum teleportation by applying entanglement swapping protocol (teleportation of entanglement) [38] [39] [40] [41] where the teleported state is itself entangled. The state we want to teleport is a two-atom maximally entangled state in which we have assigned subscripts to distinguish the atomic qubit states in the form [42]

$$|\varphi\rangle_{12} = \frac{1}{\sqrt{2}}\left(|e\rangle_1|g\rangle_2 - |g\rangle_1|e\rangle_2\right) \tag{34}$$

and it is in Alice's possession. In another location Bob is in possession of a maximally entangled qubit state $\left|\bar{\phi}_{g0}\right\rangle$ generated in the AJC interaction in Equation (21c) and expressed as

$$|\Phi\rangle_{3x} = -\frac{1}{\sqrt{2}}|g\rangle_3|0\rangle_x + \frac{1}{\sqrt{2}}|e\rangle_3|1\rangle_x \tag{35}$$

where we have also assigned subscripts to the qubits in Equation (35) to clearly distinguish them.

An observer, Charlie, receives qubit-1 from Alice and qubit-*x* from Bob. The entire state of the system

$$|\chi\rangle = |\varphi\rangle_{12} \otimes |\Phi\rangle_{3x} \tag{36a}$$

which on substituting $|\varphi\rangle_{12}$ and $|\Phi\rangle_{3x}$ from Equations (34), (35) and reorganizing takes the form

$$|\chi\rangle = \frac{1}{2}\left[|\Psi^+\rangle_{1x}\left(\frac{|e\rangle_3|g\rangle_2 + |g\rangle_3|e\rangle_2}{\sqrt{2}}\right) + |\Psi^-\rangle_{1x}\left(\frac{|e\rangle_3|g\rangle_2 - |g\rangle_3|e\rangle_2}{\sqrt{2}}\right) \right.$$
$$\left. - |\Phi^-\rangle_{1x}\left(\frac{|g\rangle_3|g\rangle_2 - |e\rangle_3|e\rangle_2}{\sqrt{2}}\right) - |\Phi^+\rangle_{1x}\left(\frac{|g\rangle_3|g\rangle_2 + |e\rangle_3|e\rangle_2}{\sqrt{2}}\right) \right] \tag{36b}$$

after introducing the emerging Bell states obtained as

$$|\Psi^+\rangle_{1x} = \frac{|e\rangle_1|1\rangle_x + |g\rangle_1|0\rangle_x}{\sqrt{2}}$$

$$|\Psi^-\rangle_{1x} = \frac{|e\rangle_1|1\rangle_x - |g\rangle_1|0\rangle_x}{\sqrt{2}}$$

$$|\Phi^-\rangle_{1x} = \frac{|e\rangle_1|0\rangle_x - |g\rangle_1|1\rangle_x}{\sqrt{2}} \tag{37}$$

$$|\Phi^+\rangle_{1x} = \frac{|e\rangle_1|0\rangle_x + |g\rangle_1|1\rangle_x}{\sqrt{2}}$$

Charlie performs Bell state projection between qubit-1 and qubit-x (Bell state measurement (BSM)) and communicates his results to Bob which we have presented in Section 5.1 below.

5.1. Bell State Measurement

BSM is realized at Charlie's end. Projection of a state $|\Lambda\rangle$ onto $|\Sigma\rangle$ is defined as [43]

$$P_\Sigma := \langle\Sigma|\Lambda\rangle|\Sigma\rangle \tag{38}$$

Using $|\chi\rangle$ from Equation (36b) and applying Equation (38) we obtain a Bell state projection outcome communicated to Bob in the form

$$_{1x}\langle\Psi^-|\chi\rangle = \frac{1}{2}\left(\frac{|e\rangle_3|g\rangle_2 - |g\rangle_3|e\rangle_2}{\sqrt{2}}\right) = \frac{1}{2}|\Psi^-\rangle_{32} \tag{39a}$$

The Bell state $|\Psi^-\rangle_{32}$ in Equation (39a) is in the form of Alice's qubit in Equation (34). Alice and Bob now have a Bell pair between qubit-2 and qubit-3. Similarly the other three Bell projections take the forms

$$_{1x}\langle\Psi^+|\chi\rangle = \frac{1}{2}\left(\frac{|e\rangle_3|g\rangle_2 + |g\rangle_3|e\rangle_2}{\sqrt{2}}\right) = \frac{1}{2}|\Psi^+\rangle_{32} \tag{39b}$$

$$_{1x}\langle\Phi^-|\chi\rangle = \frac{1}{2}\left(\frac{|e\rangle_3|e\rangle_2 - |g\rangle_3|g\rangle_2}{\sqrt{2}}\right) = \frac{1}{2}|\Phi^-\rangle_{32} \tag{39c}$$

$$_{1x}\langle\Phi^+|\chi\rangle = -\frac{1}{2}\left(\frac{|e\rangle_3|e\rangle_2 + |g\rangle_3|g\rangle_2}{\sqrt{2}}\right) = -\frac{1}{2}|\Phi^+\rangle_{32} \tag{39d}$$

For these cases of Bell state projections in Equations (39b)-(39d) it will be ne-

cessary for Bob to perform local corrections to qubit-3 by Pauli operators as shown in Table 1. We also see that the probability of measuring states $|\psi\rangle_{32}$ in Equations (39a)-(39d) in Charlie's lab is $p = \dfrac{1}{4}$. In general, by application of the entanglement swapping protocol (teleportation of entanglement), qubit-2 belonging to Alice and qubit-3 belonging to Bob despite never having interacted before became entangled. Further, we see that a maximally entangled anti-symmetric atom-field transition state $\left|\bar{\phi}_{g0}\right\rangle$ (in Equation (21c)) easily generated in the AJC interaction, can be used in quantum information processing (QIP) protocols like entanglement swapping (teleportation of entanglement) which we have demonstrated in this work. We note that it is not possible to generate such an entangled anti-symmetric state in the JC interaction starting with the atom initially in the ground state and the field mode in the vacuum state [5]. Recall that the JC interaction produces a meaningful physical effect, namely, spontaneous emission only when the atom is initially in the excited state and the field mode in the vacuum state.

5.2. Maximal Teleportation Fidelity

For any two-qubit state $\hat{\rho}$ the maximal fidelity is given by [44]

$$F_{\hat{\rho}} = \frac{2f_{\hat{\rho}} + 1}{3} \tag{40}$$

where $f_{\hat{\rho}}$ is the fully entangled fraction defined in the form [32]

$$f_{\hat{\rho}} = \max_{|\Psi\rangle} \langle \Psi | \hat{\rho} | \Psi \rangle = \left\{ tr\sqrt{\hat{\rho}_{\text{expected}}^{\frac{1}{2}} \hat{\rho}_{\text{measured}} \hat{\rho}_{\text{expected}}^{\frac{1}{2}}} \right\}^2 \tag{41}$$

From Table 1

$$\begin{aligned}
\hat{\rho}_{\text{expected}} &= |\varphi_{12}\rangle\langle\varphi_{12}| \\
&= \frac{1}{2}\left[\left(|e_1\rangle|g_2\rangle - |g_1\rangle|e_2\rangle\right) \otimes \left(\langle e_1|\langle g_2| - \langle g_1|\langle e_2|\right)\right] \\
&= \frac{1}{2}\left[|e_1\rangle\langle e_1||g_2\rangle\langle g_2| - |e_1\rangle\langle g_1||g_2\rangle\langle e_2| \right. \\
&\quad \left. - |g_1\rangle\langle e_1||e_2\rangle\langle g_2| + |g_1\rangle\langle g_1||e_2\rangle\langle e_2|\right] \\
&= \frac{1}{2}\begin{pmatrix} -1 & 0 \\ 0 & -1 \end{pmatrix}
\end{aligned} \tag{42}$$

Table 1. Showing how Bob applies an appropriate gate to his qubit based on BSM from Charlie.

$|\varphi\rangle_{12}$	$|\psi\rangle_{32}$	UNITARY OPERATION
$\frac{1}{\sqrt{2}}\left(|e\rangle_1|g\rangle_2 + |g\rangle_1|e\rangle_2\right)$	$\frac{1}{\sqrt{2}}\left(-|g\rangle_3|g\rangle_2 + |e\rangle_3|e\rangle_2\right)$	$-\hat{\sigma}_{x(\text{atom3})} \otimes \hat{I}_{(\text{atom2})}$
	$\frac{1}{\sqrt{2}}\left(-|g\rangle_3|g\rangle_2 - |e\rangle_3|e\rangle_2\right)$	$-i\hat{\sigma}_{y(\text{atom3})} \otimes \hat{I}_{(\text{atom2})}$
	$\frac{1}{\sqrt{2}}\left(|e\rangle_3|g\rangle_2 + |g\rangle_3|e\rangle_2\right)$	$\hat{\sigma}_{z(\text{atom3})} \otimes \hat{I}_{(\text{atom2})}$

$$\hat{\rho}_{\text{measured}} = |\psi_{32}\rangle\langle\psi_{32}|$$

$$= \frac{1}{2}\left[\left(|e_3\rangle|g_2\rangle - |g_3\rangle|e_2\rangle\right) \otimes \left(\langle e_3|\langle g_2| - \langle g_3|\langle e_2|\right)\right]$$

$$= \frac{1}{2}\left[|e_3\rangle\langle e_3||g_2\rangle\langle g_2| - |e_3\rangle\langle g_3||g_2\rangle\langle e_2|\right. \tag{43}$$

$$\left. - |g_3\rangle\langle e_3||e_2\rangle\langle g_2| + |g_3\rangle\langle g_3||e_2\rangle\langle e_2|\right]$$

$$= \frac{1}{2}\begin{pmatrix} -1 & 0 \\ 0 & -1 \end{pmatrix}$$

Substituting the results in Equation (42) and Equation (43) into the fully entangled fraction Equation (41) we obtain

$$f_{\hat{\rho}} = \left\{ tr \begin{pmatrix} \dfrac{1}{2} & 0 \\ 0 & \dfrac{1}{2} \end{pmatrix} \right\}^2 = 1 \tag{44}$$

Substituting the value of the fully entangled fraction into Equation (40) we get

$$F_{\hat{\rho}} = 1 \tag{45}$$

a maximal teleportation fidelity of unity, showing that the state was fully recovered, *i.e.* Alice's qubit in Equation (34) was successfully teleported to Bob. We obtain an equal outcome to all the other measured states. We have thus achieved teleportation using a maximally entangled qubit state generated in an AJC interaction, using the case where the atom and field are initially in the absolute ground state $|g\rangle$, $|0\rangle$ as an example.

6. AJC State Engineering and Experimental Implementation

In order to systematically implement the AJC Hamiltonian with a single tuned blue-sideband interaction, the simulation process will involve AJC state preparation followed by unitary transformation and measurement.

The state of the whole system as an interaction of a two-level atom and one photon where both the atom and photon are in ground state $|g\rangle$, $|0\rangle$ will take the form of Equation (18). In a field mode that keeps the cavity field with upto one photon, the main focus should be to determine the experimental values of the probability amplitudes

$$\alpha(t) = \cos\left(\bar{R}_{g0}t\right) \tag{46a}$$

$$\beta(t) = -i\sin\left(\bar{R}_{g0}t\right) \tag{46b}$$

for the initial states $|\psi_{g0}\rangle$ and $|\bar{\phi}_{g0}\rangle$ respectively in Equation (18) and show their variation with time that has a direct correspondence to Rabi frequency $\bar{R}_{g0}$, which is of the form

$$\bar{R}_{g0} = \frac{1}{2}\sqrt{16\lambda^2 + \bar{\delta}^2} \tag{46c}$$

The measurement procedure can be easily implemented using efficient experimental schemes for manipulating quantum entanglement with atoms and

photons in a cavity strictly in the AJC model, during which process difficulties can be determined as appropriate. The most common scheme being cavity quantum electrodynamics [45].

Entanglement swapping is realised in an experimental set-up through Bell state measurement. Initially, the two sets of entangled states in Equations (34) and (35) are prepared. The entire state of the system then takes the form of Equation (36b). The required Bell state measurement is achieved in this case by first applying a quantum controlled-NOT(C-NOT) gate operation followed by a quantum Hadamard gate operation to qubit 1, which we now explain with examples below. In order to realise a C-NOT quantum gate operation in this case, we note that state evolution operator in the AJC interaction is generated by the time evolution operator in Equation (12), which on substituting the Hamiltonian $\hat{\bar{H}}$ from Equation (11) and dropping the factorizable global phase factor $e^{-i\omega t\left(n+\frac{3}{2}\right)\hat{\bar{I}}_g}$, we define a C-NOT gate operator in the AJC model in the general form in Equation (10), which we rewrite here for ease of reference

$$e^{-i\theta\hat{\bar{\varepsilon}}_g} = \cos(\theta)\hat{\bar{I}}_g - i\sin(\theta)\hat{\bar{\varepsilon}}_g \tag{10'}$$

The C-NOT gate process consists of a two-level atom as the control qubit, which constitutes a two dimensional Hilbert space spanned by the atomic excited and ground states $|e\rangle$, $|g\rangle$ as basis vectors. Two non-degenerate and orthogonal polarized cavity modes C_A and C_B make the target qubit. The target qubit is defined in two-dimensional Hilbert space spanned by the state vector $|\mu_1\rangle = |1_A, 0_B\rangle$, which expresses the presence of one photon in mode A, when there is no photon in mode B, and the state vector $|\mu_2\rangle = |0_A, 1_B\rangle$, which indicates that mode A is in the vacuum state and one photon is present in mode B.

Let us consider the case when qubit 1 (in Charlie's possession) in ground state $|g\rangle_1$ enters an electromagnetic cavity with mode A in vacuum state and a single photon in mode B. The atom couples to the anti-rotating negative frequency component of the field mode undergoing an AJC qubit state transition. After the atom interacts with mode A for a time $t = \dfrac{\pi}{R_{g0}}$, equal to half Rabi oscillation time, the driving field is modulated such that

$$\theta = \bar{R}_{g0}t = 2\lambda\bar{A}_{g0}t = \pi \tag{47}$$

Redefining [5]

$$\bar{\alpha} = \frac{\bar{\delta}}{2\lambda} = \frac{\omega_0 - \omega + 2\omega}{2\lambda} = \frac{\delta}{2\lambda} + \frac{\omega}{\lambda} \tag{48}$$

and considering a resonance case where $\delta = \omega_0 - \omega = 0$ with the coupling strength λ far much greater than the quantized field mode angular frequency ω, that is $\lambda \gg \omega$ in the deep strong coupling regime of the AJC model, $\bar{\alpha}$ in Equation (48) becomes very small thus

$$\theta = \lambda t = \frac{\pi}{2} \tag{49}$$

since $\overline{A}_{g0} = 1$ in Equation (47) determined from the general form in Equation (6). The evolution of this interaction determined by applying the AJC qubit state transition operation in Equation (10) noting the definition of $\hat{\overline{I}}_g$ and $\hat{\overline{\varepsilon}}_g$ [5] in Equation (8) is of the form

$$\mathrm{e}^{-i\theta\hat{\overline{\varepsilon}}_g}\left|g,0_A\right\rangle = \cos(\theta)\left|g,0_A\right\rangle - i\sin(\theta)\left|e,1_A\right\rangle \tag{50a}$$

which reduces to

$$\left|g,0_A\right\rangle \rightarrow -i\left|e,1_A\right\rangle \tag{50b}$$

We observe that the atom interacted with mode A and completed half of the Rabi oscillation, as a result, it contributed a photon to mode A and evolved to excited state $\left|e\right\rangle$. Now, after the interaction time, it enters mode B containing a single photon, interacting with the cavity mode as follows

$$-i\mathrm{e}^{i\theta\hat{\overline{\varepsilon}}_e}\left|e,1_B\right\rangle = -i\cos(\theta)\left|e,1_B\right\rangle + \sin(\theta)\left|g,0_B\right\rangle \tag{50c}$$

After an interaction with mode B for a time $t_1 = 2t$ such that $t_1 = \dfrac{\pi\left(\overline{R}_{g0} + \overline{R}_{e1}\right)}{\overline{R}_{g0}\overline{R}_{e1}}$, the driving field is modulated such that $\theta = \left(\dfrac{\overline{R}_{g0}\overline{R}_{e1}}{\overline{R}_{g0} + \overline{R}_{e1}}\right)t = \dfrac{\pi}{2}$ with $\overline{R}_{g0} = 2\lambda\overline{A}_{g0} = 2\lambda$ since $\overline{A}_{g0} = 1$ and $\overline{R}_{e1} = 2\lambda\overline{A}_{e1} = 2\lambda$ since $\overline{A}_{e1} = 1$. Therefore, $\lambda t = \dfrac{\pi}{2}$. The form of Equation (50c) results into the evolution

$$-i\left|e,1_B\right\rangle \rightarrow \left|g,0_B\right\rangle \tag{50d}$$

The results in Equation (50d) show that the atom evolves to ground state and absorbs a photon initially in mode B. Therefore the atom clearly performs a swapping of the electromagnetic field between the two field modes by controlled interaction.

When the atom in ground state $\left|g\right\rangle$, enters the electromagnetic cavity containing a single photon in mode A and mode B in vacuum state, the atom and the field interact as follows

$$\mathrm{e}^{-i\theta\hat{\overline{\varepsilon}}_g}\left|g,0_B\right\rangle = \cos(\theta)\left|g,0_B\right\rangle - \sin(\theta)\left|e,1_B\right\rangle \tag{50e}$$

After an interaction with field mode B for a time $t = \dfrac{\pi}{\overline{R}_{g0}}$ equal to half Rabi oscillation time, the driving field is modulated such that $\theta = \overline{R}_{g0}t = \pi$, with $\overline{R}_{g0} = 2\lambda\overline{A}_{g0} = 2\lambda$ since $\overline{A}_{g0} = 1$. Therefore $\theta = \lambda t = \dfrac{\pi}{2}$. The form of Equation (50e) results in the evolution

$$\left|g,0_B\right\rangle \rightarrow -\left|e,1_B\right\rangle \tag{50f}$$

The atom then enters mode A containing one photon and interacts as follows

$$-\mathrm{e}^{i\theta\hat{\overline{\varepsilon}}_e}\left|e,1_A\right\rangle = -\cos(\theta)\left|e,1_A\right\rangle - i\sin(\theta)\left|g,0_A\right\rangle \tag{50g}$$

After an interaction with the cavity mode for a time $t_1 = 2t$ such that $t_1 = \dfrac{\pi\left(\overline{R}_{e1} + \overline{R}_{g0}\right)}{\overline{R}_{e1}\overline{R}_{g0}}$ we obtain a driving field modulation $\theta = \left(\dfrac{\overline{R}_{e1}\overline{R}_{g0}}{\overline{R}_{e1} + \overline{R}_{g0}}\right)t = \dfrac{\pi}{2}$,

with $\bar{R}_{e1} = 2\lambda \bar{A}_{e1} = 2\lambda$ since $\bar{A}_{e1} = 1$ and $\bar{R}_{g0} = 2\lambda \bar{A}_{g0} = 2\lambda$ since $\bar{A}_{g0} = 1$.

Therefore $\theta = \lambda t = \dfrac{\pi}{2}$. The form of Equation (50g) results into the evolution

$$|e, 1_A\rangle \to i |g, 0_A\rangle \tag{50h}$$

This shows that the atom evolves to ground state and performs a field swapping by absorbing a photon in mode A.

When the qubit 1, a two-level atom in excited state $|e\rangle_1$ enters mode A in vacuum state, that is target qubit $|\mu_2\rangle$, the atom propagates as a free wave without coupling to the field mode in vacuum state $|0\rangle$ [5], leaving the cavity without altering the state of the cavity-field mode. A similar observation is made when the atom in excited state $|e\rangle_1$ enters cavity B in vacuum state for the case of target qubit $|\mu_1\rangle$.

The Hadamard gate operation then follows. Noting the qubit state transition algebraic operations in Equation (9), we identify the normalized qubit state transition operator $\hat{\bar{\varepsilon}}_g$ defined in Equation (8) as the AJC Hadamard gate operator which we use Equation (4) to express in the general form

$$\hat{\bar{\varepsilon}}_g = \frac{\bar{\alpha}\hat{s}_z + \hat{a}\hat{s}_- + \hat{a}^\dagger \hat{s}_+}{\bar{A}_{gn}} \tag{51a}$$

where $\bar{A}_{gn}$ is defined in Equation (6). For the specific example where atom begins in the ground state $|g\rangle_1$ and the field mode in the vacuum state $|0\rangle$, we set $n = 0$ and take $\bar{\delta} = 4\lambda$ in Equation (6) to define the corresponding Hadamard gate operator in the form

$$\hat{\bar{\varepsilon}}_g = \frac{1}{A_{g0}}\left(2\hat{s}_z + \hat{a}\hat{s}_- + \hat{a}^\dagger \hat{s}_+\right); \quad \bar{A}_{g0} = \sqrt{2} \tag{51b}$$

Applying this Hadamard gate operator, rotates the initial atomic ground state $|g\rangle_1$ to

$$|g\rangle_1 \to \frac{1}{\sqrt{2}}\left(|e\rangle_1 - |g\rangle_1\right) \tag{51c}$$

On the other hand, if the atom starts from an initial excited state $|e\rangle_1$, the appropriate Hadamard gate operator for such a process follows from the definition of the relevant normalised qubit state transition operator $\hat{\bar{\varepsilon}}_e$ in [5], which on setting $\bar{\delta} = 4\lambda$ and $n = 1$ takes the form

$$\hat{\bar{\varepsilon}}_e = \frac{1}{A_{e1}}\left(2\hat{s}_z + \hat{a}\hat{s}_- + \hat{a}^\dagger \hat{s}_+\right); \quad \bar{A}_{e1} = \sqrt{2} \tag{52a}$$

which rotates the initial atomic excited state $|e\rangle$ to

$$|e\rangle_1 \to \frac{1}{\sqrt{2}}\left(|e\rangle_1 + |g\rangle_1\right) \tag{52b}$$

Application of the C-NOT and Hadamard gate operations using the respective operators defined in Equation (10') or earlier (10) and Equations (51b), (52a) as briefly explained in the above example, provides a practical platform for experi-

mental implementation of the AJC quantum teleportation process described in Sec. 5. Here, results of the Bell state measurement are communicated to Bob (by Charlie) who applies appropriate single-qubit rotation to qubit 3 in his possession. Details of experimental design, procedures and difficulties can be provided as appropriate, noting that the quantum Rabi interaction is generally achieved in cavity or circuit quantum electrodynamics, quantum dots or ion traps, etc.

7. Conclusion

In this paper we have analysed entanglement of a two-level atom and a quantized electromagnetic field mode in an AJC qubit formed in the AJC interaction mechanism. The effect of sum-frequency parameter and photon number on the dynamical behavior of entanglement measured by von Neumann entropy was studied which brought a clear visualization of this interaction similar to the graphical representation on Bloch sphere. The graphical representation of Rabi oscillations on the Bloch sphere demonstrated an important physical property that the AJC interaction process occurs in the reverse sense relative to the JC interaction process. We further generated an entangled AJC qubit state in the AJC interaction mechanism which we used in the entanglement swapping protocol as Bob's qubit. We obtained an impressive maximal teleportation fidelity $F_\rho = 1$ showing that the state was fully recovered. This impressive result of fidelity, opens all possible directions for future research in teleportation strictly within the AJC model. In conclusion we observe that the operator ordering that distinguishes the rotating (JC) component and anti-rotating component (AJC) has an important physical foundation with reference to the rotating positive and anti-rotating negative frequency components of the field mode which dictates the coupling of the degenerate states of a two-level atom to the frequency components of the field mode, an important basis for realizing the workings in the AJC interaction mechanism and JC interaction mechanism.

Acknowledgements

Conflicts of Interest

The authors declare no conflicts of interest regarding the publication of this paper.

References

[1] Braak, D. (2011) *Physical Review Letters*, **107**, Article ID: 100401. https://doi.org/10.1103/PhysRevLett.107.100401

[2] Xie, Q., Zhong, H., Batchelor, M.T. and Lee, C. (2017) *Journal of Physics A*: *Mathematical and Theoretical*, **50**, Article ID: 113001. https://doi.org/10.1088/1751-8121/aa5a65

[3] Omolo, J.A. (2017) Conserved Excitation Number and U(1)-Symmetry Operators

for the Anti-Jaynes-Cummings (Anti-Rotating) Component of the Rabi Hamiltonian.

[4] Omolo, J.A. (2017) Polariton and Anti-Polariton Qubits in the Rabi Model.

[5] Omolo, J.A. (2019) Photospins in the Quantum Rabi Model.

[6] Rabi, I. (1936) *Physical Review*, **49**, 324-328.
https://doi.org/10.1103/PhysRev.49.324

[7] Rabi, I.I. (1937) *Physical Review*, **51**, 652. https://doi.org/10.1103/PhysRev.51.652

[8] Jaynes, E.T. and Cummings, F.W. (1963) *Proceedings of the IEEE*, **51**, 89-109.
https://doi.org/10.1109/PROC.1963.1664

[9] Chen, Q.-H., Wang, C., He, S., Liu, T. and Wang, K.-L. (2012) *Physical Review A*,
86, Article ID: 023822. https://doi.org/10.1103/PhysRevA.86.023822

[10] Zhong, H., Xie, Q., Batchelor, M.T. and Lee, C. (2013) *Journal of Physics A*: *Mathematical and Theoretical*, **46**, Article ID: 415302.
https://doi.org/10.1088/1751-8113/46/41/415302

[11] Zhang, G. and Zhu, H. (2015) *Scientific Reports*, **5**, Article No. 1.
https://doi.org/10.1038/srep08756

[12] Born, M. and Wolf, E. (1999) Principles of Optics: Electromagnetic Theory of
Propagation, Interference and Diffraction of Light. 7th Edition, Cambridge University Press, Cambridge.

[13] Satyanarayana, M.V., Rice, P., Vyas, R. and Carmichael, H. (1989) *JOSA B*, **6**,
228-237. https://doi.org/10.1364/JOSAB.6.000228

[14] Moya-Cessa, H. and Vidiella-Barranco, A. (1995) *Journal of Modern Optics*, **42**,
1547-1552. https://doi.org/10.1080/09500349514551341

[15] Yurke, B. and Stoler, D. (1986) *Physical Review Letters*, **57**, 13-16.
https://doi.org/10.1103/PhysRevLett.57.13

[16] Gomes, A. and Vidiella-Barranco, A. (2014) *Applied Mathematics & Information
Sciences*, **8**, 727-732. https://doi.org/10.12785/amis/080232

[17] Agarwal, G.S. (1985) *JOSA B*, **2**, 480-485.

[18] Niemczyk, T., Deppe, F., Huebl, H., Menzel, E., Hocke, F., Schwarz, M., Garcia-Ripoll, J., Zueco, D., Hummer, T., Solano, E., *et al.* (2010) *Nature Physics*, **6**,
772. https://doi.org/10.1038/nphys1730

[19] Kena-Cohen, S., Maier, S.A. and Bradley, D.D. (2013) *Advanced Optical Materials*,
1, 827-833.

[20] Werlang, T., Dodonov, A., Duzzioni, E. and Villas-Boas, C. (2008) *Physical Review
A*, **78**, Article ID: 053805. https://doi.org/10.1103/PhysRevA.78.053805

[21] Wolf, F.A., Vallone, F., Romero, G., Kollar, M., Solano, E. and Braak, D. (2013)
Physical Review A, **87**, Article ID: 023835.
https://doi.org/10.1103/PhysRevA.87.023835

[22] Pedernales, J., Lizuain, I., Felicetti, S., Romero, G., Lamata, L. and Solano, E. (2015)
Scientific Reports, **5**, Article No. 1. https://doi.org/10.1038/srep15472

[23] Boyer, M., Liss, R. and Mor, T. (2017) *Physical Review A*, **95**, Article ID: 032308.
https://doi.org/10.1103/PhysRevA.95.032308

[24] Regula, B. and Adesso, G. (2016) *Physical Review Letters*, **116**, Article ID: 070504.
https://doi.org/10.1103/PhysRevLett.116.070504

[25] Nielsen, M.A. and Chuang, I.L. (2011) Quantum Computation and Quantum Information. Cambridge University Press, Cambridge.

[26] Rieffel, E.G. and Polak, W.H. (2011) Quantum Computing: A Gentle Introduction. MIT Press, Cambridge.

[27] Van Meter, R. (2014) Quantum Networking. John Wiley & Sons, Hoboken. https://doi.org/10.1002/9781118648919

[28] Enrıquez, M., Reyes, R. and Rosas-Ortiz, O. (2014) *Journal of Physics: Conference Series*, **512**, Article ID: 012021. https://doi.org/10.1088/1742-6596/512/1/012021

[29] Von Neumann, J. (2018) Mathematical Foundations of Quantum Mechanics: New Edition. Princeton University Press, Princeton. https://doi.org/10.23943/princeton/9780691178561.001.0001

[30] Wootters, W.K. (2001) *Quantum Information & Computation*, **1**, 27-44.

[31] Abdel-Khalek, S. (2011) *Journal of Russian Laser Research*, **32**, 86.

[32] Bennett, C.H., Di Vincenzo, D.P., Smolin, J.A. and Wootters, W.K. (1996) *Physical Review A*, **54**, 3824-3851. https://doi.org/10.1103/PhysRevA.54.3824

[33] Bennett, C.H., Bernstein, H.J., Popescu, S. and Schu-macher, B. (1996) *Physical Review A*, **53**, 2046-2052. https://doi.org/10.1103/PhysRevA.53.2046

[34] Mohammadi, M. and Jami, S. (2019) *Optik*, **181**, 582. https://doi.org/10.1016/j.ijleo.2018.12.096

[35] Liu, X.-J., Lu, J.-B., Zhang, S.-Q., Liu, J.-P., Li, H., Liang, Y., Ma, J., Weng, Y.-J., Zhang, Q.-R., Liu, H., *et al.* (2018) *International Journal of Theoretical Physics*, **57**, 290. https://doi.org/10.1007/s10773-017-3604-3

[36] Zhang, S.-Q., Lu, J.-B., Liu, X.-J., Liang, Y., Li, H., Ma, J., Liu, J.-P. and Wu, X.-Y. (2018) *International Journal of Theoretical Physics*, **57**, 279. https://doi.org/10.1007/s10773-017-3603-4

[37] Abdel-Khalek, S., Quthami, M. and Ahmed, M. (2015) *Optical Review*, **22**, 25-30. https://doi.org/10.1007/s10043-015-0044-2

[38] Zukowski, M., Zeilinger, A., Horne, M.A. and Ekert, A.K. (1993) *Physical Review Letters*, **71**, 4287-4290. https://doi.org/10.1103/PhysRevLett.71.4287

[39] Megidish, E., Halevy, A., Shacham, T., Dvir, T., Dovrat, L. and Eisenberg, H. (2013) *Physical Review Letters*, **110**, Article ID: 210403. https://doi.org/10.1103/PhysRevLett.110.210403

[40] Pan, J.-W., Bouwmeester, D., Weinfurter, H. and Zeilinger, A. (1998) *Physical Review Letters*, **80**, 3891-3894. https://doi.org/10.1103/PhysRevLett.80.3891

[41] Bose, S., Vedral, V. and Knight, P.L. (1998) *Physical Review A*, **57**, 822. https://doi.org/10.1103/PhysRevA.57.822

[42] Sousa, E.H. and Roversi, J. (2019) *Quantum Reports*, **1**, 63-70. https://doi.org/10.3390/quantum1010007

[43] Scherer, W. (2019) Mathematics of Quantum Computing: An Introduction. Springer Nature, Berlin. https://doi.org/10.1007/978-3-030-12358-1

[44] Horodecki, M., Horodecki, P. and Horodecki, R. (1999) *Physical Review A*, **60**, 1888. https://doi.org/10.1103/PhysRevA.60.1888

[45] Raimond, J.-M., Brune, M. and Haroche, S. (2001) *Reviews of Modern Physics*, **73**, 565. https://doi.org/10.1103/RevModPhys.73.565

Superheavy Particle Production in High Energy Heavy Ion Collisions

Alexey Kurepin

Department of Experimental Physics, Institute for Nuclear Research, Russian Academy of Sciences, Moscow, Russia
Email: kurepin@inr.ru

Abstract

The existence of several TeV superheavy particles (SHPs) is predicted by theories beyond the Standard Model. Particles with a mass exceeding the energy in the center of mass in the collision of protons with protons can be produced in subthreshold heavy ion collisions at the LHC. The purpose of the performed research was to estimate the rate of a rare process of SHPs production. It was shown that the data on the subthreshold production of antiprotons can be explained by the phenomenological parton model. The obtained parton distribution function was used to determine the number of SHPs produced in subthreshold heavy ion collisions at the LHC. In one month of collision of lead with lead, the yield of 16 TeVparticles is about 70 per year. To study the kinematically forbidden phenomena in proton-proton interactions in collisions of heavy nuclei at the LHC, an experiment on the production of antiprotons is proposed in the ALICE fixed target project.

Keywords

Particle Physics, Heavy Ion Collisions, Parton Model, Antiproton Production

1. Introduction

In Grand Unification Theory, it is assumed that the first massive particles which are responsible for the symmetry breaking up to the symmetry of the Standard Model at the distances larger than 10^{-29} cm have masses of the order of 10^{12} TeV. In the simple version of this theory next masses arise only at distances about 10^{-16} cm, where the particles with masses of the order of 10^{2} GeV should be considered. They are connected to the breaking of electroweak symmetry, so called Higgs scalar bosons. Therefore a rather artificial hypothesis was proposed on the existence of the "gauge dessert", *i.e.* no particles have masses between 0.2 - 10^{12} TeV. However, some other possibility for high mass production is predicted by

Large Extra Dimension theories, where our 3 + 1 dimensional world is considered as a "brane" in the higher dimensional space. Then the Planck mass can be brought down to a level of the order of one TeV [1]. Then Superheavy Particles with masses of several TeV, such as mini Black Holes, could be produced if the extra dimension is equal to seven.

Additionally, more complicated models have been proposed with multistep breaking of the symmetry at super high energy down to the symmetry of the Standard Model, where some new particles could be adopted with masses in the interval filling the "gauge dessert". One of the most interesting possibilities provides theory based on new symmetry principle connecting the particles with different statistics, so-called Supersymmetry Theory. New types of heavy quarks and leptons are introduced in this theory: s-quarks and s-leptons and corresponding supersymmetry partners. In that respect, we can take into account new possibilities for producing the masses up to 10^3 TeV with the LHC with heavy ions as an opportunity to search for new superheavy supersymmetry particles. We can expect rather small coupling between these new types of physical objects and particles of the ordinary world. Therefore, one can look for superheavy particles with a large lifetime. Although there are several proposals for the search for long-lived particles, none of them are considering particles with a mass of several TeV.

The unique possibility of relativistic heavy ion collisions is production with considerable probability of particles which are kinematically forbidden for nucleon-nucleon collisions with the same energy per nucleon. The essential increase in the "subthreshold" antiproton production cross section for nucleus-nucleus collision normalized per one nucleon in comparison to nucleon-nucleus collision was observed [2] [3] [4] [5] [6]. This increase can reach two orders of magnitude and cannot be explained by Fermi motion in the incident and target nuclei [7]. However, this approach took into account only nucleon-nucleon collisions. "Subthreshold" particle production could be due to multinucleon or multiquark correlation in heavy nuclei. It can be assumed that this correlation is determined by the parton distribution function with a scaling parameter greater than unity.

The total energy in the center of mass system for Pb-Pb collisions at the LHC is approximately 1150 TeV. Therefore, the unique possibility could be considered to produce Super Heavy Particles (SHPs) by nucleus-nucleus collisions with masses much larger than the center of mass energy in p-p collisions. To date, there is no theory for calculating the cross section for SHPs production in collisions of heavy ions. However, to plan a possible experiment, it is necessary to estimate the number of particles produced. In this article, it is proposed to use for this estimate the parton distribution function obtained for the subthreshold antiproton production.

2. Parton Model for Particle Production in Heavy Ion Collisions

For the analysis of the subthreshold hadron production at intermediate energies

the phenomenological parton model was proposed [8]. It was observed that the subthreshold and near threshold production cross section in proton-nucleus and nucleus collisions for pions, kaons and antiprotons could be expressed as a universal function of the scaling quark-parton parameters, such as the Bjorken scaling parameter x for deep inelastic electron scattering, but take into account the production of massive particles and is now different in incident (Z) and in target (X) nuclei. Values Z and X larger than 1 arise to provide the production of particles at subthreshold energies for nucleon-nucleon process. As usually a physical interpretation of these scaling parameters in a quark-parton model means that XP_b correspond to parton 4-momentum in a target nuclei, where P_b is 4-momentum of a nucleon in a target nucleus. X could take the values in an interval $0 < X < A$, where A is the atomic number of a target. On the other hand the same parton model could be applied to the incident particle ZP_a.

For antiproton production the value of X for fixed Z could be obtained:

$$X = \frac{Z\left(P_a P_d\right) + Z m_a m_n + \frac{1}{2}\left(m_n^2 - m_d^2\right)}{Z\left(P_a P_b\right) - Z m_a m_b - \left(P_b P_d\right) - m_b m_n} \tag{1}$$

which is derived from the conservation of the 4-momentum in the collision. Here P_d is the 4-momentum of the antiproton, $m_a m_b m_n$ -mass of the nucleon in the incident and in target nuclei, and m_d-mass of the antiproton. Because of the exponential dependence of the production cross section on the scaling parameters, this equation matches the smallest values of X and Z parameters corresponding to the smallest energy in the center of mass of partons interaction.

For proton-nucleus and nucleus-nucleus interactions, the experimental data over a wide energy interval for different incident and target nuclei could be approximated with the same scaling law. Those are the data for antiproton production with Ne and Ni nuclei with 1 - 2 GeV/nucl. at GSI [6], proton and carbon nuclei with 3.65 GeV/nucl. at JINR [2] [3], with a deuteron beam at KEK [5] and protons and a Si-beam at LBL for antiproton and K$^-$ production [4]. The scaling in **Figure 1** is observed with a Z-parameter equal 1 for proton beam, 1.3 for deuteron, 2 for carbon beams and 3 for Si, Ne, and Ni nuclei [8]. The production cross sections were reduced by $(A_1 A_2)^{0.43}$ according to A-dependence investigated in [9] and due to the different absorption nuclear effects for pions, kaons and antiprotons.

The considerable increase in the ratio of kaon to pion production rates in nucleus-nucleus collision compared to the same ratio in deuteron-nucleus collision was also explained by the scaling dependence on the Z parameter for $Z < 1$, but with the parameter $X = 2$ for incident carbon nuclei and $X = 1.5$ for incident deuterons [10].

The considerable increase in the production rates for kaons and antiprotons compared to pions in nucleus-nucleus collisions was interpreted as the indication of collective parton effect and was quantitatively reproduced by the introduction of scaling parameters larger than one. From **Figure 2** we see that the
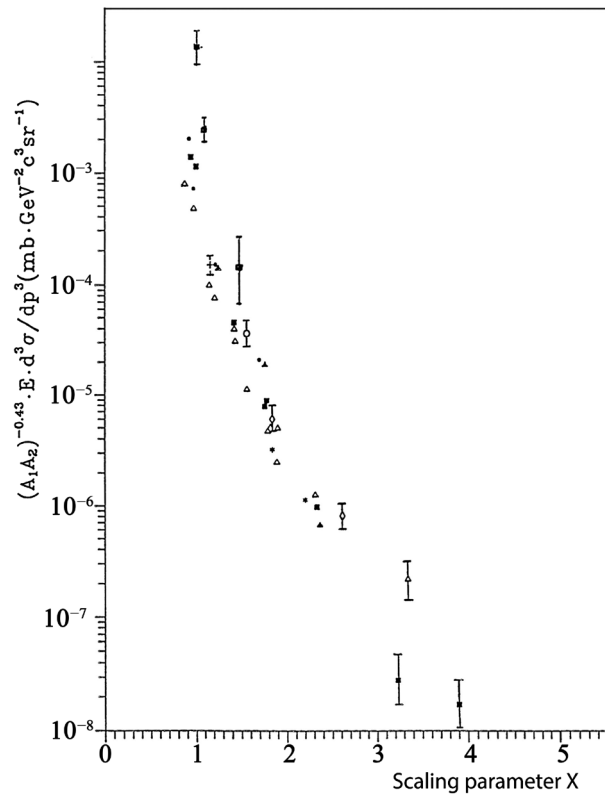
Figure 1. Systematics of Lorentz invariant antiproton subthreshold production cross section dependence on the scaling parameter X with $Z = 1$ for incident protons, $Z = 1.3$ for deuterons, $Z = 2$ for carbon ions, $Z = 3$ for heavy nuclei. Points p + C, open circles d + C, crosses C + C and C + Cu [2] [3], triangles p + C and d + C [5], squares p + Cu [7], rhombs Si + Si [4], stares Ne + Sn and Ni + Ni [6]. Only some statistical errors are presented to show the order of uncertainty for the measurements of subthreshold production.

dependence of the Lorenz invariant inclusive cross section, or of the structure function, on the scaling parameter is close to the exponent. The "subthreshold" structure function in **Figure 2** could be approximated as:

$$\left(A_1 A_2\right)^{-0.43} \cdot E_1 \frac{d^3 \sigma}{d p^3}\left[\mathrm{mb} \cdot \mathrm{GeV}^{-2} \cdot \mathrm{c}^3 \cdot \mathrm{sr}^{-1}\right] = 0.57 \exp\left(-X / 0.158\right) \qquad (2)$$

where A_1 and A_2 are the mass numbers of colliding nuclei.

This curve can be used to describe the experimental data in the range of cross section 10^{-1} - 10^{-5} mb with an accuracy less than an order of magnitude for $X = 1$ - 3 for the data from approximately 2 to 6 GeV per nucleon.

The enhancement of kaon and antiproton production is quantitatively reproduced by the introduction of a large Z scaling parameter: $Z = 1.3$ for deuterons, $Z = 3$ for all heavy colliding nuclei. For incident protons Z is equal to one.

This scaling was observed for different quark flavors. Therefore one can expect that the model can be applied to some heavier unknown quarks and that these collective phenomena could be due to some general space-time properties of nucleus-nucleus interaction or to the universal structure function of a nucleus.
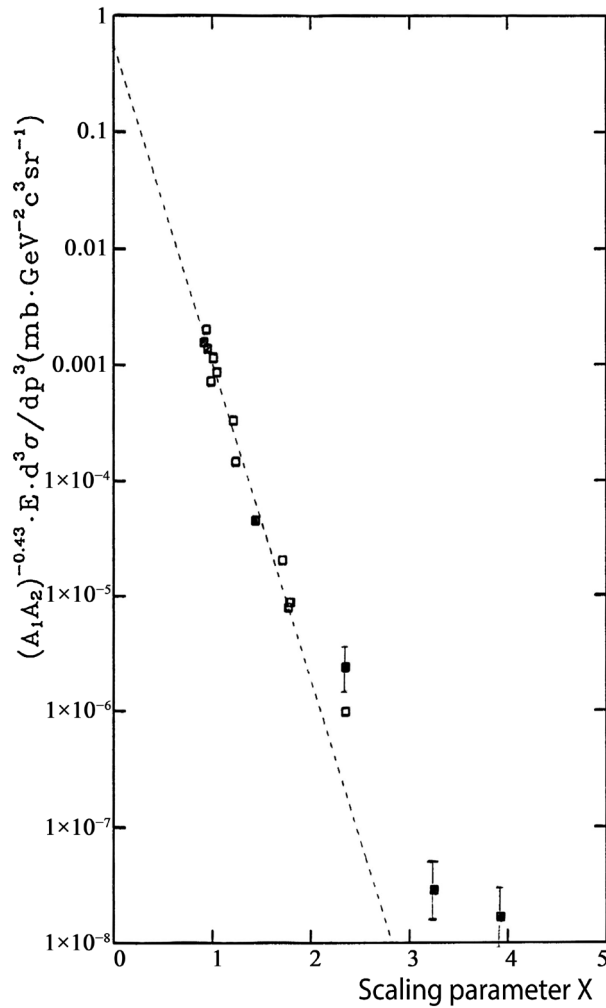
Figure 2. χ^2-Fit to the invariant antiproton production cross section dependence on the X-scaling parameter. Only data for the interaction of protons with carbon (open marks) and with copper (filled marks) are shown.

3. Estimate of Production Yield of Super Heavy Particle Production

From Equation (2) we see that the cross section strongly depends on the parameter X. Therefore, to produce SHP with considerable probability, one should look for the kinematics with the smallest X and Z possible. To estimate the SHP production cross section for the LHC using the scaling dependence of the structure function for $M \gg m_n$ we can determine Z and X from the relation on the threshold for SHP production:

$$\sqrt{S} = 2E\sqrt{X \cdot Z} = M , \tag{3}$$

where M is the mass of SHP, m_n is the mass of nucleon, E is the energy per nucleon of colliding nuclei.

To estimate the production rate of SHP with the mass M, Equation (2) could be used with $Z = 3$ for nucleus-nucleus collision and X to be determined from Equation (3).

The absolute value of the momentum P of SHP is obtained from the equation

$$X = \frac{2Z\left(E \cdot E_1 - E \cdot P \cdot \cos(\theta)\right) - M^2}{4Z \cdot E^2 - 2\left(E \cdot E_1 + E \cdot P \cdot \cos(\theta)\right)} \quad (4)$$

which is derived from the conservation of the 4-momentum in the collision. Here E_1 is the total energy of SHP, θ is the angle between SHP and Z parton.

Assuming that SHPs are produced with small transverse momentum in the narrow forward-backward cone we obtain for the masses M larger than 1 TeV, the velocities of SHP are of the order of 0.1 - 0.9 c.

Accepting that the multi quark correlations are the intrinsic property of nuclei and do not depend on the collision energy, we can try to use the "subthreshold" structure function from Equation (2) to estimate the production rate of SHPs depending on their mass in Pb-Pb collisions:

$$E_1 \frac{d^3\sigma}{dp^3}\left[\text{mb} \cdot \text{GeV}^{-2} \cdot c^3 \cdot \text{sr}^{-1}\right] = 56 \exp\left(-X/0.158\right) \quad (5)$$

For the obtained luminosity $L = 2 \times 10^{27}$ cm^{-2}·sec^{-1} for one month of the run and an opening angle of approximately 100 msr for the forward detector we obtain an estimate of the SHP yield for a mass approximately 16 TeV near the threshold on the order of 70 per year. For larger SHP masses the production cross section is greatly reduced due to the increasing parameter X in the exponential dependence. The results obtained can be used when planning an experiment at the LHC. Assuming SHPs are long-lived particles, the forward detectors will see very large signals. For a short lifetime, barrel detectors will detect events with anomalously high multiplicity.

The question remains about the possibility of applicability of the empirical scaling law, obtained at intermediate energies, to interactions at ultrahigh LHC energies. Unfortunately, it is impossible to measure the scattering and production of particles kinematically forbidden for nucleon-nucleon interactions at angles greater than 90 degrees on collider experimental facilities, that is, at $X > 1$.

Very promising possibilities for studying subthreshold phenomena are opened up in the case of experiments with a fixed target at the LHC [11] [12] [13]. The AFTER or ALICE-FT project provides for the placement of a solid or gaseous target in the beam halo when using all detectors of the ALICE facility. In this case, it is possible to measure the production of particles, in particular antiprotons, at large parameters X [13] even at $X > 1$, which will make it possible to check the existence of the scaling, considered in this work, at the energies of ion beams at the LHC. For a fixed target with a beam energy of 2.76 TeV per nucleon and $Z = 3$ from Equation (4) we obtain $X = 1.75$ for a production angle of 28 degrees.

4. Conclusion

The extrapolation of the scaling observed in the parton model for subthreshold antiproton production in the collision of heavy ions to high energies was per-

formed, in order to obtain estimates of the cross section and yield for the production of particles with masses up to 16 TeV. It is proposed to investigate subthreshold phenomena in an experiment with a fixed target at the LHC.

Acknowledgements

Conflicts of Interest

The author declares no conflicts of interest regarding the publication of this paper.

References

[1] Rubakov, V.A. (2003) *Physics-Uspekhi*, **46**, 211-218. https://doi.org/10.1070/PU2003v046n02ABEH001355

[2] Baldin, A.A., *et al*. (1988) *JETP Letters*, **48**, 137-140.

[3] Baldin, A.A., *et al*. (1990) *Nuclear Physics A*, **519**, 407-411. https://doi.org/10.1016/0375-9474(90)90644-2

[4] Carroll, J.B., *et al*. (1989) *Physical Review Letters*, **62**, 1829-1832. https://doi.org/10.1103/PhysRevLett.62.1829

[5] Chiba, J., *et al*. (1993) *Nuclear Physics A*, **553**, 771-774. https://doi.org/10.1016/0375-9474(93)90696-U

[6] Schroeter, A., *et al*. (1993) *Nuclear Physics A*, **553**, 775-778. https://doi.org/10.1016/0375-9474(93)90697-V

[7] Shor, A., Perez-Mendez, V. and Ganezer, K. (1990) *Nuclear Physics A*, **514**, 717-733. https://doi.org/10.1016/0375-9474(90)90019-I

[8] Kurepin, A.B., Shileev, K.A. and Topilskaya, N.S. (1997) *Genshiryoku Kenkyu, Tokyo*, **41**, 177-182.

[9] Baldin, A.A., *et al*. (1995) *Nuovo Cimento A*, **108**, 139-146.

[10] Kurepin, A.B., Shileev, K.A. and Topilskaya, N.S. (1996) *Acta Physica Polonica B*, **27**, 3077-3080.

[11] Kurepin, A.B., Topilskaya, N.S. and Golubeva, M.B. (2011) *Physics of Atomic Nuclei*, **74**, 446-452. https://doi.org/10.1134/S1063778811030124

[12] Brodsky, S.J., Fleuret, F., Hadjidakis, C. and Lansberg, J.P. (2013) *Physics Reports*, **522**, 239-255. https://doi.org/10.1016/j.physrep.2012.10.001

[13] Kusina, A., *et al*. (2019) Probing the High-X Content of the Nuclei in the Fixed-Target Mode at the LHC. arXiv:1901.07950 [hep-ex] https://doi.org/10.22323/1.345.0110

A Self-Linking Field Formalism

Edwin Eugene Klingman ⓘ

Cybernetic Micro Systems, Inc., San Gregorio, CA, USA
Email: klingman@geneman.com

Abstract

The Gauss-linking integral for disjoint oriented smooth closed curves is derived linking integrals from the Biot-Savart description of the magnetic field. DeTurck and Gluck extend this linking from 3-space R^3 to $SU(2)$ space of the unit 3-sphere and hyperbolic space in Minkowski $R^{1,3}$. I herein extend Gauss-linking to self-linking and develop the concept of self-dual, which is then applied to gravitomagnetic dynamics. My purpose is to redefine Wheeler's *geon* from unstable field structures based on the electromagnetic field to self-stabilized gravitomagnetic field structures.

Keywords

Gauss-Linking, Self-Linking, Biot-Savart Operator, Green's Function, Laplacian, Maxwell's Eqns, Gravitomagnetism, Self-Dual, Geons

1. Introduction

In several recent papers [1] [2] I have developed the theory of a self-interacting primordial field. Formulated in Hestenes' *Geometric Calculus*, the theory derives Heaviside's equations in a strength-independent manner. This differs from the usual derivation of the equations via linearization of Einstein's general relativistic field equations in that linearization is characterized as the *weak field approximation*. The implication of the new derivation is that not only weak fields but *all* gravitational fields obey Heaviside's equations. The fact that this appears to be true has been discussed by Clifford Will [3] and others, but no explanation has been offered.

My analysis of the Kasner metric for the primordial field [4] associates the metric with the gravitomagnetic field and emphasizes Vishwakarma's major point [5] that only density-based solutions exist. This, combined with *all-strength* solutions extends the theory of gravitation into physical ranges that have not been treated. The goal is to explore gravity in these previously ignored realms, based

on, where feasible, analogy with Maxwell's field equations, upon which Heaviside modeled his theory of gravity.

The close resemblance between Maxwell's electromagnetic field equations and Heaviside's gravitomagnetic field theory and the fact that Einstein's non-linear field equations are compatible with Heaviside's equations, suggests that we explore the physics of gravity based on similarity of the field equations while also analyzing the differences between the fields. Probably the key difference is that electromagnetic fields, being uncharged, do not interact with themselves, while the gravitomagnetic field *does* interact with itself. Thus the electromagnetic field cannot source itself while the momentum of the gravitomagnetic field *can* source a derived field, and effectively link to itself. The question explored in this paper is whether this linkage supports stable structure. This is pursued by analyzing the linking of the field to its source, and, in particular, Gauss-linking formalism developed for the electromagnetic field by DeTurck, Gluck, and others.

Gauss-linking is claimed to have originated in computing the linking number of the earth's orbit with the orbits of certain asteroids. DeTurck and Gluck [6] derive Gauss-linking integrals from the Biot-Savart description of the magnetic field, then extend the linking from 3-space $\mathfrak{R}^3$ to the $SU(2)$-space of the unit 3-sphere and hyperbolic space in Minkowski's $\mathfrak{R}^{1,3}$. This potentially extends Gauss-linking to Stern-Gerlach analysis based on $SU(2)$-space and equivalent geometric algebra of bivectors. In [7] I derive Hamiltonian physics based in Euclidean space in which Pythagorean distance is defined by $ds^2 = dt^2 + dx^2 \to \infty$ while Minkowski invariant distance is defined by photon physics: $ds^2 = dt^2 - dx^2 = 0$, where photon speed $c = 1$. This paper extends linking associated with the electromagnetic field to self-linking of the gravitomagnetic field. I ask whether self-stabilized field structures are possible in this context.

The goal of this paper is to extend the physical concepts and mathematical equations associated with Gauss-linking to self-linking in hope of deriving a framework capable of supporting calculation of self-stabilized field structures. The mathematics (calculus, topology and geometry) is complex; therefore we review the background in detail before extending Gauss- to self-linking.

The plan of this paper is as follows:

Section 1 introduces aspects of a new derivation of the law of gravity from a primordial field. The key aspect is that Heaviside's equations are strength independent. Also key is that solutions to the field equations in the Kasner metric are density-dependent. These suggest the possibility of stable field structures which we investigate in terms of Gauss-linking.

Section 2 introduces key terms and concepts associated with linking integrals in $\mathfrak{R}^3$. For completeness we define relevant concepts for S^3 and H^3; our focus will be on linking in three-space. The $SU(2)$-space relates primarily to spin and Minkowski invariance to inertial mass.

Section 3 introduces Geometric Calculus multi-vectors in field equations and multi-vector operators, including inverse operators. Green's function is then in-

troduced and explained and the linking integral of section 1 is reformulated in terms of Green's function. This is shown to allow extension of Gauss-linking from $\Re^3$ to $SU(2)$ and Minkowski invariant formalisms.

Section 4 reviews derivation of field equations from discrete inverse operators and association of the Gauss-linking terms with current-based fields in the Biot-Savart framework.

Section 5 explores the Biot-Savart formula and the definition of *helicity*. These link Gauss-linked closed curves to electromagnetism and set up Calugareanu's specialization of Gauss-linking to *twisting, writhing*, and *helicity*, all of which are relevant to self-linked solitonic structures.

Section 6 introduces the concept of *Link Duality*, which is believed to be a novel result of this paper. The physical implications are presented for electromagnetic theory.

Section 7 introduces the concept of *Helical Duality* in terms of solenoidal aspects of electromagnetism. This concept is also believed to be a novel result of this paper.

Section 8 extends the concepts of the previous sections and formulates the symmetry and asymmetry associated with the linkage of charge to electromagnetic field.

Section 9 introduces the concept of self-dual field and discusses why electromagnetism fails to be self-dual. Gravito-magnetism is then explored in these terms and we observe that the gravitomagnetic field is dualistically self-linked. The key diagram of this paper is then shown and explained as the basis of the planned study of self-stabilized structures.

Section 10 summarizes the above; the conjectured self-dual formalism has been successfully developed, and will be explored in future in terms of self-stabilized structures.

2. Relevant Background

Consider two disjoint oriented smooth closed curves in Euclidean 3-space $\Re^3$, parameterized as $\kappa_1 = \{x(s)\}$ and $\kappa_2 = \{y(t)\}$ with $\alpha(x, y)$ defined as the distance from x to y. The linking number of these two curves is defined to be the intersection number of either one of them with an oriented surface bounded by the other. The symmetry is such that the linking number does not depend on which of the curves is used to bound the surface, nor on the type of surface chosen. The formalism is based on the Euclidean inner product in $\Re^4$, $(x, y) = x_0 y_0 + x_1 y_1 + x_2 y_2 + x_3 y_3$. For completeness we define relevant concepts for unit sphere $S^3 = \{x \in R^4 : (x, x) = 1\}$ and Minkowski hyperboloid $H^3 = \{x \in \Re^{1,3} : (x, x) = 1 \text{ and } x_0 > 1\}$ although our focus will be on linking in 3-space. For example, the Biot-Savart law links circulation at a field point in 3-space, a distance r from a source point in 3-space. The topology, shown in **Figure 1**, shows two interlinked curves, $\kappa_1 = \{x(s)\}$ and $\kappa_2 = \{y(t)\}$, both of which are parameterized (by s and t respectively), with specific points $x(s)$
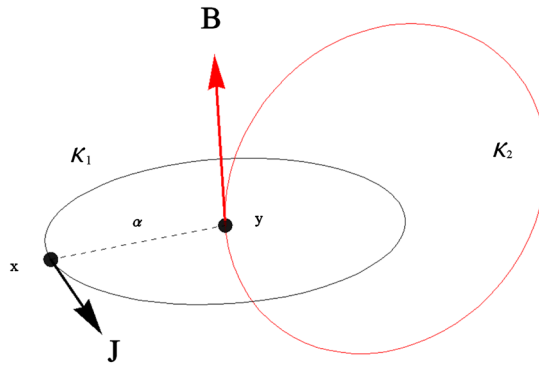
Figure 1. Two linked curves representative of the Gauss-linking problem.

and $y(t)$ a distance $\alpha(x, y) = x - y$ apart. Also shown are the tangents at $x(s)$ and $y(t)$, denoted dx/ds and dy/dt respectively. In these terms the Gauss-integral formula for linking numbers in Euclidian 3-space is given:

$$Link(\kappa_1, \kappa_2) = \frac{1}{4\pi} \int_{\kappa_1 \times \kappa_2} \frac{dx}{ds} \times \frac{dy}{dt} \cdot \frac{x - y}{|x - y|^3} \, ds \, dt \tag{1}$$

It can be seen that if both tangents are in a plane, then $\dfrac{dx}{ds} \times \dfrac{dy}{dt} = 0$ and there is no Gauss-linking.

3. Field Equations and Inverse Field Equations

We begin with Maxwell's equation for electrostatic field $\nabla \cdot E = \rho \; (\varepsilon_0 = 1)$ and the definition of the field as gradient of potential $E = -\nabla \phi$ where $\rho(x)$ is charge density distribution and potential $\phi \sim 1/r$. The geometric algebra form of Maxwell's equations:

$$\overline{\nabla} \overline{F}(x, t) = \overline{J}(x, t) \tag{2}$$

where $\overline{\nabla} = \left(\nabla + \dfrac{1}{c} \dfrac{\partial}{\partial t} \right)$ is the multi-vector differential operator, $\overline{F}(x, t)$ is the multi-vector field and $\overline{J}(x, t)$ is a multi-vector source and the overbar indicates multi-vector. The general form (including wave equations) is

$$\hat{L} \overline{F}(x) = \overline{J}(x) \tag{3}$$

where $\hat{L}$ is an operator formed from a linear combination of linear operators: $1, \nabla, \nabla^2, \partial_t, \partial_{tt}$. The solutions have a linear structure and the most general solution has the form

$$\overline{F}(x, t) = \int d^3 x' \, dt' \, G(x, x'; t, t') \overline{J}(x', t') + \overline{F}_0(x, t) \tag{4}$$

where F_0 is any solution of $LF_0 = 0$ and $G(x, x'; t, t')$ is the Green's function to be determined. To understand the meaning of the Green's function rewrite Equations (3) and (4) to obtain

$$\overline{J}(x, t) = \hat{L} \overline{F}(x, t) = \hat{L} \left(\int d^3 x' \, dt' \, G(x, x'; t, t') \overline{J}(x', t') \right)$$

Since the integral is over x' and t' and the linear operators are with respect

to x and t we can move the operators inside the integral to obtain

$$\bar{J}(x,t) = \int d^3 x' dt' \hat{L} G(x,x';t,t') \bar{J}(x',t') \tag{5}$$

We observe that the source at point x is given as an integral over all values x' in the region. If this integral is to reduce to $J(x,t)$ then function $LG(x,x';t,t')$ must pick out the value x from all possible values x' hence the generalized Green's function must behave like a Dirac delta

$$\hat{L} G(x,x';t,t') = \delta(x-x')\delta(t-t') \tag{6}$$

For static fields a Green's function for the Laplacian $\Delta = \nabla \cdot \nabla$ is $G(x,x') = \dfrac{-1}{4\pi \|x-x'\|}$ and the Laplacian-based delta function in $\Re^3$ is $\delta(x-x') = \dfrac{-1}{4\pi} \nabla^2 \left(\dfrac{1}{\|x-x'\|} \right)$. If we define $\varphi(\alpha) = 1/\alpha$ and substitute it into linking Equation (1) we obtain the equivalent:

$$Link(\kappa_1,\kappa_2) = \frac{1}{4\pi} \int_{\kappa_1 \times \kappa_2} \frac{dx}{ds} \times \frac{dy}{dt} \cdot \nabla_y \varphi(x,y) ds dt \tag{7}$$

where differentiation ∇_y is with respect to the y-variable and function φ is the fundamental solution of the Laplacian $\Delta \varphi = \delta$. In extending the linking integral from $\Re^3$ to S^3 and H^3, DeTurck and Gluck retain the Equation (7) integral but redefine the solution of the Laplacian, φ_0

$$\Re^3 : \varphi_0(\alpha) = -\left(\frac{1}{4\pi\alpha} \right) \qquad\qquad \Delta\varphi = \delta \tag{8a}$$

$$S^3 : \varphi_0(\alpha) = -\left(\frac{1}{4\pi\alpha} \right)(\pi-\alpha)\csc(\alpha) \qquad \Delta\varphi - \varphi = \delta \tag{8b}$$

$$H^3 : \varphi_0(\alpha) = -\left(\frac{1}{4\pi\alpha} \right)\operatorname{csch}(\alpha) \qquad\qquad \Delta\varphi + \varphi = \delta \tag{8c}$$

In short, field equations of the form $\Delta\varphi = s$ have a solution based on the inverse anti-derivative:

$$\Delta\varphi = s \implies \varphi = \left(\Delta^{-1} \right)s, \quad \Delta^{-1} = \int_M G + \oint_{\partial M} G \tag{9}$$

where the Green's function is calculated over the region inside the boundary and optionally a second integral of the derivatives normal to the bounding surface of the field. Boundaries are often chosen primarily to simplify the field solution. We know from vector calculus $\nabla\left(\dfrac{1}{r} \right) = \dfrac{r}{r^3}$ and we know that $\varphi(r) = -\dfrac{1}{4\pi r}$ is the fundamental solution of the Laplacian in $\Re^3$: $\Delta\varphi = \delta$ where δ is the Dirac delta function. Thus Gauss-linking of Equation (1) is equivalent to Equation (7):

$$Link(\kappa_1,\kappa_2) = \frac{1}{4\pi} \int_{\kappa_1 \times \kappa_2} \frac{dx}{ds} \times \frac{dy}{dt} \cdot \frac{x-y}{|x-y|^3} ds dt$$

$$\Rightarrow \frac{1}{4\pi} \int_{\kappa_1 \times \kappa_2} \frac{dx}{ds} \times \frac{dy}{dt} \cdot \nabla_y \varphi(x,y) ds dt \tag{10}$$

As shown in Equation (8) DeTurck and Gluck extended the linking integral to S^3 and H^3, by retaining the $\Re^3$ equation and specializing the fundamental solution of the Laplacian in $\Re^3$. This clever translation from Euclidean-specific coordinate-based function $r/r^3 \rightarrow \nabla(r^{-1}) \rightarrow \varphi(r^{-1})$ to generalized Green's function inverse operator vastly extends the topology range of linking.

4. Derivation of Field Solution from Discrete Inverse Operators

Recently an alternative technique of inverting field equations developed [8] based on exact discrete inverse operators. For magnetic field Equation (11) describing the circulation of the field induced by current density j we use the discrete inverse curl operator

$$\nabla \times f = j \quad \Rightarrow \quad f = (\nabla \times)^{-1} j, \tag{11}$$

where $(\nabla \times)^{-1}$ is proved to be $(r \times)$:

$$\nabla \times f = j \quad \Rightarrow \quad f = r \times j \tag{12}$$

In Euclidian 3-space $\Re^3$, the classical convolution formula of Biot and Savart gives the magnetic field $B(j)$ of a compactly supported current flow j:

$$B(j)(y) = \frac{1}{4\pi} \int_{\Re^3} \mathrm{d}^3 x\, j(x) \times \frac{y - x}{|y - x|^3} \tag{13}$$

Of course Biot and Savart did *not* derive this equation from a convolution formula; they derived it based on experiments with current carrying wires, compass needles, and torsion balances. Physically, if current flows in a wire loop, the circulation of the resulting magnetic field around a second disjoint from it is equal to the flux of the current through a cross-section of the wire loop multiplied by the linking number of the two loops. An example is shown in **Figure 2**. This of course agrees with loop-based formulas for induction in transformers and in solenoidal magnets.

Consider Ampere's law of magnetic circulation [9],

$$\nabla \times B \sim J \tag{14}$$

based on charge current density $J = \rho v = qv/r^3$ [where ~ implies scale factor]. The discrete inverse curl operator $(\nabla \times)^{-1} = (r \times)$ solves for magnetic field B
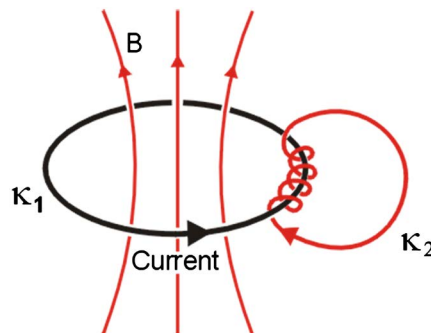
Figure 2. Multi-linking example.

in terms of current density J:

$$B = r \times J = r \times \frac{qv}{r^3} = \frac{r}{r^3} \times qv = \frac{r}{r^3} \times j \qquad (15)$$

where we let $j = qv$ represent charge q moving with velocity v, such that the magnitude of the magnetic field induced at position r with respect to q is [ignoring signs]:

$$B(r) = j \times \frac{r}{r^3} = j \times \nabla\left(\frac{1}{r}\right). \qquad (16)$$

5. The Biot-Savart Formula and Helicity

Based on Figure 1 we identify the tangent to the κ_1-curve as current at y: $j = dy/dt$ and the tangent to the κ_2-curve as magnetic field $B = dx/ds$ and substitute these into Equation (1) to obtain:

$$Link(\kappa_1, \kappa_2) = \frac{1}{4\pi} \int_{\kappa_1 \times \kappa_2} B \times j \cdot \frac{x-y}{|x-y|^3} \, ds \, dt \qquad (17)$$

We use vector identity $A \cdot (B \times C) = B \cdot (C \times A)$ to re-arrange $(r/r^3) \cdot (B \times j)$ and Equation (16) to interpret the result as follows:

$$B \cdot \left(j \times \frac{r}{r^3}\right) \quad \Rightarrow \quad B \cdot B \qquad (18)$$

In order to further understand the meaning of this term, we discuss the fact that, independently, Calugareanu [10] defined a real-valued invariant of a smooth simple closed curve in $\Re^3$ by allowing the two curves in Gauss's linking integral to come together. In the limit, points $x(s)$ and $y(t)$ now run along the same curve in Euclidean 3-space $\Re^3$, with linking number [Equation (1)]

$$Link(\kappa_1, \kappa_2) = \frac{1}{4\pi} \int_{\kappa_1 \times \kappa_2} \frac{dx}{ds} \times \frac{dy}{dt} \cdot \frac{x-y}{|x-y|^3} \, ds \, dt$$

The *helicity* of a vector field $v(x)$ defined on a boundary domain Ω in $\Re^3$ is given by

$$Heli(\Omega, \Omega) = \frac{1}{4\pi} \int_{\Omega \times \Omega} v(x) \times v(y) \cdot \frac{x-y}{|x-y|^3} \, d^3x \, d^3y . \qquad (19)$$

The integral is over the volume elements and vector field $v(x)$ is a flow density. *Helicity* is a measure of the extent to which the orbits of v wrap and coil around each other. The potential problem of $1/|x-y|$ is compensated by terms in the denominator that approach zero faster than $\varphi(\alpha)$. This new invariant measures the extent to which the curve wraps and coils around itself, and, per Parsley [11]: "*the helicity of a vector field is bounded by its L^2 energy.*" Energy density of the B-field is B^2, which corresponds to Calugareanu's construction $\kappa_1 \times \kappa_2 \rightarrow \kappa \times \kappa$. Calugareanu's specialization of Gauss-linking to *twisting, writhing,* and *helicity,* is considered relevant to self-linking into solitonic structures. The application of these concepts spans the biophysics of DNA

helices, plasma fields in solar winds, knot theory, etc. The end goal of this work will be the determination of a self-linking, self-curling stable field construction. If such exists, I postulate it will have a *boundary threshold*, below which stability does not hold.

6. Link Duality

Duality is a complicated concept. Electric field E and magnetic field B are dual in that the transformation $E \rightarrow B, B \rightarrow -E$ satisfies Maxwell's equations. In geometric algebra the duality operator $\hat{i}$ transforms elements to their dual, for example $a \wedge b = -ia \times b$ converts the *bivector* $a \wedge b$ into the (axial) *vector* cross product $a \times b$. We now consider the interesting duality of B and j implied by the linking number. The Figure 1 topology has dual nature; κ_1 can represent the magnetic field $B(x)$ induced by the current density $j(y)$ at y on κ_2 curve, but it can also represent the magnetic field at $B(y)$ on κ_2 induced by current density $j(x)$ on κ_1.

The mathematical form of the linking integral shown in Figure 1 is such that the linking number depends neither on the choice of surface (bounded by curves) nor on which of the curves is used to bound the surface. Interestingly this "equivalence" extends to the case shown in Figure 3, in which the source current J can be assigned to κ_1 with the induced field B represented by κ_2, or these can be reversed and the physics is equivalent. This differs from the principle of covariance. These linkages are shown in Figure 3 and obey the Link duality formula:

$$Link\left[\kappa_1(B), \kappa_2(j)\right] \equiv Link\left[\kappa_1(j), \kappa_2(B)\right] \tag{20}$$

as seen in Figure 3.

7. Helical Duality

We observe that the radius of κ_2 can be expanded without limit so the curve at point y becomes essentially a straight line parallel to the tangent dy/dt while curve κ_1 remains unchanged. In fact it is quite fascinating that both physical situations retain meaning in this case and display a duality or symmetry of J and B. This interesting extension of link duality exhibits scale invariance of the
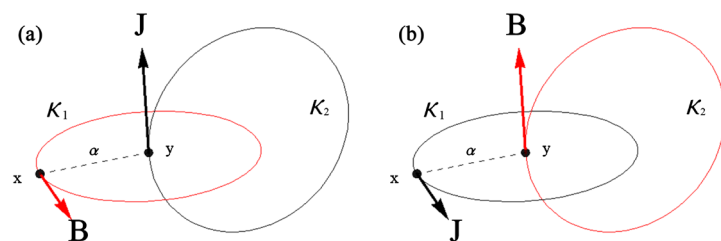
Figure 3. The linking duality is such that the linking number depends neither on the choice of surface nor which of the curves is used to bound the surface. In (a) current J induces field B in κ_1 boundary, while in (b) current in the κ_1 boundary induces field B in κ_2.

radius of curve when the radius of κ_2 grows without limit and the segment containing point y becomes a straight line parallel to the tangent, $\mathrm{d}y/\mathrm{d}t$. In **Figure 4** we illustrate the duality that is expressed as $(\nabla\times)^{-1}\boldsymbol{J}=\boldsymbol{B}\Leftrightarrow(\nabla\times)\boldsymbol{B}=\boldsymbol{J}$.

Symbolically, the discrete inverse curl operator $(\nabla\times)^{-1}\sim\dfrac{1}{\left(\dfrac{\partial}{\partial r}\times\right)}\to(r\times)$

therefore we focus on the physical meaning of $\boldsymbol{r}$, which is the directed distance from $\boldsymbol{x}$ on the source curve to $\boldsymbol{y}$ on the induced curve. In **Figure 4(a)**, the current source density $\boldsymbol{J}$ is in the wire helix with radius $|\boldsymbol{r}|$ centered on the axis of the helix. We consider the induced $\boldsymbol{B}$ field along the axis of the helix and the field is defined by $\boldsymbol{B}=\boldsymbol{r}\times\boldsymbol{J}$ as indicated. In **Figure 4(b)** the current density $\boldsymbol{J}$ flows along the center of the helix and the induced $\boldsymbol{B}$ field lies on the helix with radius $|\boldsymbol{r}|$ and is once again defined as $\boldsymbol{B}=\boldsymbol{r}\times\boldsymbol{J}$.

8. Extending Duality

Linking and helicity have been defined as integrals and associated with current source density $\boldsymbol{J}$ that induces an electromagnetic field $\boldsymbol{B}$ via the Ampere Law and the Law of Biot-Savart. As noted above, "duality" is an interesting concept. Most examples are essentially "one-dimensional"; the electromagnetic field example $\{\boldsymbol{E},\boldsymbol{B}\}\Leftrightarrow\{\boldsymbol{B},-\boldsymbol{E}\}$ swaps two fields and changes the sign (direction) of one of the fields. The duality operator in geometric algebra exchanges one geometric algebra entity with its dual entity $\{\text{vector}\}\Leftrightarrow\{\text{bivector}\}$, etc. What we have revealed above is a more complex duality involving fields, currents, geometry, and topology. We now ask whether this can be pushed further, and we do so using electromagnetic induction as an example.

$$\boldsymbol{J}\stackrel{?}{=}\boldsymbol{B}\cdot\boldsymbol{B} \tag{21}$$

The key aspect of the duality discussed above is that the helical current induces a linear field at its center and a linear current induces a helical field surrounding it. The current has charge, mass, and momentum, while the magnetic field has energy density and angular momentum. The helical duality shown in **Figure 4** is *geometrical* and *topological*. The linking is directly physical, in the sense that current flow through the surface bounded by a curve will induce a field circulation in the boundary tangent to the boundary. The inverse operation is more subtle; if the change in field occurs in a current carrying boundary, an electromotive force (a voltage) is induced that generates a change in current. The formal description of this physics is given by Lenz's Law. Hence there is a certain

(a) $(\nabla\times)^{-1}\boldsymbol{J}=\boldsymbol{B}$ **(b)** $(\nabla\times)\boldsymbol{B}=\boldsymbol{J}$
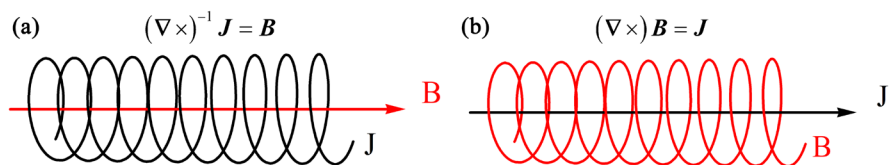
Figure 4. Solenoidal dual helical aspects of electromagnetism. The unique duality allows both source and field to link to helix of other entity.

symmetry associated with the linking, but there is an indirectness (the "emf") that corresponds to a certain asymmetry as well.

The basic experiments from which the laws were derived utilize metallic wire to conduct the charge current, but the electromagnetic laws operate without wire, as in charged plasma current flows distributed over space.

$$
\left\{ \begin{array}{c} \boldsymbol{J} \\ \text{mass} \\ \text{charge} \\ \text{momentum} \end{array} \right\} \neq \left\{ \begin{array}{c} \boldsymbol{B} \cdot \boldsymbol{B} \\ \text{mass} \\ \text{uncharged} \\ \text{momentum} \end{array} \right\} \tag{22}
$$

What we're asking in this section is how one might extend the linking phenomenon such that the field might link to itself. From the relation between the current $\boldsymbol{J}$ that induces the field, and the energy density (with mass-density-equivalence) of field $\boldsymbol{B} \cdot \boldsymbol{B}$ we observe that the field is uncharged and therefore cannot act upon itself in the manner that charge acts to produce the field. Similarly, the field acts upon the charge of the current flow. So it is *electric charge* that is at the heart of this physical phenomenon and this represents a basic asymmetry since the field is always inherently uncharged.

Our conclusion is that the electromagnetic field of Maxwell's laws will not support the hoped-for extension of duality. There is, however, an alternative, which we look at next.

9. A Self Linking Field

The above analysis indicates that the absence of charge of the electromagnetic field prevents the field from linking to itself in a "self-dual" matter. Is any other field "self-dual" as described here?

In 2011 the *Gravity Probe B* experiment proved the existence of the gravito-magnetic field, first proposed by Oliver Heaviside in 1893. I've recently published papers on different aspects of gravito-magnetism and will not go into much depth in this paper except on the question of self-linking. The gravitational field resolves into a gravito-electric field $\boldsymbol{G}$ analogous to the electric field $\boldsymbol{E}$ and a gravitomagnetic field $\boldsymbol{C}$ analogous to magnetic field $\boldsymbol{B}$. The analogy is mathematical, the gravitational field does not possess electric charge, nor does the gravitomagnetic C-field act on electric charge, per se. The gravito-dynamic equations however are almost identical to Maxwell's equations when electric charge density is replaced by mass density. Here we focus on the C-field analogy with the B-field and observe:

$$
(\nabla \times)^{-1} \boldsymbol{J} = \boldsymbol{B}, \quad (\nabla \times) \boldsymbol{B} = \boldsymbol{J} \tag{23a}
$$

$$
(\nabla \times)^{-1} \boldsymbol{P} = \boldsymbol{C}, \quad (\nabla \times) \boldsymbol{C} = \boldsymbol{P} \tag{23b}
$$

where scalar constants ($g = c = 1$) have been set to one. From previous sections we conclude that the momentum density $\boldsymbol{P} = \rho_m \boldsymbol{v}$ induces a $\boldsymbol{C}$-field circulation around $\boldsymbol{P}$ analogous to the charge density flow $\boldsymbol{J} = \rho_q \boldsymbol{v}$ inducing a $\boldsymbol{B}$

-field circulation around J. We expect the helical topology shown in Figure 4 to describe gravito-magnetism, and it does. However there is an aspect of the C-field that is missing from the magnetic B-field—the C-field interacts with itself! Like the B-field, the C-field has energy density and momentum density and we see from Equation (23b) that momentum density induces C-field circulation. This newly induced C-field circulation possesses (mass) energy density and momentum density and hence induces still more C-field circulation, etc. as shown in "*Iterating with Fuzzy Parameters…*". Compare this result with the relation

$$\left\{ \begin{array}{c} \boldsymbol{P} \\ \text{mass} \\ \text{momentum} \end{array} \right\} \cong \left\{ \begin{array}{c} \boldsymbol{C} \cdot \boldsymbol{C} \\ \text{mass} \\ \text{momentum} \end{array} \right\} \tag{24}$$

We see that the momentum $\boldsymbol{P}$ that induces $\nabla \times \boldsymbol{C}$ produces momentum associated with field energy density $\boldsymbol{C} \cdot \boldsymbol{C}$ and this field thus links to itself, which is what we were searching for.

The *physics*, *geometry*, and *topology* all support *self-linking* in the dualistic manner described. The nature of the cross product is *orthogonality*, so that circulation induced by the momentum at distance r from the momentum is orthogonal to the momentum. We next look more closely at the induced field orthogonal to the momentum. Einstein and deHaas [12] experimentally proved that the magnetic field possesses angular momentum. In fact, the gravitomagnetic field is mathematically identical to angular momentum when one ignores the scalar constants.

$$\boldsymbol{L} = \boldsymbol{r} \times \boldsymbol{P} \tag{25}$$

$$\boldsymbol{C} \sim \boldsymbol{r} \times \boldsymbol{P} \tag{26}$$

where the ~ indicates a scale factor (g/c^2) is required.

In other words the gravitomagnetic C-field circulation actually is physically circulating! For instance the *Gravity Probe B* detection [13] of the "Lenz-Thirring" effect is thought of in metric terms as 'frame dragging', but in actuality, the C-field is in motion, and this motion imparts a momentum density to the energy density of the C-field.

This momentum density $\boldsymbol{P}'$ of the induced field is, as noted, orthogonal to the inducing momentum $\boldsymbol{P}$, and the second order induction arising from $\boldsymbol{P}'$ will be orthogonal to $\boldsymbol{P}'$. We depict this in Figure 5 where *red* and *green* are used to emphasize orthogonality. *Red* is parallel to *red* and *green* is parallel to *green*, while *red* and *green* are orthogonal to each other.

We note explicitly the colors (*red* and *black*) in earlier diagrams were used to distinguish between charge current (*black*) and physical field (*red*). Our use of color here is to distinguish directions of momentum associated with higher order induction. The key result we wish to focus on here is the fact that while the first-order induction is orthogonal to the inducing momentum, the second-order induction of the induced momentum has a component that is in *exactly* the
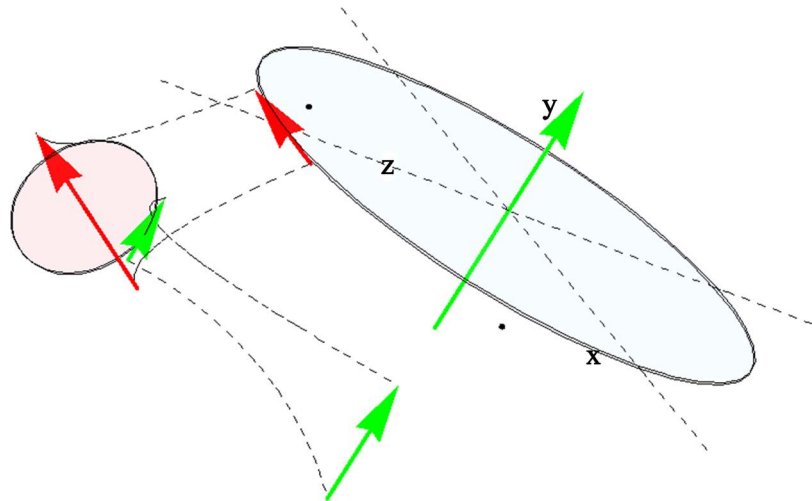
Figure 5. Color-coded diagram of first and second order induction of C-field.

same direction as the first-order momentum. This type of feedback suggests stability and thus we have grounds to hope that a self linking field may support stable field configurations.

Two aspects are key: first, the induced C-field momentum induces a second order C-field circulation. This circulation has one component, shown in **Figure 5**, that *self-reinforces* the original momentum, but the same circulation has another component (only implicitly shown) that exactly *opposes* the original momentum. But the reinforcing momentum component is closer to the original momentum, and thus the reinforcing interaction is stronger than the opposing interaction, as would be required for self-stabilizing field configurations.

Second, the Heaviside gravitomagnetic equations are generally known as the "weak field approximation" and as such are argued not to produce higher order self-interaction. This is addressed in *The Primordial Principle of Self-Interaction* where it is shown that "weak field" is a misnomer. The Heaviside equation is derived in a *strength-independent* manner, assumed valid even at the big bang, therefore the equation is for all fields, not just weak fields. Clifford Will and others have remarked on the surprising accuracy of the equation for strong fields.

10. Conclusion

We have reviewed topological linking and helicity formulas and discussed the relation of these concepts to electromagnetic phenomena. I have then introduced and focused on the concept of *duality* in this context and asked whether a self-dual or self-linking field exists which might support self-stabilized field configurations. I then review the nature of the gravitomagnetic field equations in terms of the self-dual linking and helicity that we were searching for. The combination of the mathematics, the physics, the geometry and the topology lends a certain complexity to this enterprise, but I have produced a schematic proof that the self-dual gravitomagnetic field density supports higher order stabilization

through *self-dual self-induction*.

To put things in context, Wheeler [14] believed that nature would avail itself of all opportunities offered by the equations of valid theories. In particular he defined a "geon" as a gravitating body made entirely of electromagnetic fields and hoped that they would give "*mass without mass*", but later showed that these are unstable—they would quickly self destruct if they were ever to form. I have shown herein that, although electromagnetic field structures are unstable, gravitomagnetic fields support self-stabilizing structure that may lead to *self-stabilized, soliton-like structures* that represent a resonance or even *enduring entities*. I plan to follow this paper with analysis of such.

Conflicts of Interest

The author declares no conflicts of interest regarding the publication of this paper.

References

[1] Klingman, E. (2020) *Journal of Modern Physics*, **12**, 65-81. https://doi.org/10.4236/jmp.2021.122007

[2] Klingman, E. (2019) *Applied Mathematics*, **11**, 1070-1080. https://doi.org/10.4236/am.2020.1111072

[3] Will, C. (2011) *PNAS*, **108**, 5938-5945. https://doi.org/10.1073/pnas.1103127108

[4] Klingman, E. (2019) *Prespace-Time Journal*, **10**, 671-680.

[5] Vishwakarma, R. (2013) Einstein"s Real "Biggest Blunder". https://fqxi.org/community/forum/topic/1840

[6] DeTurck, D. and Gluck, H. (2008) *Journal of Differential Geometry*, **94**, 87-128. https://doi.org/10.4310/jdg/1361889062

[7] Klingman, E. (2020) *Journal of Modern Physics*, **11**, 1950-1968. https://doi.org/10.4236/jmp.2020.1112123

[8] Klingman, E. (2020) *Journal of Applied Mathematics and Physics*, **8**, 2213-2222. https://doi.org/10.4236/jamp.2020.810166

[9] Jackson, J. (1962) Classical Electrodynamics. John Wiley, New York, 137-138. https://doi.org/10.1063/1.3057859

[10] Calugareanu, G. (1961) *Czechoslovak Mathematical Journal*, **11**, 588-625. https://doi.org/10.21136/CMJ.1961.100486

[11] Parsley, R. (2004) The Biot-Savart Operator Electrodynamics on Bounded Subdomains of the Three-Sphere. PhD Thesis, University of Pennsylvania, Philadelphia.

[12] Einstein, A. and deHaas, W. (1915) Experimental Proof of Existence of Ampere's Molecular Currents. *KNAW Proceedings*, Amsterdam, 1915, 696-711.

[13] Everitt, C.W.F., *et al.* (2011) *Physical Review Letters*, **106**, Article ID: 221101.

[14] Wheeler, J. (1998) Geons, Black Holes, and Quantum Foam. WW Norton and Co., New York.

Minimum Parametrization of the Cauchy Stress Operator

J.-F. Pommaret

CERMICS, Ecole des Ponts Paris Tech, France
Email: jean-francois.pommaret@wanadoo.fr

Abstract

When $\mathcal{D}: \xi \rightarrow \eta$ is a linear differential operator, a "direct problem" is to find the generating compatibility conditions (CC) in the form of an operator $\mathcal{D}_1: \eta \rightarrow \zeta$ such that $\mathcal{D}\xi = \eta$ implies $\mathcal{D}_1 \eta = 0$. When $\mathcal{D}$ is involutive, the procedure provides successive first order involutive operators $\mathcal{D}_1, \cdots, \mathcal{D}_n$ when the ground manifold has dimension *n*, a result first found by M. Janet as early as in 1920, in a footnote. However, the link between this "Janet sequence" and the "Spencer sequence" first found by the author of this paper in 1978 is still not acknowledged. Conversely, when $\mathcal{D}_1$ is given, a more difficult "inverse problem" is to look for an operator $\mathcal{D}: \xi \rightarrow \eta$ having the generating CC $\mathcal{D}_1 \eta = 0$. If this is possible, that is when the differential module defined by $\mathcal{D}_1$ is torsion-free, one shall say that the operator $\mathcal{D}_1$ is parametrized by $\mathcal{D}$ and there is no relation in general between $\mathcal{D}$ and $\mathcal{D}_2$. The parametrization is said to be "minimum" if the differential module defined by $\mathcal{D}$ has a vanishing differential rank and is thus a torsion module. The solution of this problem, first found by the author of this paper in 1995, is still not acknowledged. As for the applications of the "differential double duality" theory to standard equations of physics (*Cauchy* and *Maxwell* equations can be parametrized while *Einstein* equations cannot), we do not know other references. When $n = 1$ as in control theory, the fact that controllability is a "built in" property of a control system, amounting to the existence of a parametrization and thus not depending on the choice of inputs and outputs, even with variable coefficients, is still not acknowledged by engineers. The parametrization of the *Cauchy* stress operator in arbitrary dimension *n* has nevertheless attracted, "separately" and without any general "guiding line", many famous scientists (G.B. Airy in 1863 for $n = 2$, J.C. Maxwell in 1863, G. Morera and E. Beltrami in 1892 for $n = 3$, A. Einstein in 1915 for $n = 4$). The aim of this paper is to solve the minimum parametrization problem in arbitrary dimension and to apply it through effective methods that could even

be achieved by using computer algebra. Meanwhile, we prove that all these works are using the *Einstein* operator which is self-adjoint and not the *Ricci* operator, a fact showing that the *Einstein* operator, which cannot be parametrized, has already been exhibited by Beltrami more than 20 years before *Einstein*. As a byproduct, they are all based on the same confusion between the so-called *div* operator induced from the *Bianchi* operator $\mathcal{D}_2$ and the *Cauchy* operator which is the formal adjoint of the Killing operator $\mathcal{D}$ parametrizing the Riemann operator $\mathcal{D}_1$ for an arbitrary *n*. We prove that this purely mathematical result deeply questions the origin and existence of gravitational waves. We also present the similar motivating situation met in the study of contact structures when $n = 3$. Like the Michelson and Morley experiment, it is thus an open historical problem to know whether *Einstein* was aware of these previous works or not, but the comparison needs no comment.

Keywords

1. Introduction

We start recalling the basic tools from the formal theory of systems of partial differential (PD) equations and differential modules needed in order to understand and solve the parametrization problem presented in the abstract. As these new tools are difficult and not so well known, we advise the interested reader to follow them step by step on the explicit motivating examples illustrating this paper, in particular the example of the system of infinitesimal Lie equations defining contact transformations when $n = 3$. The main difficulty for the reader not familiar with these new tools is that certain concepts are evident in one framework but not at all in the other and conversely. Considering the single input/single output (SISO) classical control system $\ddot{y} - \dot{u} = 0$ with standard notations for ordinary differential (OD) equations, we notice that both y and u can be given arbitrarily *separately* but that the new quantity $z = \dot{y} - u$ *cannot* as it *must* satisfy the autonomous OD equation $\dot{z} = 0$ that, of course, cannot be controlled. This is the reason for which a controllable system cannot surely provide such elements called "*torsion elements*" in module theory. The fact that the controllability just amounts to the lack of any torsion element or, equivalently, to the possibility to parametrize the control system, is left to the reader as a tricky exercise leading to compare with the basic system $\dot{y} - u = 0$ which is controllable and can be simply parametrized by the only arbitrary potential y through the formula $\dot{y} = u, y = y$. As we shall see, the surprising fact is that the lack of torsion elements (or the generating ones) can only be tested by the possibility to parametrize the given equations (or to "measure" how it *cannot* be pa-

rametrized) and no other classical method can work.

In Section 2, once we shall have found the possibility to parametrize the system or the corresponding operator, that is to say once we know that the corresponding differential module is torsion-free, we shall discover that many possible parametrizations may exist. The idea will then be to modify the formal test in order to compute the minimum number of potentials needed and to find a constructive way to obtain *at least* one such minimum parametrization.

In Section 3, we shall study with more details the parametrization problems that are existing in continuum mechanics for an arbitrary dimension n of the ground manifold, the case $n = 2$ allowing to understand why the *Airy* operator is just the formal adjoint of the *Riemann* operator, the case $n = 3$ allowing to compare the results respectively obtained by Beltrami, Maxwell and Morera, the case $n = 4$ allowing to understand why such a parametrization problem is leading to the self-adjoint *Einstein* operator and why the so-called "gravitational waves" operator is nothing else than the formal adjoint of the *Ricci* operator without any reference to *Einstein* equations.

In Section 4, we shall finally add a few unexpected results coming from the use of the symbol sequences existing for certain generic covectors.

1.1. System Theory

If X is a manifold of dimension n with local coordinates $(x) = (x^1, \cdots, x^n)$, we denote as usual by $T = T(X)$ the *tangent bundle* of X, by $T^* = T^*(X)$ the *cotangent bundle*, by $\wedge^r T^*$ the *bundle of r-forms* and by $S_q T^*$ the *bundle of q-symmetric tensors*. More generally, let E be a *vector bundle* over X with local coordinates (x^i, y^k) for $i = 1, \cdots, n$ and $k = 1, \cdots, m$ simply denoted by (x, y), *projection* $\pi : E \to X : (x, y) \to (x)$ and changes of local coordinate $\bar{x} = \varphi(x), \bar{y} = A(x) y$. We shall denote by E^* the vector bundle obtained by inverting the matrix A of the changes of coordinates, exactly like T^* is obtained from T. We denote by $f : X \to E : (x) \to (x, y = f(x))$ a global *section* of E, that is a map such that $\pi \circ f = id_X$ but local sections over an open set $U \subset X$ may also be considered when needed. Under a change of coordinates, a section transforms like $\bar{f}(\varphi(x)) = A(x) f(x)$ and the changes of the derivatives can also be obtained with more work. We shall denote by $J_q(E)$ the *q-jet bundle* of E with local coordinates $(x^i, y^k, y_i^k, y_{ij}^k, \cdots) = (x, y_q)$ called *jet coordinates* and sections $f_q : (x) \to (x, f^k(x), f_i^k(x), f_{ij}^k(x), \cdots) = (x, f_q(x))$ transforming like the sections $j_q(f) : (x) \to (x, f^k(x), \partial_i f^k(x), \partial_{ij} f^k(x), \cdots) = (x, j_q(f)(x))$ where both f_q and $j_q(f)$ are over the section f of E. For any $q \geq 0$, $J_q(E)$ is a vector bundle over X with projection π_q while $J_{q+r}(E)$ is a vector bundle over $J_q(E)$ with projection $\pi_q^{q+r}, \forall r \geq 0$.

DEFINITION 1.1.1: A *linear system* of order q on E is a vector sub-bundle $R_q \subset J_q(E)$ and a *solution* of R_q is a section f of E such that $j_q(f)$ is a section of R_q. With a slight abuse of language, the set of local solutions will be denoted by $\Theta \subset E$.

Let $\mu = (\mu_1, \cdots, \mu_n)$ be a multi-index with *length* $|\mu| = \mu_1 + \cdots + \mu_n$, *class* i if $\mu_1 = \cdots = \mu_{i-1} = 0, \mu_i \neq 0$ and $\mu + 1_i = (\mu_1, \cdots, \mu_{i-1}, \mu_i + 1, \mu_{i+1}, \cdots, \mu_n)$. We set $y_q = \{ y_\mu^k \mid 1 \leq k \leq m, 0 \leq |\mu| \leq q \}$ with $y_\mu^k = y^k$ when $|\mu| = 0$. If E is a vector bundle over X and $J_q(E)$ is the *q-jet bundle* of E, then both sections $f_q \in J_q(E)$ and $j_q(f) \in J_q(E)$ are over the section $f \in E$. There is a natural way to distinguish them by introducing the *Spencer* operator $d : J_{q+1}(E) \to T^* \otimes J_q(E)$ with components $(df_{q+1})_{\mu,i}^k (x) = \partial_i f_\mu^k(x) - f_{\mu+1_i}^k(x)$. The kernel of d consists of sections such that $f_{q+1} = j_1(f_q) = j_2(f_{q-1}) = \cdots = j_{q+1}(f)$. Finally, if $R_q \subset J_q(E)$ is a *system* of order q on E locally defined by linear equations $\Phi^\tau (x, y_q) \equiv a_k^{\tau\mu}(x) y_\mu^k = 0$ and local coordinates (x, z) for the parametric jets up to order q, the *r-prolongation* $R_{q+r} = \rho_r(R_q) = J_r(R_q) \cap J_{q+r}(E) \subset J_r(J_q(E))$ is locally defined when $r = 1$ by the linear equations $\Phi^\tau(x, y_q) = 0$, $d_i \Phi^\tau (x, y_{q+1}) \equiv a_k^{\tau\mu}(x) y_{\mu+1_i}^k + \partial_i a_k^{\tau\mu}(x) y_\mu^k = 0$ and has *symbol* $g_{q+r} = R_{q+r} \cap S_{q+r} T^* \otimes E \subset J_{q+r}(E)$ if one looks at the *top order terms*. If $f_{q+1} \in R_{q+1}$ is over $f_q \in R_q$, differentiating the identity $a_k^{\tau\mu}(x) f_\mu^k(x) \equiv 0$ with respect to x^i and subtracting the identity $a_k^{\tau\mu}(x) f_{\mu+1_i}^k(x) + \partial_i a_k^{\tau\mu}(x) f_\mu^k(x) \equiv 0$, we obtain the identity $a_k^{\tau\mu}(x)(\partial_i f_\mu^k(x) - f_{\mu+1_i}^k(x)) \equiv 0$ and thus the restriction $d : R_{q+1} \to T^* \otimes R_q$. More generally, we have the restriction:

$$
\begin{aligned}
d : \wedge^s T^* \otimes R_{q+1} &\to \wedge^{s+1} T^* \otimes R_q : (f_{\mu,I}^k(x) dx^I) \\
&\to ((\partial_i f_{\mu,I}^k(x) - f_{\mu+1_i,I}^k(x)) dx^i \wedge dx^I)
\end{aligned}
\tag{1}
$$

using standard multi-index notation for exterior forms, namely $I = \{i_1 < i_2 < \cdots < i_r\}$, $dx^I = dx^{i_1} \wedge \cdots \wedge dx^{i_r} \in \wedge^r T^*$ for a finite basis, and one can easily check that $d \circ d = 0$. The restriction of $-d$ to the symbol is called the *Spencer* map $\delta : \wedge^s T^* \otimes g_{q+1} \to \wedge^{s+1} T^* \otimes g_q$ and $\delta \circ \delta = 0$ similarly, leading to the algebraic δ-*cohomology* $H_{q+r}^s(g_q)$ [1]-[7].

DEFINITION 1.1.2: A system R_q is said to be *formally integrable* when all the equations of order $q + r$ are obtained by r prolongations *only*, $\forall r \geq 0$ or, equivalently, when the projections $\pi_{q+r}^{q+r+s} : R_{q+r+s} \to Rq + r$ are epimorphisms $\forall r, s \geq 0$.

Finding an intrinsic test has been achieved by D.C. Spencer in 1970 [7] along coordinate dependent lines sketched by M. Janet in 1920 [8]. The next procedure providing a *Pommaret basis* and where *one may have to change linearly the independent variables if necessary*, is intrinsic even though it must be checked in a particular coordinate system called δ-*regular* [1] [4] [9].

- *Equations of class n*: Solve the maximum number β_q^n of equations with respect to the jets of order q and class n. Then call $(x^1, \cdots, x^n)$ *multiplicative variables*.

- *Equations of class $i \geq 1$*: Solve the maximum number β_q^i of *remaining* equations with respect to the jets of order q and class i. Then call $(x^1, \cdots, x^i)$ *multiplicative variables* and $(x^{i+1}, \cdots, x^n)$ *non-multiplicative variables*.

- *Remaining equations of order $\leq q - 1$*: Call $(x^1, \cdots, x^n)$ *non-multiplicative*

variables.

In actual practice, we shall use a *Janet tabular* where the multiplicative "variables" are in upper left position while the non-multiplicative variables are represented by dots in lower right position.

DEFINITION 1.1.3: A system of PD equations is said to be *involutive* if its first prolongation can be obtained by prolonging its equations only with respect to the corresponding multiplicative variables. In that case, we may introduce the

characters $\alpha_q^i = m \dfrac{(q+n-i-1)!}{(q-1)!(n-i)!} - \beta_q^i$ for $i = 1, \cdots, n$ with $\alpha_q^1 \geq \cdots \geq \alpha_q^n \geq 0$

and we have $dim(g_q) = \alpha_q^1 + \cdots + \alpha_q^n$ while $dim(g_{q+1}) = \alpha_q^1 + \cdots + n\alpha_q^n$.

REMARK 1.1.4: As long as the *Prolongation/Projection* (PP) procedure has not been achieved in order to get an involutive system, *nothing* can be said about the CC (fine examples can be found in [6] and the recent [10]). A proof that the second order system defined by *Einstein* equations is involutive has been given by J. Gasqui in 1982 but this paper cannot be applied to the minimum parametrizations that need specific δ-regular coordinates as we shall see [11].

When R_q is involutive, the linear differential operator
$\mathcal{D} : E \xrightarrow{J_q} J_q(E) \xrightarrow{\Phi} J_q(E)/R_q = F_0$ of order q is said to be *involutive*. Introducing the *Janet* bundles:

$$F_r = \wedge^r T^* \otimes J_q(E) \Big/ \left(\wedge^r T^* \otimes R_q + \delta \left(\wedge^{r-1} T^* \otimes S_{q+1} T^* \otimes E \right) \right) \tag{2}$$

we obtain the canonical linear *Janet* sequence (introduced in [1], p 185 + p 391):

$$0 \to \Theta \to E \xrightarrow{\mathcal{D}} F_0 \xrightarrow{\mathcal{D}_1} F_1 \xrightarrow{\mathcal{D}_2} \cdots \xrightarrow{\mathcal{D}_n} F_n \to 0 \tag{3}$$

where each other operator, induced by the *Spencer* operator, is first order involutive and generates the *compatibility conditions* (CC) of the preceding one. Similarly, introducing the *Spencer* bundles:

$$C_r = \wedge^r T^* \otimes R_q / \delta \left(\wedge^{r-1} T^* \otimes g_{q+1} \right) \tag{4}$$

we obtain the canonical linear *Spencer* sequence also induced by the *Spencer* operator:

$$0 \to \Theta \xrightarrow{j_q} C_0 \xrightarrow{\mathcal{D}_1} C_1 \xrightarrow{\mathcal{D}_2} \cdots \xrightarrow{\mathcal{D}_n} C_n \to 0 \tag{5}$$

1.2. Module Theory

Let K be a *differential field* with n commuting derivations $(\partial_1, \cdots, \partial_n)$ and consider the ring $D = K[d_1, \cdots, d_n] = K[d]$ of differential operators with coefficients in K with n commuting formal derivatives satisfying $d_i a = a d_i + \partial_i a$ in the operator sense. If $P = a^\mu d_\mu \in D = K[d]$, the highest value of $|\mu|$ with $a^\mu \neq 0$ is called the *order* of the *operator P* and the ring D with multiplication $(P, Q) \to P \circ Q = PQ$ is filtered by the order q of the operators. We have the *filtration* $0 \subset K = D_0 \subset D_1 \subset \cdots \subset D_q \subset \cdots \subset D_\infty = D$. As an algebra, D is generated by $K = D_0$ and $T = D_1/D_0$ with $D_1 = K \oplus T$ if we identify an element $\xi = \xi^i d_i \in T$ with the vector field $\xi = \xi^i(x) \partial_i$ of differential geometry, but

with $\xi^i \in K$ now. It follows that $D = {_D}D_D$ is a *bimodule* over itself, being at the same time a left D-module by the composition $P \to QP$ and a right D-module by the composition $P \to PQ$. We define the *adjoint* functor $ad : D \to D^{op} : P = a^\mu d_\mu \to ad(P) = (-1)^{|\mu|} d_\mu a^\mu$ and we have $ad(ad(P)) = P$ both with $ad(PQ) = ad(Q)ad(P), \forall P, Q \in D$. Such a definition can be extended to any matrix of operators by using the transposed matrix of adjoint operators (see [5] [9] [12] [13] [14] [15] [16] for more details and applications to control theory or mathematical physics).

Accordingly, if $y = (y^1, \cdots, y^m)$ are differential indeterminates, then D acts on y^k by setting $d_i y^k = y_i^k \to d_\mu y^k = y_\mu^k$ with $d_i y_\mu^k = y_{\mu+1_i}^k$ and $y_0^k = y^k$. We may therefore use the jet coordinates in a formal way as in the previous section. Therefore, if a system of OD/PD equations is written in the form $\Phi^\tau \equiv a_k^{\tau\mu} y_\mu^k = 0$ with coefficients $a \in K$, we may introduce the free differential module $Dy = Dy^1 + \cdots + Dy^m \simeq D^m$ and consider the differential *module of equations* $I = D\Phi \subset Dy$, both with the residual *differential module* $M = Dy/D\Phi$ or D-module and we may set $M = {_D}M$ if we want to specify the ring of differential operators. We may introduce the formal *prolongation* with respect to d_i by setting $d_i \Phi^\tau \equiv a_k^{\tau\mu} y_{\mu+1_i}^k + (\partial_i a_k^{\tau\mu}) y_\mu^k$ in order to induce maps $d_i : M \to M : \bar{y}_\mu^k \to \bar{y}_{\mu+1_i}^k$ by residue with respect to I if we use to denote the residue $Dy \to M : y^k \to \bar{y}^k$ by a bar like in algebraic geometry. However, for simplicity, we shall not write down the bar when the background will indicate clearly if we are in Dy or in M. As a byproduct, the differential modules we shall consider will always be *finitely generated* ($k = 1, \cdots, m < \infty$) and *finitely presented* ($\tau = 1, \cdots, p < \infty$). Equivalently, introducing the *matrix of operators* $\mathcal{D} = (a_k^{\tau\mu} d_\mu)$ with m columns and p rows, we may introduce the morphism $D^p \xrightarrow{\mathcal{D}} D^m : (P_\tau) \to (P_\tau \Phi^\tau)$ over D by acting with D *on the left of these row vectors* while acting with $\mathcal{D}$ *on the right of these row vectors* by composition of operators with $im(\mathcal{D}) = I$. The *presentation* of M is defined by the exact cokernel sequence $D^p \xrightarrow{\mathcal{D}} D^m \to M \to 0$. We notice that the presentation only depends on K, D and Φ or $\mathcal{D}$, that is to say never refers to the concept of (explicit local or formal) solutions. It follows from its definition that M can be endowed with a *quotient filtration* obtained from that of D^m which is defined by the order of the jet coordinates y_q in $D_q y$. We have therefore the *inductive limit* $0 \subseteq M_0 \subseteq M_1 \subseteq \cdots \subseteq M_q \subseteq \cdots \subseteq M_\infty = M$ with $d_i M_q \subseteq M_{q+1}$ and $M = DM_q$ for $q \gg 0$ with prolongations $D_r M_q \subseteq M_{q+r}, \forall q, r \geq 0$.

DEFINITION 1.2.1: An exact sequence of morphisms finishing at M is said to be a *resolution* of M. If the differential modules involved apart from M are free, that is isomorphic to a certain power of D, we shall say that we have a *free resolution* of M.

Having in mind that K is a left D-module with the action $(D, K) \to K : (d_i, a) \to \partial_i a$ and that D is a bimodule over itself, *we have only two possible constructions*:

DEFINITION 1.2.2: We may define the *right* (care!) differential module

$hom_D(M,D)$.

DEFINITION 1.2.3: We define the *system* $R = hom_K(M,K)$ and set $R_q = hom_K(M_q,K)$ as the *system of order q*. We have the *projective limit* $R = R_\infty \to \cdots \to R_q \to \cdots \to R_1 \to R_0$. It follows that $f_q \in R_q : y_\mu^k \to f_\mu^k \in K$ with $a_k^{\tau\mu} f_\mu^k = 0$ defines a *section at order q* and we may set $f_\infty = f \in R$ for a *section* of *R*. For an arbitrary differential field *K*, *such a definition has nothing to do with the concept of a formal power series solution* (*care*).

PROPOSITION 1.2.4: When *M* is a left *D*-module, then *R* is also a left *D*-module.

Proof: As *D* is generated by *K* and *T* as we already said, let us define:

$$(af)(m) = af(m), \quad \forall a \in K, \forall m \in M$$

$$(\xi f)(m) = \xi f(m) - f(\xi m), \quad \forall \xi = a^i d_i \in T, \forall m \in M$$

In the operator sense, it is easy to check that $d_i a = a d_i + \partial_i a$ and that $\xi\eta - \eta\xi = [\xi,\eta]$ is the standard bracket of vector fields. We finally get $(d_i f)_\mu^k = (d_i f)(y_\mu^k) = \partial_i f_\mu^k - f_{\mu+1_i}^k$ and thus recover *exactly* the Spencer operator of the previous section though *this is not evident at all*. We also get $(d_i d_j f)_\mu^k = \partial_{ij} f_\mu^k - \partial_i f_{\mu+1_j}^k - \partial_j f_{\mu+1_i}^k + f_{\mu+1_i+1_j}^k \Rightarrow d_i d_j = d_j d_i, \forall i, j = 1, \cdots, n$ and thus $d_i R_{q+1} \subseteq R_q \Rightarrow d_i R \subset R$ induces a well defined operator $R \to T^* \otimes R : f \to dx^i \otimes d_i f$. This operator has been first introduced, up to sign, by F.S. Macaulay as early as in 1916 but this is still not acknowledged [17]. For more details on the Spencer operator and its applications, the reader may look at [15] [18] [19] [20] [21].

Q.E.D.

DEFINITION 1.2.5: With any differential module *M* we shall associate the *graded module* $G = gr(M)$ over the polynomial ring $gr(D) \simeq K[\chi]$ by setting $G = \oplus_{q=0}^\infty G_q$ with $G_q = M_q/M_{q-1}$ and we get $g_q = G_q^*$ where the *symbol* g_q is defined by the short exact sequences:

$$0 \to M_{q-1} \to M_q \to G_q \to 0 \quad \Leftrightarrow \quad 0 \to g_q \to R_q \to R_{q-1} \to 0$$

We have the short exact sequences $0 \to D_{q-1} \to D_q \to S_q T \to 0$ leading to $gr_q(D) \simeq S_q T$ and we may set as usual $T^* = hom_K(T,K)$ in a coherent way with differential geometry.

The two following definitions, which are well known in commutative algebra, are also valid (with more work) in the case of differential modules (see [5] for more details or the references [9] [22] [23] [24] for an introduction to homological algebra and diagram chasing).

DEFINITION 1.2.6: The set of elements $t(M) = \{m \in M \mid \exists 0 \neq P \in D, Pm = 0\} \subseteq M$ is a differential module called the *torsion submodule* of *M*. More generally, a module *M* is called a *torsion module* if $t(M) = M$ and a *torsion-free module* if $t(M) = 0$. In the short exact sequence $0 \to t(M) \to M \to M' \to 0$, the module M' is torsion-free. Its defining module of equations I' is obtained by adding to *I* a representative basis of $t(M)$ set up to zero and we have thus $I \subseteq I'$.

DEFINITION 1.2.7: A differential module F is said to be *free* if $F \simeq D^r$ for some integer $r > 0$ and we shall *define* $rk_D(F) = r$. If F is the biggest free differential module contained in M, then M/F is a torsion differential module and $hom_D(M/F, D) = 0$. In that case, we shall *define* the *differential rank* of M to be $rk_D(M) = rk_D(F) = r$. Accordingly, if M is defined by a linear involutive operator of order q, then $rk_D(M) = \alpha_q^n$.

PROPOSITION 1.2.8: If $0 \to M' \to M \to M'' \to 0$ is a short exact sequence of differential modules and maps or operators, we have

$rk_D(M) = rk_D(M') + rk_D(M'')$.

In the general situation, let us consider the sequence $M' \overset{f}{\to} M \overset{g}{\to} M''$ of modules which may not be exact and define $B = im(f) \subseteq Z = ker(g) \Rightarrow H = Z/B$.

LEMMA 1.2.9: The kernel of the induced epimorphism $coker(f) \to coim(g)$ is isomorphic to H.

Proof: It follows from a snake chase in the commutative and exact diagram where $coim(g) \simeq im(g)$:

$$
\begin{array}{ccccccccc}
 & & & & & & 0 & & \\
 & & & & & & \downarrow & & \\
 & & 0 & & 0 & & H & & \\
 & & \downarrow & & \downarrow & & \downarrow & & \\
0 & \to & B & \to & M & \to & coker(f) & \to & 0 \\
 & & \downarrow & & \| & & \downarrow & & \\
0 & \to & Z & \to & M & \overset{g}{\to} & coim(g) & \to & 0 \\
 & & \downarrow & & \downarrow & & \downarrow & & \\
 & & H & & 0 & & 0 & & \\
 & & \downarrow & & & & & & \\
 & & 0 & & & & & &
\end{array}
$$

Q.E.D.

In order to conclude this section, we may say that the main difficulty met when passing from the differential framework to the algebraic framework is the "*inversion*" of arrows. Indeed, when an operator is injective, that is when we have the exact sequence $0 \to E \overset{\mathcal{D}}{\to} F$ with $dim(E) = m, dim(F) = p$, like in the case of the operator $0 \to E \overset{j_q}{\to} J_q(E)$, on the contrary, using differential modules, we have the epimorphism $D^p \overset{\mathcal{D}}{\to} D^m \to 0$. The case of a formally surjective operator, like the *div* operator, described by the exact sequence $E \overset{\mathcal{D}}{\to} F \to 0$ is now providing the exact sequence of differential modules

$0 \to D^p \overset{\mathcal{D}}{\to} D^m \to M \to 0$ because $\mathcal{D}$ has no CC.

2. Parametrization Problem

In this section, we shall set up and solve the minimum parametrization problem by comparing the differential geometric approach and the differential algebraic

approach. In fact, both sides are essential because certain concepts, like "torsion", are simpler in the module approach, as we already said, while others, like "involution" are simpler in the operator approach. However, the reader must never forget that the "*extension modules*" or the "*side changing functor*" are pure product of *differential homological algebra* with no system counterpart. Also, the close link existing between "*differential duality*" and "*adjoint operator*" may not be evident at all, even for people quite familiar with mathematical physics [5] [12] [15] [16].

Let us start with a given linear differential operator $\eta \xrightarrow{\mathcal{D}_1} \zeta$ between the sections of two given vector bundles F_0 and F_1 of respective fiber dimension m and p. Multiplying the equations $\mathcal{D}_1 \eta = \zeta$ by p test functions λ considered as a section of the adjoint vector bundle $ad(F_1) = \wedge^n T^* \otimes F_1^*$ and integrating by parts, we may introduce the adjoint vector bundle $ad(F_0) = \wedge^n T^* \otimes F_0^*$ with sections μ in order to obtain the adjoint operator $\mu \xleftarrow{ad(\mathcal{D}_1)} \lambda$, writing on purpose the arrow backwards, that is from right to left. As any operator is the adjoint of another operator because $ad(ad(\mathcal{D})) = \mathcal{D}$, we may *decide* to denote by $v \xleftarrow{ad(\mathcal{D})} \mu$ the generating CC of $ad(\mathcal{D}_1)$ by introducing a vector bundle E with sections ξ and its adjoint $ad(E) = \wedge^n T^* \otimes E^*$ with sections v. We have thus obtained the formally exact differential sequence:

$$v \xleftarrow{ad(\mathcal{D})} \mu \xleftarrow{ad(\mathcal{D}_1)} \lambda$$

and its formally exact adjoint sequence:

$$\xi \xrightarrow{\mathcal{D}} \eta \xrightarrow{\mathcal{D}_1} \zeta$$

providing a parametrization *if and only if* $\mathcal{D}_1$ generates the CC of $\mathcal{D}_1$. Such a situation may not be satisfied but we shall assume it from now on because otherwise $\mathcal{D}_1$ *cannot* be parametrized according to the *double differential duality* test, for example in the case of the *Einstein* equations [25] [26] [27] or the extension to the conformal group and other Lie groups of transformations [15] [19] [20] [21] [28] [29] [30]. Nevertheless, for the interested reader only, we provide the following key result on which this procedure is based (see [5] [12] [13] [14] [16] for more details):

THEOREM 2.1: If M is a differential module, we have the exact sequence of differential modules:

$$0 \to t(M) \to M \xrightarrow{\varepsilon} hom_D(hom_D(M,D),D) \tag{6}$$

where the map ε is defined by $\varepsilon(m)(f) = f(m), \forall m \in M, f \in hom_D(M,D)$. Moreover, if N is the differential module defined by $ad(\mathcal{D})$, then $t(M) = ext_D^1(N,D)$.

In order to pass to the differential module framework, let us introduce the free differential modules $D\xi \simeq D^l, D\eta \simeq D^m, D\zeta \simeq D^p$. We have similarly the ad-

joint free differential modules $Dv \simeq D^l, D\mu \simeq D^m, D\lambda \simeq D^p$, because $dim(ad(E)) = dim(E)$ and $hom_D(D^m, D) \simeq D^m$. Of course, in actual practice, *the geometric meaning is totally different* because we have volume forms in the dual framework. We have thus obtained the formally exact sequence of differential modules:

$$D^p \xrightarrow{\mathcal{D}_1} D^m \xrightarrow{\mathcal{D}} D^l$$

and the formally exact adjoint sequence:

$$D^p \xleftarrow{ad(\mathcal{D}_1)} D^m \xleftarrow{ad(\mathcal{D})} D^l$$

The procedure with 4 steps is as follows in the operator language:

- STEP 1: Start with the formally exact *parametrizing sequence* already constructed by differential biduality. We have thus $im(\mathcal{D}) = ker(\mathcal{D}_1)$ and the corresponding differential module M_1 defined by $\mathcal{D}_1$ is torsion-free by assumption.
- STEP 2: Construct the adjoint sequence which is also formally exact by assumption.
- STEP 3: Find a *maximum* set of differentially independent CC $ad(\mathcal{D}'): \mu \to v'$ among the generating CC $ad(\mathcal{D}): \mu \to v$ of $ad(\mathcal{D}_1)$ in such a way that $im(ad(\mathcal{D}'))$ is a maximum free differential submodule of $im(ad(\mathcal{D}))$ that is any element in $im(ad(\mathcal{D}))$ is differentially algebraic over $im(ad(\mathcal{D}'))$.
- STEP 4: Using differential duality, construct $\mathcal{D}' = ad(ad(\mathcal{D}'))$.

It remains to prove that $\mathcal{D}_1$ generates the CC of $\mathcal{D}'$ in the following diagram:

$$
\begin{array}{c}
\boxed{4} \qquad \xi' \\[4pt]
\uparrow \quad \searrow^{\mathcal{D}'} \\[4pt]
\xi \xrightarrow{\mathcal{D}} \eta \xrightarrow{\mathcal{D}_1} \zeta \qquad \boxed{1} \\[8pt]
v \xleftarrow{ad(\mathcal{D})} \mu \xleftarrow{ad(\mathcal{D}_1)} \lambda \quad \boxed{2} \\[4pt]
\uparrow \quad \nearrow^{ad(\mathcal{D}')} \\[4pt]
\boxed{3} \qquad v' \\[4pt]
\swarrow \quad \uparrow \\[4pt]
0 \qquad 0
\end{array}
\tag{7}
$$

PROPOSITION 2.2: $\mathcal{D}'$ is a minimum parametrization of $\mathcal{D}_1$.

Proof: Let us denote the number of potentials ξ by l (respectively ξ' by l'), the number of unknowns η by m and the number of given equations ζ by p. As $ad(\mathcal{D}')$ has no CC by construction, then $ad(\mathcal{D}'): \mu \to v'$ is a formally surjective operator. On the differential module level, we have the injective operator $ad(\mathcal{D}'): D^{l'} \to D^m$ because there are no CC. Applying $hom_D(\bullet, D)$ or duality, we get an operator $D^m \to D^{l'}$ with a cokernel which is a torsion module because it has rank $l' - rk_D(\mathcal{D}') = l' - rk_D(ad(\mathcal{D}')) = l' - l' = 0$.

However, in actual practice as will be seen in the contact case, things are not so simple and we shall use the following commutative and exact diagram of differential modules based on a long *ker*/*coker* long exact sequence (compare to [31] and [32]):

$$0 \to ker\big(ad(\mathcal{D})\big) \to \quad D^l \quad \overset{ad(\mathcal{D})}{\to} \quad D^m \quad \to coker\big(ad(\mathcal{D})\big) \to 0$$

$$\begin{array}{ccc} & \searrow & \nearrow \\ & L & \\ \nearrow & \uparrow & \searrow \\ 0 \qquad D^{l'} \qquad 0 \\ & \uparrow & \\ & 0 & \end{array} \tag{8}$$

Setting $L = D^l / ker\big(ad(\mathcal{D})\big)$ and introducing the biggest free differential module $D^{l'} \subseteq L$ we have $rk_D\big(D^{l'}\big) = rk_D(L) \le rk_D\big(D^l\big) \Rightarrow l' \le l$, we may *define* the injective (*care*) operator $ad(\mathcal{D}')$ by the composition of monomorphisms $D^{l'} \to L \to D^m$ where the second is obtained by picking a basis of $D^{l'}$, lifting it to D^l and pushing it to D^m by applying $ad(\mathcal{D})$. We notice that L can be viewed as the differential module defined by the generating CC of $ad(\mathcal{D})$ that could also be used as in [31].

Then we have $ad(\mathcal{D}') \circ ad(\mathcal{D}_1) = ad(\mathcal{D}_1 \circ \mathcal{D}') = 0 \Rightarrow \mathcal{D}_1 \circ \mathcal{D}' = 0$ and thus $\mathcal{D}_1$ is surely *among* the CC of $\mathcal{D}'$. Therefore, the differential sequence $\xi' \overset{\mathcal{D}'}{\to} \eta \overset{\mathcal{D}_1}{\to} \zeta$ on the operator level or the sequence $D^p \overset{\mathcal{D}_1}{\to} D^m \overset{\mathcal{D}'}{\to} D^{l'}$ on the differential module level may not be exact and we can thus apply the previous Lemma. Changing slightly the notations, we have now
$B = im(\mathcal{D}_1) = ker(\mathcal{D}) \subseteq ker(\mathcal{D}') = Z$. But we have also $rk_D(B) = m - rk_D(\mathcal{D})$, $rk(Z) = m - rk_D(\mathcal{D}') \Rightarrow rk_D(H) = rk_D(\mathcal{D}) - rk_D(\mathcal{D}') = 0$ by construction.

Taking into account the previous Lemma, we may set $coim(\mathcal{D}_1) = M_1 \subseteq D^l$ by assumption and consider $im(\mathcal{D}') = M_1' \subseteq D^{l'}$ in order to obtain the short exact sequence of differential modules $0 \to H \to M_1 \to M_1' \to 0$. As H is a torsion module and the differential module M_1 defined by $\mathcal{D}_1$ is torsion-free by assumption, the only possibility is that $H = 0$ and thus $im(\mathcal{D}_1) = ker(\mathcal{D}')$, that is $\mathcal{D}'$ is a minimum parametrization of $\mathcal{D}_1$ with $l' \le l$ potentials.

Q.E.D.

EXAMPLE 2.3: *Contact transformations*

With $m = n = 3, K = \mathbb{Q}\big(x^1, x^2, x^3\big) = \mathbb{Q}(x)$, we may introduce the so-called *contact* 1-form $\alpha = dx^1 - x^3 dx^2$. The system of infinitesimal Lie equations defining the infinitesimal contact transformations is obtained by eliminating the factor $\rho(x)$ in the equations $\mathcal{L}(\xi)\alpha = \rho\alpha$ where $\mathcal{L}$ is the standard Lie derivative. This system is thus only generated by η^1 and η^2 below but is not involutive and one has to introduce η^3 defined by the first order CC:

$$\zeta \equiv \partial_3 \eta^1 - \partial_2 \eta^2 - x^3 \partial_1 \eta^2 + \eta^3 = 0$$

in order to obtain the following involutive system with two equations of class 3

and one equation of class 2, a result leading to $\beta_1^3 = 2, \beta_1^2 = 1, \beta_1^1 = 0$:

$$\begin{cases} \eta^3 \equiv \partial_3 \xi^3 + \partial_2 \xi^2 + 2x^3 \partial_1 \xi^2 - \partial_1 \xi^1 = 0 \\ \eta^2 \equiv \partial_3 \xi^1 - x^3 \partial_3 \xi^2 = 0 \\ \eta^1 \equiv \partial_2 \xi^1 - x^3 \partial_2 \xi^2 + x^3 \partial_1 \xi^1 - \left(x^3\right)^2 \partial_1 \xi^2 - \xi^3 = 0 \end{cases}$$

$$\begin{array}{|ccc|} 1 & 2 & 3 \\ 1 & 2 & 3 \\ 1 & 2 & \bullet \end{array}$$

The characters are thus $\alpha_1^3 = 3 - 2 = 1 < \alpha_1^2 = 3 - 1 = 2, \alpha_1^1 = 3 - 0 = 3$ with sum equal to $1 + 2 + 3 = 6 = dim(g_1) = 3 \times 3 - 3$. In this situation, if M is the differential module defined by this system or the corresponding operator $\mathcal{D}$, we know that $rk_D(M) = \alpha_1^3 = 1 = 3 - 2 = rk_D(D\xi) - rk_D(\mathcal{D})$. Of course, a differential transcendence basis for $\mathcal{D}$ can be the operator $\mathcal{D}' : \xi \to \{\eta^2, \eta^3\}$ but, in view of the CC, we may equally choose any couple among $\{\eta^1, \eta^2, \eta^3\}$ and we obtain $rk_D(\mathcal{D}') = rk_D(\mathcal{D}) = 2$ in any case, but now $\mathcal{D}'$ is formally surjective, contrary to $\mathcal{D}$. The same result can also be obtained directly from the unique CC or the corresponding operator $\mathcal{D}_1$ defining the differential module M_1. Finally, we have $rk_D(M_1) = 3 - 1 = 2 = rk_D(D\eta) - rk_D(\mathcal{D}_1)$ and we check that we have indeed $rk_D(M) + rk_D(M_1) = 1 + 2 = 3 = rk_D(D\xi)$.

It is well known that such a system can be parametrized by the injective parametrization (see [2] and [3] for more details and the study of the general dimension $n = 2p + 1$):

$$-x^3 \partial_3 \phi + \phi = \xi^1, \; -\partial_3 \phi = \xi^2, \; \partial_2 \phi + x^3 \partial_1 \phi = \xi^3 \Rightarrow \xi^1 - x^3 \xi^2 = \phi$$

It is however not so well known and quite striking that such a parametrization can be recovered independently by using the parametrization of the differential module defined by $\eta^1 = 0$ with potentials ξ^1 and ξ^2 while setting:

$$\left(\xi^1, \xi^2\right) \to \xi^3 = \partial_2 \xi^1 - x^3 \partial_2 \xi^2 + x^3 \partial_1 \xi^1 - \left(x^3\right)^2 \partial_1 \xi^2$$

Taking into account the differential constraint $\eta^2 \equiv \partial_3 \xi^1 - x^3 \partial_3 \xi^2 = 0$, that is $\xi^2 = -\partial_3 \left(\xi^1 - x^3 \xi^2\right)$ and substituting in $\eta^3 = 0$, we get no additional constraint. We finally only need to modify the potentials while "*defining*" now $\phi = \xi^1 - x^3 \xi^2 = \bar{\xi}^1$ as before.

The associated differential sequence is:

$$0 \to \phi \xrightarrow{\mathcal{D}_{-1}} \xi \xrightarrow{\mathcal{D}} \eta \xrightarrow{\mathcal{D}_1} \zeta \to 0$$

$$0 \to 1 \to 3 \to 3 \to 1 \to 0$$

with Euler-Poincaré characteristic $1 - 3 + 3 - 1 = 0$ but is *not* a Janet sequence because $\mathcal{D}_{-1}$ is not involutive, its completion to involution being the trivially involutive operator $j_1 : \phi \to j_1(\phi)$.

Introducing the ring $D = K[d_1, d_2, d_3] = K[d]$ of linear differential operators with coefficients in the differential field K, the corresponding differential module $M \simeq D$ is projective and even free, thus torsion-free or 0-pure, being defined by the split exact sequence of free differential modules:

$$0 \to D \xrightarrow{\mathcal{D}_1} D^3 \xrightarrow{\mathcal{D}} D^3 \xrightarrow{\mathcal{D}_{-1}} D \to 0$$

We let the reader prove as an exercise that the adjoint sequence:

$$\overset{ad(\mathcal{D}_{-1})}{0 \leftarrow \theta \leftarrow} \overset{ad(\mathcal{D})}{v \leftarrow} \overset{ad(\mathcal{D}_1)}{\mu \leftarrow} \lambda \leftarrow 0$$

$$0 \leftarrow 1 \leftarrow 3 \leftarrow 3 \leftarrow 1 \leftarrow 0$$

starting from the Lagrange multiplier λ is also a split exact sequence of free differential modules.

We finally prove that the situation met for the contact structure is *exactly* the same as the one that we shall meet in the metric structure, namely that one can identify $\mathcal{D}_{-1}$ not with $\mathcal{D}_1$ of course but with $ad(\mathcal{D}_1)$. For this, let us modify the "basis" linearly by setting $\left(\overline{\xi}^1 = \xi^1 - x^3\xi^2, \overline{\xi}^2 = \xi^2, \overline{\xi}^3 = \xi^3 \right)$ and suppressing the bar for simplicity, we obtain the new injective parametrization:

$$\phi = \xi^1, -\partial_3\phi = \xi^2, \partial_2\phi + x^3\partial_1\phi = \xi^3$$

and may eliminate ϕ in order to consider the new involutive system, renumbering the equations through a cyclic permutation of $(1,2,3)$:

$$\begin{cases} \eta^1 \equiv \partial_3\xi^3 + \partial_2\xi^2 + x^3\partial_1\xi^2 - \partial_1\xi^1 = 0 & \boxed{\begin{array}{ccc} 1 & 2 & 3 \end{array}} \\ \eta^3 \equiv \partial_3\xi^1 + \xi^2 = 0 & \boxed{\begin{array}{ccc} 1 & 2 & 3 \end{array}} \\ \eta^2 \equiv \partial_2\xi^1 + x^3\partial_1\xi^1 - \xi^3 = 0 & \boxed{\begin{array}{ccc} 1 & 2 & \bullet \end{array}} \end{cases}$$

with the unique first order CC defining $\mathcal{D}_1$:

$$\zeta \equiv \partial_3\eta^2 - \partial_2\eta^3 - x^3\partial_1\eta^3 + \eta^1 = 0$$

Multiplying by λ and integrating by parts, we obtain for $ad(\mathcal{D}_1)$:

$$\eta^1 \to \lambda = \mu^1, \eta^2 \to -\partial_3\lambda = \mu^2, \eta^3 \to \partial_2\lambda + x^3\partial_1\lambda = \mu^3$$

obtaining therefore $\mathcal{D}_{-1} = ad(\mathcal{D}_1) \Leftrightarrow \mathcal{D}_1 = ad(\mathcal{D}_{-1})$ *exactly*.

As for $\mathcal{D}\xi = \eta$, we obtain the formal operator matrix:

$$\begin{pmatrix} -d_1 & d_2 + x^3d_1 & d_3 \\ d_2 + x^3d_1 & 0 & -1 \\ d_3 & 1 & 0 \end{pmatrix}$$

Similarly, for $ad(\mathcal{D})$ we obtain the formal operator matrix:

$$\begin{pmatrix} d_1 & -(d_2 + x^3d_1) & -d_3 \\ -(d_2 + x^3d_1) & 0 & 1 \\ -d_3 & -1 & 0 \end{pmatrix}$$

and finally discover that $ad(\mathcal{D}) = -\mathcal{D}$, a striking result showing that both operators have the same CC and parametrization even though $\mathcal{D}$ is *not* self-adjoint.

3. *Einstein* Equations

Linearizing the *Ricci* tensor ρ_{ij} over the Minkowski metric ω, we obtain the usual second order homogeneous *Ricci* operator $\Omega \to R$ with 4 terms:

$$2R_{ij} = \omega^{rs}\left(d_{rs}\Omega_{ij} + d_{ij}\Omega_{rs} - d_{ri}\Omega_{sj} - d_{sj}\Omega_{ri} \right) = 2R_{ji} \tag{9}$$

$$tr(R) = \omega^{ij}R_{ij} = \omega^{ij}d_{ij}tr(\Omega) - \omega^{ru}\omega^{sv}d_{rs}\Omega_{uv} \tag{10}$$

We may define the *Einstein* operator by setting $E_{ij} = R_{ij} - \frac{1}{2}\omega_{ij}tr(R)$ and obtain the 6 terms [33]:

$$2E_{ij} = \omega^{rs}\left(d_{rs}\Omega_{ij} + d_{ij}\Omega_{rs} - d_{ri}\Omega_{sj} - d_{sj}\Omega_{ri}\right)$$
$$-\omega_{ij}\left(\omega^{rs}\omega^{uv}d_{rs}\Omega_{uv} - \omega^{ru}\omega^{sv}d_{rs}\Omega_{uv}\right) \tag{11}$$

We have the (locally exact) differential sequence of operators acting on sections of vector bundles where the order of an operator is written under its arrow:

$$T \overset{Killing}{\underset{1}{\to}} S_2T^* \overset{Riemann}{\underset{2}{\to}} F_1 \overset{Bianchi}{\underset{1}{\to}} F_2 \tag{12}$$

$$n \overset{\mathcal{D}}{\to} n(n+1)/2 \overset{\mathcal{D}_1}{\to} n^2\left(n^2-1\right)/12 \overset{\mathcal{D}_2}{\to} n^2\left(n^2-1\right)(n-2)/24$$

Our purpose is now to study the differential sequence onto which its right part is projecting:

$$S_2T^* \overset{Einstein}{\underset{2}{\to}} S_2T^* \overset{div}{\underset{1}{\to}} T^* \to 0$$

$$n(n+1)/2 \to n(n+1)/2 \to n \to 0$$

and the following adjoint sequence where we have set [15] [19] [20] [31] [34]:

$$Cauchy = ad(Killing), Beltrami = ad(Riemann), Lanczos = ad(Bianchi)$$

$$ad(T) \overset{Cauchy}{\leftarrow} ad(S_2T^*) \overset{Beltrami}{\leftarrow} ad(F_1) \overset{Lanczos}{\leftarrow} ad(F_2) \tag{13}$$

In this sequence, if E is a vector bundle over the ground manifold X with dimension n, we may introduce the new vector bundle $ad(E) = \wedge^n T^* \otimes E^*$ where E^* is obtained from E by inverting the transition rules exactly like T^* is obtained from T. We have for example $ad(T) = \wedge^n T^* \otimes T^* \simeq \wedge^n T^* \otimes T \simeq \wedge^{n-1}T^*$ because T^* is isomorphic to T by using the metric ω. The 10×10 *Einstein* operator matrix is induced from the 10×20 *Riemann* operator matrix and the 10×4 *div* operator matrix is induced from the 20×20 *Bianchi* operator matrix. We advise the reader not familiar with the formal theory of systems or operators to follow the computation in dimension $n = 2$ with the 1×3 *Airy* operator matrix, which is the formal adjoint of the 3×1 *Riemann* operator matrix, and $n = 3$ with the 6×6 Beltrami operator matrix which is the formal adjoint of the 6×6 *Riemann* operator matrix which is easily seen to be self-adjoint up to a change of basis.

With more details, we have:

- $n = 2$: The stress equations become $d_1\sigma^{11} + d_2\sigma^{12} = 0, d_1\sigma^{21} + d_2\sigma^{22} = 0$. Their second order parametrization $\sigma^{11} = d_{22}\phi, \sigma^{12} = \sigma^{21} = -d_{12}\phi, \sigma^{22} = d_{11}\phi$ has been provided by George Biddell *Airy* in 1863 [35] and is well known [5]. We get the second order system:

$$\begin{cases} \sigma^{11} \equiv d_{22}\phi = 0 \\ -\sigma^{12} \equiv d_{12}\phi = 0 \\ \sigma^{22} \equiv d_{11}\phi = 0 \end{cases} \begin{array}{|cc|} 1 & 2 \\ 1 & \bullet \\ 1 & \bullet \end{array}$$

which is involutive with one equation of class 2, 2 equations of class 1 and it is easy to check that the 2 corresponding first order CC are just the *Cauchy* equations. Of course, the *Airy* function (1 term) has absolutely nothing to do with the perturbation of the metric (3 terms). With more details, when ω is the Euclidean metric, we may consider the only component:

$$tr(R) = (d_{11} + d_{22})(\Omega_{11} + \Omega_{22}) - (d_{11}\Omega_{11} + 2d_{12}\Omega_{12} + d_{22}\Omega_{22})$$
$$= d_{22}\Omega_{11} + d_{11}\Omega_{22} - 2d_{12}\Omega_{12}$$

Multiplying by the *Airy* function ϕ and integrating by parts, we discover that:

$$Airy = ad(Riemann) \Leftrightarrow Riemann = ad(Airy)$$

in the following differential sequences:

$$2 \xrightarrow[1]{Killing} 3 \xrightarrow[2]{Riemann} 1 \to 0$$

$$0 \leftarrow 2 \xleftarrow[1]{Cauchy} 3 \xleftarrow[2]{Airy} 1$$

- $n = 3$: It is more delicate to parametrize the 3 PD equations:

$$d_1\sigma^{11} + d_2\sigma^{12} + d_3\sigma^{13} = 0,$$
$$d_1\sigma^{21} + d_2\sigma^{22} + d_3\sigma^{23} = 0,$$
$$d_1\sigma^{31} + d_2\sigma^{32} + d_3\sigma^{33} = 0$$

A direct computational approach has been provided by Eugenio Beltrami in 1892 [36] [37], James Clerk Maxwell in 1870 [38] and Giacinto Morera in 1892 [37] [39] by introducing the 6 *stress functions* $\phi_{ij} = \phi_{ji}$ in the *Beltrami parametrization*. The corresponding system:

$$\begin{cases} \sigma^{11} \equiv d_{33}\phi_{22} + d_{22}\phi_{33} - 2d_{23}\phi_{23} = 0 & \begin{array}{|ccc|} 1 & 2 & 3 \end{array} \\ -\sigma^{12} \equiv d_{33}\phi_{12} + d_{12}\phi_{33} - d_{13}\phi_{23} - d_{23}\phi_{13} = 0 & \begin{array}{ccc} 1 & 2 & 3 \end{array} \\ \sigma^{22} \equiv d_{33}\phi_{11} + d_{11}\phi_{33} - 2d_{13}\phi_{13} = 0 & \begin{array}{ccc} 1 & 2 & 3 \end{array} \\ \sigma^{13} \equiv d_{23}\phi_{12} + d_{12}\phi_{23} - d_{22}\phi_{13} - d_{13}\phi_{22} = 0 & \begin{array}{ccc} 1 & 2 & \bullet \end{array} \\ -\sigma^{23} \equiv d_{23}\phi_{11} + d_{11}\phi_{23} - d_{12}\phi_{13} - d_{13}\phi_{12} = 0 & \begin{array}{ccc} 1 & 2 & \bullet \end{array} \\ \sigma^{33} \equiv d_{22}\phi_{11} + d_{11}\phi_{22} - 2d_{12}\phi_{12} = 0 & \begin{array}{|ccc|} 1 & 2 & \bullet \end{array} \end{cases}$$

is involutive with 3 equations of class 3, 3 equations of class 2 and no equation of class 1. The three characters are thus
$$\alpha_2^3 = 1 \times 6 - 3 = 3 < \alpha_2^2 = 2 \times 6 - 3 = 9 < \alpha_2^1 = 3 \times 6 - 0 = 18 \quad \text{and we have}$$

$$dim(g_2) = \alpha_2^1 + \alpha_2^2 + \alpha_2^3 = 18 + 9 + 3 = 30$$
$$= dim(S_2T^* \otimes S_2T^*) - dim(S_2T^*) = 6 \times 6 - 6 \quad [1]. \text{ The 3 CC are describing}$$

the stress equations which admit therefore a parametrization... but without any geometric framework, in particular without any possibility to imagine that the above second order operator is *nothing else but* the *formal adjoint* of the *Riemann operator*, namely the (linearized) *Riemann* tensor with $n^2(n^2-1)/2 = 6$ independent components when $n = 3$ [31]. Breaking the canonical form of the six equations which is associated with the Janet tabular, we may rewrite the Bel-

trami parametrization of the *Cauchy* stress equations as follows, after exchanging the third row with the fourth row, keeping the ordering
$$\{(11) < (12) < (13) < (22) < (23) < (33)\}:$$

$$\begin{pmatrix} d_1 & d_2 & d_3 & 0 & 0 & 0 \\ 0 & d_1 & 0 & d_2 & d_3 & 0 \\ 0 & 0 & d_1 & 0 & d_2 & d_3 \end{pmatrix} \begin{pmatrix} 0 & 0 & 0 & d_{33} & -2d_{23} & d_{22} \\ 0 & -d_{33} & d_{23} & 0 & d_{13} & -d_{12} \\ 0 & d_{23} & -d_{22} & -d_{13} & d_{12} & 0 \\ d_{33} & 0 & -2d_{13} & 0 & 0 & d_{11} \\ -d_{23} & d_{13} & d_{12} & 0 & -d_{11} & 0 \\ d_{22} & -2d_{12} & 0 & d_{11} & 0 & 0 \end{pmatrix} \equiv 0$$

as an identity where 0 on the right denotes the zero operator. However, if Ω is a perturbation of the metric ω, the standard implicit summation used in continuum mechanics is, when $n = 3$:

$$\sigma^{ij}\Omega_{ij} = \sigma^{11}\Omega_{11} + 2\sigma^{12}\Omega_{12} + 2\sigma^{13}\Omega_{13} + \sigma^{22}\Omega_{22} + 2\sigma^{23}\Omega_{23} + \sigma^{33}\Omega_{33}$$
$$= \Omega_{22}d_{33}\phi_{11} + \Omega_{33}d_{22}\phi_{11} - 2\Omega_{23}d_{23}\phi_{11} + \cdots$$
$$+ \Omega_{23}d_{13}\phi_{12} + \Omega_{13}d_{23}\phi_{12} - \Omega_{12}d_{33}\phi_{12} - \Omega_{33}d_{12}\phi_{12} + \cdots$$

because *the stress tensor density σ is supposed to be symmetric*. Integrating by parts in order to construct the adjoint operator, we get:

$$\phi_{11} \to d_{33}\Omega_{22} + d_{22}\Omega_{33} - 2d_{23}\Omega_{23}$$
$$\phi_{12} \to d_{13}\Omega_{23} + d_{23}\Omega_{13} - d_{33}\Omega_{12} - d_{12}\Omega_{33}$$

and so on, obtaining therefore the striking identification:

$$Riemann = ad(Beltrami) \quad \Leftrightarrow \quad Beltrami = ad(Riemann)$$

between the (linearized) *Riemann* tensor and the Beltrami parametrization.

Taking into account the factor 2 involved by multiplying the second, third and fifth row by 2, we get the new 6×6 operator matrix with rank 3:

$$\begin{pmatrix} 0 & 0 & 0 & d_{33} & -2d_{23} & d_{22} \\ 0 & -2d_{33} & 2d_{23} & 0 & 2d_{13} & -2d_{12} \\ 0 & 2d_{23} & -2d_{22} & -2d_{13} & 2d_{12} & 0 \\ d_{33} & 0 & -2d_{13} & 0 & 0 & d_{11} \\ -2d_{23} & 2d_{13} & 2d_{12} & 0 & -2d_{11} & 0 \\ d_{22} & -2d_{12} & 0 & d_{11} & 0 & 0 \end{pmatrix}$$

clearly providing a self-adjoint operator.

Surprisingly, the Maxwell parametrization is obtained by keeping
$\phi_{11} = A, \phi_{22} = B, \phi_{33} = C$ while setting $\phi_{12} = \phi_{23} = \phi_{31} = 0$ in order to obtain the system:

$$\begin{cases} \sigma^{11} \equiv d_{33}B + d_{22}C = 0 & \boxed{\begin{matrix} 1 & 2 & 3 \\ 1 & 2 & 3 \\ 1 & 2 & \bullet \\ 1 & 2 & \bullet \\ 1 & \bullet & \bullet \\ 1 & \bullet & \bullet \end{matrix}} \\ \sigma^{22} \equiv d_{33}A + d_{11}C = 0 \\ -\sigma^{23} \equiv d_{23}A = 0 \\ \sigma^{33} \equiv d_{22}A + d_{11}B = 0 \\ -\sigma^{13} \equiv d_{13}B = 0 \\ -\sigma^{12} \equiv d_{12}C = 0 \end{cases}$$

However, *this system may not be involutive* and no CC can be found "*a priori*" because the coordinate system is surely not δ-regular. Indeed, effecting the linear change of coordinates $\overline{x}^1 = x^1, \overline{x}^2 = x^2, \overline{x}^3 = x^3 + x^2 + x^1$ and taking out the bar for simplicity, we obtain the new involutive system:

$$\begin{cases} d_{33}C + d_{13}C + d_{23}C + d_{12}C = 0 & | 1 \quad 2 \quad 3 \\ d_{33}B + d_{13}B = 0 & | 1 \quad 2 \quad 3 \\ d_{33}A + d_{23}A = 0 & | 1 \quad 2 \quad 3 \\ d_{23}C + d_{22}C - d_{13}C - d_{13}B - d_{12}C = 0 & | 1 \quad 2 \quad \bullet \\ d_{23}A - d_{22}C + d_{13}B + 2d_{12}C - d_{11}C = 0 & | 1 \quad 2 \quad \bullet \\ d_{22}A + d_{22}C - 2d_{12}C + d_{11}C + d_{11}B = 0 & | 1 \quad 2 \quad \bullet \end{cases}$$

and it is easy to check that the 3 CC obtained just amount to the desired 3 stress equations when coming back to the original system of coordinates. However, the three characters are different as we have now

$\alpha_2^3 = 3 - 3 = 0 < \alpha_2^2 = 2 \times 3 - 3 = 3 < \alpha_2^1 = 3 \times 3 - 0 = 9$ with sum equal to

$dim(g_2) = 6 \times 3 - 6 = 18 - 6 = 12$. *We have thus a minimum parametrization that cannot be parametrized again.*

Again, *if there is a geometrical background, this change of local coordinates is hidding it totally.* Moreover, we notice that the stress functions kept in the procedure are just the ones on which d_{33} is acting. The reason for such an apparently technical choice is related to very general deep arguments in the theory of differential modules that will only be explained at the end of the paper.

The Morera parametrization is obtained similarly by keeping now

$\phi_{23} = L, \phi_{13} = M, \phi_{12} = N$ while setting $\phi_{11} = \phi_{22} = \phi_{33} = 0$, namely:

$$\begin{cases} d_{23}L = 0 \\ d_{33}N - d_{13}L - d_{23}M = 0 \\ d_{13}M = 0 \\ d_{22}M - d_{23}N - d_{12}L = 0 \\ d_{11}L - d_{12}M - d_{13}N = 0 \\ d_{12}N = 0 \end{cases}$$

Using now the same change of coordinates as the one already done for the Maxwell parametrization, we obtain the following system with 3 equations of (full) class 3 and 3 equations of class 2 in the Pommaret basis corresponding to the Janet tabular:

$$\begin{cases} d_{33}N + d_{23}N + d_{13}N + d_{12}N = 0 & | 1 \quad 2 \quad 3 \\ d_{33}M + d_{13}M = 0 & | 1 \quad 2 \quad 3 \\ d_{33}L + d_{23}L = 0 & | 1 \quad 2 \quad 3 \\ (d_{23}N + d_{23}M - d_{23}L) + (d_{13}N - d_{13}M + d_{13}L) + d_{12}N = 0 & | 1 \quad 2 \quad \bullet \\ 2d_{23}M + (d_{13}N - d_{13}M - d_{13}L) + d_{12}M - d_{11}L = 0 & | 1 \quad 2 \quad \bullet \\ d_{22}M + (d_{12}N - d_{12}M - d_{12}L) + d_{11}L = 0 & | 1 \quad 2 \quad \bullet \end{cases}$$

After elementary but tedious computations (*that could not be avoided!*), one can prove that the 3 CC corresponding to the 3 dots are effectively satisfied and

that they correspond to the 3 *Cauchy* stress equations which are therefore parametrized. The parametrization is thus provided by an involutive operator defining a torsion module because the character α_2^3 is vanishing in δ-regular coordinates, just like before for the Maxwell parametrization. *We have thus another minimum parametrization that cannot be parametrized again*. Of course, such a result could not have been understood by Beltrami in 1892 because the work of Cartan could not be adapted easily as it is using the language of exterior forms and the work of Janet only appeared in 1920 with no explicit reference to involution because only Janet bases are used [8] while the Pommaret bases have only been introduced in 1978 [1].

On a purely computational level, we may also keep only $\{\phi_{11}, \phi_{12}, \phi_{22}\}$ and obtain the different involutive system with the same characters and, *in particular*, $\alpha_2^3 = 0$:

$$\begin{cases} \sigma^{11} \equiv d_{33}\phi_{22} = 0 \\ -\sigma^{12} \equiv d_{33}\phi_{12} = 0 \\ \sigma^{22} \equiv d_{33}\phi_{11} = 0 \\ \sigma^{13} \equiv d_{23}\phi_{12} - d_{13}\phi_{22} = 0 \\ -\sigma^{23} \equiv d_{23}\phi_{11} - d_{13}\phi_{12} = 0 \\ \sigma^{33} \equiv d_{22}\phi_{11} + d_{11}\phi_{22} - 2d_{12}\phi_{12} = 0 \end{cases} \qquad \begin{array}{|ccc|} \hline 1 & 2 & 3 \\ 1 & 2 & 3 \\ 1 & 2 & 3 \\ 1 & 2 & \bullet \\ 1 & 2 & \bullet \\ 1 & 2 & \bullet \\ \hline \end{array}$$

So far, we have thus obtained three explicit local minimum parametrizations of the *Cauchy* stress equations with $n(n-1)/2 = 3$ stress potentials but there may be others [21].

- $n = 4$: It just remains to explain the relation of the previous results with *Einstein* equations. The first surprising link is provided by the following technical proposition:

PROPOSITION 3.1: The Beltrami parametrization is just described by the *Einstein* operator when $n = 3$. The same confusion existing between the *Bianchi* operator and the *Cauchy* operator has been made by both *Einstein* and Beltrami because the *Einstein* operator and the Beltrami operator are self-adjoint in arbitrary dimension $n \geq 3$, contrary to the *Ricci* operator.

Proof: The number of components of the *Riemann* tensor is $dim(F_1) = n^2(n^2-1)/12$. We have the combinatorial formula $n^2(n^2-1)/12 - n(n+1)/2 = n(n+1)(n+2)(n-3)/12$ expressing that the number of components of the *Riemann* tensor is always greater or equal to the number of components of the *Ricci* tensor whenever $n > 2$. Also, we have shown in many books [1] [2] [3] [4] [15] [19] or papers [10] [21] [29] [30] that the number of *Bianchi* identities is equal to $n^2(n^2-1)(n-2)/24$, that is 3 when $n = 3$ and 20 when $n = 4$. Of course, it is well known that the *div* operator, induced as CC of the *Einstein* operator, has n components in arbitrary dimension $n \geq 3$.

Accordingly, when $n = 3$ we have $n^2(n^2-1)/12 = n(n+1)/2 = 6$ and it only remains to prove that the *Einstein* operator reduces to the Beltrami operator *and not just to the Ricci operator*. The following formulas can be found in any textbook on general relativity:

Hence the difference can only be seen when $\omega_{i \neq j} = 0$. In our situation with $n = 3$ and the Euclidean metric for simplicity, we have:

$$2R_{12} = 2E_{12} = \left(d_{11} + d_{22} + d_{33}\right)\Omega_{12} + d_{12}\left(\Omega_{11} + \Omega_{22} + \Omega_{33}\right)$$
$$- \left(d_{11}\Omega_{12} + d_{12}\Omega_{22} + d_{13}\Omega_{23}\right) - \left(d_{12}\Omega_{11} + d_{22}\Omega_{12} + d_{23}\Omega_{13}\right)$$
$$= d_{33}\Omega_{12} + d_{12}\Omega_{33} - d_{13}\Omega_{23} - d_{23}\Omega_{13}$$

$$2R_{11} = \left(d_{11} + d_{22} + d_{33}\right)\Omega_{11} + d_{11}\left(\Omega_{11} + \Omega_{22} + \Omega_{33}\right)$$
$$- 2\left(d_{11}\Omega_{11} + d_{12}\Omega_{12} + d_{13}\Omega_{13}\right)$$
$$= \left(d_{22} + d_{33}\right)\Omega_{11} + d_{11}\left(\Omega_{22} + \Omega_{33}\right) - 2\left(d_{12}\Omega_{12} + d_{13}\Omega_{13}\right)$$

$$tr\left(R\right) = \left(d_{11}\Omega_{22} + d_{11}\Omega_{33} + d_{22}\Omega_{11} + d_{22}\Omega_{33} + d_{33}\Omega_{11} + d_{33}\Omega_{22}\right)$$
$$- 2\left(d_{12}\Omega_{12} + d_{13}\Omega_{13} + d_{23}\Omega_{23}\right)$$

$$-2E_{11} = d_{22}\Omega_{33} + d_{33}\Omega_{22} - 2d_{23}\Omega_{23}$$

In the light of modern differential geometry, comparing these results with the works of both Maxwell, Morera, Beltrami and *Einstein*, it becomes clear that they have been confusing the *div* operator induced from the *Bianchi* operator with the *Cauchy* operator. However, it is also clear that they both obtained a possibility to parametrize the *Cauchy* operator by means of 3 arbitrary potential like functions in the case of Maxwell and Morera, 6 in the case of Beltrami who explains the previous choices, and 10 in the case of *Einstein*. Of course, as they were ignoring that the *Einstein* operator was self-adjoint whenever $n \geq 3$, they did not notice that we have $Cauchy = ad\left(Killing\right)$ and they were unable to compare their results with the *Airy* operator found as early as in 1870 for the same mechanical purpose when $n = 2$. To speak in a rough way, the situation is similar to what could happen in the study of contact structures if one should confuse $\mathcal{D}_{-1}$ with $\mathcal{D}_1$ [29]. Finally, using Theorem 2.1 or Proposition 2.2, we can choose a differential transcendence basis with $n(n-1)/2$ potentials that can be indexed by $\phi_{ij} = \phi_{ji}$ with $i < j$ or $1 \leq i, j \leq n-1$ or even $2 \leq i, j \leq n$ when the dimension $n \geq 2$ is arbitrary (see [2] or [40] for more details on differential algebra).

Q.E.D.

REMARK 3.2: In the opinion of the author of this paper who is not a historian of sciences but a specialist of mathematical physics interested in the analogy existing between *electromagnetism* (EM), *elasticity* (EL) and *gravitation* (GR) by using the conformal group of space-time (see [3] [10] [28] [29] [30] [41] [42] [43] [44] for related works), it is difficult to imagine that *Einstein* could not have been aware of the works of Maxwell and Beltrami on the foundations of EL and tensor calculus. Indeed, not only they were quite famous when he started his research work but it must also be noticed that the Mach-Lippmann analogy [45] [46] [47] [48] was introduced at the same time (see [3] and [49] for more details on the field-matter couplings and the phenomenological law discovered by... Maxwell too). The main idea is that classical variational calculus using a Lagran-

gian formalism must be only considered as the basic scheme of a more general and powerful "*duality theory*" that only depends on new purely mathematical tools, namely "*group theory*" and "*differential homological algebra*" (see [4] or [15] for the theory and [21] for the applications).

The two following crucial results, still neither known nor acknowledged today, are provided by the next proposition and corresponding corollary [40]:

PROPOSITION 3.3: The *Cauchy* operator can be parametrized by the formal adjoint of the *Ricci* operator (4 terms) and the *Einstein* operator (6 terms) is thus useless. The so-called gravitational waves equations are thus nothing else than the formal adjoint of the linearized *Ricci* operator.

Proof: The *Einstein* operator $\Omega \to E$ is defined by setting

$E_{ij} = R_{ij} - \frac{1}{2}\omega_{ij}tr(R)$ that we shall write *Einstein* = $C \circ Ricci$ where

$C : S_2T^* \to S_2T^*$ is a symmetric matrix only depending on ω, which is invertible whenever $n \geq 3$. *Surprisingly*, we may also introduce the *same* linear trans-

formation $C : \Omega \to \bar{\Omega} = \Omega - \frac{1}{2}\omega tr(\Omega)$ and the unknown composite operator

$\mathcal{X} : \bar{\Omega} \to \Omega \to E$ in such a way that *Einstein* = $\mathcal{X} \circ C$ where $\mathcal{X}$ is defined by (see [33], 5.1.5 p 134):

$$2E_{ij} = \omega^{rs}d_{rs}\bar{\Omega}_{ij} - \omega^{rs}d_{ri}\bar{\Omega}_{sj} - \omega^{rs}d_{sj}\bar{\Omega}_{ri}$$
$$+ \omega_{ij}\omega^{ru}\omega^{sv}d_{rs}\bar{\Omega}_{uv}$$

Now, introducing the test functions λ^{ij}, we get:

$$\lambda^{ij}E_{ij} = \lambda^{ij}\left(R_{ij} - \frac{1}{2}\omega_{ij}tr(R)\right)$$
$$= \left(\lambda^{ij} - \frac{1}{2}\lambda^{rs}\omega_{rs}\omega^{ij}\right)R_{ij} = \bar{\lambda}^{ij}R_{ij}$$

Integrating by parts while setting as usual $\square = \omega^{rs}d_{rs}$, we obtain:

$$\left(\square\bar{\lambda}^{rs} + \omega^{rs}d_{ij}\bar{\lambda}^{ij} - \omega^{sj}d_{ij}\bar{\lambda}^{ri} - \omega^{ri}d_{ij}\bar{\lambda}^{sj}\right)\Omega_{rs} = \sigma^{rs}\Omega_{rs} \qquad (14)$$

Moreover, suppressing the "bar" for simplicity, we have:

$$d_r\sigma^{rs} = \omega^{ij}d_{rij}\lambda^{rs} + \omega^{rs}d_{rij}\lambda^{ij} - \omega^{sj}d_{rij}\lambda^{ri} - \omega^{ri}d_{rij}\lambda^{sj}$$
$$= 0$$

As *Einstein* is a self-adjoint operator (contrary to the *Ricci* operator), we have the identities:

$$ad(Einstein) = ad(C) \circ ad(\mathcal{X}) \Rightarrow Einstein = C \circ ad(\mathcal{X})$$
$$\Rightarrow ad(\mathcal{X}) = Ricci \Rightarrow \mathcal{X} = ad(Ricci)$$

Indeed, $ad(C) = C$ because C is a symmetric matrix and we know that $ad(Einstein) = Einstein$. Accordingly, the operator $ad(Ricci)$ parametrizes the *Cauchy* equations, *without any reference* to the *Einstein* operator which has no mathematical origin, in the sense that it cannot be obtained by any diagram chasing. The three terms after the *Dalembert* operator factorize through the *di-*

*v*ergence operator $d_i \lambda^{ri}$. We may thus add the *differential constraints* $d_i \lambda^{ri} = 0$ *without any reference to a gauge transformation* in order to obtain a (minimum) *relative parametrization* (see [14] and [18] for details and explicit examples). When $n = 4$ we finally obtain the adjoint sequences:

$$4 \xrightarrow{\text{Killing}} 10 \xrightarrow{\text{Ricci}} 10$$

$$0 \leftarrow 4 \xleftarrow{\text{Cauchy}} 10 \xleftarrow{\text{ad}(\text{Ricci})} 10$$

without any reference to the *Bianchi* operator and the induced *div* operator.

Finally, using Theorem 2.1 or Proposition 2.2, we may choose a differential transcendence basis made by $\{\lambda^{ij} \mid i < j\}$ or $\{\lambda^{ij} \mid 1 < i, j < n-1\}$ or even $\{\lambda^{ij} \mid 2 < i, j < n\}$ when the dimension $n \geq 2$ is arbitrary (see again [2] or [40] for more details on differential algebra).

Q.E.D.

COROLLARY 3.4: The differential module *N* defined by the *Ricci* or the *Einstein* operator is not torsion-free and cannot therefore be parametrized. Its torsion submodule is generated by the 10 components of the *Weyl* operator that are *separately* killed by the Dalembert operator.

Proof: In order to avoid using extension modules, we present the 5 steps of the *double differential duality test* in this framework:

Step 1: Start with the *Einstein* operator $\mathcal{D}_1 : 10 \xrightarrow{\text{Einstein}} 10$.

Step 2: Consider its formal adjoint: $ad(\mathcal{D}_1) : 10 \xleftarrow{\text{Einstein}} 10$.

Step 3: Compute the generating CC, namely the *Cauchy* operator:
$ad(\mathcal{D}) : 4 \xleftarrow{\text{Cauchy}} 10$.

Step 4: Consider its formal adjoint: $\mathcal{D} = ad(ad(\mathcal{D})) : 4 \xrightarrow{\text{Killing}} 10$.

Step 5: Compute the generating CC, namely the *Riemann* operator:
$\mathcal{D}_1' : 10 \xrightarrow{\text{Riemann}} 20$.

With a slight abuse of language, we have the direct sum *Riemann = Ricci ⊕ Weyl* with $20 = 10 + 10$. It follows from differential homological algebra that the 10 additional CC in $\mathcal{D}_1'$ that are *not* in $\mathcal{D}_1$, are generating the torsion submodule $t(N)$ of the differential module *N* defined by the *Einstein* or *Ricci* operator. In general, if *K* is a differential field with commuting derivations $\partial_1, \cdots, \partial_n$, we way consider the ring $D = K[d_1, \cdots, d_n] = K[d]$ of differential operators with coefficients in *K* and it is known that $rk_D(\mathcal{D}) = rk_D(ad(\mathcal{D}))$ for any operator matrix $\mathcal{D}$ with coefficients in *K*. In the present situation, as the Minkowski metric has coefficients equal to $0, 1, -1$, we may choose the ground differential field to be $K = \mathbb{Q}$. Hence, there exist operators $\mathcal{P}$ and $\mathcal{Q}$ such that we have an identity:

$$\mathcal{P} \circ Weyl = \mathcal{Q} \circ Ricci$$

One may also notice that $rk_D(Einstein) = rk_D(Ricci)$ with:

$$rk_D\left(Einstein\right)=\frac{n\left(n+1\right)}{2}-n=\frac{n\left(n-1\right)}{2},$$

$$rk_D\left(Riemann\right)=\frac{n\left(n+1\right)}{2}-n=\frac{n\left(n-1\right)}{2}$$

The differential ranks of the *Einstein* and *Riemann* operators are thus equal, but *this is a pure coincidence* because $rk_D\left(Einstein\right)$ has only to do with the *div* operator induced by contracting the *Bianchi* operator, while $rk_D\left(Riemann\right)$ has only to do with the classical *Killing* operator and the fact that the corresponding differential module is a torsion module because we have a Lie group of transformations having $n+\frac{n\left(n-1\right)}{2}=\frac{n\left(n+1\right)}{2}$ parameters (translations + rotations). Hence, as the *Riemann* operator is a direct sum of the *Weyl* operator and the *Einstein* or *Ricci* operator according to the previous theorem, each component of the *Weyl* operator must be killed by a certain operator whenever the *Einstein* or *Ricci* equations in vacuum are satisfied. *It is not at all evident* that we have $\mathcal{P}=\square$ acting on each component of the *Weyl* operator. A direct tricky computation can be found in ([49], p 206), ([50], exercise 7.7) and ([15], p 95). With more details, we may start from the long exact sequence:

$$0\to\Theta\to4\overset{Killing}{\to}10\overset{Riemann}{\to}20\overset{Bianchi}{\to}20\to6\to0$$

This resolution of the set of *Killing* vector fields is *not* a *Janet* sequence because the *Killing* operator is not involutive as it is an operator of finite type with symbol of dimension $n\left(n-1\right)/2=6$ and one should need one prolongation for getting an involutive operator with vanishing second order symbol. Splitting the *Riemann* operator we get the commutative and exact diagram:

$$
\begin{array}{ccccccccc}
 & & & 0 & & 0 & & 0 & \\
 & & & \downarrow & & \downarrow & & \downarrow & \\
 & & 0 & & 10 & \to & 16 & \to & 6 & \to 0 \\
 & & \downarrow & & \downarrow\uparrow & & \downarrow & & \| \\
4 & \overset{Killing}{\to} & 10 & \overset{Riemann}{\to} & 20 & \overset{Bianchi}{\to} & 20 & \to & 6 & \to 0 \\
 & & \| & & \downarrow\uparrow & & \downarrow & & \downarrow \\
 & & 10 & \overset{Einstein}{\to} & 10 & \overset{div}{\to} & 4 & \to & 0 \\
 & & \downarrow & & \downarrow & & \downarrow & & \\
 & & 0 & & 0 & & 0 & &
\end{array}
$$

Passing to the module point of view, we have the long exact sequence:

$$0\to D^6\to D^{20}\overset{Bianchi}{\to}D^{20}\overset{Riemann}{\to}D^{10}\overset{Killing}{\to}D^4\to M\to0$$

which is a resolution of the *Killing* differential module $M=coker\left(Killing\right)$ and we check that we have indeed the vanishing of the *Euler-Poincaré characteristic* $6-20+20-10+4=0$. Accordingly, we have $N'=coker\left(Riemann\right)\simeq im\left(Killing\right)\subset D^4$ and thus N' is torsion-free with

$rk_D(N') = 4 - 0 = 4 = n$ because $rk_D(M) = 0$.

We have the following commutative and exact diagram where $N = coker(Einstein)$:

$$
\begin{array}{ccccccccc}
&&&&&&&& 0 \\
&&&&&&&& \downarrow \\
&& 0 && 0 && 0 && t(N) \\
&& \downarrow && \downarrow && \downarrow && \downarrow \\
0 & \to & D^4 & \xrightarrow{div} & D^{10} & \xrightarrow{Einstein} & D^{10} & \to & N & \to 0 \\
& & \downarrow && \downarrow && \downarrow && \| && \downarrow \\
0 \to & D^6 & \to & D^{20} & \xrightarrow{Bianchi} & D^{20} & \xrightarrow{Riemann} & D^{10} & \to & N' & \to 0 \\
& \| && \downarrow && \downarrow && \downarrow && \downarrow \\
0 \to & D^6 & \to & D^{16} & \to & D^{10} && 0 && 0 \\
& \downarrow && \downarrow && \downarrow \\
& 0 && 0 && 0
\end{array}
$$

If L is the kernel of the epimorphism $N \to N'$, it is a torsion module because $rk_D(L) = rk_D(N) - rk_D(N') = 4 - 4 = 0$. We have thus $L \subseteq t(N)$ in the following commutative and exact diagram:

$$
\begin{array}{ccc}
0 && 0 \\
\downarrow && \downarrow \\
0 \to \quad L & \to & t(N) \\
\downarrow && \downarrow \\
0 \to \quad N & = & N \quad \to 0 \\
\downarrow && \downarrow \\
N' & \to & N/t(N) \quad \to 0 \\
\downarrow && \downarrow \\
0 && 0
\end{array}
$$

where $N/t(N)$ is a torsion-free module by definition. A snake chase allows to prove that the cokernel of the monomorphism $L \to t(N)$ is isomorphic to the kernel of the induced epimorphism $N' \to N/t(N)$ and must be therefore, at the same time, a torsion module because $rk_D(L) = rk_D(t(N)) = 0$ and a torsion-free module because $N' \subset D^4$, a result leading to a contradiction unless it is zero and thus $L = t(N)$. A snake chase in the previous diagram allows to exhibit the long exact connecting sequence:

$$0 \to D^6 \to D^{16} \to D^{10} \to t(N) \to 0$$

It must be noticed that one cannot find canonical morphisms between the classical and conformal resolutions constructed similarly because we recall that, for $n = 4$ (*only*), the CC of the *Weyl* operator are of order 2 and *not* 1 like the *Bianchi* CC for the *Riemann* operator (see [37] for a computer algebra check-

ing !). However, it follows from the last theorem that the short exact sequence $0 \to D^{10} \to D^{20} \to D^{10} \to 0$ splits with $D^{20} \simeq D^{10} \oplus D^{10}$ but the existence of a canonical lift $D^{20} \to D^{10} \to 0$ in the above diagram does not allow to split the right column and thus $N \neq N' \oplus t(N)$ as N' is not even free. Hence, one can only say that the space of solutions of *Einstein* equations in vacuum contains the generic solutions of the *Riemann* operator which are parametrized by arbitrary vector fields. As for the torsion elements, we have $t(N) = coker\left(D^{16} \to D^{10}\right)$ and we may thus represent them by the components of the *Weyl* tensor, killed by the Dalembertian. This module interpretation may thus question the proper origin and existence of gravitational waves because the *div* operator on the upper left part of the diagram has *strictly nothing to do* with the $Cauchy = ad\left(Killing\right)$ operator which cannot appear *anywhere* in this diagram.

<div align="right">Q.E.D.</div>

COROLLARY 3.5: More generally, when $\mathcal{D}$ is a Lie operator of *finite type*, that is when $[\Theta, \Theta] \subset \Theta$ under the ordinary bracket of vector fields or $\left[R_q, R_q\right] \subset R_q$ under the bracket of Lie algebroids and $g_{q+r} = 0$ for r large enough, then the Spencer sequence is locally isomorphic to the tensor product of the Poincaré sequence for the exterior derivative by a finite dimensional Lie algebra. It is thus formally exact both with its adjoint sequence. As it is known that the extension modules do not depend on the resolution used, this is the reason for which not only the *Cauchy* operator can be parametrized but also the *Cosserat couple-stress equations* $ad\left(\mathcal{D}_1\right)$ can be parametrized by $ad\left(\mathcal{D}_2\right)$, a result not evident at all (see [41] and [43] for explicit computations).

REMARK 3.6: A similar situation is well known for the *Cauchy-Riemann* equations when $n = 2$. Indeed, any infinitesimal complex transformation ξ must be solution of the linear first order homogeneous system $\xi_2^2 - \xi_1^1 = 0, \xi_2^1 + \xi_1^2 = 0$ of infinitesimal Lie equations though we obtain $\xi_{11}^1 + \xi_{22}^1 = 0, \xi_{11}^2 + \xi_{22}^2 = 0$, that is ξ^1 and ξ^2 are *separately* killed by the second order *Laplace* operator $\Delta = d_{11} + d_{22}$.

REMARK 3.7: A similar situation is also well known for the wave equations for the EM field F in electromagnetism. Indeed, starting with the first set of *Maxwell* equations $dF = 0$ and using the *Minkowski* constitutive law in vacuum with electric constant ε_0 and magnetic constant μ_0 such that $\varepsilon_0 \mu_0 c^2 = 1$ for the seconf set of *Maxwell* equations, a standard tricky differential elimination allows to avoid the *Lorenz* (*no* "t") gauge condition for the EM potential and to obtain *directly* $\Box F = 0$ (see [15] and [40] for the details).

Using computer algebra or a direct checking with the ordering $11 < 12 < 13 < 22 < 23 < 33$, we obtain:

$$E_{33} = \omega^{44} d_{44} \Omega_{33} + lower\, terms$$

$$E_{23} = \omega^{44} d_{44} \Omega_{23} \cdots$$

We have therefore the following Janet tabular:

$$
\begin{array}{|cccc|}
\hline
1 & 2 & 3 & 4 \\
1 & 2 & 3 & 4 \\
1 & 2 & 3 & 4 \\
1 & 2 & 3 & 4 \\
1 & 2 & 3 & 4 \\
1 & 2 & 3 & 4 \\
1 & 2 & 3 & \bullet \\
1 & 2 & 3 & \bullet \\
1 & 2 & 3 & \bullet \\
1 & 2 & 3 & \bullet \\
\hline
\end{array}
$$

we are in the position to compute the characters of the *Einstein* operator but a similar procedure could be followed with the *Ricci* operator. We obtain at once:

$$\beta_2^4 = 6 \Rightarrow \alpha_2^4 = (10 \times 1) - 6 = 4$$

$$\beta_2^3 = 4 \Rightarrow \alpha_2^3 = (10 \times 2) - 4 = 16$$

$$\beta_2^2 = 0 \Rightarrow \alpha_2^2 = (10 \times 3) - 0 = 30$$

$$\beta_2^1 = 0 \Rightarrow \alpha_2^1 = (10 \times 4) - 0 = 40$$

a result leading to $dim(g_2) = \alpha_2^1 + \alpha_2^2 + \alpha_2^3 + \alpha_2^4 = 90$ and

$dim(g_3) = \alpha_2^1 + 2\alpha_2^2 + 3\alpha_2^3 + 4\alpha_2^4 = 164$ along with the long exact sequences:

$$0 \to g_2 \to S_2 T^* \otimes S_2 T^* \to S_2 T^* \to 0$$

$$0 \to g_3 \to S_3 T^* \otimes S_2 T^* \to T^* \otimes S_2 T^* \to T^* \to 0$$

Now, we have by definition $div = (d_1, d_2, d_3, d_4)$ and $div \circ Einstein = (0, 0, 0, 0)$.

As the *Einstein* operator is a self-adjoint 10×10 operator matrix up to a change of basis [27], we obtain therefore, with a slight abuse of language, $det(Einstein) = 0$ because:

$$
\begin{pmatrix}
d_1 & d_2 & d_3 & d_4 & 0 & 0 & 0 & 0 & 0 & 0 \\
0 & d_1 & 0 & 0 & d_2 & d_3 & d_4 & 0 & 0 & 0 \\
0 & 0 & d_1 & 0 & 0 & 0 & 0 & d_2 & d_3 & d_4 \\
0 & 0 & 0 & d_1 & 0 & 0 & d_2 & 0 & d_3 & d_4
\end{pmatrix}
\begin{pmatrix}
E_{11} \\
E_{12} \\
E_{13} \\
E_{14} \\
E_{22} \\
E_{23} \\
E_{24} \\
E_{33} \\
E_{34} \\
E_{44}
\end{pmatrix}
=
\begin{pmatrix}
0 & \cdots & 0 \\
0 & \cdots & 0 \\
0 & \cdots & 0 \\
0 & \cdots & 0
\end{pmatrix}
$$

a result not evident at first sight that must be compared with the Poincaré situation when $n = 3$:

$$
\begin{pmatrix} d_1 & d_2 & d_3 \end{pmatrix}
\begin{pmatrix}
0 & -d_3 & d_2 \\
d_3 & 0 & -d_1 \\
-d_2 & d_1 & 0
\end{pmatrix}
= \begin{pmatrix} 0 & 0 & 0 \end{pmatrix}
$$

4. Symbol Sequences

A way to study the formal properties of a linear differential operator $\mathcal{D} : E \to F = F_0$ of order q between the sections of two vector bundles over a manifold X with dimension n is to consider the symbol of $\mathcal{D}$ at the covector $\chi \in T^*(X)$, namely the map $\sigma_\chi(\mathcal{D})$ obtained from the leading terms of order q. With more details, if $\mathcal{D}$ is described by the operator matrix $\left(a_k^{\tau\mu} d_\mu \right)$ with $0 \le |\mu| \le q$ and $\chi = \chi_i dx^i \in T^*$, then $\sigma_\chi(\mathcal{D}) : E \to F_0$ is described by the polynomial matrix $\left(a_k^{\tau\mu} \chi_\mu \right)$ with $|\mu| = q$. When $\mathcal{D}$ is formally integrable, then χ is said to be *characteristic* if $\sigma_\chi(\mathcal{D})$ fails to be injective and we may introduce the characteristic set V as usual. When $\mathcal{D}$ is involutive, it is known after the work of M. Janet (1920) that one can construct *first order* operators $\mathcal{D}_1, \cdots, \mathcal{D}_n$, each one generating the compatibility conditions (CC) of the preceding one. However, the symbol maps $\sigma_\chi(\mathcal{D}_i) : F_{i-1} \to F_i$ for $i = 1, \cdots, n$ may not provide an exact sequence and any non-zero covector is characteristic for these operators. A comparison of the operators involved in a control system with $n = 1$, in the study of the contact transformations with $n = 3$ and of the linearized *Einstein* equations with $n = 4$ proves that the preceding definition must be conveniently refined by saying that a covector is *systatic* if the matrix $\sigma_\chi(\mathcal{D})$ fails to have its maximum generic rank and the previous symbol sequence is exact otherwise and we may introduce the *systatic set W* as in [1] [4] [5]. What we have done with the Janet sequence can also be done with the Spencer sequence that only involves first order operators induced by the Spencer operator. A close link with differential homological algebra and the corresponding differential extension modules can also be established and illustrated [14]. These new results are adding doubts to the ones we have already expressed on the origin and existence of gravitational waves as follows.

First of all, we must distinguish two cases:

- $max_\chi rk\left(\sigma_\chi(\mathcal{D}) \right) < m \Leftrightarrow \alpha_q^n > 0$: Any covector is characteristic and we have $W \subset V = T^*$ with a slight abuse of language. This is the situation for each of the operators $\mathcal{D}_1, \cdots, \mathcal{D}_n$.
- $max_\chi rk\left(\sigma_{chi}(\mathcal{D}) \right) = m \Leftrightarrow \alpha_q^n = 0$: The symbol map $\sigma_\chi(\mathcal{D})$ fails to be injective if and only if all the $m \times m$ submatrices have vanishing determinants and we have $W = V \subset T^*$.

PROPOSITION 4.1: If $\mathcal{D}$ is involutive, the symbol sequence of the Janet sequence:

$$0 \to ker\left(\sigma_\chi(\mathcal{D}) \right) \to E \xrightarrow{\sigma_\chi(\mathcal{D})} F_0 \xrightarrow{\sigma_\chi(\mathcal{D}_1)} \cdots \xrightarrow{\sigma_\chi(\mathcal{D}_n)} F_n \to 0 \tag{15}$$

is exact if and only if $\chi \notin W$.

Proof: Using the Janet tabulars for $\mathcal{D}$ and $\mathcal{D}_1$ with $dim(E) = m$, we get:

$$dim\left(im\left(\sigma_\chi(\mathcal{D}) \right) \right) = rk\left(\sigma_\chi(\mathcal{D}) \right) = m - \alpha_q^n(\mathcal{D}) = \beta_q^n(\mathcal{D})$$
$$= \alpha_1^n(\mathcal{D}_1) = dim\left(ker\left(\sigma_\chi(\mathcal{D}_1) \right) \right)$$

and so on.

Q.E.D.

When $n = 3$, coming back to the Beltrami operator, that is the *Einstein* operator which is known to be involutive, we may change the local coordinates as we did for the Maxwell and Morera parametrizations. With $\bar{\chi} = d\bar{x}^3 = dx^1 + dx^2 + dx^3 = (1,1,1)$, then $ker\left(\sigma_{\bar{\chi}}(\mathcal{D})\right)$ is defined by:

$$\begin{cases} \phi_{22} + \phi_{33} - 2\phi_{23} = 0 \\ \phi_{12} + \phi_{33} - \phi_{23} - \phi_{13} = 0 \\ \phi_{11} + \phi_{33} - 2\phi_{13} = 0 \\ \phi_{12} + \phi_{23} - \phi_{13} - \phi_{22} = 0 \\ \phi_{11} + \phi_{23} - \phi_{13} - \phi_{12} = 0 \\ \phi_{11} + \phi_{22} - 2\phi_{12} = 0 \end{cases}$$

Multiplying the fourth equation by 2 and substituting the first, the third and the sixth, we get:

$$\left(\phi_{11} + \phi_{22}\right) + \left(\phi_{22} + \phi_{33}\right) - \left(\phi_{11} + \phi_{33}\right) - 2\phi_{22} = 0$$

whenever $2\phi_{23} = \phi_{22} + \phi_{33}, 2\phi_{13} = \phi_{11} + \phi_{33}, 2\phi_{12} = \phi_{11} + \phi_{22}$. This unexpected result, which has only to do with the use of δ-regular local coordinates, is proving that the choice of the stress potentials has *strictly nothing to do* with the complementary cancellations respectively adopted by Maxwell or Morera according to Beltrami because, in both cases, $\bar{\chi} \notin V = W$ but $\chi = dx^3 = (0,0,1) \in V = W$. This result can be extended to an arbitrary dimension.

5. Conclusion

After teaching elasticity for 25 years to high level students in some of the best french civil engineering schools, the author of this paper still keeps in mind one of the most fascinating exercises that he has set up. The purpose was to explain why a dam made with concrete is *always* vertical on the water-side with a slope of about 42 degrees on the other free side in order to obtain a minimum cost and the auto-stability under cracking of the surface under water (see the introduction of [5] for more details). Surprisingly, the main tool involved is the approximate computation of the *Airy* function inside the dam. The author discovered at that time that no one of the other teachers did know that the *Airy* parametrization is nothing else than the adjoint of the linearized *Riemann* operator used as generating CC for the deformation tensor by any engineer. Being involved in General Relativity (GR) at that time, it took him 25 years (1970-1995) to prove that the *Einstein* equations could not be parametrized [25] [26] [27]. However, nobody is a prophet in his own country and it is only recently that he discovered that GR could be considered as a way to parametrize the *Cauchy* operator. It follows that *exactly the same confusion* has been done by Maxwell, Morera, Beltrami and *Einstein* because, in all these cases, the operator considered is self-adjoint. As a byproduct, the variational formalism cannot allow to discover it as no engineer could have had in mind to confuse the deformation tensor with its CC in the

Lagrangian used for finite elements computations. It is thus an open historical problem to know whether *Einstein* knew any one of the previous works done as all these researchers were quite famous at the time he was active. In our opinion at least, the comparison of the various parametrizations described in this paper needs no comment as we have only presented *facts, just facts*.

Conflicts of Interest

The author declares no conflicts of interest regarding the publication of this paper.

References

[1] Pommaret, J.-F. (1978) Systems of Partial Differential Equations and Lie Pseudo-groups. Gordon and Breach, New York; Russian Translation: MIR, Moscow (1983).

[2] Pommaret, J.-F. (1983) Differential Galois Theory. Gordon and Breach, New York.

[3] Pommaret, J.-F. (1988) Lie Pseudogroups and Mechanics. Gordon and Breach, New York.

[4] Pommaret, J.-F. (1994) Partial Differential Equations and Group Theory. Kluwer, Dordrecht. https://doi.org/10.1007/978-94-017-2539-2

[5] Pommaret, J.-F. (2001) Partial Differential Control Theory. Kluwer, Dordrecht. https://doi.org/10.1007/978-94-010-0854-9

[6] Pommaret, J.-F. (2019) *Journal of Modern Physics*, **10**, 371-401. https://doi.org/10.4236/jmp.2019.103025

[7] Spencer, D.C. (1965) *Bulletin of the AMS*, **75**, 1-114.

[8] Janet, M. (1920) *Journal de Mathematique*, **8**, 65-151.

[9] Pommaret, J.-F. (2005) Algebraic Analysis of Control Systems Defined by Partial Differential Equations. In: *Advanced Topics in Control Systems Theory*, Springer, Berlin, Lecture Notes in Control and Information Sciences 311, Chapter 5, 155-223. https://doi.org/10.1007/11334774_5

[10] Pommaret, J.-F. (2020) *Journal of Modern Physics*, **11**, 1672-1710. https://doi.org/10.4236/jmp.2020.1110104

[11] Gasqui, J. (1982) *Compositio Mathematica*, **47**, 43-69.

[12] Bjork, J.E. (1993) Analytic D-Modules and Applications. Kluwer, Dordrecht. https://doi.org/10.1007/978-94-017-0717-6

[13] Kashiwara, M. (1995) Algebraic Study of Systems of Partial Differential Equations. Mémoires de la Société Mathématique de France, 63 (Transl. from Japanese of His 1970 Master's Thesis).

[14] Pommaret, J.-F. (2015) *Multidimensional Systems and Signal Processing*, **26**, 405-437. https://doi.org/10.1007/s11045-013-0265-0

[15] Pommaret, J.-F. (2018) New Mathematical Methods for Physics. Mathematical Physics Books, Nova Science Publishers, New York, 150 p.

[16] Schneiders, J.-P. (1994) *Bulletin de la Société Royale des Sciences de Liège*, **63**, 223-295.

[17] Macaulay, F.S. (1916) The Algebraic Theory of Modular Systems. Cambridge Tract 19, Cambridge University Press, London. (Reprinted by Stechert-Hafner Service Agency, New York, 1964) https://doi.org/10.3792/chmm/1263317740

[18] Pommaret, J.-F. (2012) Spencer Operator and Applications: From Continuum Mechanics to Mathematical Physics. In: Yong, G., Ed., *Continuum Mechanics-Progress in Fundamentals and Engineering Applications*, InTech, Rijeka, 1-32.
https://doi.org/10.5772/35607

[19] Pommaret, J.-F. (2016) Deformation Theory of Algebraic and Geometric Structures. Lambert Academic Publisher (LAP), Saarbrucken.
http://arxiv.org/abs/1207.1964
https://doi.org/10.1007/BFb0083506

[20] Pommaret, J.-F. (2016) *Journal of Modern Physics*, **7**, 699-728.
https://arxiv.org/abs/1803.09610

[21] Pommaret, J.-F. (2019) *Journal of Modern Physics*, **10**, 1454-1486.
https://doi.org/10.4236/jmp.2019.1012097

[22] Hu, S.-T. (1968) Introduction to Homological Algebra. Holden-Day, San Francisco.

[23] Northcott, D.G. (1966) An Introduction to Homological Algebra. Cambridge University Press, Cambridge.

[24] Rotman, J.J. (1979) An Introduction to Homological Algebra (Pure and Applied Mathematics). Academic Press, Cambridge.

[25] Pommaret, J.-F. (1995) *Comptes Rendus Académie des Sciences Paris*, *Série I*, **320**, 1225-1230.

[26] Zerz, E. (2000) Topics in Multidimensional Linear Systems Theory. Lecture Notes in Control and Information Sciences, LNCIS 256, Springer, Berlin.

[27] Pommaret, J.-F. (2013) *Journal of Modern Physics*, **4**, 223-239.
https://doi.org/10.4236/jmp.2013.48A022

[28] Pommaret, J.-F. (2014) *Journal of Modern Physics*, **5**, 157-170.
https://doi.org/10.4236/jmp.2014.55026

[29] Pommaret, J.-F. (2020) The Conformal Group Revisited.
https://arxiv.org/abs/2006.03449

[30] Pommaret, J.-F. (2020) Nonlinear Conformal Electromagnetism and Gravitation.
https://arxiv.org/abs/2007.01710

[31] Pommaret, J.-F. (2016) *Journal of Modern Physics*, **7**, 699-728.
https://doi.org/10.4236/jmp.2016.77068

[32] Pommaret, J.-F. and Quadrat, A. (1999) *Systems & Control Letters*, **37**, 247-260.
https://doi.org/10.1016/S0167-6911(99)00030-4

[33] Foster, J. and Nightingale, J.D. (1979) A Short Course in General Relativity. Longman, London.

[34] Lanczos, C. (1962) *Reviews of Modern Physics*, **34**, 379-389.
https://doi.org/10.1103/RevModPhys.34.379

[35] Airy, G.B. (1863) *Philosophical Transactions of the Royal Society of London*, **153**, 49-80. https://doi.org/10.1098/rstl.1863.0004

[36] Beltrami, E. (1892) *Atti della Accademia Nazionale dei Lincei*, **1**, 141-142.

[37] Landriani, G.S. (2017) *Meccanica*, **52**, 2801-2806.
https://doi.org/10.1007/s11012-016-0611-z

[38] Maxwell, J.C. (1870) *Transactions of the Royal Society of Edinburgh*, **26**, 1-40.
https://doi.org/10.1017/S0080456800026351

[39] Morera, G. (1892) *Atti della Accademia Nazionale dei Lincei*, **1**, 137-141 + 233-234.

[40] Pommaret, J.-F. (2017) *Journal of Modern Physics*, **8**, 2122-2158.

https://doi.org/10.4236/jmp.2017.813130

[41] Cosserat, E. and Cosserat, F. (1909) Théorie des Corps Déformables. Hermann, Paris.

[42] Pommaret, J.-F. (1997) *Annales des Ponts et Chaussées*, **82**, 59-66.

[43] Pommaret, J.-F. (2010) *Acta Mechanica*, **215**, 43-55.
https://doi.org/10.1007/s00707-010-0292-y

[44] Pommaret, J.-F. (2019) *Journal of Modern Physics*, **10**, 1566-1595.
http://arxiv.org/abs/1802.02430
https://doi.org/10.4236/jmp.2019.1013104

[45] Adler, F.W. (1907) *Annalen der Physik und Chemie*, **22**, 578-594.
https://doi.org/10.1002/andp.19073270314

[46] Lippmann, G. (1876) *Comptes rendus de l'Académie des Sciences*, **82**, 1425-1428.

[47] Lippmann, G. (1907) *Annalen der Physik und Chemie*, **23**, 994-996.
https://doi.org/10.1002/andp.19073281017

[48] Mach, E. (1900) Prinzipien der Wärmelehre, 2, Aufl. J.A. Barth, Leipzig, 330.

[49] Choquet-Bruhat, Y. (2015) Introduction to General Relativity, Black Holes and Cosmology. Oxford University Press, Oxford.

[50] Hughston, L.P. and Tod, K.P. (1990) An Introduction to General Relativity. London Mathematical Society Student Texts 5. Cambridge University Press, Cambridge.
https://doi.org/10.1017/CBO9781139171977

Christoffel Symbols and Chiral Properties of the Space-Time Geometry for the Atomic Electron States

Claude Daviau, Jacques Bertrand

Fondation Louis de Broglie, Paris, France
Email: daviau.claude@orange.fr, bertrandjacques-m@orange.fr

Abstract

Quantum electron states, in the case of an improved Dirac equation, are linked to the Christoffel symbols of the connection of space-time geometry. Each solution of the wave equation, in the case of the hydrogen atom induces a connection which is completely calculated. This allows us to discover the global and chiral properties of the space-time connection, with spin 2.

Keywords

Quantum Mechanics, Clifford Algebra, Differential Geometry, Dirac Equation, Hydrogen Atom, Chirality

1. Introduction

After L. de Broglie's discovery of the quantum wave [1], Dirac formulated his relativistic wave equation for the electron [2], correcting the non-relativistic Schrödinger equation, and conserving the probability density linked to the wave. The main success of this wave equation was its application to the case of the hydrogen atom: all the expected quantum numbers were obtained, as well as the true number of states, and the true energy levels [3]. Moreover, the Dirac equation explained the spin 1/2 of the electron. The main problem was the presence of negative energies which were then accounted for as due to charge conjugation.

Following de Broglie's ideas on the necessity of non-linearity to unify quantum physics and gravitation, an improved Dirac equation was studied [4]-[43]. This relativistic wave equation was extended to a wave equation of all fermions and anti-fermions of the first generation, as described in "Developing a Theory of Everything" [41]. The resolution of the wave equation in the case of the hy-

drogen atom was completed in [42]. The aim of the present work is the use of these solutions as physical examples of the differential geometry linked to the quantum wave. The calculation of the Christoffel symbols was previously made only in the case of plane waves: geometry of space-time was characterized by a not null torsion and a null curvature. The torsion was linked to the mass term of the electron. The case of the electron in the hydrogen atom is much more complicated indeed, and also much more interesting because it will allow us to encounter the geometric aspect of chirality in quantum mechanics.

2. Tensorial Densities without Derivative

Early on, the Dirac theory encountered 16 of the 36 tensorial densities that may be computed without derivatives from the electron wave. This is easy to see with the Pauli algebra [5] [7] [8]. From the wave of the electron, $\phi = \phi(\mathrm{x})$, we get four space-time vectors (16 densities):

$$D_\mu := \phi\sigma_\mu\phi^\dagger, \mu = 0,1,2,3; \phi := \sqrt{2}\begin{pmatrix} \xi_1 & -\bar{\eta}_2 \\ \xi_2 & \bar{\eta}_1 \end{pmatrix}; \phi^\dagger = \sqrt{2}\begin{pmatrix} \bar{\xi}_1 & \bar{\xi}_2 \\ -\eta_2 & \eta_1 \end{pmatrix}. \tag{1}$$

And we get 20 densities (2 with S_0 and 6 for each S_k) as the components of:

$$S_\mu := \phi\sigma_\mu\bar{\phi}; \bar{\phi} := \sqrt{2}\begin{pmatrix} \bar{\eta}_1 & \bar{\eta}_2 \\ -\xi_2 & \xi_1 \end{pmatrix}. \tag{2}$$

The previous equalities use the three well-known Pauli matrices σ_1, σ_2, σ_3 and we let $\sigma_0 := 1$, identifying real numbers and scalar matrices. The 16 densities of the early theory were the components of the probability current $\mathrm{J} := D_0$, the $\mathrm{K} := D_3$ current, the S_3 bivector (6 components) and the Ω_1 and Ω_2 invariants, satisfying:

$$S_0 = \phi\bar{\phi} = \det(\phi) = 2(\xi_1\bar{\eta}_1 + \xi_2\bar{\eta}_2) = \rho\mathrm{e}^{i\beta} = \Omega_1 + i\Omega_2 = 2(\eta_1 \ \eta_2)^\dagger\begin{pmatrix} \xi_1 \\ \xi_2 \end{pmatrix}, \tag{3}$$

where β is the Yvon-Takabayasi angle. We just encountered the right (ξ) and left (η) parts of the wave. We also need:

$$\hat{\phi} := \bar{\phi}^\dagger = \sqrt{2}\begin{pmatrix} \eta_1 & -\bar{\xi}_2 \\ \eta_2 & \bar{\xi}_1 \end{pmatrix}; \mathrm{R} := \sqrt{2}\begin{pmatrix} \xi_1 & 0 \\ \xi_2 & 0 \end{pmatrix}; \hat{\mathrm{L}} := \sqrt{2}\begin{pmatrix} \eta_1 & 0 \\ \eta_2 & 0 \end{pmatrix} \tag{4}$$

$$D_R := \mathrm{RR}^\dagger; D_L := \mathrm{LL}^\dagger.$$

Currents D_R and D_L are the chiral currents that dominate in weak interactions. They satisfy:

$$D_0 = D_R + D_L; D_3 = D_R - D_L. \tag{5}$$

From the beginning of Dirac's research, relativistic quantum mechanics is a non-local theory, because the wave equation is not the only condition that governs the dynamics of the wave:

$$\iiint \mathrm{d}v \frac{\mathrm{J}^0}{\hbar c} = 1. \tag{6}$$

We explained in 1.5.5 of [41] how this condition is a physical law that issues from the principle of equivalence. This law, joined with the invariance under the greater group Cl_3^*, implies the quantization of the kinetic momentum [41] [43]. The four D_μ currents form an orthogonal basis of space-time because they satisfy:

$$D_\mu \cdot D_\nu = 0, \mu \neq \nu; D_0 \cdot D_0 = \rho^2 = -D_1 \cdot D_1 = -D_2 \cdot D_2 = -D_3 \cdot D_3. \tag{7}$$

The ϕ wave of the electron defines a similitude:

$$D_x : X = X^\mu \sigma_\mu \mapsto \mathrm{x} = \phi X \phi^\dagger = \phi X^\nu \sigma_\nu \phi^\dagger = X^\nu D_\nu, \tag{8}$$

$$D_\nu = D_\nu^\mu \sigma_\mu = \phi \sigma_\nu \phi^\dagger. \tag{9}$$

This variable basis is then associated with an affine connection. This also allows us to use the Cartan's mobile basis (D_0, D_1, D_2, D_3). This connection was first studied in [15]. We let:

$$\partial_\nu = \frac{\partial}{\partial X^\nu} = D_\nu^\mu \partial_\mu; \mathrm{d}x = \mathrm{d}X^\nu D_\nu, \tag{10}$$

$$\mathrm{d}D_\mu = \Gamma_{\mu\nu}^\beta \mathrm{d}X^\nu D_\beta. \tag{11}$$

This gives if $\rho \neq 0$:

$$\mathrm{d}x = \mathrm{d}x^\mu \sigma_\mu = D_\nu^\mu \sigma_\mu \mathrm{d}X^\nu = D_\nu \mathrm{d}X^\nu,$$

$$D_\nu = \phi \sigma_\nu \phi^\dagger = D_\nu^\mu \sigma_\mu; \ \sigma_\mu = \left(D^{-1}\right)_\mu^\beta D_\beta. \tag{12}$$

Now we use the similitude $\bar{D}$ such as:

$$\bar{D}(\mathrm{x}) = \bar{\phi} \mathrm{x} \hat{\phi}. \tag{13}$$

We have

$$D \circ \bar{D}(\mathrm{x}) = D\left[\bar{D}(\mathrm{x})\right] = \phi\bar{\phi} \mathrm{x} \hat{\phi}\phi^\dagger = \rho e^{i\beta} \mathrm{x} \rho e^{-i\beta} = \rho^2 \mathrm{x},$$
$$D \circ \left(\rho^{-2}\bar{D}\right)(\mathrm{x}) = \mathrm{x}, \tag{14}$$
$$D^{-1}(\mathrm{x}) = \rho^{-2}\bar{D}(\mathrm{x}).$$

And we get:

$$\mathrm{d}D_\mu = \partial_\nu\left(D_\mu\right)\mathrm{d}X^\nu = \partial_\nu\left(D_\mu^\xi \sigma_\xi\right)\mathrm{d}X^\nu = \partial_\nu\left(D_\mu^\xi\right)\sigma_\xi \mathrm{d}X^\nu$$
$$= \partial_\nu\left(D_\mu^\xi\right)\left(D^{-1}\right)_\xi^\beta D_\beta \mathrm{d}X^\nu = \Gamma_{\mu\nu}^\beta D_\beta \mathrm{d}X^\nu. \tag{15}$$

Therefore the coefficients of the connection satisfy:

$$\Gamma_{\mu\nu}^\beta = \partial_\nu\left(D_\mu^\xi\right)\left(D^{-1}\right)_\xi^\beta; \ \partial_\nu = D_\nu^\tau \partial_\tau. \tag{16}$$

By using the $\bar{D}$ similitude we get:

$$\Gamma_{\mu\nu}^\beta = \rho^{-2}\partial_\nu\left(D_\mu^\xi\right)\bar{D}_\xi^\beta; \ \partial_\nu = D_\nu^\tau \partial_\tau. \tag{17}$$

Since $\bar{D}_0^0 = D_0^0$ and $\bar{D}_j^0 = -D_0^j$ we have:

$$\Gamma_{0\nu}^0 = \Gamma_{1\nu}^1 = \Gamma_{2\nu}^2 = \Gamma_{3\nu}^3 = \partial_\nu\left[\ln(\rho)\right] = D_\nu^\mu \partial_\mu\left[\ln(\rho)\right]. \tag{18}$$

The Christoffel symbols of this connection satisfy (see [41] 4.1):

$$\mathrm{x}'^{\alpha} = \mathrm{x}^{\alpha} + \mathrm{d}\mathrm{x}^{\alpha} + \Gamma^{\alpha}_{\beta\gamma}\mathrm{x}^{\beta}\mathrm{d}\mathrm{x}^{\gamma}, \tag{19}$$

For the complete calculation of these coefficients of the connection we need the following quantities:

$$\mathcal{S}_{(k)} + i\mathcal{S}'_{(k)} := \frac{\nabla S^{\dagger}_k}{\det\left(\phi^{\dagger}\right)}; \mathcal{A}_{(k)} + i\mathcal{A}'_{(k)} := \frac{AS^{\dagger}_k}{\det\left(\phi^{\dagger}\right)}. \tag{20}$$

With the improved wave equation of the electron, we obtained in D.4 of [41] the following symbols:

$$\Gamma^0_{1\mu} = D_{\mu}\cdot\left[\mathcal{S}_{(1)} - 2q\mathcal{A}_{(2)}\right] + 2m\rho\delta^2_{\mu}, \tag{21}$$

$$\Gamma^0_{2\mu} = D_{\mu}\cdot\left[\mathcal{S}_{(2)} + 2q\mathcal{A}_{(1)}\right] - 2m\rho\delta^1_{\mu}, \tag{22}$$

$$\Gamma^0_{3\mu} = D_{\mu}\cdot\mathcal{S}_{(3)}, \tag{23}$$

$$\Gamma^2_{3\mu} = -D_{\mu}\cdot\left[\mathcal{S}'_{(1)} - 2q\mathcal{A}'_{(2)}\right], \tag{24}$$

$$\Gamma^3_{1\mu} = -D_{\mu}\cdot\left[\mathcal{S}'_{(2)} + 2q\mathcal{A}'_{(1)}\right], \tag{25}$$

$$\Gamma^1_{2\mu} = -D_{\mu}\cdot\left[\mathcal{S}'_{(3)} + 2qA\right] - 2m\rho\delta^0_{\mu}, \tag{26}$$

$$\Gamma^0_{0\mu} = \Gamma^1_{1\mu} = \Gamma^2_{2\mu} = \Gamma^3_{3\mu} = D_{\mu}\cdot\nabla\ln\left(\rho\right), \tag{27}$$

$$\Gamma^j_{0\nu} = \Gamma^0_{j\nu}, \quad j = 1,2,3, \tag{28}$$

$$\Gamma^j_{k\nu} = -\Gamma^k_{j\nu}, \quad j = 1,2,3, \quad k = 1,2,3, \quad k \neq j. \tag{29}$$

with $\delta^0_0 = 1$, $\delta^j_j = -1, j = 1,2,3$ and $\delta^{\nu}_{\mu} = 0, \mu \neq \nu$. Since these tensorial densities are defined through partial derivatives of the ϕ wave of the electron, these definitions need the wave equation that we present now.

3. Improved Dirac Wave Equation

The improvement of the Dirac equation was first presented in the frame of the Clifford algebra of space-time used by Hestenes, who considered the γ_{μ} matrices of the Dirac theory as a basis of space-time [44] [45]. Read now in Cl_3 the Lagrangian density of the Dirac equation is:

$$\mathcal{L} := \left\langle \overline{\phi}\nabla\hat{\phi}\sigma_{21} + \overline{\phi}qA\hat{\phi} \right\rangle + m\rho\cos\left(\beta\right), \tag{30}$$

where $\sigma_{21} := \sigma_2\sigma_1 = -i\sigma_3$, A is the electromagnetic potential space-time vector and $\langle X \rangle$ is the real part of X. The improved wave equation is obtained by simplifying the Lagrangian density as:

$$\mathcal{L} := \left\langle \overline{\phi}\nabla\hat{\phi}\sigma_{21} + \overline{\phi}qA\hat{\phi} \right\rangle + m\rho. \tag{31}$$

The improved equation which comes from this simplified Lagrangian density reads:

$$0 = \nabla\hat{\phi}\sigma_{21} + qA\hat{\phi} + me^{-i\beta}\phi. \tag{32}$$

This non-linear wave equation has the Dirac equation as linear approximation when the Yvon-Takabayasi β angle is null or negligible:

$$0 = \nabla \hat{\phi} \sigma_{21} + qA\hat{\phi} + m\phi. \tag{33}$$

The mass term of the improved Equation (32) comes from Lochak's theory of the magnetic monopole [46]-[53] in the particular case where the Dirac Lagrangian is the linear approximation of the simplified Lagrangian density. The first improvement of this simplification is the resolution of the problem of the negative energies, because the positron is no longer associated with non-physical negative energy (see for instance [41] 1.5.3 and 1.5.6). Another improvement is the partial decoupling of the left and right spinors, the wave equation also reads:

$$0 = \nabla \hat{\phi} \sigma_{21} + (qA + m\mathrm{v})\hat{\phi}; \; \mathrm{v} := \frac{D_0}{\rho}. \tag{34}$$

The momentum-energy of the electron $qA + m\mathrm{v}$ is the sum of an electromagnetic part qA and an inertial part $m\mathrm{v}$. Hence the improved equation may be generalized to all fermions, it is compatible with the entire gauge group of the Standard Model, $U(1) \times SU(2) \times SU(3)$, and it is also compatible with the relativistic invariance of general relativity. This is the reason for the appearance of the Christoffel symbols that we will calculate from the solutions of the improved equation in the case of the hydrogen atom.

4. Resolution in the Case of the Hydrogen Atom

The Dirac equation was solved as early as 1928 by the mathematician C. G. Darwin using the previous resolution of the non-relativistic equation for an electron with spin found by Pauli. This method used kinetic momentum operators, which is ill-suited to the resolution of a non-linear equation like (32). Fortunately another method exists, found more recently by H. Krüger [54], who discovered a very astute method of separation of variables in spherical coordinates. This uses:

$$x^1 = r\sin\theta\cos\varphi; \; x^2 = r\sin\theta\sin\varphi; \; x^3 = r\cos\theta. \tag{35}$$

We use the following notations:

$$i_1 := \sigma_{23} = i\sigma_1; \; i_2 := \sigma_{31} = i\sigma_2; \; i_3 := \sigma_{12} = i\sigma_3, \tag{36}$$

$$S := e^{-\frac{\varphi}{2}i_3} e^{-\frac{\theta}{2}i_2}; \; \Omega := \hat{\Omega} = r^{-1}(\sin\theta)^{-\frac{1}{2}} S, \tag{37}$$

$$\vec{\partial}' := \sigma_3 \partial_r + \frac{1}{r}\sigma_1 \partial_\theta + \frac{1}{r\sin\theta}\sigma_2 \partial_\varphi. \tag{38}$$

H. Krüger obtained the remarkable identity:

$$\vec{\partial} = \Omega \vec{\partial}' \Omega^{-1}, \tag{39}$$

which with:

$$\nabla' := \partial_0 - \vec{\partial}' = \partial_0 - \left(\sigma_3 \partial_r + \frac{1}{r}\sigma_1 \partial_\theta + \frac{1}{r\sin\theta}\sigma_2 \partial_\varphi\right), \tag{40}$$

gives also:

$$\Omega^{-1}\nabla = \nabla'\Omega^{-1}. \tag{41}$$

For either the Dirac equation or the improved equation, to obtain the separation of the temporal variable $x^0 = ct$ and the angular variable φ from the radial variable r and the other angular variable θ, we let:

$$\phi = \Omega X e^{\zeta i_3}; \ \zeta = \lambda\varphi - Ex^0 + \delta, \tag{42}$$

where X is a function, with value in the Pauli algebra, of only r and θ, $\hbar cE$ is the energy of the electron, and δ is an arbitrary phase that plays no role here because the wave equations are electric gauge invariant. We get:

$$\Omega^{-1}\phi = X e^{\zeta i_3}; \ \Omega^{-1}\hat{\phi} = \hat{X} e^{\zeta i_3}. \tag{43}$$

For the ρ density that satisfies (7) we also have:

$$\rho e^{i\beta} = \det(\phi) = \det(\Omega)\det(X)\det\left(e^{\zeta i_3}\right), \tag{44}$$

$$\det(\Omega) = r^{-2}(\sin\theta)^{-1}; \det\left(e^{\zeta i_3}\right) = 1; \ \rho e^{i\beta} = \frac{\det(X)}{r^2\sin\theta}. \tag{45}$$

Then if we let:

$$\rho_X e^{i\beta_X} := \det(X), \tag{46}$$

we get:

$$\rho = \frac{\rho_X}{r^2\sin\theta}; \ \beta = \beta_X. \tag{47}$$

Then the Yvon-Takabayasi angle depends neither on the time nor on the φ angle. It depends only on r and θ. Therefore the separation of variables can begin similarly for both the Dirac equation and the improved equation. We have:

$$\nabla'\Omega^{-1}\hat{\phi} = \left(\partial_0 - \sigma_3\partial_r - \frac{1}{r}\sigma_1\partial_\theta - \frac{1}{r\sin\theta}\sigma_2\partial_\varphi\right)\left[\hat{X}e^{\zeta i_3}\right], \tag{48}$$

$$\partial_0\left(\hat{X}e^{\zeta i_3}\right) = -E\hat{X}i_3 e^{\zeta i_3}; \partial_r\left(\hat{X}e^{\zeta i_3}\right) = \left(\partial_r\hat{X}\right)e^{\zeta i_3} \tag{49}$$

$$\partial_\theta\left(\hat{X}e^{\zeta i_3}\right) = \left(\partial_\theta\hat{X}\right)e^{\zeta i_3}; \partial_\varphi\left(\hat{X}e^{\zeta i_3}\right) = \lambda\hat{X}i_3 e^{\zeta i_3}. \tag{50}$$

We then get:

$$\nabla\hat{\phi} = \Omega\left(-E\hat{X}i_3 - \sigma_3\partial_r\hat{X} - \frac{1}{r}\sigma_1\partial_\theta\hat{X} - \frac{\lambda}{r\sin\theta}\sigma_2\hat{X}i_3\right)e^{\zeta i_3}. \tag{51}$$

For the hydrogen atom we have:

$$qA = qA^0 = -\frac{\alpha}{r}; \ \alpha = \frac{e^2}{\hbar c}, \tag{52}$$

where α is the fine structure constant. We have:

$$qA\hat{\phi}\sigma_{12} = -\frac{\alpha}{r}\hat{\phi}i_3 = -\frac{\alpha}{r}\Omega\hat{X}i_3 e^{\zeta i_3} = \Omega\left(-\frac{\alpha}{r}\hat{X}i_3\right)e^{\zeta i_3}. \tag{53}$$

Also the improved Equation (32) becomes:

$$-E\hat{X}i_3 - \sigma_3\partial_r\hat{X} - \frac{1}{r}\sigma_1\partial_\theta\hat{X} - \frac{\lambda}{r\sin\theta}\sigma_2\hat{X}i_3 - \frac{\alpha}{r}\hat{X}i_3 + me^{-i\beta}Xi_3 = 0. \tag{54}$$

This means:

$$\left(E+\frac{\alpha}{r}\right)\hat{X}i_3 + \sigma_3\partial_r\hat{X} + \frac{1}{r}\sigma_1\partial_\theta\hat{X} + \frac{\lambda}{r\sin\theta}\sigma_2\hat{X}i_3 = me^{-i\beta}Xi_3, \tag{55}$$

while the Dirac equation gives:

$$\left(E+\frac{\alpha}{r}\right)\hat{X}i_3 + \sigma_3\partial_r\hat{X} + \frac{1}{r}\sigma_1\partial_\theta\hat{X} + \frac{\lambda}{r\sin\theta}\sigma_2\hat{X}i_3 = mXi_3. \tag{56}$$

Now we let:

$$X := \begin{pmatrix} R_1 & -\overline{L}_2 \\ R_2 & \overline{L}_1 \end{pmatrix}; \det(X) = R_1\overline{L}_1 + R_2\overline{L}_2, \tag{57}$$

where R_1, R_2, L_1, L_2 are functions with complex values of the real variables r and θ. We get:

$$\hat{X} = \begin{pmatrix} L_1 & -\overline{R}_2 \\ L_2 & \overline{R}_1 \end{pmatrix}; X^\dagger = \begin{pmatrix} \overline{R}_1 & \overline{R}_2 \\ -L_2 & L_1 \end{pmatrix}; \overline{X} = \hat{X}^\dagger = \begin{pmatrix} \overline{L}_1 & \overline{L}_2 \\ -R_2 & R_1 \end{pmatrix}. \tag{58}$$

Therefore the improved equation reads:

$$i\left(E+\frac{\alpha}{r}\right)\begin{pmatrix} L_1 & \overline{R}_2 \\ L_2 & -\overline{R}_1 \end{pmatrix} + \begin{pmatrix} \partial_r L_1 & -\partial_r\overline{R}_2 \\ -\partial_r L_2 & -\partial_r\overline{R}_1 \end{pmatrix} + \frac{1}{r}\begin{pmatrix} \partial_\theta L_2 & \partial_\theta\overline{R}_1 \\ \partial_\theta L_1 & -\partial_\theta\overline{R}_2 \end{pmatrix}$$
$$+ \frac{\lambda}{r\sin\theta}\begin{pmatrix} L_2 & -\overline{R}_1 \\ -L_1 & -\overline{R}_2 \end{pmatrix} = ie^{-i\beta}\begin{pmatrix} mR_1 & m\overline{L}_2 \\ mR_2 & -m\overline{L}_1 \end{pmatrix}. \tag{59}$$

Conjugating the equations containing the conjugates we obtain the system:

$$i\left(E+\frac{\alpha}{r}\right)L_1 + \partial_r L_1 + \frac{1}{r}\left(\partial_\theta + \frac{\lambda}{\sin\theta}\right)L_2 = ime^{-i\beta}R_1,$$
$$-i\left(E+\frac{\alpha}{r}\right)R_2 - \partial_r R_2 + \frac{1}{r}\left(\partial_\theta - \frac{\lambda}{\sin\theta}\right)R_1 = -ime^{i\beta}L_2,$$
$$i\left(E+\frac{\alpha}{r}\right)L_2 - \partial_r L_2 + \frac{1}{r}\left(\partial_\theta - \frac{\lambda}{\sin\theta}\right)L_1 = ime^{-i\beta}R_2,$$
$$-i\left(E+\frac{\alpha}{r}\right)R_1 + \partial_r R_1 + \frac{1}{r}\left(\partial_\theta + \frac{\lambda}{\sin\theta}\right)R_2 = -ime^{i\beta}L_1. \tag{60}$$

Next we let:

$$R_1 := AU; \quad L_2 := BV; \quad R_2 := CV; \quad L_1 := DU, \tag{61}$$

where A, B, C and D are functions of r while U and V are functions of θ. The (60) system becomes:

$$i\left(E+\frac{\alpha}{r}\right)DU + D'U + \frac{1}{r}\left(V' + \frac{\lambda}{\sin\theta}V\right)B = ime^{-i\beta}AU,$$
$$-i\left(E+\frac{\alpha}{r}\right)CV - C'V + \frac{1}{r}\left(U' - \frac{\lambda}{\sin\theta}U\right)A = -ime^{i\beta}BV,$$
$$i\left(E+\frac{\alpha}{r}\right)BV - B'V + \frac{1}{r}\left(U' - \frac{\lambda}{\sin\theta}U\right)D = ime^{-i\beta}CV,$$
$$-i\left(E+\frac{\alpha}{r}\right)AU + A'U + \frac{1}{r}\left(V' + \frac{\lambda}{\sin\theta}V\right)C = -ime^{i\beta}DU. \tag{62}$$

Then using a κ constant satisfying:

$$U' - \frac{\lambda}{\sin\theta}U = -\kappa V; \ V' + \frac{\lambda}{\sin\theta}V = \kappa U, \tag{63}$$

the (62) system becomes:

$$
\begin{aligned}
i\left(E + \frac{\alpha}{r}\right)D + D' + \frac{\kappa}{r}B &= ime^{-i\beta}A \\
-i\left(E + \frac{\alpha}{r}\right)C - C' - \frac{\kappa}{r}A &= -ime^{i\beta}B \\
i\left(E + \frac{\alpha}{r}\right)B - B' - \frac{\kappa}{r}D &= ime^{-i\beta}C \\
-i\left(E + \frac{\alpha}{r}\right)A + A' + \frac{\kappa}{r}C &= -ime^{i\beta}D
\end{aligned}
\tag{64}
$$

5. Christoffel Symbols

We need to calculate $\nabla(\ln\rho)$ and the $\nabla S_k^\dagger, k = 1,2,3$ terms. We use:

$$\nabla(\ln\rho) = \frac{1}{2}\left[\frac{\nabla(\hat{\phi}\phi^\dagger)}{\hat{\phi}\phi^\dagger} + \left(\frac{\nabla(\hat{\phi}\phi^\dagger)}{\hat{\phi}\phi^\dagger}\right)^\dagger\right]; \ \mathcal{S}_{(3)} + i\mathcal{S}'_{(3)} = \frac{\nabla(\hat{\phi}\sigma_3\phi^\dagger)}{\hat{\phi}\phi^\dagger}, \tag{65}$$

$$\mathcal{S}_{(3)} = \frac{1}{2}\left[\frac{\nabla(\hat{\phi}\sigma_3\phi^\dagger)}{\hat{\phi}\phi^\dagger} + \left(\frac{\nabla(\hat{\phi}\sigma_3\phi^\dagger)}{\hat{\phi}\phi^\dagger}\right)^\dagger\right] \tag{66}$$

$$\nabla(\hat{\phi}\phi^\dagger) = \Omega\nabla'\left(\hat{X}X^\dagger\Omega^\dagger\right); \nabla\left(S_3^\dagger\right) = \Omega\nabla'\left(\hat{X}\sigma_3 X^\dagger\Omega^\dagger\right), \tag{67}$$

$$\nabla\left(S_1^\dagger \pm iS_2^\dagger\right) = \Omega\nabla'\left[\hat{X}e^{2\zeta i_3}\left(\sigma_1 \pm i\sigma_2\right)X^\dagger\Omega^\dagger\right]. \tag{68}$$

These terms have the form:

$$\Omega\nabla'\left(M\Omega^\dagger\right) = \Omega(\nabla'M)\Omega^\dagger + \Omega\underline{\nabla}'M\underline{\Omega}^\dagger, \tag{69}$$

where the underlined refers to:

$$\underline{\nabla}'M\underline{\Omega}^\dagger = M\partial_0\Omega^\dagger - \sigma_3 M\partial_r\Omega^\dagger - \sigma_1 M\frac{1}{r}\partial_\theta\Omega^\dagger - \sigma_2 M\frac{1}{r\sin\theta}\partial_\varphi\Omega^\dagger. \tag{70}$$

We let $M = \begin{pmatrix} u & v \\ w & s \end{pmatrix}$, we then get:

$$
\begin{aligned}
\underline{\nabla}'M\underline{\Omega}^\dagger &= 0 - \sigma_3 M\partial_r\Omega^\dagger - \sigma_1 M\frac{1}{r}\partial_\theta\Omega^\dagger - \sigma_2 M\frac{1}{r\sin\theta}\partial_\varphi\Omega^\dagger \\
&= r^{-2}(\sin\theta)^{-\frac{1}{2}}\begin{pmatrix} u & v \\ -w & -s \end{pmatrix}S^\dagger \\
&\quad + r^{-2}(\sin\theta)^{-\frac{1}{2}}\begin{pmatrix} -w & -s \\ -u & -v \end{pmatrix}\begin{pmatrix} -\dfrac{\cos\theta}{2\sin\theta} & \dfrac{1}{2} \\ -\dfrac{1}{2} & -\dfrac{\cos\theta}{2\sin\theta} \end{pmatrix}S^\dagger
\end{aligned}
\tag{71}
$$

490

$$+r^{-2}\left(\sin\theta\right)^{-\frac{3}{2}}\begin{pmatrix} iw & is \\ -iu & -iv \end{pmatrix}\begin{pmatrix} \cos\theta & \sin\theta \\ -\sin\theta & \cos\theta \end{pmatrix}\begin{pmatrix} \dfrac{i}{2} & 0 \\ 0 & -\dfrac{i}{2} \end{pmatrix}S^{\dagger}$$

$$=r^{-2}\left(\sin\theta\right)^{-\frac{1}{2}}\begin{pmatrix} u+s & v+s\dfrac{\cos\theta}{\sin\theta} \\ -w+u\dfrac{\cos\theta}{\sin\theta} & -(s+u) \end{pmatrix}S^{\dagger}. \tag{72}$$

If $M = \hat{X}X^{\dagger} = \hat{X}\sigma_0 X^{\dagger}$ and since:

$$\hat{X}X^{\dagger} = \det\left(X^{\dagger}\right) = \rho_X e^{-i\beta} = u = s; v = w = 0, \tag{73}$$

we get:

$$\frac{\underline{\nabla}'\hat{X}\sigma_0 X^{\dagger}\underline{\Omega}^{\dagger}}{\det\left(X^{\dagger}\right)} = \left[\frac{2}{r}\sigma_3 + \frac{\cos\theta}{r\sin\theta}\sigma_1\right]\Omega^{\dagger}; \rho = \frac{\rho_X}{r^2\sin\theta} = \frac{\left|D\overline{A}U^2 + B\overline{C}V^2\right|}{r^2\sin\theta}. \tag{74}$$

5.1. Terms with Index 0 and 3

For the σ_0 case we have:

$$\frac{\nabla\left(\rho e^{-i\beta}\right)}{\rho e^{-i\beta}} = \frac{\left(\nabla\rho\right)e^{-i\beta} - i\left(\nabla\beta\right)\rho e^{-i\beta}}{\rho e^{-i\beta}} = \nabla\left(\ln\rho\right) - i\nabla\beta$$

$$= \frac{\nabla\left(\hat{\phi}\phi^{\dagger}\right)}{\hat{\phi}\phi^{\dagger}} = \frac{\Omega\nabla'\left(\hat{X}X^{\dagger}\Omega^{\dagger}\right)}{\Omega\hat{X}X^{\dagger}\Omega^{\dagger}} = \frac{\Omega\nabla'\left(\hat{X}X^{\dagger}\right)\Omega^{\dagger} + \Omega\underline{\nabla}'\hat{X}X^{\dagger}\underline{\Omega}}{\hat{X}X^{\dagger}\Omega\Omega^{\dagger}} \tag{75}$$

$$= S\frac{\nabla'\left(\hat{X}X^{\dagger}\right)}{\hat{X}X^{\dagger}}S^{\dagger} + S\left[\frac{2}{r}\sigma_3 + \frac{\cos\theta}{r\sin\theta}\sigma_1\right]S^{\dagger}.$$

Next we have:

$$\nabla'\left(\hat{X}X^{\dagger}\right) = -\left(\sigma_3\partial_r + \sigma_1\frac{1}{r}\partial_\theta\right)\left(D\overline{A}U^2 + B\overline{C}V^2\right)$$

$$= -\left(D'\overline{A}U^2 + D\overline{A}'U^2 + B'\overline{C}V^2 + B\overline{C}'V^2\right)\sigma_3 \tag{76}$$

$$-\frac{2}{r}\left(D\overline{A}UU' + B\overline{C}VV'\right)\sigma_1$$

Using (63) and (64) we obtain:

$$\overline{A}' = -i\left(E+\frac{\alpha}{r}\right)\overline{A} - \frac{\kappa}{r}\overline{C} + ime^{-i\beta}\overline{D},$$

$$B' = i\left(E+\frac{\alpha}{r}\right)B - \frac{\kappa}{r}D - ime^{-i\beta}C,$$

$$\overline{C}' = i\left(E+\frac{\alpha}{r}\right)\overline{C} - \frac{\kappa}{r}\overline{A} - ime^{-i\beta}\overline{B} \tag{77}$$

$$D' = -i\left(E+\frac{\alpha}{r}\right)D - \frac{\kappa}{r}B + ime^{-i\beta}A,$$

$$U' = \frac{\lambda}{\sin\theta}U - \kappa V; V' = -\frac{\lambda}{\sin\theta}V + \kappa U. \tag{78}$$

We let:

$$r_1 := \frac{\left(B\bar{B} + C\bar{C}\right)V^2 - \left(A\bar{A} + D\bar{D}\right)U^2}{\left|\det\left(X^\dagger\right)\right|}; \quad p_1 + ip_2 := \frac{\left(D\bar{A} - B\bar{C}\right)UV}{\det\left(X^\dagger\right)} \tag{79}$$

$$q_1 + iq_2 := \frac{\left(D\bar{C} + B\bar{A}\right)\left(U^2 + V^2\right)}{\det\left(X^\dagger\right)}; \quad s_1 + is_2 := \frac{D\bar{A}U^2 - B\bar{C}V^2}{\det\left(X^\dagger\right)}.$$

These functions $r_1, p_1, p_2, q_1, q_2, s_1, s_2$ depend on r and θ, with values in $\mathbb{R}$. We get:

$$\frac{\nabla'\left(\hat{X}X^\dagger\right)}{\hat{X}X^\dagger} = \left[-2i\left(E + \frac{\alpha}{r}\right)\left(s_1 + is_2\right) + \frac{\kappa}{r}\left(q_1 + iq_2\right) + imr_1\right]\sigma_3$$
$$+ \left[-\frac{2\lambda}{r\sin\theta}\left(s_1 + is_2\right) + \frac{2\kappa}{r}\left(p_1 + ip_2\right)\right]\sigma_1. \tag{80}$$

We then get:

$$S^\dagger\left[\nabla\left(\ln\rho\right) - i\nabla\beta\right]S = \left[-\frac{2\lambda}{r\sin\theta}\left(s_1 + is_2\right) + \frac{2\kappa}{r}\left(p_1 + ip_2\right) + \frac{\cos\theta}{r\sin\theta}\right]\sigma_1$$
$$+ \left[2i\left(E + \frac{\alpha}{r}\right)\left(s_1 + is_2\right) + \frac{\kappa}{r}\left(q_1 + iq_2\right) + imr_1 + \frac{2}{r}\right]\sigma_3. \tag{81}$$

This gives:

$$\nabla\left(\ln\rho\right) = S\left[\left(-\frac{2\lambda}{r\sin\theta}s_1 + \frac{2\kappa}{r}p_1 + \frac{\cos\theta}{r\sin\theta}\right)\sigma_1 + \left(\frac{\kappa}{r}q_1 + \frac{2}{r}\right)\sigma_3\right]S^\dagger \tag{82}$$

$$\nabla\left[\ln\left(\rho\right)\right] = S\vec{\mathbf{K}}_0 S^\dagger; \quad \mathbf{K}_0 := \mathbf{K}_0^\mu \sigma_\mu; \quad \mathbf{K}_0^0 = 0, \tag{83}$$

$$\mathbf{K}_0^2 = 0; \quad \mathbf{K}_0^1 = \frac{\cos\theta - 2\lambda s_1}{r\sin\theta} + \frac{2\kappa}{r}p_1; \quad \mathbf{K}_0^3 = \frac{2}{r} + \frac{\kappa}{r}q_1 - 2\left(E + \frac{\alpha}{r}\right)s_2. \tag{84}$$

We let:

$$r_2 := \frac{\left(A\bar{A} + D\bar{D}\right)U^2 + \left(B\bar{B} + C\bar{C}\right)V^2}{\left|\det\left(X^\dagger\right)\right|}; \quad r_3 := \frac{\Re\left(D\bar{B} - A\bar{C}\right)UV}{\left|\det\left(X^\dagger\right)\right|},$$

$$r_4 := \frac{\Im\left(B\bar{D} - C\bar{A}\right)UV}{\left|\det\left(X^\dagger\right)\right|}; \quad v_1 + iv_2 := \frac{\left(D\bar{C} - B\bar{A}\right)\left(U^2 - V^2\right)}{\det\left(X^\dagger\right)}, \tag{84}$$

$$t_1 + it_2 := \frac{\left(D\bar{C} - B\bar{A}\right)UV}{\det\left(X^\dagger\right)}; \quad u_1 + iu_2 := \frac{\left(D\bar{C} + B\bar{A}\right)UV}{\det\left(X^\dagger\right)}$$

where $r_2, r_3, r_4, v_1, v_2, t_1, t_2, u_1, u_2$ depend on r and θ, with values in $\mathbb{R}$. The σ_3 case gives:

$$M := \hat{X}\sigma_3 X^\dagger = \begin{pmatrix} L_1\bar{R}_1 - L_2\bar{R}_2 & 2L_1\bar{R}_2 \\ 2L_2\bar{R}_1 & -L_1\bar{R}_1 + L_2\bar{R}_2 \end{pmatrix}, \tag{85}$$

$$u = L_1\bar{R}_1 - L_2\bar{R}_2; \quad v = 2L_1\bar{R}_2; \quad w = 2L_2\bar{R}_1; \quad s = -u, \tag{86}$$

Using (72) we get:

$$\underline{\nabla}' M \underline{\Omega}^\dagger = r^{-2} \left(\sin\theta\right)^{-\frac{1}{2}} \begin{pmatrix} 0 & v - u\dfrac{\cos\theta}{\sin\theta} \\ -w + u\dfrac{\cos\theta}{\sin\theta} & 0 \end{pmatrix} S^\dagger$$

$$\frac{\Omega \underline{\nabla}' M \underline{\Omega}^\dagger}{\det\left(\phi^\dagger\right)} = S \frac{1}{r} \left[\begin{array}{c} +\dfrac{L_1 \overline{R}_2 - L_2 \overline{R}_1}{L_1 \overline{R}_1 + L_2 \overline{R}_2}\sigma_1 \\[2mm] +\dfrac{L_1 \overline{R}_2 + L_2 \overline{R}_1}{L_1 \overline{R}_1 + L_2 \overline{R}_2} i\sigma_2 + \dfrac{L_2 \overline{R}_2 - L_1 \overline{R}_1}{L_1 \overline{R}_1 + L_2 \overline{R}_2}\dfrac{\cos\theta}{\sin\theta}i\sigma_2 \end{array} \right] S^\dagger \tag{87}$$

$$= S \frac{1}{r}\left[\left(t_1 + it_2\right)\sigma_1 + \left(u_1 + iu_2\right)i\sigma_2 - \left(s_1 + is_2\right)\frac{\cos\theta}{\sin\theta}i\sigma_2 \right] S^\dagger.$$

Next we have the following, with the radial and angular functions previously defined in (61):

$$\nabla'\left[\hat{X}\sigma_3 X^\dagger\right] = \begin{pmatrix} -\partial_r & -\dfrac{1}{r}\partial_\theta \\ -\dfrac{1}{r}\partial_\theta & \partial_r \end{pmatrix} \begin{pmatrix} D\overline{A}U^2 - B\overline{C}V^2 & 2D\overline{C}UV \\ 2B\overline{A}UV & B\overline{C}V^2 - D\overline{A}U^2 \end{pmatrix}$$

$$= \left[-\left(D\overline{A}\right)' U^2 + \left(B\overline{C}\right)' V^2 - \frac{2}{r}B\overline{A}\left(UV\right)' \right]\frac{1+\sigma_3}{2}$$

$$+ \left[-\left(D\overline{A}\right)' U^2 + \left(B\overline{C}\right)' V^2 - \frac{2}{r}D\overline{C}\left(UV\right)' \right]\frac{1-\sigma_3}{2} \tag{88}$$

$$+ \left[-\frac{D\overline{A}}{r}UU' + \frac{B\overline{C}}{r}VV' + \left(B\overline{A}\right)' UV \right]\left(\sigma_1 - i\sigma_2\right)$$

$$+ \left[+\frac{D\overline{A}}{r}UU' - \frac{B\overline{C}}{r}VV' - \left(D\overline{C}\right)' UV \right]\left(\sigma_1 + i\sigma_2\right).$$

$$\nabla'\left(\hat{X}\sigma_3 X^\dagger\right) = -\left(D\overline{A}\right)' U^2 + \left(B\overline{C}\right)' V^2 - \frac{B\overline{A} + D\overline{C}}{r}\left(UV\right)'$$

$$+ \frac{1}{r}\left(D\overline{C} - B\overline{A}\right)\left(UV\right)'\sigma_3 + \left(B\overline{A} - D\overline{C}\right)' UV \sigma_1 \tag{89}$$

$$+ \left[\frac{2}{r}\left(D\overline{A}UU' - B\overline{C}VV'\right) - \left(B\overline{A} + D\overline{C}\right)' UV \right]i\sigma_2.$$

And we get, using (77) and (78):

$$\frac{\nabla'\left(\hat{X}\sigma_3 X^\dagger\right)}{\hat{X}X^\dagger} = 2i\left(E + \frac{\alpha}{r}\right) - imr_2 + \frac{\kappa}{r}\left(v_1 + iv_2\right)\sigma_3 + 2mr_3\sigma_2$$

$$+ \left(\frac{2\lambda}{r\sin\theta} + 2mr_4\right)i\sigma_2. \tag{90}$$

We then get:

$$S^\dagger \frac{\nabla\left(\hat{\phi}\sigma_3\phi^\dagger\right)}{\det\left(\phi^\dagger\right)} S = 2i\left(E + \frac{\alpha}{r}\right) - imr_2 + \frac{t_1 + it_2}{r}\sigma_1 + 2mr_3\sigma_2$$

$$+ \left[2imr_4 + \frac{2i\lambda}{r\sin\theta} + \frac{iu_1 - u_2}{r} + \frac{\left(s_2 - is_1\right)\cos\theta}{r\sin\theta} \right]\sigma_2 \tag{91}$$

$$+ \frac{\kappa}{r}\left(v_1 + iv_2\right)\sigma_3,$$

$$\mathcal{S}_{(3)} = \frac{1}{2}\left[\frac{\nabla\left(\hat{\phi}\sigma_3\phi^\dagger\right)}{\det\left(\phi^\dagger\right)} + \left(\frac{\nabla\left(\hat{\phi}\sigma_3\phi^\dagger\right)}{\det\left(\phi^\dagger\right)}\right)^\dagger\right] = S\mathbf{K}_3 S^\dagger$$

$$= S\left[\frac{t_1}{r}\sigma_1 + \left(-\frac{u_2}{r} + \frac{s_2\cos\theta}{r\sin\theta}\right)\sigma_2 + \frac{\kappa}{r}v_1\sigma_3\right]S^\dagger \tag{92}$$

$$\mathbf{K}_3^0 = 0; \mathbf{K}_3^1 = \frac{t_1}{r}; \mathbf{K}_3^2 = 2mr_3 - \frac{u_2}{r} + \frac{s_2}{r}\frac{\cos\theta}{\sin\theta}; \mathbf{K}_3^3 = \frac{\kappa}{r}v_1. \tag{93}$$

5.2. Calculation of the Currents

We have:

$$D_\mu = \phi\sigma_\mu\phi^\dagger = \Omega X e^{\zeta i_3}\sigma_\mu e^{-\zeta i_3}X^\dagger\Omega^\dagger = S\frac{X e^{\zeta i_3}\sigma_\mu e^{-\zeta i_3}X^\dagger}{r^2\sin\theta}S^\dagger. \tag{94}$$

We then let, for any space-time vector $\mathcal{V}$:

$$\mathbf{V} := S^\dagger\mathcal{V}S; \mathrm{d}_\mu := X e^{\zeta i_3}\sigma_\mu e^{-\zeta i_3}X^\dagger. \tag{95}$$

We then have:

$$2D_\mu \cdot \mathcal{V} = D_\mu\hat{\mathcal{V}} + \mathcal{V}\hat{D}_\mu = S\mathrm{d}_\mu S^\dagger S\hat{\mathbf{V}}S^\dagger + S\mathbf{V}S^\dagger S\hat{\mathrm{d}}_\mu S^\dagger$$

$$= S\left(\mathrm{d}_\mu\hat{\mathbf{V}} + \mathbf{V}\hat{\mathrm{d}}_\mu\right)S^\dagger = S\left(2\mathrm{d}_\mu \cdot \mathbf{V}\right)S^\dagger = 2\mathrm{d}_\mu \cdot \mathbf{V}SS^\dagger = 2\mathrm{d}_\mu \cdot \mathbf{V}. \tag{96}$$

This allows us a simplification of the scalar product. We get:

$$\mathrm{d}_0 = XX^\dagger = \begin{pmatrix} R_1\bar{R}_1 + L_2\bar{L}_2 & R_1\bar{R}_2 - L_1\bar{L}_2 \\ R_2\bar{R}_1 - L_2\bar{L}_1 & L_1\bar{L}_1 + R_2\bar{R}_2 \end{pmatrix}, \tag{97}$$

$$\mathrm{d}_0^0 + \mathrm{d}_0^3 = R_1\bar{R}_1 + L_2\bar{L}_2; \mathrm{d}_0^1 - i\mathrm{d}_0^2 = R_1\bar{R}_2 - L_1\bar{L}_2, \tag{98}$$

$$\mathrm{d}_0^0 - \mathrm{d}_0^3 = L_1\bar{L}_1 + R_2\bar{R}_2; \mathrm{d}_0^1 + i\mathrm{d}_0^2 = R_2\bar{R}_1 - L_2\bar{L}_1. \tag{99}$$

Similarly we have:

$$\mathrm{d}_3 = X\sigma_3 X^\dagger = \begin{pmatrix} R_1\bar{R}_1 - L_2\bar{L}_2 & R_1\bar{R}_2 + L_1\bar{L}_2 \\ R_2\bar{R}_1 + L_2\bar{L}_1 & -L_1\bar{L}_1 + R_2\bar{R}_2 \end{pmatrix}, \tag{100}$$

$$\mathrm{d}_3^0 + \mathrm{d}_3^3 = R_1\bar{R}_1 - L_2\bar{L}_2; \mathrm{d}_3^1 - i\mathrm{d}_3^2 = R_1\bar{R}_2 + L_1\bar{L}_2, \tag{101}$$

$$\mathrm{d}_3^0 - \mathrm{d}_3^3 = -L_1\bar{L}_1 + R_2\bar{R}_2; \mathrm{d}_3^1 + i\mathrm{d}_3^2 = R_2\bar{R}_1 + L_2\bar{L}_1. \tag{102}$$

Sum and difference of d_0 and d_3 are simple, which will be useful. We get:

$$\mathrm{d}_0 + \mathrm{d}_3 = X\left(1+\sigma_3\right)X^\dagger = 2\begin{pmatrix} R_1\bar{R}_1 & R_1\bar{R}_2 \\ R_2\bar{R}_1 & R_2\bar{R}_2 \end{pmatrix}, \tag{103}$$

$$\mathrm{d}_0 - \mathrm{d}_3 = X\left(1-\sigma_3\right)X^\dagger = 2\begin{pmatrix} L_2\bar{L}_2 & -L_1\bar{L}_2 \\ -L_2\bar{L}_1 & L_1\bar{L}_1 \end{pmatrix}. \tag{104}$$

Next we have:

$$\mathrm{d}_1 + i\mathrm{d}_2 = X e^{2\zeta i_3}\left(\sigma_1 + i\sigma_2\right)X^\dagger = 2e^{2i\zeta}\begin{pmatrix} -R_1L_2 & R_1L_1 \\ -R_2L_2 & R_2L_1 \end{pmatrix}, \tag{105}$$

$$d_1 - id_2 = X e^{2\zeta i_3} \left(\sigma_1 - i\sigma_2 \right) X^{\dagger} = 2e^{-2i\zeta} \begin{pmatrix} \overline{L}_2 \overline{R}_1 & -\overline{L}_2 \overline{R}_2 \\ \overline{L}_1 \overline{R}_1 & \overline{L}_1 \overline{R}_2 \end{pmatrix}. \tag{106}$$

5.3. Calculation of 12 Christoffel Symbols

We have:

$$\Gamma^0_{0\mu} = D_\mu \cdot \nabla \left(\ln \rho \right) = d_\mu \cdot \mathbf{K}_0 ; \Gamma^0_{3\mu} = D_\mu \cdot \mathcal{S}_{(3)} = d_\mu \cdot \mathbf{K}_3. \tag{107}$$

We also get the symbols:

$$\begin{aligned}
\Gamma^0_{30} + \Gamma^0_{33} &= -\left(d^1_0 + d^1_3 \right) \mathbf{K}^1_3 - \left(d^2_0 + d^2_3 \right) \mathbf{K}^2_3 - \left(d^3_0 + d^3_3 \right) \mathbf{K}^3_3 \\
&= -\left(R_1 \overline{R}_2 + R_2 \overline{R}_1 \right) \mathbf{K}^1_3 - 2\Im \left(R_1 \overline{R}_2 \right) \mathbf{K}^2_3 - \left(R_1 \overline{R}_1 - R_2 \overline{R}_2 \right) \mathbf{K}^3_3,
\end{aligned} \tag{108}$$

$$\begin{aligned}
\Gamma^0_{30} - \Gamma^0_{33} &= -\left(d^1_0 - d^1_3 \right) \mathbf{K}^1_3 - \left(d^2_0 - d^2_3 \right) \mathbf{K}^2_3 - \left(d^3_0 - d^3_3 \right) \mathbf{K}^3_3 \\
&= \left(L_1 \overline{L}_2 + L_2 \overline{L}_1 \right) \mathbf{K}^1_3 + 2\Im \left(L_2 \overline{L}_1 \right) \mathbf{K}^2_3 + \left(L_1 \overline{L}_1 - L_2 \overline{L}_2 \right) \mathbf{K}^3_3
\end{aligned} \tag{109}$$

$$\begin{aligned}
\Gamma^0_{31} + i\Gamma^0_{32} &= -\left(d^1_1 + id^1_2 \right) \mathbf{K}^1_3 - \left(d^2_1 + id^2_2 \right) \mathbf{K}^2_3 - \left(d^3_1 + id^3_2 \right) \mathbf{K}^3_3 \\
&= -e^{2i\zeta} \left(R_1 L_1 - R_2 L_2 \right) \mathbf{K}^1_3 + ie^{2i\zeta} \left(R_1 L_1 + R_2 L_2 \right) \mathbf{K}^2_3 \\
&\quad + e^{2i\zeta} \left(R_1 L_2 - R_2 L_1 \right) \mathbf{K}^3_3.
\end{aligned} \tag{110}$$

We obtain also:

$$\begin{aligned}
\mathbf{K}'_3 &= S^{\dagger} \left(\mathcal{S}'_{(3)} + 2qA \right) S = \frac{S^{\dagger}}{2i} \left[\frac{\nabla \left(\hat{\phi} \sigma_3 \phi^{\dagger} \right)}{\det \left(\phi^{\dagger} \right)} - \left(\frac{\nabla \left(\hat{\phi} \sigma_3 \phi^{\dagger} \right)}{\det \left(\phi^{\dagger} \right)} \right)^{\dagger} - 2i\frac{\alpha}{r} \right] S \\
&= 2E - mr_2 + \left(2mr_3 + \frac{t_2}{r} \right) \sigma_1 + \left(2mr_4 + \frac{2\lambda - s_1 \cos\theta}{r\sin\theta} + \frac{u_1}{r} \right) \sigma_2 + \frac{\kappa}{r} v_2 \sigma_3
\end{aligned} \tag{111}$$

$$\mathbf{K}'^0_3 = 2E - mr_2 ; \mathbf{K}'^1_3 = 2mr_3 + \frac{t_2}{r} \tag{112}$$

$$\mathbf{K}'^2_3 = 2mr_4 + \frac{2\lambda}{r\sin\theta} + \frac{u_1}{r} - \frac{s_1}{r} \frac{\cos\theta}{\sin\theta} ; \mathbf{K}'^3_3 = \frac{\kappa}{r} v_2. \tag{113}$$

We then get from (15):

$$\Gamma^1_{2\mu} = -2m\rho\delta^0_\mu - d_\mu \cdot \mathbf{K}'_3, \tag{113}$$

$$\begin{aligned}
\Gamma^1_{20} &= -2m\rho - d_0 \cdot \mathbf{K}'_3 \\
&= -2m\rho - \frac{1}{2} \left(R_1 \overline{R}_1 + R_2 \overline{R}_2 + L_1 \overline{L}_1 + L_2 \overline{L}_2 \right) \mathbf{K}'^0_3 \\
&\quad + \Re \left(R_1 \overline{R}_2 - L_1 \overline{L}_2 \right) \mathbf{K}'^1_3 + \Im \left(R_1 \overline{R}_2 + L_1 \overline{L}_2 \right) \mathbf{K}'^2_3 \\
&\quad + \frac{1}{2} \left(R_1 \overline{R}_1 - R_2 \overline{R}_2 - L_1 \overline{L}_1 + L_2 \overline{L}_2 \right) \mathbf{K}'^3_3,
\end{aligned} \tag{114}$$

$$\begin{aligned}
\Gamma^1_{23} &= -d_3 \cdot \mathbf{K}'_3 = -\frac{1}{2} \left(R_1 \overline{R}_1 - R_2 \overline{R}_2 - L_1 \overline{L}_1 + L_2 \overline{L}_2 \right) \mathbf{K}'^0_3 \\
&\quad + \Re \left(R_1 \overline{R}_2 + L_1 \overline{L}_2 \right) \mathbf{K}'^1_3 + \Im \left(R_1 \overline{R}_2 + L_1 \overline{L}_2 \right) \mathbf{K}'^2_3 \\
&\quad + \frac{1}{2} \left(R_1 \overline{R}_1 - R_2 \overline{R}_2 - L_1 \overline{L}_1 + L_2 \overline{L}_2 \right) \mathbf{K}'^0_3,
\end{aligned}$$

$$\Gamma_{21}^1 + i\Gamma_{22}^1 = -\left(d_1 \cdot \mathbf{K}_3' + id_2 \cdot \mathbf{K}_3'\right)$$
$$= e^{2i\zeta}\left(-R_1 L_2 + R_2 L_1\right)\mathbf{K}_3'^0 + e^{2i\zeta}\left(R_1 L_1 - R_2 L_2\right)\mathbf{K}_3'^1 \qquad (115)$$
$$- ie^{2i\zeta}\left(R_1 L_1 + R_2 L_2\right)\mathbf{K}_3'^2 + e^{2i\zeta}\left(-R_1 L_2 - R_2 L_1\right)\mathbf{K}_3'^3.$$

5.4. Terms with Index 1 and 2

Now we consider:

$$M^+ := \hat{X}e^{2\zeta i_3}\left(\sigma_1 + i\sigma_2\right)X^\dagger; M^- := \hat{X}e^{2\zeta i_3}\left(\sigma_1 - i\sigma_2\right)X^\dagger, \qquad (116)$$

This gives:

$$\underline{\nabla}'M^+\underline{\Omega}^\dagger = \frac{e^{2i\zeta}}{r^2\sqrt{\sin\theta}}\left[\left(L_1^2 + L_2^2\right)\sigma_1 + i\left(L_1^2 - L_2^2 + 2L_1 L_2\frac{\cos\theta}{\sin\theta}\right)\sigma_2\right]S^\dagger \qquad (117)$$

$$\underline{\nabla}'M^-\underline{\Omega}^\dagger = \frac{e^{-2i\zeta}}{r^2\sqrt{\sin\theta}}\left[-\left(\overline{R}_1^2 + \overline{R}_2^2\right)\sigma_1 + i\left(\overline{R}_1^2 - \overline{R}_2^2 + 2\overline{R}_1\overline{R}_2\frac{\cos\theta}{\sin\theta}\right)\sigma_2\right]S^\dagger. \qquad (118)$$

Then we have:

$$\frac{\nabla\left[\hat{\phi}\left(\sigma_1 + i\sigma_2\right)\phi^\dagger\right]}{\hat{\phi}\phi^\dagger} = \frac{\Omega\nabla'\left[\hat{X}e^{\zeta i_3}\left(\sigma_1 + i\sigma_2\right)e^{-\zeta i_3}X^\dagger\Omega^\dagger\right]}{\Omega\hat{X}X^\dagger\Omega^\dagger}$$

$$= \frac{\Omega\nabla'\left[\hat{X}e^{2\zeta i_3}\left(\sigma_1 + i\sigma_2\right)X^\dagger\right]\Omega^\dagger}{\Omega\hat{X}X^\dagger\Omega^\dagger} + \frac{\Omega\underline{\nabla}'\hat{X}e^{2\zeta i_3}\left(\sigma_1 + i\sigma_2 X^\dagger\right)\underline{\Omega}^\dagger}{\Omega\hat{X}X^\dagger\Omega^\dagger}$$

$$= S\left[\frac{\nabla'\left[\hat{X}e^{2\zeta i_3}\left(\sigma_1 + i\sigma_2\right)X^\dagger\right]}{\hat{X}X^\dagger}\right. \qquad (119)$$

$$\left. + \frac{2e^{2i\zeta}\frac{1}{r}\left[\left(L_1^2 + L_2^2\right)\sigma_1 + \left(L_1^2 - L_2^2 + 2L_1 L_2\frac{\cos\theta}{\sin\theta}\right)i\sigma_2\right]}{\hat{X}X^\dagger}\right]S^\dagger.$$

So we get:

$$\frac{\nabla\left(S_1^\dagger + iS_2^\dagger\right) + 2iqA\left(S_1^\dagger + iS_2^\dagger\right)}{\det\left(\phi^\dagger\right)} = \frac{\nabla\left[\hat{\phi}\left(\sigma_1 + i\sigma_2\right)\phi^\dagger\right] + 2iqA\hat{\phi}\left(\sigma_1 + i\sigma_2\right)\phi^\dagger}{\hat{\phi}\phi^\dagger}$$

$$= S\left[\frac{\nabla'M^+ - 2i\frac{\alpha}{r}M^+}{\hat{X}X^\dagger} + \frac{2e^{2i\zeta}\frac{1}{r}\left[\left(L_1^2 + L_2^2\right)\sigma_1 + \left(L_1^2 - L_2^2 + 2L_1 L_2\frac{\cos\theta}{\sin\theta}\right)i\sigma_2\right]}{\hat{X}X^\dagger}\right]S^\dagger. \qquad (120)$$

We calculate now:

$$\nabla'M^+ + 2iqAM^+$$

$$= \left(\partial_0 - \sigma_3\partial_r - \sigma_1\frac{1}{r}\partial_\theta - \sigma_2\frac{1}{r\sin\theta}\partial_\varphi\right)\left[\hat{X}e^{2\zeta i_3}\left(\sigma_1 + i\sigma_2\right)X^\dagger\right] - 2i\frac{\alpha}{r}M^+ \qquad (121)$$

$$= \begin{pmatrix}\mathcal{A} & \mathcal{C} \\ \mathcal{B} & \mathcal{D}\end{pmatrix} - 4i\frac{\alpha}{r}e^{2i\zeta}\begin{pmatrix}-BDUV & D^2U^2 \\ -B^2V^2 & BDUV\end{pmatrix}$$

$$\mathcal{A} = \left(\partial_0 - \partial_r\right)\left(-2e^{2i\zeta} DBUV\right) + \left(-\frac{1}{r}\partial_\theta + \frac{i}{r\sin\theta}\partial_\varphi\right)\left(-2e^{2i\zeta} B^2V^2\right), \quad (122)$$

$$\mathcal{B} = \left(\partial_0 + \partial_r\right)\left(-2e^{2i\zeta} B^2V^2\right) + \left(-\frac{1}{r}\partial_\theta + \frac{i}{r\sin\theta}\partial_\varphi\right)\left(-2e^{2i\zeta} DBUV\right), \quad (123)$$

$$\mathcal{C} = \left(\partial_0 - \partial_r\right)\left(2e^{2i\zeta} D^2U^2\right) + \left(-\frac{1}{r}\partial_\theta + \frac{i}{r\sin\theta}\partial_\varphi\right)\left(2e^{2i\zeta} DBUV\right), \quad (124)$$

$$\mathcal{D} = \left(\partial_0 + \partial_r\right)\left(2e^{2i\zeta} DBUV\right) + \left(-\frac{1}{r}\partial_\theta - \frac{i}{r\sin\theta}\partial_\varphi\right)\left(2e^{2i\zeta} D^2U^2\right). \quad (125)$$

This gives:

$$\frac{\nabla\left[\hat{\phi}(\sigma_1 + i\sigma_2)\phi^\dagger\right]}{\det(\phi^\dagger)} + 2iqA\frac{\hat{\phi}(\sigma_1 + i\sigma_2)\phi^\dagger}{\det(\phi^\dagger)} = S\begin{pmatrix} \mathcal{A}' & \mathcal{C}' \\ \mathcal{B}' & \mathcal{D}' \end{pmatrix}S^\dagger \quad (126)$$

$$\mathcal{A}' = \frac{2e^{2i\zeta} UV}{\det(X^\dagger)}\begin{bmatrix} 2i\left(E + \dfrac{\alpha}{r}\right)DB + ime^{-i\beta}\left(AB - CD\right) \\ + \dfrac{\kappa}{r}\left(B^2 - D^2\right) \end{bmatrix}, \quad (127)$$

$$\mathcal{D}' = \frac{2e^{2i\zeta} UV}{\det(X^\dagger)}\begin{bmatrix} -2i\left(E + \dfrac{\alpha}{r}\right)DB + ime^{-i\beta}\left(AB - CD\right) \\ - \dfrac{\kappa}{r}\left(B^2 - D^2\right) \end{bmatrix}, \quad (128)$$

$$\mathcal{B}' = \frac{2e^{2i\zeta}}{\det(X^\dagger)}\begin{bmatrix} \dfrac{B^2V^2}{r} + 2ime^{-i\beta} BCV^2 + \dfrac{\kappa}{r}BD\left(U^2 + V^2\right) \\ - \dfrac{2\lambda + \cos\theta}{r\sin\theta}BDUV \end{bmatrix}, \quad (129)$$

$$\mathcal{C}' = \frac{2e^{2i\zeta}}{\det(X^\dagger)}\begin{bmatrix} \dfrac{D^2U^2}{r} - 2ime^{-i\beta} ADU^2 + \dfrac{\kappa}{r}BD\left(U^2 + V^2\right) \\ - \dfrac{2\lambda - \cos\theta}{r\sin\theta}BDUV \end{bmatrix}. \quad (130)$$

Similarly we have:

$$\frac{\nabla\left[\hat{\phi}(\sigma_1 - i\sigma_2)\phi^\dagger\right]}{\hat{\phi}\phi^\dagger} = S\left[\frac{\nabla'\left[\hat{X}e^{2\zeta i_3}(\sigma_1 - i\sigma_2)X^\dagger\right]}{\hat{X}X^\dagger}\right.$$

$$\left. + \frac{e^{-2i\zeta}\left[-\left(\bar{R}_1^2 + \bar{R}_2^2\right)\sigma_1 + i\left(\bar{R}_1^2 - \bar{R}_2^2 + 2\bar{R}_1\bar{R}_2\dfrac{\cos\theta}{\sin\theta}\right)\sigma_2\right]}{\hat{X}X^\dagger}\right]S^\dagger. \quad (131)$$

We calculate now:

$$\nabla'M^- - 2iqAM^- = \begin{pmatrix} \mathcal{A}_- & \mathcal{C}_- \\ \mathcal{B}_- & \mathcal{D}_- \end{pmatrix} + 4i\frac{\alpha}{r}e^{-2i\zeta}\begin{pmatrix} -\bar{A}\bar{C}UV & -\bar{C}^2U^2 \\ \bar{A}^2V^2 & \bar{A}\bar{C}UV \end{pmatrix} \quad (132)$$

$$\mathcal{A}_- = \left(\partial_0 - \partial_r\right)\left(-2e^{-2i\zeta}\,\overline{A}\overline{C}UV\right) - \left(\frac{1}{r}\partial_\theta - \frac{i}{r\sin\theta}\partial_\varphi\right)\left(2e^{-2i\zeta}\,\overline{A}^2U^2\right), \quad (133)$$

$$\mathcal{B}_- = \left(\partial_0 + \partial_r\right)\left(2e^{-2i\zeta}\,\overline{A}^2U^2\right) + \left(\frac{1}{r}\partial_\theta + \frac{i}{r\sin\theta}\partial_\varphi\right)\left(2e^{-2i\zeta}\,\overline{A}\overline{C}UV\right), \quad (134)$$

$$\mathcal{C}_- = \left(\partial_0 - \partial_r\right)\left(-2e^{-2i\zeta}\,\overline{C}^2V^2\right) + \left(-\frac{1}{r}\partial_\theta + \frac{i}{r\sin\theta}\partial_\varphi\right)\left(2e^{-2i\zeta}\,\overline{A}\overline{C}UV\right), \quad (135)$$

$$\mathcal{D}_- = \left(\partial_0 + \partial_r\right)\left(2e^{-2i\zeta}\,\overline{A}\overline{C}UV\right) + \left(\frac{1}{r}\partial_\theta + \frac{i}{r\sin\theta}\partial_\varphi\right)\left(2e^{-2i\zeta}\,\overline{C}^2V^2\right). \quad (136)$$

This gives:

$$\frac{\nabla\left[\hat{\phi}(\sigma_1 - i\sigma_2)\phi^\dagger\right]}{\det(\phi^\dagger)} - 2iqA\frac{\hat{\phi}(\sigma_1 - i\sigma_2)\phi^\dagger}{\det(\phi^\dagger)} = S\begin{pmatrix}\mathcal{A}'_- & \mathcal{C}'_- \\ \mathcal{B}'_- & \mathcal{D}'_-\end{pmatrix}S^\dagger \quad (137)$$

$$\mathcal{A}'_- = \frac{2e^{-2i\zeta}UV}{\det(X^\dagger)}\begin{bmatrix}-2i\left(E + \frac{\alpha}{r}\right)\overline{A}\overline{C} + ime^{-i\beta}\left(\overline{D}\overline{C} - \overline{A}\overline{B}\right) \\ \\ \frac{\kappa}{r}\left(\overline{A}^2 - \overline{C}^2\right)\end{bmatrix}, \quad (138)$$

$$\mathcal{D}'_- = \frac{2e^{2i\zeta}UV}{\det(X^\dagger)}\begin{bmatrix}2i\left(E + \frac{\alpha}{r}\right)\overline{A}\overline{C} - \frac{\kappa}{r}\left(\overline{A}^2 - \overline{C}^2\right) \\ \\ +ime^{-i\beta}\left(\overline{D}\overline{C} - \overline{A}\overline{B}\right)\end{bmatrix}, \quad (139)$$

$$\mathcal{B}'_- = \frac{2e^{-2i\zeta}}{\det(X^\dagger)}\begin{bmatrix}-\frac{\kappa}{r}\overline{A}\overline{C}\left(U^2 + V^2\right) + 2ime^{-i\beta}\overline{D}\overline{A}U^2 \\ \\ -\frac{\overline{A}^2U^2}{r} + \frac{2\lambda - \cos\theta}{r\sin\theta}\overline{A}\overline{C}UV\end{bmatrix}, \quad (140)$$

$$\mathcal{C}'_- = \frac{2e^{-2i\zeta}}{\det(X^\dagger)}\begin{bmatrix}-\frac{\kappa}{r}\overline{A}\overline{C}\left(U^2 + V^2\right) + 2ime^{-i\beta}\overline{B}\overline{C}V^2 \\ \\ -\frac{\overline{C}^2V^2}{r} + \frac{2\lambda + \cos\theta}{r\sin\theta}\overline{A}\overline{C}UV\end{bmatrix}. \quad (141)$$

5.5. Calculation of 16 Christoffel Symbols

We finally have all the pieces to finish the calculation of the Christoffel symbols. We encountered in (21) to (26) left and right terms:

$$\begin{aligned}\mathcal{L} :=&\ \frac{\nabla\left[\hat{\phi}(\sigma_1 + i\sigma_2)\phi^\dagger\right]}{\det(\phi^\dagger)} + 2iqA\frac{\hat{\phi}(\sigma_1 + i\sigma_2)\phi^\dagger}{\det(\phi^\dagger)} \\ =&\ \mathcal{S}_{(1)} + i\mathcal{S}'_{(1)} + i\left(\mathcal{S}_{(2)} + i\mathcal{S}'_{(2)}\right) + 2iq\left[\mathcal{A}_{(1)} + i\mathcal{A}'_{(1)} + i\left(\mathcal{A}_{(2)} + i\mathcal{A}'_{(2)}\right)\right] \\ =&\ \mathcal{S}_{(1)} - 2q\mathcal{A}_{(2)} - \left(\mathcal{S}'_{(2)} + 2q\mathcal{A}'_{(1)}\right) + i\left[\left(\mathcal{S}'_{(1)} - 2q\mathcal{A}'_{(2)}\right) + \left(\mathcal{S}_{(2)} + 2q\mathcal{A}_{(1)}\right)\right].\end{aligned} \quad (142)$$

This allows us to calculate the four $\Gamma^0_{1\mu} + \Gamma^3_{1\mu} + i\left(\Gamma^0_{2\mu} - \Gamma^2_{3\mu}\right)$. Similarly:

$$\begin{aligned}\mathcal{R} :=&\ \frac{\nabla\left[\hat{\phi}(\sigma_1 - i\sigma_2)\phi^\dagger\right]}{\det(\phi^\dagger)} - 2iqA\frac{\hat{\phi}(\sigma_1 - i\sigma_2)\phi^\dagger}{\det(\phi^\dagger)} \\ =&\ \mathcal{S}_{(1)} + i\mathcal{S}'_{(1)} - i\left(\mathcal{S}_{(2)} + i\mathcal{S}'_{(2)}\right) - 2iq\left[\mathcal{A}_{(1)} + i\mathcal{A}'_{(1)} - i\left(\mathcal{A}_{(2)} + i\mathcal{A}'_{(2)}\right)\right]\end{aligned}$$

$$= \mathcal{S}_{(1)} - 2q\mathcal{A}_{(2)} + \left(\mathcal{S}'_{(2)} + 2q\mathcal{A}'_{(1)}\right) + i\left[\left(\mathcal{S}'_{(1)} - 2q\mathcal{A}'_{(2)}\right) - \left(\mathcal{S}_{(2)} + 2q\mathcal{A}_{(1)}\right)\right] \qquad (143)$$

This allows to calculate the four $\Gamma^0_{1\mu} - \Gamma^3_{1\mu} - i\left(\Gamma^0_{2\mu} + \Gamma^2_{3\mu}\right)$. We let:

$$\mathcal{L} =: S\left(\mathbf{L}_1 + i\mathbf{L}_2\right)S^\dagger; \mathbf{L}_1 = \mathbf{L}_1^\dagger; \mathbf{L}_2 = \mathbf{L}_2^\dagger, \qquad (144)$$

$$\mathcal{R} =: S\left(\mathbf{R}_1 + i\mathbf{R}_2\right)S^\dagger; \mathbf{R}_1 = \mathbf{R}_1^\dagger; \mathbf{R}_2 = \mathbf{R}_2^\dagger, \qquad (145)$$

We obtain:

$$\frac{\nabla\left[\hat{\phi}\left(\sigma_1 + i\sigma_2\right)\phi^\dagger\right]}{\det\left(\phi^\dagger\right)} + 2iqA\frac{\hat{\phi}\left(\sigma_1 + i\sigma_2\right)\phi^\dagger}{\det\left(\phi^\dagger\right)} \qquad (146)$$

$$= \mathcal{S}_{(1)} - 2q\mathcal{A}_{(2)} + i\left(\mathcal{S}'_{(1)} - 2q\mathcal{A}'_{(2)}\right) + i\left[\mathcal{S}_{(2)} + 2q\mathcal{A}_{(1)} + i\left(\mathcal{S}'_{(2)} + 2q\mathcal{A}'_{(1)}\right)\right]$$

$$\Gamma^0_{1\mu} - i\Gamma^2_{3\mu} + i\left(\Gamma^0_{2\mu} - i\Gamma^3_{1\mu}\right) = \mathrm{d}_\mu \cdot \mathbf{L}_1 + i\mathrm{d}_\mu \cdot \mathbf{L}_2 + 2m\rho\left(\delta^2_\mu - i\delta^1_\mu\right). \qquad (147)$$

The separation between real and imaginary parts of this equality gives:

$$\Gamma^0_{1\mu} + \Gamma^3_{1\mu} = \mathrm{d}_\mu \cdot \mathbf{L}_1 + 2m\rho\delta^2_\mu = \mathrm{d}^0_\mu\mathbf{L}^0_1 - \mathrm{d}^1_\mu\mathbf{L}^1_1 - \mathrm{d}^2_\mu\mathbf{L}^2_1 - \mathrm{d}^3_\mu\mathbf{L}^3_1 + 2m\rho\delta^2_\mu, \qquad (148)$$

$$-\Gamma^2_{3\mu} + \Gamma^0_{2\mu} = \mathrm{d}_\mu \cdot \mathbf{L}_2 - 2m\rho\delta^1_\mu = \mathrm{d}^0_\mu\mathbf{L}^0_2 - \mathrm{d}^1_\mu\mathbf{L}^1_2 - \mathrm{d}^2_\mu\mathbf{L}^2_2 - \mathrm{d}^3_\mu\mathbf{L}^3_2 - 2m\rho\delta^1_\mu, \qquad (149)$$

Now we need:

$$\frac{1}{2}\left(\mathcal{A}' + \mathcal{D}'\right) = \mathbf{L}^0_1 + i\mathbf{L}^0_2 = 2imUV\mathrm{e}^{2i\zeta}\frac{AB - CD}{\left|\det\left(X^\dagger\right)\right|} \qquad (150)$$

$$\frac{1}{2}\left(\mathcal{A}' - \mathcal{D}'\right) = \mathbf{L}^3_1 + i\mathbf{L}^3_2 = 2UV\mathrm{e}^{2i\zeta}\frac{2i\left(E + \dfrac{\alpha}{r}\right)DB + \dfrac{\kappa}{r}\left(B^2 - D^2\right)}{\det\left(X^\dagger\right)}, \qquad (151)$$

$$\frac{1}{2}\left(\mathcal{B}' + \mathcal{C}'\right) = \mathbf{L}^1_1 + i\mathbf{L}^1_2$$

$$= 2im\mathrm{e}^{2i\zeta}\frac{BCV^2 - ADU^2}{\left|\det\left(X^\dagger\right)\right|} \qquad (152)$$

$$+ \mathrm{e}^{2i\zeta}\frac{B^2V^2 + D^2U^2 + 2\kappa\left(U^2 + V^2\right)BD - \dfrac{4\lambda}{\sin\theta}BDUV}{r\det\left(X^\dagger\right)},$$

$$-\frac{1}{2}\left(\mathcal{B}' - \mathcal{C}'\right) = -\mathbf{L}^2_2 + i\mathbf{L}^2_1$$

$$= -2\mathrm{e}^{2i\zeta}\frac{im\left(ADU^2 + BCV^2\right)}{\left|\det\left(X^\dagger\right)\right|} \qquad (153)$$

$$+ \frac{\mathrm{e}^{2i\zeta}}{\det\left(X^\dagger\right)}\left[\frac{1}{r}\left(D^2U^2 - B^2V^2\right) + 2BDUV\frac{\cos\theta}{r\sin\theta}\right].$$

We let:

$$\rho_0\mathrm{e}^{i\delta_0} := \left(\mathbf{L}^0_1 + i\mathbf{L}^0_2\right)\mathrm{e}^{-2i\zeta}; \rho_3\mathrm{e}^{i\delta_3} := \left(\mathbf{L}^3_1 + i\mathbf{L}^3_2\right)\mathrm{e}^{-2i\zeta}, \qquad (154)$$

$$\rho_1\mathrm{e}^{i\delta_1} := \left(\mathbf{L}^1_1 + i\mathbf{L}^1_2\right)\mathrm{e}^{-2i\zeta}; \rho_2\mathrm{e}^{i\delta_2} := \left(\mathbf{L}^2_1 + i\mathbf{L}^2_2\right)\mathrm{e}^{-2i\zeta}. \qquad (155)$$

This gives:

$$\mathbf{L}_1^0 = \rho_0 \cos\left(2\zeta + \delta_0\right); \mathbf{L}_2^0 = \rho_0 \sin\left(2\zeta + \delta_0\right) \tag{156}$$

$$\mathbf{L}_1^1 = \rho_1 \cos\left(2\zeta + \delta_1\right); \mathbf{L}_2^1 = \rho_1 \sin\left(2\zeta + \delta_1\right) \tag{157}$$

$$\mathbf{L}_1^2 = -\rho_2 \cos\left(2\zeta + \delta_2\right); \mathbf{L}_2^2 = \rho_2 \sin\left(2\zeta + \delta_2\right) \tag{158}$$

$$\mathbf{L}_1^3 = \rho_3 \cos\left(2\zeta + \delta_3\right); \mathbf{L}_2^3 = \rho_3 \sin\left(2\zeta + \delta_3\right). \tag{159}$$

Then (148) and (149) read:

$$\begin{aligned}
\Gamma_{1\mu}^0 + \Gamma_{1\mu}^3 &= d_\mu^0 \rho_0 \cos\left(2\zeta + \delta_0\right) - d_\mu^1 \rho_1 \cos\left(2\zeta + \delta_1\right) \\
&+ d_\mu^2 \rho_2 \cos\left(2\zeta + \delta_2\right) - d_\mu^3 \rho_3 \cos\left(2\zeta + \delta_3\right) + 2m\rho\delta_\mu^2,
\end{aligned} \tag{160}$$

$$\begin{aligned}
\Gamma_{2\mu}^0 - \Gamma_{3\mu}^2 &= d_\mu^0 \rho_0 \sin\left(2\zeta + \delta_0\right) - d_\mu^1 \rho_1 \sin\left(2\zeta + \delta_1\right) \\
&- d_\mu^2 \rho_2 \sin\left(2\zeta + \delta_2\right) - d_\mu^3 \rho_3 \sin\left(2\zeta + \delta_3\right) - 2m\rho\delta_\mu^1,
\end{aligned} \tag{161}$$

These equations give for instance:

$$\begin{aligned}
\Gamma_{10}^0 + \Gamma_{10}^3 &= d_0^0 \rho_0 \cos\left(2\zeta + \delta_0\right) - d_0^1 \rho_1 \cos\left(2\zeta + \delta_1\right) \\
&+ d_0^2 \rho_2 \cos\left(2\zeta + \delta_2\right) - d_0^3 \rho_3 \cos\left(2\zeta + \delta_3\right),
\end{aligned} \tag{162}$$

$$\begin{aligned}
&\Gamma_{11}^0 + i\Gamma_{12}^0 + \Gamma_{11}^3 + i\Gamma_{12}^3 \\
&= \left(d_1^0 + id_2^0\right)\rho_0 \cos\left(2\zeta + \delta_0\right) - \left(d_1^1 + id_2^1\right)\rho_1 \cos\left(2\zeta + \delta_1\right) \\
&+ \left(d_1^2 + id_2^2\right)\rho_2 \cos\left(2\zeta + \delta_2\right) - \left(d_1^3 + id_2^3\right)\rho_3 \cos\left(2\zeta + \delta_3\right) + 2im\rho \\
&= e^{2i\zeta}\left(-R_1 L_2 + R_2 L_1\right)\rho_0 \cos\left(2\zeta + \delta_0\right) - e^{2i\zeta}\left(R_1 L_1 - R_2 L_2\right)\rho_1 \cos\left(2\zeta + \delta_1\right) \\
&+ e^{2i\zeta}\left(iR_1 L_1 + iR_2 L_2\right)\rho_2 \cos\left(2\zeta + \delta_2\right) \\
&- e^{2i\zeta}\left(-R_1 L_1 - R_2 L_2\right)\rho_3 \cos\left(2\zeta + \delta_3\right) + 2im\rho.
\end{aligned} \tag{163}$$

The same calculation must be made for the right terms:

$$\begin{aligned}
&\frac{\nabla\left[\hat{\phi}\left(\sigma_1 - i\sigma_2\right)\phi^\dagger\right]}{\det\left(\phi^\dagger\right)} - 2iqA\frac{\hat{\phi}\left(\sigma_1 - i\sigma_2\right)\phi^\dagger}{\det\left(\phi^\dagger\right)} \\
&= \mathcal{S}_{(1)} - 2q\mathcal{A}_{(2)} + i\left(\mathcal{S}_{(1)}' - 2q\mathcal{A}_{(2)}'\right) - i\left[\mathcal{S}_{(2)} + 2q\mathcal{A}_{(1)} + i\left(\mathcal{S}_{(2)}' + 2q\mathcal{A}_{(1)}'\right)\right]
\end{aligned} \tag{164}$$

$$\Gamma_{1\mu}^0 - i\Gamma_{3\mu}^2 - i\left(\Gamma_{2\mu}^0 - i\Gamma_{1\mu}^3\right) = d_\mu \cdot \mathbf{R}_1 + id_\mu \cdot \mathbf{R}_2 + 2m\rho\left(\delta_\mu^2 + i\delta_\mu^1\right). \tag{165}$$

The separation between real and imaginary parts of this equality gives:

$$\Gamma_{1\mu}^0 - \Gamma_{1\mu}^3 = d_\mu \cdot \mathbf{R}_1 + 2m\rho\delta_\mu^2 = d_\mu^0 \mathbf{R}_1^0 - d_\mu^1 \mathbf{R}_1^1 - d_\mu^2 \mathbf{R}_1^2 - d_\mu^3 \mathbf{R}_1^3 + 2m\rho\delta_\mu^2, \tag{166}$$

$$-\Gamma_{3\mu}^2 - \Gamma_{2\mu}^0 = d_\mu \cdot \mathbf{R}_2 + 2m\rho\delta_\mu^1 = d_\mu^0 \mathbf{R}_2^0 - d_\mu^1 \mathbf{R}_2^1 - d_\mu^2 \mathbf{R}_2^2 - d_\mu^3 \mathbf{R}_2^3 + 2m\rho\delta_\mu^1, \tag{167}$$

Now we need (with $\rho_X = \left|\det\left(X^\dagger\right)\right|$):

$$\frac{1}{2}\left(\mathcal{A}_-' + \mathcal{D}_-'\right) = \mathbf{R}_1^0 + i\mathbf{R}_2^0 = 2imUVe^{-2i\zeta}\frac{\overline{D}\overline{C} - \overline{A}\overline{B}}{\rho_X} \tag{168}$$

$$\frac{1}{2}\left(\mathcal{A}_-' - \mathcal{D}_-'\right) = \mathbf{R}_1^3 + i\mathbf{R}_2^3 = 2UVe^{-2i\zeta}\frac{-2i\left(E + \frac{\alpha}{r}\right)\overline{A}\overline{C} + \frac{\kappa}{r}\left(\overline{A}^2 - \overline{C}^2\right)}{\det\left(X^\dagger\right)}, \tag{169}$$

$$\frac{1}{2}\left(\mathcal{B}'_- + \mathcal{C}'_-\right) = \mathbf{R}_1^1 + i\mathbf{R}_2^1$$

$$= 2ime^{-2i\zeta}\,\frac{\overline{D}\overline{A}U^2 + \overline{B}\overline{C}V^2}{\rho_X} \tag{170}$$

$$+ e^{-2i\zeta}\,\frac{-\left(\overline{C}^2V^2 + \overline{A}^2U^2\right) + 2\kappa\left(U^2+V^2\right)\overline{A}\overline{C} + \dfrac{4\lambda}{\sin\theta}\,\overline{A}\overline{C}UV}{r\det\left(X^\dagger\right)},$$

$$-\frac{1}{2}\left(\mathcal{B}'_- - \mathcal{C}'_-\right) = -\mathbf{R}_2^2 + i\mathbf{R}_1^2$$

$$= \frac{e^{-2i\zeta}}{\det\left(X^\dagger\right)}\left[\frac{1}{r}\left(\overline{A}^2U^2 - \overline{C}^2V^2\right) + 2\overline{A}\overline{C}UV\,\frac{\cos\theta}{r\sin\theta}\right] \tag{171}$$

$$+ 2e^{-2i\zeta}\,im\,\frac{\overline{B}\overline{C}V^2 - \overline{A}\overline{D}U^2}{\rho_X}.$$

We let:

$$\rho'_0 e^{i\delta'_0} := e^{2i\zeta}\left(\mathbf{R}_1^0 + i\mathbf{R}_2^0\right); \; \rho'_3 e^{i\delta'_3} := e^{2i\zeta}\left(\mathbf{R}_1^3 + i\mathbf{R}_2^3\right), \tag{172}$$

$$\rho'_1 e^{i\delta'_1} := e^{2i\zeta}\left(\mathbf{R}_1^1 + i\mathbf{R}_2^1\right); \; \rho'_2 e^{i\delta'_2} := e^{2i\zeta}\left(\mathbf{R}_1^1 + i\mathbf{R}_2^1\right). \tag{173}$$

This gives:

$$\mathbf{R}_1^0 = \rho'_0\cos\left(-2\zeta + \delta'_0\right); \mathbf{R}_2^0 = \rho'_0\sin\left(-2\zeta + \delta'_0\right) \tag{174}$$

$$\mathbf{R}_1^1 = \rho'_1\cos\left(-2\zeta + \delta'_1\right); \mathbf{R}_2^1 = \rho'_1\sin\left(-2\zeta + \delta'_1\right) \tag{175}$$

$$\mathbf{R}_1^2 = -\rho'_2\cos\left(-2\zeta + \delta'_2\right); \mathbf{R}_2^2 = \rho'_2\sin\left(-2\zeta + \delta'_2\right) \tag{176}$$

$$\mathbf{R}_1^3 = \rho'_3\cos\left(-2\zeta + \delta'_3\right); \mathbf{R}_2^3 = \rho'_3\sin\left(-2\zeta + \delta'_3\right) \tag{177}$$

Then (166) and (167) read:

$$\Gamma_{1\mu}^0 - \Gamma_{1\mu}^3 = d_\mu^0\rho'_0\cos\left(-2\zeta + \delta'_0\right) - d_\mu^1\rho'_1\cos\left(-2\zeta + \delta'_1\right)$$
$$+ d_\mu^2\rho'_2\cos\left(-2\zeta + \delta'_2\right) - d_\mu^3\rho'_3\cos\left(-2\zeta + \delta'_3\right) + 2m\rho\delta_\mu^2, \tag{178}$$

$$-\Gamma_{2\mu}^0 - \Gamma_{3\mu}^2 = d_\mu^0\rho'_0\sin\left(-2\zeta + \delta'_0\right) - d_\mu^1\rho'_1\sin\left(-2\zeta + \delta'_1\right)$$
$$- d_\mu^2\rho'_2\sin\left(-2\zeta + \delta'_2\right) - d_\mu^3\rho'_3\sin\left(-2\zeta + \delta'_3\right) - 2m\rho\delta_\mu^1, \tag{179}$$

6. Torsion and Symmetric Part of the Connection

The 64 Christoffel symbols may be calculated from the $4\times 7 = 28$ independent terms, using the 36 relations described in (16), (17) and (18):

$$\Gamma_{0\mu}^0 = d_\mu \cdot \mathbf{K}_0; \Gamma_{3\mu}^0 = d_\mu \cdot \mathbf{K}_3; \Gamma_{2\mu}^1 = -d_\mu \cdot \mathbf{K}'_3 - 2m\rho\delta_\mu^0 \tag{180}$$

$$\Gamma_{1\mu}^0 = d_\mu \cdot \frac{\mathbf{L}_1 + \mathbf{R}_1}{2} + 2m\rho\delta_\mu^2; \Gamma_{1\mu}^3 = d_\mu \cdot \frac{\mathbf{L}_1 - \mathbf{R}_1}{2} \tag{181}$$

$$\Gamma_{2\mu}^0 = d_\mu \cdot \frac{\mathbf{L}_2 - \mathbf{R}_2}{2} - 2m\rho\delta_\mu^1; \Gamma_{3\mu}^2 = d_\mu \cdot \frac{-\mathbf{L}_2 - \mathbf{R}_2}{2}. \tag{182}$$

The torsion tensor is usually defined as:

$$\mathbf{T}_{jk}^\mu := \frac{1}{2}\left(\Gamma_{jk}^\mu - \Gamma_{kj}^\mu\right); \; jk = 01, 02, 03, 12, 23, 31, \mu = 0, 1, 2, 3. \tag{183}$$

This tensor is then antisymmetric: ($\mathbf{T}^\mu_{kj} := -\mathbf{T}^\mu_{jk}$). Here, for instance, eight terms contain the $\mathbf{K}$ space-time vectors, without other terms:

$$\mathbf{T}^0_{30} = -\mathbf{T}^0_{03} = \frac{1}{2}\left[-\mathrm{d}_3 \cdot \mathbf{K}_0 + \mathrm{d}_0 \cdot \mathbf{K}_3\right], \tag{184}$$

$$\mathbf{T}^1_{12} = -\mathbf{T}^1_{21} = \frac{1}{2}\left[\mathrm{d}_1 \cdot \mathbf{K}'_3 + \mathrm{d}_2 \cdot \mathbf{K}_0\right], \tag{185}$$

$$\mathbf{T}^2_{12} = -\mathbf{T}^2_{21} = \frac{1}{2}\left[\mathrm{d}_2 \cdot \mathbf{K}'_3 - \mathrm{d}_1 \cdot \mathbf{K}_0\right], \tag{186}$$

$$\mathbf{T}^3_{30} = -\mathbf{T}^3_{03} = \frac{1}{2}\left[\mathrm{d}_0 \cdot \mathbf{K}_0 - \mathrm{d}_3 \cdot \mathbf{K}_3\right], \tag{187}$$

Rodichev [55] studied the torsion in the frame of a Euclidean geometry with torsion. The present study acts in the frame of a space-time manifold, not Euclidean, so we get very different properties. In space-time the torsion tensor has 24 independent components while the connection contains 28 independent Christoffel symbols. We obtain these 28 symbols from the $4 \times 8 = 32$ functions a^n_μ defining a dilator M (see ([41] 4.1.2), satisfying:

$$M = 1 + \mathrm{d}x^\mu\left(a^0_\mu + a^j_\mu \sigma_j + a^{3+j}_\mu i\sigma_j + a^7_\mu i\right), \tag{188}$$

where we have:

$$\Gamma^0_{0\mu} = \Gamma^1_{1\mu} = \Gamma^2_{2\mu} = \Gamma^3_{3\mu} = 2a^0_\mu, \tag{189}$$

$$\Gamma^1_{0\mu} = \Gamma^0_{1\mu} = 2a^1_\mu; \ \Gamma^2_{0\mu} = \Gamma^0_{2\mu} = 2a^2_\mu; \ \Gamma^3_{0\mu} = \Gamma^0_{3\mu} = 2a^3_\mu, \tag{190}$$

$$\Gamma^2_{3\mu} = -\Gamma^3_{2\mu} = 2a^4_\mu; \ \Gamma^3_{1\mu} = -\Gamma^1_{3\mu} = 2a^5_\mu; \ \Gamma^1_{2\mu} = -\Gamma^2_{1\mu} = 2a^6_\mu. \tag{191}$$

7. Concluding Remarks

The principle of equivalence between inertia and gravitation being simply the equality between the $\Gamma^\rho_{\mu\nu}$ and the $\Gamma^\rho_{\mu\nu}$, the solutions studied here show that all 28 functions come simply from scalar products of the four contravariant D_μ by the seven covariant vectors:

$$\mathbf{V}_0 := S\mathbf{K}_0 S^\dagger; \ \mathbf{V}_3 := S\mathbf{K}_3 S^\dagger; \ \mathbf{V}_6 := S\mathbf{K}'_3 S^\dagger, \tag{192}$$

$$2\mathcal{L}_1 := S\mathbf{L}_1 S^\dagger; \ 2\mathcal{R}_1 := S\mathbf{R}_1 S^\dagger; \ 2\mathcal{L}_2 := S\mathbf{L}_2 S^\dagger; \ 2\mathcal{R}_2 := S\mathbf{R}_2 S^\dagger.$$

These vectors allow us to obtain all Christoffel symbols as scalar products:

$$\Gamma^0_{0\mu} = \Gamma^1_{1\mu} = \Gamma^2_{2\mu} = \Gamma^3_{3\mu} = 2a^0_\mu = D_\mu \cdot \mathbf{V}_0, \tag{193}$$

$$\Gamma^3_{0\mu} = \Gamma^0_{3\mu} = 2a^3_\mu = D_\mu \cdot \mathbf{V}_3, \tag{194}$$

$$\Gamma^1_{2\mu} = -\Gamma^2_{1\mu} = 2a^6_\mu = D_\mu \cdot \mathbf{V}_6 - 2m\rho\delta^0_\mu, \tag{195}$$

while the 32 other symbols use the right and left vectors:

$$\Gamma^1_{0\mu} = \Gamma^0_{1\mu} = 2a^1_\mu = D_\mu \cdot \left(\mathcal{L}_1 + \mathcal{R}_1\right) + 2m\rho\delta^2_\mu, \tag{196}$$

$$\Gamma^2_{0\mu} = \Gamma^0_{2\mu} = 2a^2_\mu = D_\mu \cdot \left(\mathcal{L}_2 - \mathcal{R}_2\right) - 2m\rho\delta^1_\mu, \tag{197}$$

$$\Gamma^2_{3\mu} = -\Gamma^3_{2\mu} = 2a^4_\mu = D_\mu \cdot \left(-\mathcal{L}_2 - \mathcal{R}_2\right), \qquad (198)$$

$$\Gamma^3_{1\mu} = -\Gamma^1_{3\mu} = 2a^5_\mu = D_\mu \cdot \left(\mathcal{L}_1 - \mathcal{R}_1\right). \qquad (199)$$

The chiral structure of the connection appears here, from the fact that three definitions only act with indexes 0 and 3 while four definitions act with the left and right vectors. Moreover only the symbols containing the three indexes 1, 2, 0, contain the mass term $2m\rho$. This chirality is also linked to the electric gauge transformation, which acts everywhere in quantum mechanics, even in the non-relativistic case. It induces a rotation in the 1-2 plane, in the direction from 1 to 2: the rotation transforming 1 into 2 transforms 2 into -1. This partially remains in non-relativistic quantum mechanics, where the conservation of the probability density still acts.

The previous calculation must be completed by the examination of the different cases corresponding to the different quantum numbers characterizing the electron states. This will be carried out in the second part of this work. These states are different first from the sign of the κ number. This number is present in the previous calculation, not only by the value of E which contains κ^2, but also directly in the $\dfrac{\kappa}{r}$ terms, and also in the λ terms: the values of λ are $-j, -j+1, \cdots, j-1, j$ with $j = |\kappa| - \dfrac{1}{2}$. The linking of the states with $\kappa > 0$ to the states with $\kappa < 0$ is not a one-to-one link: the other quantum numbers are the integer degree n_1 of angular polynomial functions and the integer degree n_2 of radial polynomial functions, and there is no state with $\kappa < 0$ and $n_2 = 0$. Consequently $\mathbf{n}(\mathbf{n}+1)$ states exist with $\kappa > 0$ and only $\mathbf{n}(\mathbf{n}-1)$ states with $\kappa < 0$, for each principal quantum number $\mathbf{n}$. The symmetry between these two kinds of states is then a false symmetry. This mainly comes from the property demonstrated in the next appendix: even if Gegenbauer's polynomials are different in the cases $\kappa > 0$ and $\kappa < 0$, the angular functions U and V encountered in the previous calculation are exactly proportional. The result of this similarity is the very popular Pauli's tale of the spin-up, spin-down states which doubles the $\mathbf{n}^2$ number issued from the spectroscopy and also from the Schrödinger wave equation.

It is only a tale, even if $\mathbf{n}(\mathbf{n}+1) + \mathbf{n}(\mathbf{n}-1) = 2\mathbf{n}^2$, as may be seen in our previous calculation: the spin effect is much more complicated. The λ factor (with half-integer value) present in the $\zeta = \lambda\varphi - Ex^0 + \delta$ electric phase of the electron wave is doubled in all the 2ζ terms, but is even quadrupled in the $\mathrm{e}^{2i\zeta}\cos(2\zeta + \delta_n)$ terms in (163). It then happens that space-time turns more rapidly than the wave (or the wave turns less rapidly than the space time). Space-time geometry defined by the Christoffel symbols is animated not only by waves with a 2ζ phase, but also by waves with a 4ζ phase. This kind of phase was first encountered in general relativity as waves with spin 2. Our calculation shows that it is linked to the quantum wave of the electron, as suspected by Feynman [56].

Conflicts of Interest

The authors declare no conflicts of interest regarding the publication of this paper.

References

[1] de Broglie, L. (1924) Recherches sur la théorie des quantas.

[2] Dirac, P.A.M. (1928) *Proceedings of the Royal Society of London*, **117**, 610-624. https://doi.org/10.1098/rspa.1928.0023

[3] de Broglie, L. (1934) L'électron magnétique. Hermann, Paris.

[4] Daviau, C. (1993) Equation de Dirac non linéaire. Ph.D. Thesis, Université de Nantes, Nantes.

[5] Daviau, C. (1996) Dirac Equation in the Clifford Algebra of Space. In: *Clifford Algebras and Their Application in Mathematical Physics*, Springer, Boston, 67-88. https://doi.org/10.1007/978-94-011-5036-1_8

[6] Daviau, C. (1997) *Advances in Applied Clifford Algebras*, **7**, 175-194.

[7] Daviau, C. (1997) *Annales de la Fondation Louis de Broglie*, **22**, 87-103.

[8] Daviau, C. (1998) *Annales de la Fondation Louis de Broglie*, **23**, 27-37.

[9] Daviau, C. (1998) *Annales de la Fondation Louis de Broglie*, **26**, 149-171.

[10] Daviau, C. (2004) Chiral Dirac Equations. In: *Clifford Algebras: Applications to Mathematics, Physics, and Engineering*, Birkhäuser, Boston, 431-450. https://doi.org/10.1007/978-1-4612-2044-2_28

[11] Daviau, C. (2005) *Annales de la Fondation Louis de Broglie*, **30**, 409-428. https://aflb.minesparis.psl.eu/AFLB-303/aflb303m398.pdf

[12] Daviau, C. (2008) *Annales de la Fondation Louis de Broglie*, **33**, 53-67. https://aflb.minesparis.psl.eu/AFLB-331/aflb331m626.pdf

[13] Daviau, C. (2009) *Annales de la Fondation Louis de Broglie*, **34**, 45-65. https://aflb.minesparis.psl.eu/AFLB-341/aflb341m648.pdf

[14] Daviau, C. (2010) *Annales de la Fondation Louis de Broglie*, **35**, 51-78. https://aflb.minesparis.psl.eu/AFLB-351/aflb351m687.htm

[15] Daviau, C. (2011) L'espace-temps double. JePublie, Pouillé-les-coteaux. http://www.jepublie.com/livre-l-espace-temps-double-622.aspx

[16] Daviau, C. (2012) *Advances in Applied Clifford Algebras*, **22**, 611-623. https://doi.org/10.1007/s00006-012-0351-7

[17] Daviau, C. (2009) *Annales de la Fondation Louis de Broglie*, **37**, 253-268. https://aflb.minesparis.psl.eu/AFLB-371/aflb371m744.pdf

[18] Daviau, C. (2012) Double Space-Time and More. JePublie, Pouillé-les-coteaux. http://www.jepublie.com/livre-double-space-time-800.aspx

[19] Daviau, C. (2012) Nonlinear Dirac Equation, Magnetic Monopoles and Double Space-Time. CISP, Cambridge. https://hal.archives-ouvertes.fr/hal-01058706/document

[20] Daviau, C. and Bertrand, J. (2013) *Annales de la Fondation Louis de Broglie*, **38**, 57.

[21] Daviau, C. (2013) *Advances in Imaging and Electron Physics*, **179**, 1-136. https://doi.org/10.1016/B978-0-12-407700-3.00001-6

[22] Daviau, C. (2014) *Advances in Applied Clifford Algebras*, **22**, 611-623. https://doi.org/10.1007/s00006-012-0351-7

[23] Daviau, C. and Bertrand, J. (2014) New Insights in the Standard Model of Quantum Physics in Clifford Algebra. Je Publie, Pouillé-les-coteaux.
https://doi.org/10.1142/9780
https://hal.archives-ouvertes.fr/hal-00907848

[24] Daviau, C. and Bertrand, J. (2014) *Journal of Modern Physics*, **5**, 1001-1022.
https://doi.org/10.4236/jmp.2014.511102

[25] Daviau, C. and Bertrand, J. (2014) *Journal of Modern Physics*, **5**, 2149-2173.
https://doi.org/10.4236/jmp.2014.518210

[26] Daviau, C. and Bertrand, J. (2014) *Annales de la Fondation Louis de Broglie*, **40**, 181-209.
https://aflb.minesparis.psl.eu/AFLB-401/aflb401m842.pdf

[27] Daviau, C. (2015) *Annales de la Fondation Louis de Broglie*, **40**, 113-138.
https://aflb.minesparis.psl.eu/AFLB-401/aflb401m807.pdf

[28] Daviau, C. and Bertrand, J. (2015) *Journal of Modern Physics*, **6**, 2080-2092.
https://doi.org/10.4236/jmp.2015.614215

[29] Daviau, C. and Bertrand, J. (2015) *Journal of Applied Mathematics and Physics*, **3**, 46-61. https://doi.org/10.4236/jamp.2015.31007

[30] Daviau, C. and Bertrand, J. (2015) *Journal of Modern Physics*, **6**, 1647-1656.
https://doi.org/10.4236/jmp.2015.611166

[31] Daviau, C. (2016) *Annales de la Fondation Louis de Broglie*, **41**, 73-97.
https://aflb.minesparis.psl.eu/AFLB-401/aflb401m807.pdf

[32] Daviau, C. and Bertrand, J. (2016) The Standard Model of Quantum Physics in Clifford Algebra. World Scientific, Singapore.
https://www.worldscientific.com/worldscibooks/10.1142/9780
https://doi.org/10.1142/9780

[33] Daviau, C. and Bertrand, J. (2016) *Journal of Modern Physics*, **7**, 936-951.
https://doi.org/10.4236/jmp.2016.79086

[34] Daviau, C., Bertrand, J. and Girardot, D. (2016) *Journal of Modern Physics*, **7**, 1568-1590. https://doi.org/10.4236/jmp.2016.712143

[35] Daviau, C., Bertrand, J. and Girardot, D. (2016) *Journal of Modern Physics*, **7**, 2398-2417. https://doi.org/10.4236/jmp.2016.716207

[36] Daviau, C., Bertrand, J., Girardot, D. and Socroun, T. (2017) *Annales de la Fondation Louis de Broglie*, **42**, 351-378.
https://aflb.minesparis.psl.eu/AFLB-422/aflb422m873.pdf

[37] Daviau, C. and Bertrand, J. (2016) *Journal of Modern Physics*, **9**, 250-258.
https://doi.org/10.4236/jmp.2018.92017

[38] Daviau, C. (2019) *Annales de la Fondation Louis de Broglie*, **44**, 163-186.
https://aflb.minesparis.psl.eu/AFLB-441/aflb441m920.pdf

[39] Daviau, C., Bertrand, J., Socroun, T. and Girardot, D. (2019) Modèle Standard et Gravitation. Presses des Mines, Paris.
https://www.pressesdesmines.com/produit/modele-standard-et-gravitation

[40] Daviau, C. (2020) Dialogue pour une nouvelle physique (secondeödition). Ed. St Honoré, Paris.
https://www.editions-saint-honore.com/produit/dialogue-pour-une-nouvelle-physique

[41] Daviau, C., Bertrand, J., Socroun, T. and Girardot, D. (2020) Developing a Theory of Everything. Annales de la Fondation Louis de Broglie, Paris.
https://aflb.minesparis.psl.eu/MEMOS/ToEAFLB.pdf

[42] Daviau, C., Bertrand, J. and Ng, R.A. (2020) *Journal of Modern Physics*, **11**, 1075-1090. https://doi.org/10.4236/jmp.2020.117068

[43] Daviau, C. and Bertrand, J. (2020) *Journal of Modern Physics*, **11**, 1263-1278. https://doi.org/10.4236/jmp.2020.119079

[44] Hestenes, D. (2020) *Journal of Mathematical Physics*, **14**, 893-905. https://doi.org/10.1063/1.1666413

[45] Hestenes, D. (1986) A Unified Language for Mathematics and Physics and Clifford Algebra and the Interpretation of Quantum Mechanics. Reidel, Dordrecht. https://doi.org/10.1007/978-94-009-4728-3_27

[46] Lochak, G. (1983) *Annales de la Fondation Louis de Broglie*, **8**, 345.

[47] Lochak, G. (1984) *Annales de la Fondation Louis de Broglie*, **9**, 5e30.

[48] Lochak, G. (1985) *International Journal of Theoretical Physics*, **24**, 1019-1050. https://doi.org/10.1007/BF00670815

[49] Lochak, G. (1995) The Symmetry between Electricity and Magnetism and the Problem of the Existence of a Magnetic Monopole. In: Barrett, T.W. and Grimes, D.M., Eds., *Advanced Electromagnetism*, World Scientific, Singapore, 105-147. https://doi.org/10.1142/9789812831323_0004

[50] Lochak, G. (2004) *Annales de la Fondation Louis de Broglie*, **29**, 297-316. https://aflb.minesparis.psl.eu/AFLB-291/aflb291p297.htm

[51] Lochak, G. (2006) *Annales de la Fondation Louis de Broglie*, **31**, 193-206. https://aflb.minesparis.psl.eu/AFLB-312/aflb312m508.htm

[52] Lochak, G. (2007) *Annales de la Fondation Louis de Broglie*, **32**, 125-136. https://aflb.minesparis.psl.eu/AFLB-322/aflb322m610.htm

[53] Lochak, G. (2010) *Annales de la Fondation Louis de Broglie*, **35**, 1-18. https://aflb.minesparis.psl.eu/AFLB-351/aflb351m704.htm

[54] Krüger, H. (1991) New Solutions of the Dirac Equation for Central Fields. In: Hestenes, D. and Weingartshofer, A., Eds., *The Electron*, Kluwer, Dordrecht, 49-81. https://link.springer.com/chapter/10.1007/978-94-011-3570-2_4 https://doi.org/10.1007/978-94-011-3570-2_4

[55] Rodichev, V.I. (1961) *Journal of Experimental and Theoretical Physics*, **40**, 1469-1472. http://www.jetp.ac.ru/cgi-bin/dn/e_013_05_1029.pdf

[56] Feynman, R. (1995) Lectures on Gravitation. Addison-Wesley, Boston.

Appendix: Angular Functions

The angular functions are calculated from the auxiliary $C(\theta)$ function using the differential equation of Gegenbauer's polynomials (see [41] C.2):

$$C(\theta) = \sum_{n=0}^{\infty} \frac{\left(|\lambda| - \kappa - \frac{1}{2}\right)_n \left(|\lambda| + \kappa + \frac{1}{2}\right)_n}{\left(\frac{1}{2} + |\lambda|\right)_n n!} \sin^{2n}\left(\frac{\theta}{2}\right), \tag{200}$$

where κ is any integer not equal to zero. This condition on κ results from the necessity of the normalization of the ϕ wave. We first consider the case $\kappa > 0$ and $\lambda > 0$ for which we must have $\lambda = \frac{1}{2}, \frac{3}{2}, \cdots, \kappa - \frac{1}{2}$ (for other values of λ and if $\kappa = 0$ the ϕ function is ill-defined):

$$C(\theta) = \sum_{n=0}^{\infty} \frac{\left(\lambda - \kappa - \frac{1}{2}\right)_n \left(\lambda + \kappa + \frac{1}{2}\right)_n}{\left(\frac{1}{2} + \lambda\right)_n n!} \sin^{2n}\left(\frac{\theta}{2}\right), \tag{201}$$

with:

$$(a)_0 := 1; (a)_1 := a; (a)_{n+1} := a(a+1)\cdots(a+n). \tag{202}$$

We then have:

$$\left(\lambda - \kappa - \frac{1}{2}\right)_{-\lambda+\kappa+\frac{1}{2}+1} = \left(\lambda - \kappa - \frac{1}{2}\right)\cdots(-2)(-1)0 = 0. \tag{203}$$

And any other term with upper n is also null. Then the infinite sum is reduced to:

$$C(\theta) = \sum_{n=0}^{n=\kappa-\lambda+\frac{1}{2}} \frac{\left(\lambda - \kappa - \frac{1}{2}\right)_n \left(\lambda + \kappa + \frac{1}{2}\right)_n}{\left(\frac{1}{2} + \lambda\right)_n n!} \sin^{2n}\left(\frac{\theta}{2}\right), \tag{204}$$

whose derivative is:

$$C'(\theta) = \cos\left(\frac{\theta}{2}\right) \sum_{n=1}^{n=\kappa-\lambda+\frac{1}{2}} \frac{\left(\lambda - \kappa - \frac{1}{2}\right)_n \left(\lambda + \kappa + \frac{1}{2}\right)_n}{\left(\frac{1}{2} + \lambda\right)_n n!} n \sin^{2n-1}\left(\frac{\theta}{2}\right). \tag{205}$$

All angular functions satisfy:

$$\frac{U}{\sin^\lambda(\theta)} = \left[\sin\left(\frac{\theta}{2}\right)C' - \left(\kappa - \lambda + \frac{1}{2}\right)\cos\left(\frac{\theta}{2}\right)C\right], \tag{206}$$

$$\frac{V}{\sin^\lambda(\theta)} = \left[\cos\left(\frac{\theta}{2}\right)C' + \left(\kappa - \lambda + \frac{1}{2}\right)\sin\left(\frac{\theta}{2}\right)C\right]. \tag{207}$$

Since the term of C' with rank 0 is null from the n factor:

$$\frac{U}{\sin^{\lambda}(\theta)} = \cos\left(\frac{\theta}{2}\right)\sum_{n=0}^{n=\kappa-\lambda+\frac{1}{2}}\left(\begin{array}{c} \dfrac{\left(\lambda-\kappa-\dfrac{1}{2}\right)_n\left(\lambda+\kappa+\dfrac{1}{2}\right)_n}{\left(\dfrac{1}{2}+\lambda\right)_n n!}n\sin^{2n}\left(\dfrac{\theta}{2}\right) \\ -\left(\kappa-\lambda+\dfrac{1}{2}\right)\dfrac{\left(\lambda-\kappa-\dfrac{1}{2}\right)_n\left(\lambda+\kappa+\dfrac{1}{2}\right)_n}{\left(\dfrac{1}{2}+\lambda\right)_n n!}\sin^{2n}\left(\dfrac{\theta}{2}\right) \end{array}\right). \quad (208)$$

The last term of this sum is null, as it is a difference of two equal terms. Then the sum contains one term less and we obtain:

$$\frac{U}{\sin^{\lambda}(\theta)} = \cos\left(\frac{\theta}{2}\right)\sum_{n=0}^{n=\kappa-\lambda-\frac{1}{2}}\left[n-\left(\kappa-\lambda+\frac{1}{2}\right)\right]\frac{\left(\lambda-\kappa-\dfrac{1}{2}\right)_n\left(\lambda+\kappa+\dfrac{1}{2}\right)_n}{\left(\dfrac{1}{2}+\lambda\right)_n n!}\sin^{2n}\left(\frac{\theta}{2}\right). \quad (209)$$

And we have:

$$(a)_n(a+n) = \left[a(a+1)\cdots(a+n-1)\right](a+n)$$
$$= a\left[(a+1)\cdots(a+n-1)(a+n)\right] = a(a+1)_n. \quad (210)$$

which implies:

$$\left[n-\left(\kappa-\lambda+\frac{1}{2}\right)\right]\left(\lambda-\kappa-\frac{1}{2}\right)_n = \left(\lambda-\kappa-\frac{1}{2}\right)\left(\lambda-\kappa+\frac{1}{2}\right)_n. \quad (211)$$

We then finally obtain:

$$\frac{U}{\sin^{\lambda}(\theta)} = \left(\lambda-\kappa-\frac{1}{2}\right)\cos\left(\frac{\theta}{2}\right)\sum_{n=0}^{n=\kappa-\lambda-\frac{1}{2}}\frac{\left(\lambda-\kappa+\dfrac{1}{2}\right)_n\left(\lambda+\kappa+\dfrac{1}{2}\right)_n}{\left(\dfrac{1}{2}+\lambda\right)_n n!}\sin^{2n}\left(\frac{\theta}{2}\right). \quad (212)$$

Next for V we have:

$$\frac{V}{\sin^{\lambda}(\theta)} = \left[1-\sin^2\left(\frac{\theta}{2}\right)\right]\sum_{n=0}^{n=\kappa-\lambda+\frac{1}{2}}n\frac{\left(\lambda-\kappa-\dfrac{1}{2}\right)_n\left(\lambda+\kappa+\dfrac{1}{2}\right)_n}{\left(\dfrac{1}{2}+\lambda\right)_n n!}\sin^{2n-1}\left(\frac{\theta}{2}\right)$$
$$+\left(\kappa+\frac{1}{2}-\lambda\right)\sum_{n=0}^{n=\kappa-\lambda+\frac{1}{2}}\frac{\left(\lambda-\kappa-\dfrac{1}{2}\right)_n\left(\lambda+\kappa+\dfrac{1}{2}\right)_n}{\left(\dfrac{1}{2}+\lambda\right)_n n!}\sin^{2n+1}\left(\frac{\theta}{2}\right) \quad (213)$$

Therefore we have:

$$\frac{V}{\sin^{\lambda}(\theta)} = \sum_{n=1}^{n=\kappa-\lambda+\frac{1}{2}}n\frac{\left(\lambda-\kappa-\dfrac{1}{2}\right)_n\left(\lambda+\kappa+\dfrac{1}{2}\right)_n}{\left(\dfrac{1}{2}+\lambda\right)_n n!}\sin^{2n-1}\left(\frac{\theta}{2}\right)$$
$$+\left(-n+\kappa+\frac{1}{2}-\lambda\right)\sum_{n=0}^{n=\kappa-\lambda+\frac{1}{2}}\frac{\left(\lambda-\kappa-\dfrac{1}{2}\right)_n\left(\lambda+\kappa+\dfrac{1}{2}\right)_n}{\left(\dfrac{1}{2}+\lambda\right)_n n!}\sin^{2n+1}\left(\frac{\theta}{2}\right) \quad (214)$$

In the first sum we let $n = 1 + n'$ while in the second sum we use the cancellation of the last term, so we have one term less:

$$
\frac{V}{\sin^\lambda(\theta)} = \sum_{n'=0}^{n'=\kappa-\lambda-\frac{1}{2}} \frac{\left(\lambda-\kappa-\frac{1}{2}\right)_{1+n'}\left(\lambda+\kappa+\frac{1}{2}\right)_{1+n'}}{\left(\frac{1}{2}+\lambda\right)_{1+n'} n'!} \sin^{2n'+1}\left(\frac{\theta}{2}\right)
$$

$$
+ \sum_{n=0}^{n=\kappa-\lambda-\frac{1}{2}} \frac{\left(\lambda-\kappa-\frac{1}{2}\right)_{n}\left(\lambda+\kappa+\frac{1}{2}\right)_{n}}{\left(\frac{1}{2}+\lambda\right)_{n} n!}\left(-n+\kappa+\frac{1}{2}-\lambda\right) \sin^{2n+1}\left(\frac{\theta}{2}\right).
$$

(215)

In the first sum the n' variable is replaced by n. In the second sum the $\left(-n+\kappa+\frac{1}{2}-\lambda\right)$ factor gives also one term less and we obtain:

$$
\frac{V}{\sin^\lambda(\theta)} = \sum_{n=0}^{n=\kappa-\lambda-\frac{1}{2}} \frac{\left(\lambda-\kappa-\frac{1}{2}\right)_{1+n}\left(\lambda+\kappa+\frac{1}{2}\right)_{1+n}}{\left(\frac{1}{2}+\lambda\right)_{1+n} n!} \sin^{2n+1}\left(\frac{\theta}{2}\right)
$$

$$
+ \sum_{n=0}^{n=\kappa-\lambda-\frac{1}{2}} \frac{\left(\lambda-\kappa-\frac{1}{2}\right)_{n}\left(\lambda+\kappa+\frac{1}{2}\right)_{n}}{\left(\frac{1}{2}+\lambda\right)_{n} n!}\left(-n+\kappa+\frac{1}{2}-\lambda\right) \sin^{2n+1}\left(\frac{\theta}{2}\right).
$$

(216)

And we have:

$$
\left(\lambda-\kappa-\frac{1}{2}\right)_{1+n} = \left(\lambda-\kappa-\frac{1}{2}\right)\left(\lambda-\kappa+\frac{1}{2}\right)_{n}, \tag{217}
$$

$$
\left(\lambda+\kappa+\frac{1}{2}\right)_{1+n} = \left(\lambda+\kappa+\frac{1}{2}\right)_{n}\left(\lambda+\kappa+\frac{1}{2}+n\right), \tag{218}
$$

$$
\left(\lambda-\kappa-\frac{1}{2}\right)_{n}\left(-n+\kappa+\frac{1}{2}-\lambda\right) = -\left(\lambda-\kappa-\frac{1}{2}\right)\left(\lambda-\kappa+\frac{1}{2}\right)_{n}. \tag{219}
$$

Then we obtain:

$$
\frac{V}{\sin^\lambda(\theta)} = \left(\lambda-\kappa-\frac{1}{2}\right) \sum_{n=0}^{n=\kappa-\lambda-\frac{1}{2}} \frac{\left(\lambda-\kappa+\frac{1}{2}\right)_{n}\left(\lambda+\kappa+\frac{1}{2}\right)_{n}}{\left(\frac{1}{2}+\lambda\right)_{n} n!}
$$

$$
\times \left[\frac{\lambda+\kappa+\frac{1}{2}+n}{\lambda+\frac{1}{2}+n} - 1\right]\sin^{2n+1}\left(\frac{\theta}{2}\right)
$$

(220)

$$
= \kappa\left(\lambda-\kappa-\frac{1}{2}\right) \sum_{n=0}^{n=\kappa-\lambda-\frac{1}{2}} \frac{\left(\lambda-\kappa+\frac{1}{2}\right)_{n}\left(\lambda+\kappa+\frac{1}{2}\right)_{n}}{\left(\frac{1}{2}+\lambda\right)_{1+n} n!} \sin^{2n+1}\left(\frac{\theta}{2}\right).
$$

Consider now the case $\kappa < 0$ that means $\kappa = -|\kappa|$. Still for $\lambda > 0$ we have

now $\lambda = \dfrac{1}{2}, \dfrac{3}{2}, \cdots, |\kappa| - \dfrac{1}{2}$, and:

$$C(\theta) = \sum_{n=0}^{\infty} \frac{\left(\lambda + |\kappa| - \dfrac{1}{2}\right)_n \left(\lambda - |\kappa| + \dfrac{1}{2}\right)_n}{\left(\dfrac{1}{2} + \lambda\right)_n n!} \sin^{2n}\left(\frac{\theta}{2}\right) \tag{221}$$

Now it is the second factor which contains a negative integer and then this product cancels from some rank. Since this rank is (for a negative $-a$ integer) the a rank, we have:

$$C(\theta) = \sum_{n=0}^{n=|\kappa|-\lambda-\frac{1}{2}} \frac{\left(\lambda + |\kappa| - \dfrac{1}{2}\right)_n \left(\lambda - |\kappa| + \dfrac{1}{2}\right)_n}{\left(\dfrac{1}{2} + \lambda\right)_n n!} \sin^{2n}\left(\frac{\theta}{2}\right), \tag{222}$$

We see that this sum has one term less than in the case $\kappa > 0$. We could expect that U and V should be very different from the functions previously calculated. Yet we will see that this is untrue. We have:

$$C'(\theta) = \cos\left(\frac{\theta}{2}\right) \sum_{n=0}^{n=|\kappa|-\lambda-\frac{1}{2}} n \frac{\left(\lambda + |\kappa| - \dfrac{1}{2}\right)_n \left(\lambda - |\kappa| + \dfrac{1}{2}\right)_n}{\left(\dfrac{1}{2} + \lambda\right)_n n!} \sin^{2n-1}\left(\frac{\theta}{2}\right) \tag{223}$$

(206) gives for U:

$$\frac{U}{\sin^\lambda(\theta)} = \sin\left(\frac{\theta}{2}\right)\cos\left(\frac{\theta}{2}\right) \sum_{n=0}^{n=|\kappa|-\lambda-\frac{1}{2}} n \frac{\left(\lambda + |\kappa| - \dfrac{1}{2}\right)_n \left(\lambda - |\kappa| + \dfrac{1}{2}\right)_n}{\left(\dfrac{1}{2} + \lambda\right)_n n!} \sin^{2n-1}\left(\frac{\theta}{2}\right)$$

$$+ \left(\lambda + |\kappa| - \frac{1}{2}\right)\cos\left(\frac{\theta}{2}\right) \sum_{n=0}^{n=|\kappa|-\lambda-\frac{1}{2}} \frac{\left(\lambda + |\kappa| - \dfrac{1}{2}\right)_n \left(\lambda - |\kappa| + \dfrac{1}{2}\right)_n}{\left(\dfrac{1}{2} + \lambda\right)_n n!} \sin^{2n}\left(\frac{\theta}{2}\right). \tag{224}$$

Then distributing the product in the second sum, we have:

$$\frac{U}{\sin^\lambda(\theta)} = \cos\left(\frac{\theta}{2}\right) \sum_{n=0}^{n=|\kappa|-\lambda-\frac{1}{2}} \left(n + \lambda + |\kappa| - \frac{1}{2}\right)$$

$$\times \frac{\left(\lambda + |\kappa| - \dfrac{1}{2}\right)_n \left(\lambda - |\kappa| + \dfrac{1}{2}\right)_n}{\left(\dfrac{1}{2} + \lambda\right)_n n!} \sin^{2n}\left(\frac{\theta}{2}\right). \tag{225}$$

And we have with (211):

$$\left(n + \lambda + |\kappa| - \frac{1}{2}\right)\left(\lambda + |\kappa| - \frac{1}{2}\right)_n = \left(\lambda + |\kappa| - \frac{1}{2}\right)\left(\lambda + |\kappa| + \frac{1}{2}\right)_n. \tag{226}$$

We then obtain:

$$\frac{U}{\sin^{\lambda}(\theta)} = \left(\lambda + |\kappa| - \frac{1}{2}\right)\cos\left(\frac{\theta}{2}\right)\sum_{n=0}^{n=|\kappa|-\lambda-\frac{1}{2}}\frac{\left(\lambda + |\kappa| + \frac{1}{2}\right)_n\left(\lambda - |\kappa| + \frac{1}{2}\right)_n}{\left(\frac{1}{2} + \lambda\right)_n n!}\sin^{2n}\left(\frac{\theta}{2}\right).$$

(227)

Comparison with (212) indicates, for $\lambda > 0$:

$$U_{(\kappa = |\kappa|)} = \frac{\lambda + |\kappa| - \frac{1}{2}}{\lambda - |\kappa| - \frac{1}{2}}U_{(\kappa = -|\kappa|)}.$$

(228)

Next for V we start from (207) which gives:

$$\frac{V}{\sin^{\lambda}(\theta)} = \cos^2\left(\frac{\theta}{2}\right)\sum_{n=0}^{n=|\kappa|-\lambda-\frac{1}{2}}n\frac{\left(\lambda + |\kappa| - \frac{1}{2}\right)_n\left(\lambda - |\kappa| + \frac{1}{2}\right)_n}{\left(\frac{1}{2} + \lambda\right)_n n!}\sin^{2n-1}\left(\frac{\theta}{2}\right)$$

$$-\left(\lambda + |\kappa| - \frac{1}{2}\right)\sum_{n=0}^{n=|\kappa|-\lambda-\frac{1}{2}}\frac{\left(\lambda + |\kappa| - \frac{1}{2}\right)_n\left(\lambda - |\kappa| + \frac{1}{2}\right)_n}{\left(\frac{1}{2} + \lambda\right)_n n!}\sin^{2n+1}\left(\frac{\theta}{2}\right).$$

(229)

The first sum splits into two sums by using $\cos^2(a) = 1 - \sin^2(a)$:

$$\frac{V}{\sin^{\lambda}(\theta)} = \sum_{n=0}^{n=|\kappa|-\lambda-\frac{1}{2}}n\frac{\left(\lambda + |\kappa| - \frac{1}{2}\right)_n\left(\lambda - |\kappa| + \frac{1}{2}\right)_n}{\left(\frac{1}{2} + \lambda\right)_n n!}\sin^{2n-1}\left(\frac{\theta}{2}\right)$$

$$-\sum_{n=0}^{n=|\kappa|-\lambda-\frac{1}{2}}n\frac{\left(\lambda + |\kappa| - \frac{1}{2}\right)_n\left(\lambda - |\kappa| + \frac{1}{2}\right)_n}{\left(\frac{1}{2} + \lambda\right)_n n!}\sin^{2n+1}\left(\frac{\theta}{2}\right)$$

$$-\left(\lambda + |\kappa| - \frac{1}{2}\right)\sum_{n=0}^{n=|\kappa|-\lambda-\frac{1}{2}}\frac{\left(\lambda + |\kappa| - \frac{1}{2}\right)_n\left(\lambda - |\kappa| + \frac{1}{2}\right)_n}{\left(\frac{1}{2} + \lambda\right)_n n!}\sin^{2n+1}\left(\frac{\theta}{2}\right).$$

(230)

The first sum begins truly with $n = 1$ and we let $n = 1 + n'$. We group together the last two sums:

$$\frac{V}{\sin^{\lambda}(\theta)} = \sum_{1+n'=1}^{1+n'=|\kappa|-\lambda-\frac{1}{2}}\frac{\left(\lambda + |\kappa| - \frac{1}{2}\right)_{1+n'}\left(\lambda - |\kappa| + \frac{1}{2}\right)_{1+n'}}{\left(\frac{1}{2} + \lambda\right)_{1+n'} n'!}\sin^{2n'+1}\left(\frac{\theta}{2}\right)$$

$$-\left(n + \lambda + |\kappa| - \frac{1}{2}\right)\sum_{n=0}^{|\kappa|-\lambda-\frac{1}{2}}\frac{\left(\lambda + |\kappa| - \frac{1}{2}\right)_n\left(\lambda - |\kappa| + \frac{1}{2}\right)_n}{\left(\frac{1}{2} + \lambda\right)_n n!}\sin^{2n+1}\left(\frac{\theta}{2}\right).$$

(231)

In the first sum we replace n' by n and we add a null term that changes

nothing. In the second sum we again use (211), this gives:

$$
\frac{V}{\sin^{\lambda}(\theta)} = \sum_{n=0}^{n=|\kappa|-\lambda-\frac{1}{2}} \frac{\left(\lambda+|\kappa|-\frac{1}{2}\right)_{1+n}\left(\lambda-|\kappa|+\frac{1}{2}\right)_{1+n}}{\left(\frac{1}{2}+\lambda\right)_{1+n} n!} \sin^{2n+1}\left(\frac{\theta}{2}\right)
$$
$$
-\left(\lambda+|\kappa|-\frac{1}{2}\right)\sum_{n=0}^{|\kappa|-\lambda-\frac{1}{2}} \frac{\left(\lambda+|\kappa|+\frac{1}{2}\right)_{n}\left(\lambda-|\kappa|+\frac{1}{2}\right)_{n}}{\left(\frac{1}{2}+\lambda\right)_{n} n!} \sin^{2n+1}\left(\frac{\theta}{2}\right).
$$

(232)

This implies:

$$
\frac{V}{\sin^{\lambda}(\theta)} = \left(\lambda+|\kappa|-\frac{1}{2}\right)\sum_{n=0}^{n=|\kappa|-\lambda-\frac{1}{2}} \frac{\left(\lambda-|\kappa|+\frac{1}{2}\right)_{n}\left(\lambda+|\kappa|+\frac{1}{2}\right)_{n}}{\left(\frac{1}{2}+\lambda\right)_{n} n!}
$$
$$
\times \left[\frac{\lambda-|\kappa|+\frac{1}{2}+n}{\lambda+\frac{1}{2}+n}-1\right]\sin^{2n+1}\left(\frac{\theta}{2}\right)
$$
$$
= -|\kappa|\left(\lambda+|\kappa|-\frac{1}{2}\right)\sum_{n=0}^{n=|\kappa|-\lambda-\frac{1}{2}} \frac{\left(\lambda-|\kappa|+\frac{1}{2}\right)_{n}\left(\lambda+|\kappa|+\frac{1}{2}\right)_{n}}{\left(\frac{1}{2}+\lambda\right)_{1+n} n!} \sin^{2n+1}\left(\frac{\theta}{2}\right).
$$

(233)

Comparison with (220) proves:

$$
V_{|\kappa>0} = -\frac{\lambda-|\kappa|-\frac{1}{2}}{\lambda+|\kappa|-\frac{1}{2}} V_{|\kappa<0}; \; UV_{|\kappa>0} = -UV_{|\kappa<0}
$$

(234)

Neutrino Temporal Oscillation

Russell Bagdoo

Saint-Bruno-de-Montarville, Quebec, Canada
Email: rbagdoo@gmail.com, rbagdoo@yahoo.ca

Abstract

We conjecture the existence of massless neutrinos that are in the line of Standard Model (unable to account for the neutrino mass) but have characteristics that are not accounted for the Standard Model: they use a shorter radial path than the photon and possess bosonic flavors, considered like bosons instead of fermions. We call this theory "neutrino temporal oscillation". Faced with some experimental comparisons solar neutrinos, neutrinos from SN 1987A, cosmological neutrinos, the theory gives better results, explanations and sense than the complicated theory of neutrino oscillations (transformism). The deficit of detection of solar neutrinos would have been blindly attributed to the "neutrino oscillation" by physicists who quickly concluded that the neutrino and the photon follow the same transverse path. The "OPERA" experiment which measured the speed of neutrinos in 2011 resulted, after a "superluminal" saga, in neutrino speeds consistent with the speed of light, in data that the three existing types of neutrinos cannot explain, with the final outcome of a fourth "sterile" neutrino with non-standard interaction. OPERA findings aren't just in conflict with existing theory, but other measurements as well. For example, a study from the Kamiokande II experiment in Japan of the supernova SN1987A found that light and neutrinos that departed this exploded star arrived at Earth within hours of each other. Even though measurements of the neutrinos emitted by this supernova strongly suggest that their speeds differ from light by less than one part in a billion, the fact remains that two types of data were collected, and that only one was retained to be consistent with the existing theory. Thus, the OPERA observation is in conflicts with the result of SN1987A, which itself is highly doubtful. And what about the neutrinos and antineutrinos born during the big bang, except that they were never detected and there is nothing to indicate that their speed could be other than that of light. Neutrino physics seems sick, belief is transformed into evidence. The theory of "Neutrino temporal oscillation" shows hint that massless neutrinos can take a shortcut through the three spatial dimensions of the space-time that we know. It represents within the Standard Model an open window on a "new physics" that has a connection

with physical reality.

Keywords

1. Introduction

1.1. History of the Neutrino

In 1930, Wolfgang Pauli rescues conservation of energy by hypothesizing an unseen particle that takes away energy missing from some radioactive decays. Enrico Fermi in 1933 formulates the theory of beta-decay incorporating Pauli's particle, called the neutrino (little neutral one). Frederick Reines and Clyde Cowen first detect the neutrino in 1956 and at Brookhaven in 1962 the first accelerator beam of neutrinos proves the distinction between electron-neutrinos and muon-neutrinos. In 1969, Raymond Davis, Jr., first measures neutrinos from the Sun, using 600 tons of cleaning fluid in a mine in Homestake, S.D. The tau lepton and b quark are discovered in 1975-1977, revealing a third generation of quarks and leptons. W and Z bosons are discovered at CERN in 1983: they are carriers of the weak force, which mediates neutrino reactions. The Z decay rate was measured at SLAC and CERN in 1989, showing there are only three active neutrino generations. In 1987, the IMB and Kamiokande proton decay experiments detect 19 neutrinos from Supernova 1987A in the Large Magellanic Cloud [1].

1.2. The Theory of Neutrino Oscillations

The theory of neutrino oscillations arises in the late 1990s. Neutrinos were found to have mass and a speed under the light speed after having thought the opposite for decades. Since then, neutrinos metamorphose: they shift among three known neutrino types. As they propagate at nearly the speed of light through space, the celestial bodies, or our body, they often change identities, oscillating between three varieties, or "flavors", the electron, the muon and the tau. Quantum mechanics permits neutrinos to oscillate between flavors only if they have mass and if each flavor has a different mass. Super-K in 1998 assembles evidence of neutrino oscillation using atmospheric neutrinos [2].

1.3. Cosmic Mismatch Hints at the Existence of an Enormously Heavy Neutrino or a Lightly Sterile Neutrino

All neutrinos are classified as leptons, meaning that they do not feel the strong force and, lacking electrical charge, they do not feel electromagnetic forces, ei-

ther. That leaves the weak interaction and the force of gravity for the three known flavors. Neutrinos must be left-handed to feel the weak force, responsible for radioactive decay. Theorists know that they have mass (a rest mass referring to the mass that matter is made out) but not how much, that they come in at least three flavors but there may be more. They hint that a fourth type of hitherto unseen neutrino exists. Even if particles physicists would prefer a new type of neutrino enormously heavy, theorists perceive them with a little bit of mass, enough to have the ability to swap flavors [3]. Very sensitive experiments have revealed that neutrinos do have a very small non-zero rest mass: in 2019, KATRIN (Karlsruhe Tritium Neutrino experiment) scientists estimated that the range for the rest mass of the neutrino is no larger than about 1 eV. Therefore, they travel at a speed very close to *c* but slightly lower.

1.4. Neutrinos with Zero Rest Mass

In 2007, an experiment on neutrinos created at Fermilab in Illinois and beamed through the Earth to the Soudan Mine in Minnesota showed that the neutrino speeds were consistent with the speed of light. Measurements of neutrinos emitted from a supernova in the Large Magellanic Cloud in 1987, moreover, suggested that their speeds differed from light by less than one part in a billion. This suggests the existence of neutrinos without rest mass, as originally planned. Once thought to be massless and to travel at the speed of light, the neutrinos can sail through walls and planets like wind through a screen door. By Einstein's equation $E = mc^2$, a particle's total energy or *mass-energy* includes the particle's rest mass and momentum. When a nucleus goes through the process of beta decay, the electrons that are emitted have a range of kinetic energies. This variation confirms that there is an extra particle in the mix. If neutrinos have a nonzero rest mass, then the very high end of the electron energy spectrum will be slightly distorted, and the highest electron energy will be less than the maximum possible energy by a very small amount—the tiny mass of the neutrino. So far, investigators have managed to observe only a non-significant distortion at the end of the energy spectrum. Therefore we still can consider that a moving neutrino's mass-energy comes mainly from its momentum [4]. Neutrinos are massless in the Glashow-Salam-Weinberg Standard Model [5] [6] [7].

During the years 2009 to 2011, neutrino beams were fired repeatedly from CERN towards a detector in Italy's Gran Sasso tunnel, some 4° south and 7° east of CERN, at a distance of 730 km, in the shape of short bunches of particles. Their time of flight (2.5 msec) was measured at high accuracy (ns) with caesium clocks. In 2011, the CNRS team found a deficit of ~57.8 ns compared with propagation at the speed of light, and announced a superluminal speed. In 2012, the Italian OPERA scientists reported that the neutrinos "respect the cosmic speed limit" and that there was an error in the speed measurement due to an incorrectly screwed cable of the experiment's fiber-optic timing system [8]. It turns out the master clock in charge of keeping time for the experiment was also

improperly calibrated. Ironically enough, this miscalibration would make the neutrinos appear to travel slower, but this error wasn't large enough to cancel out the faulty cable. Accounting for these two sources of error eliminated the faster-than-light results. The difference between the measured and expected arrival time of neutrinos (compared to the speed of light) was approximately 6.5 ± 15 ns. Thus, the speed of neutrinos is consistent with the speed of light within the margin of error. It was the end of the apparently faster-than-light neutrino anomaly for most scientists.

For some, it is always an open question. We agree that the speed of neutrinos is consistent with the speed of light. But the difference between the measured and expected arrival time of neutrinos, although it was greatly reduced compared to the initial results (from ~57.8 ns to ~6.5 ± 7.4 ns), is still longer than the expected time of the neutrinos. This is an indication that even if there is no faster-than-light neutrino speed, the neutrinos followed a shorter path and makes our theory plausible.

Even though OPERA's counter-expertise is convincing, its findings do not fall within the margin that would make the faster-than-light appearance indefensible. Often theorists take the results of some retests for granted because they reinforce their definitive conceptions of science. We have set out this point of view in the article *Recycled Relativity* [9]. In this regard, we present in Section 2 an *ad hoc* formula for the CERN apparently superluminal neutrino while respecting the principle of the speed limit of light. In Section 3 we submit the theory of neutrino temporal oscillation which incorporates the longitudinal wave. In section 4 we confront this theory with the experimental observations relating to the solar neutrino, the supernova 1987A and the cosmological neutrino. We suggest the new "bosonic" flavors. Discussion in Section 5: Analysis of the proposed theory where neutrinos at the speed of light follow a shortcut in space-time and of the current theory where massive neutrinos metamorphose by moving with a speed below the speed of light. Finally, we conclude in Section 6.

2. *Ad Hoc* Formula for the CERN Apparent Superluminal Neutrinos

Are we going to believe a measure of complacency? Recall that the physics is not completed, as well as those experiences, and we want to explore the hypothesis that neutrinos detected by Opera have apparently traveled faster than light, while respecting the inviolability of the speed of light which is the pivot of relativity. We suggest the following *ad hoc* formula which gives the apparent drift of the supraluminal neutrino without violating the sacred principle of speed light invariance

$$v_o = c / \left(1 - v^2/c^2\right)^{1/2} = c / \left[1 - GM_E / \left(R \sin x c^2\right)\right]^{1/2}. \tag{1}$$

(GM_E/c^2 is the Schwarzschild radius of Earth, or the interval the space ds^2; v_o is the apparent superluminal speed of the neutrino; c is the static speed of propa-

gation; v is the velocity of the source; R is the distance done by the photon between the emitter and the receiver; $R\sin x$ is the distance traveled by the neutrino between the transmitter and the receiver.)

Since we know the distance (730 km), the journey time (2.4 milliseconds) and the anticipation of neutrinos of 60 nanoseconds on this distance compared with photons, one can express 60 nsec in terms of distance on the distance of 730 km, or 18.25 m (750 km × 60 nsec/2.4 msec).

We assume that the apparent superluminal velocity of the neutrino at the end of the trip of 2.4 milliseconds is at least 299,792,476.3 m/s ($v_o = c + 18.25$ m $= 299792476.3$ m/s).

299792476.3 m/s $= c/\left(1 - v^2/c^2\right)^{1/2}$; v^2 is equivalent to 105 km/s squared. In general relativity, v^2 acts as gravitational potential.

$$299792476.3 \text{ m/s} = c/\left(1 - \Phi/c^2\right)^{1/2} = c/\left[1 - GM_t/\left(Rc^2\right)\right]^{1/2} \tag{2}$$

Although GM_E/c^2 is the Schwarzschild radius, or the interval of space ds^2, R is not the radius of the Earth but represents a journey of 730 km that a photon would do if he left from the Earth's center. However, a neutrino would not follow the transversal path of the photon but a radial path that would be 730 $\sin x$ km.

$$299792476.3 \text{ m/s} = c/\left(1 - GM_t/730000\sin xc^2\right)^{1/2}$$
$$= c/\left[1 - G5.98 \times 10^{24} \text{kg}/\left(730000\sin 2.85° c^2\right)\right]^{1/2} \tag{3}$$

$x = 2.85°$ indicates a radial path. 730,000 $\sin 2.85°$ reduces to 36.3 km the path radially traveled by the neutrino at speed apparently superior to light.

We can imagine with difficulty that a neutrino crosses radially 36.3 km through the superimposed curvatures of the Earth to arrive slightly before a photon having traveled 730 km. This formula is not a guarantee of validity, but an interesting mathematical option. It has the merit of leaving the speed apparently faster than the speed of light and illustrates the trend of the neutrino to follow a shortened radial path rather than a transverse path. Without significant comparison with what follows, except for the shortened course, it preludes the "neutrino temporal oscillation" which stands out with a non-exceeded speed of light.

3. Theory of Neutrino Temporal Oscillation

3.1. Uncertainty of Neutrino Oscillations

Scientists of neutrino do not know its mass, its energy, the distance it travels, and if they know how much between two points they are unable to tell what path he traveled. Moreover, they ignore its speed. What do they know? Statistical averages. And a nice theory, the neutrino oscillations, which says that the neutrino has a mass and this ability to metamorphose. Like all elementary matter particles, they come in three versions, called flavors. The electron (e) has two heavier replicas, the muon (μ) and the tau (τ), and each has a neutrino partner: the

electron-neutrino (v_e), the muon-neutrino (v_μ) and the tau-neutrino (v_τ). But whereas the electron, the muon and the tau have specific masses, the three neutrino flavors do not. If you measure the mass of a neutrino with a given flavor, you get one of three answers at random, with a certain probability for each. Conversely, if you measure the flavor of a neutrino with a given mass, you get one of three answers. A neutrino can have either a specific flavor or specific mass but not both at the same time. Neutrinos thus violate a basic intuition we have about objects [10]. With the glorious uncertainty of this dominant theory, an alternative or complementary theory would not be superfluous.

3.2. Neutrino Temporal Oscillation

We term "temporal oscillation" an economy of time generated by a wave intrinsically less broad than the standard wave. It is also a quantum mechanical phenomenon whereby a neutrino created with a specific bosonic flavor (neutrino-photon, neutrino-graviton) can later be measured to have a different flavor. Flavors will be addressed in Section 5. We begin by the first part of the definition.

3.3. What Is the Shortest Line? Transversal Way for the Photons and Shorter Longitudinal Way for the Neutrinos

Right now the path taken by a photon actually defines what a straight line is. But is it the shortest distance between two points? Concerning an undulation, we think it is the longest path. Grossly, we consider two kinds of paths for a particle at the speed of light: transversal way and longitudinal way (or radial). Science picks up electromagnetic waves and so measures the universe. They follow a transversal path. There is a transverse wave when the oscillatory motion of any part of the system is at right angles to the direction in which the wave is traveling. There is a longitudinal wave when the oscillatory motion of a part of the system is in the same direction that the wave is traveling.

The sinusoid ACBDE of the following drawing shows two semi-circumferences ACB and BDE. If we put the two half-circumferences of the sinusoid directly on top of each other, they form a concentric circle. The diameter d (AOB = BO'E) divides the circumference and the circle into two equal parts. The radius OC, OB, O'B, O'D are equal.

The photon follows a transverse wave at the speed of light. Its measurement between A and E is that of the sinusoid ACBDE, or the circumference of the concentric circle having O (or O') at the center. We postulate the existence of a sort of neutrinos with a mass equal to the mass of light, the lightest known mass. The measurement of the neutrino at the speed of light between A and T (we use T of the word Time in Figure 1) is the radial line (or longitudinal) AOBO'ET. When the photon has traveled the metric of the sinusoid ACBDE equivalent to the circumference of a circle with O (or O') at the center, the neutrino has traveled radially πd, as if we undid the circumference for stretch it in a straight line (Figure 2). We associate the photon to the circumference and the neutrino to the diameter.
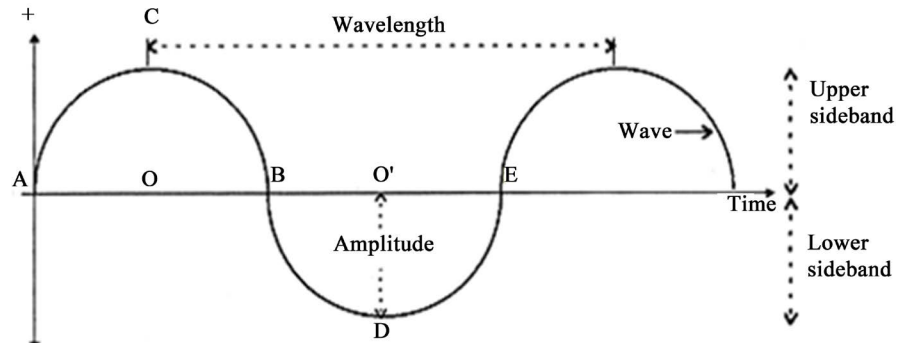
Figure 1. Sinusoid. (While the photon follows the transverse wave $t_o c$ on the sine wave ACBDE (equivalent to a circle) at the speed of light, the neutrino follows the longitudinal wave tc along the radial sinusoid AOBO'ET(equivalent to ~π diameter) at the speed of light. The ordinary transverse second of the photon is ~π times longer than the longitudinal second of the neutrino: 1 second t = ~π second t_o.)
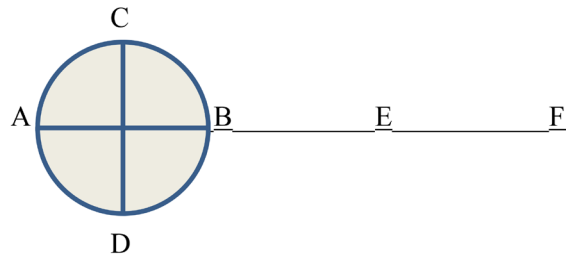
Figure 2. "Radial" sinusoid. (The longitudinal wave $t_o c$ of the neutrino follows the flattened sinusoid ABEF while the transverse wave tc of the photon follows the sinusoid ACBDE of **Figure 1**, equivalent to the ACBD circumference in **Figure 2**. The neutrino is associated with diameter. The photon is associated with the circumference.)

In other words, we pretend that the massless neutrino follows the longitudinal way (or radial) while the photon follows the transversal way. The term $t_o c$ represents a longitudinal wave and 1 sec (t_o) is the second of the neutrino associated with the longitudinal way. The term tc means a transverse wave and 1 sec (t) is the second of the particle associated with transversal way. In circular time (or Newtonian time), which is the one we use, 1 second corresponds to π linear seconds: 1 sec (t) = π sec (t_o). The ordinary transverse second t is 3.1416 times longer than the longitudinal second t_o. Both particles go to the speed of light, so

$$t_o c / t_o = \pi t_o c / \pi t_o = tc/t = c . \tag{4}$$

This means that if a particle has to travel the distance $AB = \lambda = t_o c$, it will take t_o time. Then the wave and the particle are propagating at the speed of light, and the direction in which the wave is traveling and the line of the oscillatory motion of the particle are making one line. But if the oscillatory motion of the particle is at right angles to the direction in which the wave is traveling, the time required for the particle to travel from A to B is $\pi t_o c$, because the particle is covering $\pi t_o c$ distance, running in circle around the line AB. Note that we should say about π, or about 3, because we must envision the encirclement of a spiral structure instead of a closed two dimensions circle.

3.4. Discussion: Range of Longitudinal Waves and the Rule of the Displacement of the Nodes Due to the Inverse Sine

We suppose that in most of the cases, the neutrino follows a different path from the photon to browse the same distance, even if it keeps the speed of light. It means that the sinusoid traveled by the neutrino flattens, becomes "radial", what drives knots further away on the straight line AF (Figure 2). The sinusoid being completely spread over the radial line, we can say that when a photon travels a radius with regard to a circumference, the neutrino browses linearly π time this distance, what amounts to a half-circumference; when the photon travels a diameter, the neutrino travels radially π diameters, *i.e.* equivalent to a circumference.

Most neutrino physicists believe that the neutrino follows the same path the photon and that the transverse path of the photon is the straight line. That is not supported by the fact that according to our theory of temporal oscillations, the longitudinal path of the neutrino turns out to be the straight line. It follows that an observer B, who anticipates to receive from A in one ordinary second (transverse), a full neutrino flux will be surprised to receive just about thirty-three percent of the expected flux, the two other thirds having already reached the F point. However, it is assumed that there is a range of wavelength between the transverse wave and the radial wave. The current theory of neutrino oscillation (transformism) follows the transverse way perpendicular to the radial direction of the wave. In this case, the neutrino, lively at speed c, follows the same sinusoid that the photon between nodes A and E on Figure 1 and travels the same metric at the same time. The second of the photon is then equivalent to the second of the neutrino and can be imagined by using a kind of rule of displacement of nodes due to the trigonometric function cosecant defined as the inverse sine. This rule of an angular cosecant is a simple supposition. So, for the time factor:

$$1 \sec t_o \text{ for the neutrino} (v) \big/ \text{sine} \, 90° = 1 \sec t \text{ for the photon} (\gamma). \qquad (5)$$

The intent is to show that the photon travels from A to B via C in one transversal sec and that the neutrino flies in the same way from A to B in one transversal sec. Sine 90° indicates that they follow the same transverse path, or *spiral*. Considering the distance factor in this case, the photon and the neutrino travel the same distance, we can write

$$1 \text{ m } t(\gamma) \big/ \text{sine} \, 90° = 1 \text{ m } t_o(v). \qquad (6)$$

If we suppose in terms of time a displacement of the nodes due to the inverse sine 85°, we obtain

$$1 \sec t_o(v) \big/ \text{sine} \, 85° = 1.0038198 \sec t(\gamma). \qquad (7)$$

Thus, we can say that to go from to A to F (due to sine 85°), the neutrino uses 1 longitudinal sec whereas the photon uses 1.0038198 transversal sec. In terms of length, we can put

$$1 \text{ m } t(\gamma) \big/ \text{sine} \, 85° = 1.0038198 \text{ m } t_o(v). \qquad (8)$$

Consider the 730-kilometre trip from CERN in Switzerland to the Gran Sasso

underground laboratory in Italy. Suppose that photons and neutrinos start at the same time and make the journey in a straight line. The agreed line is that of the transverse photon. While the photon complete 730 km, the longitudinal neutrino passing through the Earth at light speed would have traveled 2294 km (730 × π). If we apply in terms of distance the displacement of the nodes due to the inverse sine,

$$1 \text{ m } t(\gamma)\big/\text{sine}\,18°.5607 = 3.14159 \text{ m } t_o(v). \tag{9}$$

While the photon travels a circle that seems to merge with a diameter in the radial direction of propagation, the neutrino moves around 3.14159 m; the length of the straight neutrinos is

$$730 \text{ km } t\big/\text{sine}\,18°.56075 = 2294 \text{ km } t_o. \tag{10}$$

This means that the 730 km serpentine path of the electromagnetic particle is radially stretched over a distance of 2294 km. In terms of time,

$$1 \sec t_o(v)\big/\text{sine}\,18°.56075 = 3.14159 \sec t(\gamma), \tag{11}$$

which signifies that the photon goes from A to E along a transverse path (sinusoid ACBDE on **Figure 1**) in 3.1415917 radial sec while the neutrino travels from A to B along a longitudinal path in one radial sec. We can also say that the photon travels from A to B along a transverse path (equal to the straight line ABEF on **Figure 2**) in 1 sec *t* while the neutrino goes radially from A to B in 1 sec *t*/π.

3.5. About the Longitudinal Wave

By scanning the history of longitudinal and transverse waves we notice a kind of cycle, the periods of longitudinal wave which alternate with the periods of transverse wave. The theory of Huygens, contemporary of Newton, was based on a profound analogy between light and sound waves. One hundred fifty years later, Fresnel was led to assume that light does not consist of longitudinal vibrations, such as those of sound in air, as Huygens thought, but transversal, and that alone a special medium having the properties of a hard body could convey them in universal space. Poisson discovered that the waves in an elastic solid are of both kinds: transverse and longitudinal. To rule out the contradictions which, in a series of cases arose from both theories, Maxwell thought that light does not consist of Huygen's longitudinal waves neither of Fresnel's transverse waves of ether, but in waves of an autonomous electromagnetic field. H.A. Lorentz showed that the electromagnetic theory of Maxwell, explained by the mechanical theory of ether, required the introduction, in addition to the light waves, of longitudinal waves of ether [11] [12] [13].

While it is recognized that the longitudinal waves propagate in air, liquid and solid, modern mainstream technology has been optimized to deal solely with transverse waves and is therefore largely incapable of measuring, let alone detecting, longitudinal waves. We still found some books on physical electronic introducing longitudinal theories, such as the longitudinal space-charge wave theory [14].

Since Einstein rejected the ether as superfluous, only the transverse waves can propagate in the vacuum. Physicists consider that it is mathematically and geometrically impossible for a longitudinal wave to have both electric and magnetic components simultaneously. For this reason physicists dismiss the possibility of longitudinal E/M waves.

A changing voltage field can give rise to concussive waves that are radiated away in the direction of propagation. The fluctuations, with a curl-free vector potential and without magnetic fields, are longitudinal rather than transverse. These longitudinal waves are what Maxwell termed *displacement* current. They do not violate Maxwell's equations that state there must be an induced magnetic field for every change in the electric field. There is a longitudinal E/M wave when *all the magnetic fields cancel and yet there is still a displacement current*. Usually current is defined as a flow of charges, but across a capacitor consisting of two conductors separated by an insulator that allows no charge to pass, oscillating energy can still transfer. Aside from a changing voltage field, current flows from a large flat metal plate charged to a steady high voltage can give rise to a steady electric field pointing out and away from the plate in the direction of radiation. The resulting wave that also fluctuates in the direction of propagation is longitudinal.

Maxwell equations allow two possibilities: transverse EM waves and longitudinal E/M wave. Longitudinal E/M waves are just as real as transverse EM waves but are more difficult to detect. The assumption that "what cannot be measured does not exist" fails to take into account that the shortcoming might be with technology rather than reality.

4. Comparisons with Experimental Observations

4.1. Solar Neutrino

In the 1929s and 1930s, scientists proposed [15] [16] [17] that nuclear fusion reactions among light elements occur near the centre of the Sun and provide the energy that the Sun has emitted for four-and-a-half billion years [18]. The simplest of all possible reactions is the nuclear reaction in proton-proton (p-p) collisions, which yields low-energy neutrinos: $H + H = D + e^+ + v$. The deuterons formed will quickly react further, and the end product of p-p reaction of hydrogen is helium. 98 percent of the Sun energy comes from the nuclear reaction chain p-p [19]. While most of this energy ends up as electromagnetic radiation from the surface, approximately three per cent are believed to be emitted directly from the centre of the Sun in the form of neutrinos [20].

Knowing the energy radiated by the Sun and the part of fusion energy carried away by a neutrino, we easily deduce the amount of neutrinos escaping from the Sun per unit of time. The Sun produces only electron neutrinos. We therefore deduce, aware of the Earth-Sun distance, the theoretical neutrino flux per unit area and per unit time at the level of Earth. The flux of neutrinos at Earth is several tens of billions per square centimetre per second. They cross the entire

Earth, interact weakly with matter and are difficult to detect. From the characteristics of the detector, the amount of neutrinos that is to be detected per day in this flux is found. All experiments (on different time scales, with many detectors based on different principles) to measure the flow of electronic neutrinos from the Sun showed that the number detected was much lower than predicted. In various experiments, with detectors that became very sensitive, the number deficit was between one half and two thirds.

Few separate experiments to detect neutrinos from the Sun which confirmed a deficit in the flux relative to the predictions of standard theories of nuclear physics, have led to suggestions that neutrinos may have small masses and may oscillate between different types. In 1968, Pontecorvo proposed that if neutrinos had mass, then they could change from one type to another [21]. Essentially, the "missing" solar neutrinos could be electron neutrinos which changed into other types along the way to Earth and therefore were not seen by the detectors in the Homestake Mine in the late 1960s and contemporary neutrino observatories. Thus, the discrepancy between measurements of the numbers of neutrinos flowing through the Earth and theoretical models of the solar interior, lasting from the mid-1960s to about 2002, has since presumably been resolved by new understanding of neutrino physics, requiring a modification of the Standard Model of particle physics—specifically, neutrino oscillation.

That being said, we believe that a significant alternative could explain why the measurements of solar neutrino fluxes all agree with theoretical expectations to within a factor of two or three and why persistent deficits of electron-type neutrinos exist in all solar-neutrino experiments. In line with the theory "neutrino temporal oscillation", the fundamental error is to believe that the neutrino and the photon follow the same transverse path, and that it is the shortest way. The longitudinal path (straight line) is shorter than the traverse path (the curve). The solar neutrino would have a longitudinal wave and its time would be about one third of the time of the photon. The second of the neutrino is therefore approximately one third of the second of the photon (or the Newtonian second). If $1t_o$ is the second of the neutrino, then t, or $1\pi t_o$, is the second of the photon ($1\pi t_o = 1t$). During one second of the photon, the neutrino will have travel $1\pi t_o c$, say π times more distance in straight line than the photon ($1t/\pi = 1t_o c$). As physics uses the ordinary transverse second of the photon which is ~3.1416 times longer than the longitudinal second to calculate the neutrino flux, it appears that the neutrino flux for the distance $1t_o c$ will be about 3 times less dense, because the flux of neutrinos expected by the usual second of the light is spread over a radial path two or three times more distant.

In short, physicists have predicted detect in one "ordinary" second a number of electron neutrinos consistent with physical models of the Sun's interior. Only a third to half the predicted number of neutrinos has been detected. The theory of neutrino temporal oscillation, without requiring a neutrino rest mass, explains the difference like this: the neutrino flux travels radially, not transversely, which means a solar neutrino flux anticipated in an ordinary second divided by

a number between two or three.

Imagine that a flux of 730 million solar neutrinos per second, having theoretically traveled through a transverse wave, is expected on Earth as predicted from the luminosity of the Sun. We can write

$$730 \text{ million } \sin 90° = \text{flux of 730 million neutrinos per second.} \qquad (12)$$

If the flux measured directly is 243 million neutrinos, *i.e.* one third of what was expected; we are entitled, to explain the difference, to assume that the neutrinos traveled a less transverse, more longitudinal wave, as if the nodes were stretched radially. Depending on the flow detected we can calculate

$$730 \text{ million } \sin 19.451° = \text{flux of 243 million neutrinos per second.} \qquad (13)$$

4.2. Supernova 1987A

In February 1987, SN 1987A was the first nearby supernova that could be seen well since 1604. It was located about 168,000 light years (ly) from Earth in the Large Magellanic Cloud, a small galaxy gravitationally linked to the Milky Way. The energy calculated to be produced from the collapse of type II supernovae is almost 1000 times larger than that observed as light. Standard astrophysical theory indicates that more than 99 per cent of the energy is emitted in the form of neutrinos [22] and holds that a collapsing star should release a burst of neutrinos before the light from the explosions.

The Mont Blanc team believed that they had discovered such a burst. On 24 February 1987, the Italian/Soviet collaboration was the first to report a burst of neutrinos from SN 1987A, detected at their underground observatory at Mont Blanc, after other astronomers had reported optical observation of the supernova [23]. But four and a half hours (h) after the Mont Blanc burst, which consisted of five events over several seconds, a series of pulses in two water Cerenkov detectors were recorded independently, Kamiokande [24] in Japan, IMB [25] in the United States and also by the Baksan detector in Russia. In all, 24 neutrinos were captured. Given both bursts, 7.7 h had elapsed before the first light was observed [26] [27].

According to the basic theory of stellar collapse, there is an expected time delay of approximately 3 h between the collapse of the core and the production of visible light at the surface of the star, due to the propagation of a shock wave through the stellar material. How come that the first neutrinos of the supernova 1987A arrived 7.7 h before the first photons? The currently-accepted interpretation of this data is that the first burst of neutrinos must not have been associated with the supernova because there is no conventional explanation for how the neutrinos could have arrived at that time. In addition, the fact that the first burst of neutrinos was only detected by the Mont Blanc detector and not the other two detectors, which were assumed at the time to have higher sensitivities, further suggested that the first burst of neutrinos must have been an anomaly that was not associated with Supernova 1987A. This suggests that the first observation of the visible light from the supernova is compatible only with the second burst of

neutrinos that occurred about three h before, which corresponds to the time for any light produced inside the star to be prevented, due to the diffusion, from reaching immediately the surface.

Nevertheless, we agree with some experts in the field who consider the origin of the first burst of neutrinos to be an open question because the probability of such an event having occurred at random has been estimated to be less than 10^{-4} [28] [29]. The material used in the Mont Blanc detector was different from that used in the other two detectors and the expected sensitivity of detection for the kind of neutrinos in the first burst has been estimated to be a factor of 20 higher in the Mont Blanc detector than the other detectors, which is consistent with the observations [29].

4.2.1. Scenario of a Double Collapse

The possibility was expressed that both the Mont Blanc detection and the later bursts recorded simultaneously in the United States and Japan, could have been genuine events linked to SN 1987A [28]. This would require the star to have collapsed initially to a neutron star, releasing low-energy neutrinos picked up at Mont Blanc, but below the energy threshold on the IMB and Kamiokande devices. A second collapse to a black hole would then explain the neutrino burst recorded by IMB and Kamiokande. At Mont Blanc, this burst may have been indistinguishable from the background noise [30] [31].

This scenario is not expected from the models which predict only a single neutrino burst from a collapsing star and which anticipate the first observation of visible light from the supernova approximately 3 h after the burst of neutrinos. It is the expected time delay between the collapse of the core and the production of light at the surface of the star due to the propagation of a shock wave through the stellar material. The usual interpretation of this data is that the first burst of neutrinos must not have been associated with the supernova because there is no conventional explanation for how the neutrinos could have arrived at that time. Only the observed by IMB and Kamiokande 3 h fit with the conventional models.

4.2.2. The Theory of Neutrino Temporal Oscillation Justifies the Scenario of a Double Collapse

The theory of neutrino temporal oscillation offers an adequate explanation for the possibility of a double collapse of the core and the observations associated with SN 1987A. According to this theory, the neutrino is moving in a longitudinal wave, that is, the oscillatory motion of the neutrino is in the same direction that the wave is traveling. As mentioned earlier, the second of the neutrino belongs to the longitudinal wave, and is about one third $(1/\pi)$ of the Newtonian second, which is linked to transverse wave. It means that the neutrino browses π times more length in a radial path than the photon in a transverse path.

The two bursts of neutrinos from SN1987A were captured in longitudinal time, that is to say in the time associated with the longitudinal wave, while physicists believed to have captured them in transverse waves that are within the

transverse electromagnetic wave. This means that the 7.7 h between the first burst at Mont Blanc and the appearance of light are in longitudinal time, not in transverse time. 7.7 longitudinal h translate into 2.45 transverse h (7.7 h t_o/π = 2.45 h t). These 2.45 h correspond to the time predicted from the standard models, that is to say the approximate 3 h for the light to occur on the surface. This is the anticipated collapse of the star into neutron star.

It took 4.7 h between the second burst of neutrinos observed by Mont Blanc and the second burst of neutrinos observed by Kamiokande and IMB. These longitudinal 4.7 h are translated into transverse 1.5 h (4.7 h t_o/π = 1.5 h t). It means that the second burst of neutrinos, the one of the collapse of neutron star into black hole, starts 1.5 h after the first collapse. The second burst of neutrinos, 4.7 h after the first burst, 3 h before the light, signaled the second collapse of the core. It should be associated to a second production of visible light characterized by the increase in its intensity roughly 4.7 h after the initial onset of the light.

4.2.3. Confusion of Running Times

In our view, the 3 h between the second burst of neutrinos observed by IMB and Kamiokande and the arrival of light were wrongly coupled with the 3 h for that the shock wave coming from the core of the supernova reaches the surface. Because the IMB and Kamiokande observations fitted well with theoretical predictions based only on the transversal path of the photon, the general perception among astrophysicists was that the Mont Blanc burst was background noise, most probably caused by penetrating radiation from the surrounding rock, expected about once every three years from random fluctuations [22]. In addition, the detection of two distinct signals implies that the theory predicting only a single neutrino burst from a collapsing star is not right and has suggested that the first burst of neutrinos must have been an anomaly that was not associated with Supernova 1987A [26].

The 2 bursts of neutrinos match the 2 collapses of the supernova. Thus, the arrival time of the first burst of neutrinos is consistent with the observed light curve [26], and the second collapse of the core would have produced an increase in the intensity of the visible light not long after the arrival of first photons. This is consistent with the observation that the light signal increased more rapidly than would have otherwise been expected during that time interval. The theory of neutrino temporal oscillation is hence in reasonable agreement with the experimental observations and it provides a possible explanation for the first burst of neutrinos which is inconsistent with the conventional model of the supernova.

4.3. "Cosmological" Neutrinos

Under the Big Bang Standard Model, in the early days of the universe, there were as many particles of matter as there was antimatter. They interacted, met, and annihilated each other to become photons which in turn disappeared to give rise to particle-antiparticle pairs. These photons, later weakened by the expansion of the universe and its cooling, could no longer give birth to particles and antipar-

ticles. Nature having a preference for matter will ensure that for every billion particles and antiparticles that will annihilate to give 1 billion photons, only one particle of matter will remain, exactly the proportion that is observed in the current universe. All the antimatter disappears [32].

But a species born out of the big bang resisted: cosmological neutrinos and their *alter ego*, the antineutrinos. Their interactions ceased before their energy, which had become too low, forced them to annihilate like other particles. There are now more than a billion neutrinos and as many antineutrinos for a single proton. The existence and the precise abundance of cosmological neutrinos are confirmed by the study of primordial nucleosynthesis, when a few minutes after the Big Bang the temperature of the universe has dropped below a few billion degrees and protons and neutrons have could combine to form helium nuclei.

One can imagine that when the early universe was hot and dense, neutrinos were moving at the speed of light. In this state, they were not agglomerated under the force of their own gravitational pull. However, after the universe had cooled down and crossed the energy threshold, the neutrinos would have become relativistic, slowed down, and began to move with subluminal speeds. The three known types or "flavors" of neutrinos would therefore have acquired a low mass and the ability to transform from one flavor to another. This phenomenon, the oscillation of neutrinos, was discovered in the late 1990s. As a result, these neutrinos constitute a form of "dark" matter, that is, without significant interaction with matter other than through the force of gravity. Even though at least two of the three types of neutrinos have low mass, and participate in the formation of large structures in the universe, their influence on this formation is negligible. Although their eventual mass is not well known due to their weak interactions with matter, oscillations of neutrinos indicate that the mass of all three types confers on them a contribution of at least 0.13% in the total energy budget of the universe, where dark matter accounts for about 25% [33]. Neutrinos from the big bang have an energy that is millions of times lower than that of solar neutrinos and their direct detection is perhaps an unattainable dream.

4.3.1. "Sterile" Cosmological Neutrinos at the Speed of Light

There would be, according to us, another "sterile" type of neutrino which would not have slowed down and continued moving at light-speeds after the universe cooled. It would not be able to switch leptonic flavors, like the three types of neutrino with mass (neutrino-electron, neutrino-muon, neutrino-tau), but it would be able to switch *bosonic flavors* with the photon and the graviton [34]. It would interact less with ordinary matter than the known flavors, which already had become very reluctant to do so after the cooling of the universe.

This would not be the massive neutrino presaged by scientists who think that could explain the mismatch between observations of galaxy clusters and the cosmic microwave background (CMB) if neutrinos were more massive than is usually thought [35]. They suggest the possibility of discovering a right-handed neutrinos impervious to the weak force with a huge mass that does not rely on

the Higgs field, or to detect a heavy flavor that may emerge from a different mechanism altogether at the extremely high energies of grand unification [2]. "Sterile" cosmological neutrino at the speed of light would be akin to the concept of massless neutrino of the original Standard Model. All along the expansion, always at light speed, the frequency of elusive sterile neutrinos decreases. The lost energy is transformed into mass, clustering along with the rest of the matter, making a larger contribution to the total density of the universe. Besides being a cosmic chameleon which can change bosonic identity, this neutrino would have the peculiarity to follow a longitudinal wave. Thus, if the age of the universe was around 5 billion transverse ly, that would be tantamount to more than 15 billion longitudinal ly (5 billion ly $t \times \pi$). As known, in various ways, but based on electromagnetic waves, astrophysicists have established the age of the universe around fifteen billion ly. This would mean that there are neutrino waves that traveled radially over 45 billion ly, and that the linear radius of the universe would measure more than 45 billion ly (15×10^9 ly $t \times \pi =\sim 47 \times 10^9$ ly t_o).

We noticed that this last length had a link with an intriguing feature in the WMAP cosmic maps [36]: the early universe does not have a voice on the long wavelengths and does not sound like it would do if the space was apparently Euclidean and infinite. To explain, let's say that CMB temperature fluctuations can be decomposed into a combination of spherical harmonics. The relative magnitude of each spherical harmonic sets the "power spectrum" containing a signature of the geometry of the universe and the conditions at the time of emission of radiation. The power spectrum exhibits a series of peaks when the distance is measured between the regions of the sky of small and medium dimensions. In harmonic analysis of WMAP, these peaks are consistent with what is provided by the "Standard Model" for small angles. For separate regions of more than 60°, there is a loss of power that is not consistent with the predictions of the Standard Model. WMAP observed a quadrupole (harmonic which corresponds to an observation angle of 90°) seven times lower than what is expected with 0.2% probability that this difference occurs by chance. The low value of the quadrupole means it lacks the very long wavelengths [37].

Some cosmologists have proposed to attribute this anomaly to undiscovered physical laws that have governed the early universe. Our explanation for this phenomenon, which seems geometric, hinges on a space model in which large angular scales contain the largest "voids" of which the size of the space imposes a maximum length at the longitudinal wavelength, whence the ~45 billion ly t_o.

4.3.2. New "Bosonic" Flavors: Photonic Neutrino, Gravitonic Neutrino

We envisage the existence of massless sterile neutrinos, without charge, at the speed of light, under the aspect of a family other than that of the leptons, preferably the bosons, which implies spin quantum numbers with integer values. There are no theoretical arguments which forbid the neutrinos to not have rest mass or to have transitions between various sorts of bosons. Although they remain without rest mass, they have an intrinsic mass (or motion mass) that al-

lows them to oscillate.

If we consider that the sterile neutrinos propagate at the speed of light, in space or in matter, nothing forbids them to change identities often, to oscillate between two types of bosonic neutrinos: photon and graviton. The oscillation requires the existence of diverse flavors of bosons-neutrinos and differences between the intrinsic masses of the flavors. These alterations are related to the frequency of the oscillations, so that new oscillations measurements in the future could suggest how large the dissimilarities might be. Thus, photons and neutrinos-photons would have photon flavor, gravitons and neutrinos-graviton would have graviton flavor. The change from one flavor to another could provide a coherent explanation for the cosmological waves pattern (electromagnetic waves, gravitational waves, neutrino waves) [34].

5. Discussion

We think that the controversial experiment of 2011, carried out over a short distance, would have established the existence of massless sterile neutrinos without charge at the speed of light. During these oscillations neutrinos have disappeared from view. What did they do during this short period of time where they were undetectable?

Some scientists think that photon and neutrino invariably follow the same path, but that the speed of the neutrino is truly "superluminal". Others have raised the possibility that the particle has taken a shortcut through space-time. It's been a few decades that the scientific community is considering the existence of dimensions beyond the three that we perceive. To understand that, imagine that we lived on a sheet of paper two-dimensional, without that our senses reveal the third dimension of space. This sheet is bent and, to go from point A to point B, we are obliged to follow its curvature. While if we could take a third dimension, the path from A to B would be shorter. So if the neutrinos are experiencing one (or more) extra dimension to what we perceive, they were able to follow a shorter path than light. Hence the neutrinos apparently faster than light.

According to the theory of "neutrino temporal oscillation", neutrinos at the constant speed of light would follow a shortcut in the *space-time of three spatial dimensions that we perceive.* It is not the same thing as to take a shortcut in extra dimensions. Imagine that we lived in a tunnel in three dimensions, with our senses conditioned to always use the three dimensions of space. To move forward from point A to point B, regardless of whether the tunnel is straight or curved, we are obliged to follow the rule of the three dimensions which wants that we move away simultaneously our legs to the left and to the right, bring them back, then make a small jump forward, and continue like this up to point B. While if one could just put one foot before the other in order to take only one dimension, the path would be shortened. Thus, contrary to light (photons), certain particles (neutrinos) would be able to go through one (or two) of the three spatial dimensions we perceive. Neutrinos would have traveled faster than the

photon, not because they are faster, but because they have taken a shortcut through one dimension among those we perceive. This shorter path of the world in three spatial dimensions is similar to a longitudinal wave.

However, it appears that the most trivial explanation is that of massive neutrinos oscillations. This phenomenon would be deeply related to that of the disappearance of neutrinos: we cannot see the neutrinos during the quantum oscillations, because they move in metamorphosing at a speed under c, which remains in the vagueness but gives the certainty of a mass, which does not infringe causality based on the radial arrow of time of special relativity.

In strictly deterministic physics such a ghostly behaviour is as strange as the neutrino oscillations itself. It is legitimate to wonder if the currently accepted interpretation below the speed of light is really final and if behind the apparent rigor of retesting, some experiments do not conceal a part of the real profound nature of the neutrino. It is not only a question to challenge the statistical value of elegant and imprecise formalisms with which theorists of neutrinos juggle, but also to ask whether the interpretation being proposed for the 2011-2012 experience has reached finality and the bottom of things. Several observers have been led through the media to monitor the saga that led to the current interpretation of the neutrino velocity under c. They were able to find some weak points, like the optical cable errors which have at first reduced the velocity of propagation of neutrino to that of light, and then that one promptly has put slightly less than the speed of light in a vacuum. It suggests a retest having been oriented by the formalism of the postulates of relativity that, perhaps, paradoxically, does not correspond to the physical reality.

As currently formulated (see Section 3.1), the Standard Model has no explanations for neutrino mass. The original Standard Model prohibited neutrinos from having rest masses. Three types of neutrinos have long been established and, though by quite indirect evidence, they seem to transform into each other. In 1997-98, physicists have theorized that a neutrino must have mass by arguing that the mechanism of transformation does not allow for massless particles. The experiments concerned with oscillations did not make it possible to determine the absolute mass of each of the three types of neutrinos but to measure the difference between their masses.

A particle's total energy or *mass-energy* includes the particle's rest mass and momentum. Determining what portion of a moving particle's mass-energy comes from its rest mass and what portion is momentum turns out to be a thorny problem with neutrinos. In fact, we should just say that neutrinos *oscillate*: They change from one flavor to another. And to do this there must be differences between the masses of the different flavors; these differences are related to the frequency of the oscillation, and so the new oscillation measurements begin to suggest how large the differences might be. Neutrino physicists have two ways of observing oscillations: by neutrino disappearance or by neutrino appearance. If they make a beam of neutrinos with a single flavor, then find that some of the

neutrinos in the beam have disappeared, they can guess that the neutrinos have "oscillated" into a flavor that the detector is not sensitive to. Appearance experiments are more satisfying but much rarer: In this case, they detect a new neutrino flavor that was not produced by the original source. In both cases, the evidence is most convincing if the number of neutrinos varies as a function of distance traveled and energy according to the prediction [4]. The basic strategy for measuring neutrino oscillations seems simple: Take a source of neutrinos, either natural or artificial, let the neutrinos propagate for a known distance, and then measure as much as you can about their energy and flavor. If the amount of a given flavor (as a function of energy and distance) turns out to be what is expected according to the quantum-mechanical prediction that arises from the oscillation hypothesis, we had a spontaneous change of flavor.

In line with the transformist theory (see Section 3.1), two-thirds of the missing solar neutrinos would transform into muon neutrinos and tau neutrinos. Electron detectors can only pick up electron neutrinos, which would explain the deficit of solar neutrinos. The Sudbury Observatory detector in Ontario was designed to detect some of the neutrinos produced by the Sun. It contains heavy water: in a molecule of heavy water the hydrogen atoms ($_1H^1$) of light water are replaced by deuterium atoms ($_1H^2$). In a tank of light water, all neutrinos, regardless of their flavor (electron, muon or tau), can react with an electron and give off a flash of light. But only neutrinos-electrons can react with a deuterium atom, an element in heavy water, and give rise to two protons and an electron. Since the flash of light from this reaction is different from that of light water, physicists are able to determine the proportion of neutrinos-electrons that reach the Earth. Result: they enumerated a third of neutrinos-electrons and two thirds of neutrinos—muons and tau. For the theory of oscillation, this is direct proof of the transformation from one species to another.

Since the reasoning is perfect, experts believe it must be done this way. The fact remains that believing and proving make two. Are we dealing with the expert who overheard the theorist who saw the experimenter who saw with certainty such a neutrino transforming into another type of neutrino? A shortage of neutrinos of some type from the atmosphere and the Sun was recorded compared to what was expected by theory. All the experiments confirmed the phenomenon, not only for the neutrinos detected of natural origin, but also for the neutrinos captured by the detectors which are produced by nuclear power plants in normal operation or those emitted by particle accelerators. To explain the deficit observed in the flow of neutrinos produced by nuclear power plants, the assumption has been made of the presence of a fourth type of neutrino, the "sterile" neutrino, more massive than the three others and which would interact even less with ordinary matter. The major result of these experiments led to the conclusion that the enigma of the neutrino deficit stems from their oscillations and that this transformism can only be explained because they have mass. It is possible that it is wrong and we can see how.

But before, let's mention that highly qualified people can develop a theory, with relentless rigor, mathematics provided, reasoning without flaw, and yet the whole thing is false because the basic premises, postulated without proven foundation, turn out to be false. It is the same for a technological experiment; we can use advanced technicality, reduce uncertainties to a minimum, go through the stages with consistency, rigor and coordination, obtain an irreproachable result taking into account statistical uncertainties and systematic errors, and yet we can swim in error because of a conceptual error.

The truth is that scientists are unable to measure the energy of a neutrino and to know how far it traveled. Not knowing where he finished in the cycle of oscillations, they cannot calculate the relative proportions of the three flavors. Over large distances and long times, neutrinos oscillate so many time that they cannot keep track of the flavor mix it looks like a blur to them. Instead they take a "statistical average", described by a so-called flavor propagation matrix. From this matrix, astronomers can deduce what an observed ratio must originally have been [10]. Precision is missing over long and short distances, which gives as much certainty for a rest mass as for an intrinsic mass.

The whole system can turn out to be a lie because an alternative has been overlooked. Physicists failed to assume that the fluxes of muon and tau flavors could originate from the cosmos, that they could be cosmic neutrinos having a longitudinal wave as we saw in Section 4.1. According to the theory of temporal oscillation, the neutrino travel time is about a third of the photon travel time. The conceptual error is to believe that neutrino time is the same as photon time: this is why we perceive in a transverse second only one third of the predicted solar neutrinos. The same applies to muon-neutrinos and tau-neutrinos. The deuterium detector captures only one third of the electron neutrinos because it can capture only these. The light water electron detector, capable of capturing all three types of neutrino, captures one-third of what is expected from solar neutrinos, and one-third of what is expected for each of the other two kinds of neutrinos that come not from the Sun but from space. Each type of neutrino contributes one-third of the flux, hence all three-thirds. For the theory of neutrino temporal oscillation, it is the proof of the longitudinal (radial) wave which multiplies by three the ordinary flux.

In short, there is a distinction to be made between the true flow of neutrinos, which we equate to "radialism", and the false flow of neutrinos assimilated to "transformism". Physicists consider that the photon and the neutrino follow the same path. In our opinion, they do not follow the same path: the neutrino follows a radial path while the photon follows a transverse path. The radial path is, linearly (radially) speaking, ~ pi (π) times longer than the transverse path; it is like the length of an unfolded circumference becoming a straight line. This radial path of the neutrino is that of the true flux of the neutrinos. With respect to the radial reference, we can say that a photon flux travels one diameter while a neutrino flux travels the length of three diameters. This radial path of the photon,

used indiscriminately for the neutrino, is that of the false flux of the neutrinos. Since physicists do not differentiate between true neutrino flux and false neutrino flux, and only use the latter, it is no surprise that they almost always get a deficit of about two thirds of solar electron neutrinos.

6. Conclusions

We surmise the existence of non-sterile and sterile neutrinos, very light, conform to the Standard Model (original model prohibited neutrinos from having rest masses), but with two novel features: they use a shorter radial path than the photon and have bosonic flavors. We name this phenomenon "neutrino temporal oscillation". It is an alternative to the hypothesis of neutrino oscillation. The latter gives a complicated explanation of the periodic disappearance of neutrinos by allowing the three flavors of neutrinos electronic, muonic and tauic, all supposed of different masses, to metamorphose from one flavor to another. The somewhat *ad hoc* change in flavor of neutrinos during their journey appears to be supported by theory and therefore has the assent of the majority of cosmologists.

The measures of the observations of neutrinos and antineutrinos, based on the calculation of the probabilities of oscillation, bring into playing several parameters: the differences in mass from one flavor to another (although we always ignore the mass of the flavors, which seems paradoxical), the mixing angles between the different flavors and other complex numbers. They show more visible neutrinos that disappear than invisible ones that appear. These measures are quite indirect evidence of transgender metamorphoses during the journey. They quickly turned into conclusive evidence that can dispense with alternatives. Oddly, however, the observations show that in practice one can explain the detection of neutrinos by assuming that it is, on the one hand, transformist and, on the other hand, governed by longitudinal paths. This would not be so much a statistical error or a systematic error as a conceptual error.

To reconcile theory and observation, the two options seem *a priori* equally admissible. However, the theory of neutrino temporal oscillation, which implies an intrinsic mass of particles, gives the periodic disappearance of neutrinos a more sensible and fact-compatible explanation. It does not use superluminal speed; neither do the membranes of the eleven-dimensional universe of M-theory, nor the strings of string theory. Its interpretation has the merit of revealing the longitudinal wave which is sorely lacking in current physics while respecting the inviolability of the speed of light of special relativity in our four-dimensional universe. This imbalance, between the "neutrino oscillation" which transforms the flavors of neutrinos and the "neutrino temporal oscillation" which transforms the path of the neutrino over time, can evolve, and possibly even toggle.

Conflicts of Interest

The author declares no conflicts of interest regarding the publication of this paper.

References

[1] Kearns, E., Kajita, T. and Totsuka, Y. (1999) *Scientific American*, **281**, 64-71. https://doi.org/10.1038/scientificamerican0899-64

[2] Hirsch, M., Päs, H. and Porod, W. (2013) *Scientific American*, **308**, 40-47.

[3] Overbye, D. (2011) Tiny Neutrinos May Have Broken Cosmic Speed Limit. *IIT-BHU Chronicle*, September 22.

[4] Kaneyuki, K. and Scholberg, K. (1999) *American Scientist*, **87**, 222-231. https://doi.org/10.1511/1999.24.817

[5] Glashow, S.L. (1961) *Nuclear Physics*, **22**, 579-588. https://doi.org/10.1016/0029-5582(61)90469-2

[6] Weinberg, S. (1967) *Physical Review Letters*, **19**, 1264-1266. https://doi.org/10.1103/PhysRevLett.19.1264

[7] Salam, A. (1994) Weak and Electromagnetic Interactions. World Scientific Series in 20th Century Physics Selected Papers, World Scientific, Singapore, 244-254. https://doi.org/10.1142/9789812795915_0034

[8] Brumfiel, G. (2012) Neutrinos Not Faster than Light. *Nature*. https://doi.org/10.1038/nature.2012.10249

[9] Bagdoo, R. (2015) Recycled Relativity. https://vixra.org/abs/1506.0125

[10] Gelmini, G.B., Kusenko, A. and Weiler, T.J. (2010) *Scientific American*, **302**, 38-45. https://doi.org/10.1038/scientificamerican0510-38

[11] Maitte, B. (1981) La lumière, Points. Édition du Seuil, Paris, 159, 233, 236-238.

[12] Whittaker, E.T. (1910) A History of the Theories of Aether and Electricity from the Age of Descartes to the Close of the Nineteenth Century. Dublin University Press Series, Dublin. https://doi.org/10.5962/bhl.title.19630

[13] Radounskaïa, I. (1972) Idées folles. Éditions MIR, Moscou, 15-17, 23, 56.

[14] Trotman, R.E. (1966) Longitudinal Space-Charge Waves. Chapman and Hall Ltd., London.

[15] Bethe, H.A. (1939) *Physical Review*, **55**, 434-456. https://doi.org/10.1103/PhysRev.55.434

[16] Gamow, G. (1938) *Physical Review*, **53**, 595-604. https://doi.org/10.1103/PhysRev.53.595

[17] Trefil, J. (1988) The Darkside of the Universe. Anchor Books, Doubleday, New York, 156-157.

[18] Bahcall, J.N., *et al.* (1995) *Nature*, **375**, 29-34. https://doi.org/10.1038/375029a0

[19] Bethe, H.A. (1991) The Road from Los Alamos. Touchtone Book, Simon & Schuster, New York, 246-251.

[20] Bahcall, J.N. (1989) Neutrino Astrophysics. Cambridge University Press, Cambridge.

[21] Close, F. (2010) Neutrino. Oxford University Press, Oxford, 29-35.

[22] Bethe, H.A. and Brown, G. (1985) *Scientific American*, **252**, 60-68. https://doi.org/10.1038/scientificamerican0585-60

[23] Aldhous, P. (1991) *Nature*, **350**, 643. https://doi.org/10.1038/350643a0

[24] Hirata, K.S., *et al.* (1987) *Physical Review Letters*, **58**, 1490-1493. https://doi.org/10.1103/PhysRevLett.58.25

[25] Bionta, R.M., *et al.* (1987) *Physical Review Letters*, **58**, 1494-1496.

[26] Arnett, W.D., Bahcall, J.N., Kirshner, R.P. and Woosley, S.E. (1989) *Annual Review of Astronomy and Astrophysics*, **27**, 629.
https://doi.org/10.1146/annurev.aa.27.090189.003213

[27] Franson, J.D. (2011) Apparent Correction to the Speed of Light in a Gravitational Potential.

[28] Panagia, N. (2008) *Chinese Journal of Astronomy and Astrophysics*, **8**, 155.

[29] Chen, P., Bloom, E., Madejski, G. and Patrosian, V. (2004) Proceedings of the 22nd Texas Symposium on Relativistic Astrophysics.
https://www.osti.gov/biblio/878411-proceedings-texas-symposium-relativistic

[30] Imshennik, V.S. and Ryazhskaya, O.G. (2004) *Astronomy Letters*, **30**, 14.
https://doi.org/10.1134/1.1647473

[31] Lychkovskiy, O. (2008) Analysis of the SN 1987A Two-Stage Explosion Hypothesis with Account for the MSW Neutrino Flavour Conversion.

[32] Trinh, X.T. (1988) La mélodie secrète. Fayard, Paris, 153.

[33] Riazuelo, A. (2020) Les neutrinos cosmologiques. Pour la Science, Paris, Hors-Série, No. 106, 72, 73.

[34] Bagdoo, R. (2020) *Journal of Modern Physics*, **11**, 616-647.
https://doi.org/10.4236/jmp.2020.115041

[35] Jayawardhana, R. (2013) Neutrino Hunters. HarperCollins Publishers Ltd., New York, 14, 110, 172.

[36] Smoot, G. and Davidson, K. (1994) Wrinkles in Time. Harper Perennial, New York, 276, 277, 281-283.

[37] Luminet, J.-P. (2001) L'Univers chiffonné. Folio essais, 444-446.

A Lunar LIGO for NASA's Return to the Moon

Thomas L. Wilson

NASA, Johnson Space Center, Houston, TX, USA
Email: Thomas.Wilson@cern.ch

Abstract

The feasibility of a Lunar LIGO (Laser Interferometer Gravitational-Wave Observatory) was introduced in 1986 as part of NASA's planned return to the Moon by the end of the last century. That return to the Moon mission was cancelled, but is once again planned as Artemis in 2024. In this paper, the feasibility of such a Lunar LIGO as part of NASA's return there will be discussed for that program. Details of the physics of the original Lunar LIGO proposal as a potential portion of future lunar base astronomy and astrophysics designs are presented. Results from NASA's original planned return to the Moon to establish a gravitational wave observatory there are presented and discussed.

Keywords

Gravitational Waves, Astronomy on the Moon, Astrophysics

1. Introduction

The conceptual design of NASA's planned Lunar base was addressed at Stanford University in 1989 [1] [2] [3], with a Lunar LIGO (Laser Interferometer Gravitational-Wave Observatory) first discussed in [3]. The present author organized the Stanford workshop and its focus on gravitational radiation, and pursued the Lunar LIGO concept for years thereafter [4]-[10] while serving as lead for physics and astrophysics mission development in the Solar System Exploration Division at NASA's Johnson Space Center. That lunar return effort continued until it was terminated for lack of funding in 1998.

The subsequent work was presented in various ways [4]-[10] while the Earth-based LIGO concepts were undergoing initial development. The latter obviously have come to marvelous fruition in the quarter century since, with the advent of Advanced LIGO and Advanced VIRGO systems [11] [12] [13] in the LIGO and LISA [14] Scientific Collaborations (LSC) established in 1997. In-

cluded are their marvelous discoveries in Earth-based gravitational wave astronomy, not to mention the discovery of gravitational waves *per se* [16].

The question presented here is the virtue of adding a Lunar LIGO to these conceptual configurations [3]-[16], and how that can augment the Earth-based LIGO systems. The result is a superior gravitational wave measurement system for examining gravitational waves and their astrophysical sources in the solar system and surrounding galaxies. This is not available using the Earth-based systems alone.

2. Why Lunar LIGO?

The preliminary proposal [8] [9] that the Earth-based multi-LIGO system can be augmented with a Lunar LIGO appears promising. It consists of emplacing a modest LIGO optical system on the Moon, proving to be a simple and advantageous application in the vacuum environment of the lunar surface. Less seismic, gravity gradient, tidal, and acoustic noise will yield greater sensitivity at frequencies between 0.25 and 3 Hz on the lunar surface.

Emplacement can be accomplished using unmanned robotic landers such as the Artemis project or by any manned landing program.

Mechanical decoupling from the Earth-based antennas will yield a method of noise filtering (coincidence with terrestrial antennas over their common frequencies) and provide a significant sanity check on wave versus pulse events.

Operating along with Earth-based antennas, it will provide a longer baseline for the localization of gravitational wave sources. This gives 50 times better angular resolution than the Earth-based antennas alone. Also the lunar antenna will not be mechanically or geophysically coupled to the terrestrial antennas, thus providing a significant confidence or voting factor for detected events.

The distance between the Earth and Moon provides a long parallax baseline with terrestrial antennas for locating the sources of a gravitational event. Given that the lunar vacuum eliminates the need for long evacuated tunnels, a minimal Fabry-Perot antenna could be placed on the Moon using three robotic landers, one containing the laser source, the beam splitter, the detector, recycle mirrors, cavity mirrors, and other optics. The other two landers would contain the end mirrors of the interferometer arms, and provide closure phase along the third leg.

The lack of arm enclosures allows the arms to be extremely long, limited only by a lunar radius of 1738 km. Appropriate choice of landing sites could allow for longer arms by taking advantage of local topography. One can easily adjust the length of the arms by moving the landers containing the end mirrors [7]. The entire Moon can also be visualized as a gravitational detector itself [15] by configuring it with an array of seismometers.

The lunar environment will likewise provide significant advantages. It will eliminate the need to maintain a vacuum in the interferometer arms over the life-cycle of the antenna. This, coupled with the lack of construction costs

needed to enclose and pull a vacuum in the arms, should offset much or all of the cost of launch and delivery. Lesser surface gravity will prove better for mechanical isolation of optics [6].

Obviously, there are distinct advantages through which Lunar LIGO and LISA Pathfinder programs can mutually overlap and supplement one another. One might even begin by transporting other configurations to the lunar base to become a lunar LIGO.

An advanced, man-tended version of the Lunar LIGO would allow for even more flexibility (for instance **Figure 1**, adapted from [8]). Detectors and mirrors could be repaired and/or upgraded by the lunar base personnel. The antenna could be actively monitored and seismic data could be screened using gravimeters to aid in the data's noise analysis. For instance, a large array of antennas could be built to allow for better spurious signal elimination by coincidence [7]. A large number of antennas would be easier to build and maintain on the Moon than on the Earth due to the lack of evacuated tunnels.

3. Conclusions

In conclusion, this investigation shows that a lunar-based Fabry-Perot gravitational wave antenna would provide a valuable complement to Earth-based systems, both for conclusive first detection and for continued gravitational wave astronomy there. Furthermore, due to unique features of the lunar environment, the life-cycle costs could be competitive with Earth-based antennas.

This investigation further shows that a lunar-based Fabry-Perot gravitational wave antenna would provide a valuable complement to the Earth-based systems, both for conclusive, first detection and for continued gravitational wave astronomy. Furthermore, due to unique features of the lunar environment, the life-cycle costs could be competitive with Earth-based antenna systems.

After decades of studying the elusive phenomena predicted by Einstein's general
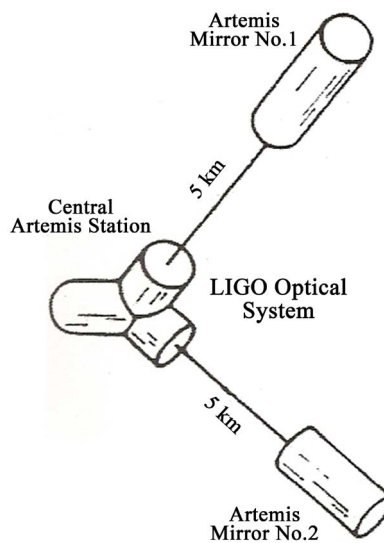
Figure 1. Lunar LIGO using Artemis.

theory of relativity, gravitational radiation has been discovered [16]. It is important that such research be continued, and one way to do so is to expand our notions of the Moon to serve as another platform for enhancing these investigations.

In closing, other proposals have also been developed, which include DECIGO, GLOC [15] [17] [18].

This very preliminary proposal that the Earth-based multi-LIGO system can be supplemented by a lunar LIGO system appears promising.

Conflicts of Interest

The author declares no conflicts of interest regarding the publication of this paper.

References

[1] Potter, A. and Wilson, T.L. (1989) Physics & Astrophysics from a Lunar Base. AIP Conference Proceedings, No. 202, American Institute of Physics, New York.

[2] Weber, J. (1990) *AIP Conference Proceedings*, **202**, 159-202.
https://doi.org/10.1063/1.39128

[3] Stebbins, R.T. and Bender, P.L. (1990) *AIP Conference Proceedings*, **202**, 188-201.
https://doi.org/10.1063/1.39103

[4] Wilson, T.L., Blome, H.J. and LaFave, N. (1996) *Space V, Proc. of Fifth Int'l. Conf. on Space'96*, **2**, 861-863.

[5] LaFave, N. and Wilson, T.L. (1995) Gravitational Wave Astronomy from the Moon. *Lunar and Planetary Science Conference*, Houston, 13-17 March 1995, 817-818.

[6] Wilson, T. and LaFave, N. (1994) Astronomy Session: Gravitational Wave Astronomy & the Lunar LIGO Concept. *Space IV*, Vol. 2, 1442-1451.

[7] Wilson, T.L. and LaFave, N. (1994) Lunar LIGO & Gravitational Wave Astronomy on the Moon. *Lunar & Planetary Science Conference*, Vol. 3, Houston, 1499.

[8] LaFave, N. and Wilson, T.L. (1993) Lunar LIGO: A New Concept in Gravitational Wave Astronomy. *Lunar & Planetary Science Conference*, Houston, 15-19 March 1993, 841.

[9] LaFave, N. and Wilson, T.L. (1992) Astronomy on the Moon. *Lunar & Planetary Science Conference*, Houston, 16-20 March 1992, 751.

[10] Wilson, T., *et al.* (2005) Gravitational Wave Astronomy on the Moon. *Proceedings of the Space Nuclear Conference*, San Diego, 5-9 June 2005, Paper 1158.

[11] Abramovici, A., *et al.* (1992) *Science*, **256**, 325.
https://doi.org/10.1126/science.256.5055.325

[12] LIGO Details Can Be Found at ligo.caltech.edu.

[13] VIRGO Is a Large European Michelson Interferometer Operating in Italy.

[14] LISA (Laser Interferometer Space Antenna) Is the First Proposed Orbital Space-Based Gravitational Wave Antenna. See lisa.nasa.gov.

[15] DECIGO (DECi-hertz Interferometer Grav. Wave Observatory).

[16] Abbott, B.P., *et al.* (2016) *Physical Review Letters*, **116**, Article ID: 061102.
https://doi.org/10.1103/PhysRevLett.116.061102

[17] GLOC, Gravitational-Wave Lunar Observatory for Cosmology.

[18] Johnson, W.W. (1989) *AIP Conference Proceedings*, **202**, 183-187.

Call for Papers

Journal of Modern Physics

Journal of Modern Physics **(JMP)** is an international journal dedicated to the latest advancement of modern physics. The goal of this journal is to provide a platform for scientists and academicians all over the world to promote, share, and discuss various new issues and developments in different areas of modern physics.

Editor-in-Chief

Prof. Yang-Hui He   City University, UK

Subject Coverage

Journal of Modern Physics publishes original papers including but not limited to the following fields:

Biophysics and Medical Physics	New Materials: Micro and Nano-Mechanics and Homogeneization
Complex Systems Physics	Non-Equilibrium Thermodynamics and Statistical Mechanics
Computational Physics	Nuclear Science and Engineering
Condensed Matter Physics	Optics
Cosmology and Early Universe	Physics of Nanostructures
Earth and Planetary Sciences	Plasma Physics
General Relativity	Quantum Mechanical Developments
High Energy Astrophysics	Quantum Theory
High Energy/Accelerator Physics	Relativistic Astrophysics
Instrumentation and Measurement	String Theory
Interdisciplinary Physics	Superconducting Physics
Materials Sciences and Technology	Theoretical High Energy Physics
Mathematical Physics	Thermology
Mechanical Response of Solids and Structures	

We are also interested in: 1) Short Reports—2-5 page papers where an author can either present an idea with theoretical background but has not yet completed the research needed for a complete paper or preliminary data; 2) Book Reviews—Comments and critiques.

Notes for Intending Authors

Submitted papers should not have been previously published nor be currently under consideration for publication elsewhere. Paper submission will be handled electronically through the website. All papers are refereed through a peer review process. For more details about the submissions, please access the website.

Website and E-Mail

https://www.scirp.org/journal/jmp   E-mail: jmp@scirp.org

What is SCIRP?

Scientific Research Publishing (SCIRP) is one of the largest Open Access journal publishers. It is currently publishing more than 200 open access, online, peer-reviewed journals covering a wide range of academic disciplines. SCIRP serves the worldwide academic communities and contributes to the progress and application of science with its publication.

What is Open Access?

All original research papers published by SCIRP are made freely and permanently accessible online immediately upon publication. To be able to provide open access journals, SCIRP defrays operation costs from authors and subscription charges only for its printed version. Open access publishing allows an immediate, worldwide, barrier-free, open access to the full text of research papers, which is in the best interests of the scientific community.

- High visibility for maximum global exposure with open access publishing model
- Rigorous peer review of research papers
- Prompt faster publication with less cost
- Guaranteed targeted, multidisciplinary audience